NASA RESEARCH PROGRAM

Final Technical Report

The Roles of Fluid Motion and Other Transport Phenomena
in the
Morphology of Materials

Contract NAG8-749

September 1988 - December 1992

Prepared for

Marshall Space Flight Center

November 1993

D. A. Saville
Department of Chemical Engineering
Princeton University
Princeton, NJ 08544

TABLE OF CONTENTS

      The role of transport phenomena in protein crystal growth
        J. Crystal Growth **108** 8-18 (1991)

      Electrostatic interactions between a protein molecule and a charged surface:
      Part I, Development and testing of a computational model.
        (manuscript to be submitted to *J. Colloid Interface Science*)

      Electrostatic interactions between a protein molecule and a charged surface:
      Part II, The free energy of a lysozyme molecule near a flat plate.
        (manuscript to be submitted to *J. Physical Chemistry*)

      Protein crystal growth: the influence of colloidal interactions.
        PhD Thesis by M. L. Grant accepted by Princeton University,
        January 1992

ABSTRACT

We studied two crystallization problems: the growth of protein crystals, in particular the influence of colloidal forces and convection, and the influence of interface resistance on the growth of dendritic crystals. The protein study involved both experimental and theoretical work; the work on dendrites was entirely theoretical.

In our study of protein crystallization, we carried out experiments where crystals were grown in the presence and absence of natural convection. No evidence was found that convection retards crystal growth. The theoretical study focused on the influence of colloidal forces (electrostatic and London-van der Waals) on the interaction between a protein molecule and a flat crystal surface. It was shown that the interaction is extremely sensitive to colloidal forces and that electrostatic interactions play a strong role in deciding whether or not a molecule will find a favorable site for adsorption.

In our study of dendritic growth, we examined the role of an interfacial resistance on the selection processes. Using a computational scheme we found that the selected velocity is strongly dependent on the magnitude of the interfacial resistance to heat transfer. This is a possible explanation for discrepancies between the theoretical and experimental results on succinonitrile.

SUMMARY OF THE WORK ON DENDRITIC GROWTH

The work on proteins is summarized in the attached thesis and papers; the work on dendritic growth is in progress (C. A. Martin's PhD thesis) and so a short description of the results thus far will be given here.

One outstanding problem in dendritic growth is to understand the mechanism by which the tip velocity and shape are determined. The currently accepted model is called *microscopic solvability*. According to that theory, the tip radius and velocity are set by the anisotropic nature of the surface energy of the crystal melt interface. The differential equations describing the tip growth balance the freezing process against heat conduction to the melt with the interface temperature governed, in part, by the Gibbs-Thomson condition. The Gibbs-Thomson effect describes how interface curvature alters the melting point and this is where the anisotropic nature of the surface energy (the so-called interfacial tension) enters. The selected velocity and curvature are determined by insisting that the tip must be smooth, i.e., have a continuously turning tangent. This theory does not agree well with existing data on several soft materials. Our approach has been to include the effect of a resistance to heat transfer at the surface. We use a boundary integral technique to solve the relevant equations which include the Gibbs-Thomson effect as well as an anisotropic resistance. We find that smooth tips can be obtained with an *isotropic* interfacial tension but an *anisotropic* interface resistance. Our results were reported at the AICHE Meeting in November of 1992; publications and Martin's PhD thesis are in preparation.

Ivantsov[1] identified the shape of a single needle crystal growing into its supercooled melt as a paraboloid with Péclét number $Pe = \rho V/2D$, where ρ is the tip radius, V is the freezing velocity, and D is the thermal diffusivity. For a given supercooling, Ivantsov theory allows a family of solutions satisfying $\rho V = $ constant, but provides no means for distinguishing the shape and velocity. Current work addresses the dendrite shape selection problem using the approach of microscopic solvability theory, but allows a deviation from equilibrium due to anisotropic interfacial attachment kinetics, introduced through a transport coefficient empiricism.

Microscopic solvability theory[2] is the most recent of shape selection theories focusing on the role of interfacial free energy ("surface tension"), a force which typically acts over microscopic length scales, in shape selection. The Ivantsov solution appears under this approach only in the limiting case of zero surface tension. In the general case, surface tension must act anisotropically in order for the solvability condition of a smooth tip (one with zero slope) to be satisfied; the selected shape and velocity depend on the degree of anisotropy.

The current work explores the two-dimensional shape selection problem as a synthesis of the effects of interfacial free energy and attachment kinetics, each of which may act anisotropically. A kinetic resistance to interfacial growth depresses the interface temperature T relative to its equilibrium (Gibbs-Thomson) value T_{EQ}; the resulting boundary condition replaces the equilibrium assumption and introduces the interphase transport coefficient h,

$$LV \cos \theta = h(\theta) (T_{EQ} - T),$$

where L is the latent heat per unit volume and θ is the angle between the crystal axis and a unit normal to the interface. The strength of the kinetic effect is described by a reciprocal Biot number $1/Bi = kV/(2Dh)$, where k is the thermal conductivity.

[1] G. P. Ivantsov, *Dokl. Akad. Nauk, SSSR* **58** (1947) 567.

[2] D. A. Kessler, J. Koplik and H. Levine, *Adv. in Phys.* **37** (1988) 255.

Figure 1 shows the interaction between kinetic and surface tension mechanisms in shape selection. When the dimensionless surface tension parameter d_0 is zero, three zero-tip-slope solutions exist including the Ivantsov case at $1/Bi = 0$. In the range $0 < d_0 < 00767$ two solutions exist, and beyond that range the effect of isotropic surface tension is sufficiently strong to prohibit the existence of smooth-tipped shapes.

The method developed for the current work approximates the shape of the interface by a series of orthogonal (Laguerre) polynomials, and has proved useful in generating results in the low-Pe regime relevant for comparison with experimental data. Figure 2 shows the shape selection parameter $\sigma^* = d_0 / Pe^2$ approaches a constant value of .0142 in the low Pe limit, under the given conditions of 10% anisotropy of surface tension and no kinetic resistance. Continuing work focuses on introducing kinetic effects at low Pe, to allow fitting of kinetic parameters to published data for succinonitrile and pivalic acid.
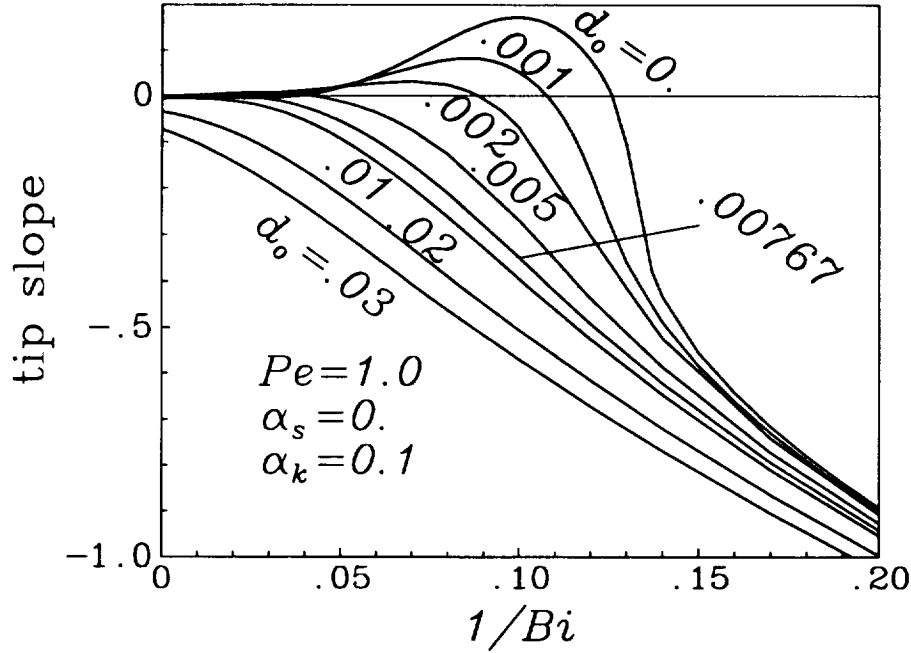

Figure 1: Shape selection curve under conditions of anisotropic kinetics ($\alpha_k = 0.1$) and isotropic surface tension ($\alpha_s = 0$) at $Pe = 1$. Admissible shapes have zero tip slope.
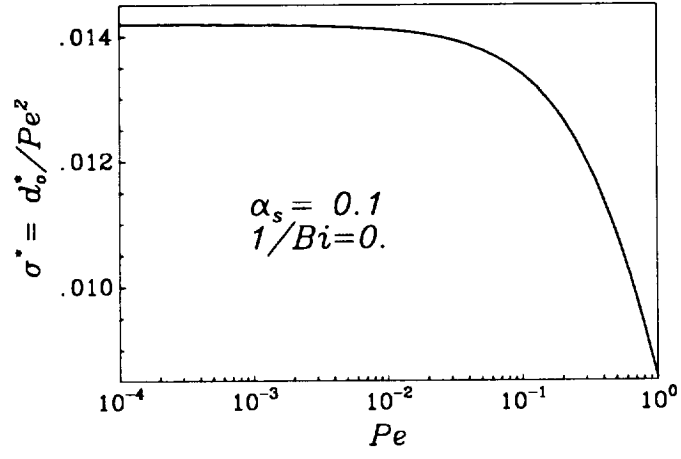
Figure 2: Shape selection parameter σ^* as a function of Pe, under conditions of anisotropic surface tension ($\alpha_s = 0.1$) and no kinetic resistance.

BIBLIOGRAPHY OF THESES, PUBLICATIONS, AND PRESENTATIONS FROM THIS WORK

1. M. L. Grant *Protein crystal growth: the influence of colloidal interactions*. PhD Thesis, January 1992, (223 pages).

2. C. A. Martin *The influence of interfacial resistance on the dendrite velocity selection problem* (tentative title) PhD Thesis in preparation.

3. The role of transport phenomena in protein crystal growth. *J. Crystal Growth* **108** 8-18 (1991)

4. Electrostatic interactions between a protein molecule and a charged surface:
   Part I Development and testing of a computational model.
   (manuscript to be submitted to *J. Colloid Interface Science*)

5. Electrostatic interactions between a protein molecule and a charged surface:
   Part II The free energy of a lysozyme molecule near a flat plate.
   (manuscript to be submitted to *J. Physical Chemistry*)

6. Convection and diffusion around a needle-shaped crystal.
   AICHE Annual Meeting, San Francisco November 1989.

7. Applications of the boundary integral method to problems in needle-shaped crystal growth.
   Fifth International Colloquium on Free Boundary Problems and Applications, Montreal Canada, June 1990.

8. The role of transport processes in protein crystallization.
   Gordon Conference on Gravitation al Processes, London, NH June 1991.

9. Kinetic effects in 2D dendritic crystal growth.
   AICHE Annual Meeting, Miami, November 1992.

APPENDICES

The role of transport phenomena in protein crystal growth

M.L. Grant and D.A. Saville

Department of Chemical Engineering, Princeton University CN 5263, Princeton, New Jersey 08544-5263, USA

The idiosyncrasies of protein crystal growth are widely known: crystals often stop growing before reaching a size adequate for X-ray diffraction studies: sometimes their quality is poor. The reasons for this behavior are not well understood. We investigated several transport mechanisms to ascertain whether they might play significant roles in protein crystal growth. Scale analyses were used to establish the order-of-magnitude of forces arising from natural convection. They show that shear forces are probably too small to dislodge molecules from the crystal surface or alter protein structure by unfolding. Strong shear fields can align molecules, but we find that the shear arising from natural convection is much too weak to alter the orientation distribution of protein molecules. Crystal growth rates are set by a balance between attachment kinetics and transport to the crystal surface and, according to our analysis, crystals prepared in growth rate studies are usually too small to be affected by either diffusion or convective transport. The role of salt rejection at the crystal–fluid interface was also investigated. Salt rejection could influence growth by changing the transport velocity normal to the interface or by changing the driving force for diffusion. The magnitude of each effect appears too small to be significant.

1. Introduction

Obtaining suitable crystals is frequently the rate-limiting step in the process of determining the full three-dimensional structure of protein molecules by X-ray diffraction. Protein crystallographers are familiar with the difficulties of finding conditions which produce crystals of any sort, let alone the large single crystals desired for diffraction studies. Protein crystals tend to grow slowly and often reach a terminal size too small to produce acceptable diffraction patterns. Occasionally, protein crystals grow readily but are too disordered to diffract well. The outcome of any crystal growth experiment depends on the complex interactions among the protein, solvent, buffer, and precipitating agent(s) which are present in the system. Few of these interactions are well characterized and many of them are highly specific to a given system. A discussion of all these phenomena is beyond the scope of this work. We focus, instead, on the possible effects of transport phenomena on protein crystal growth.

Crystallization is an inherently nonequilibrium process which creates gradients in system properties such as solute concentration. The gradients produced are affected by various transport processes and so the relative rates of growth kinetics and transport to the crystal surface determine the path the system takes towards equilibrium. Any process which alters those rates changes the properties of the resultant crystals. For example, recent work by Pusey, Witherow and Naumann [1] clearly shows the presence of buoyancy-driven flows and indicates that crystals grown in the presence of forced convection grow slower than in its absence. The reasons for this behavior are unknown.

Convection might alter growth processes by retarding attachment at the surface (which inhibits kinetics) or by feeding the crystal more protein (which enhances mass transfer). Three mechanisms have been proposed whereby shear produced by flow could inhibit growth kinetics: stripping molecules from the surface, imposing a preferred (unfavorable) orientation on protein molecules near the crystal, or denaturing protein molecules as they approach the surface. If, in the

attachment process, a molecule samples many orientations and possible binding sites before settling into its ultimate location, it is important that each molecule has ample time at the attachment site before the arrival of the next growth unit. Convection might increase the arrival rate to the point where protein molecules are trapped in unfavorable positions; this would produce defects which inhibit further growth.

There are other processes which affect the relative rates of transport and attachment. Several solutes are present in the system, and each must be transported to or from the surface as the crystal grows. Interactions between the protein and precipitating agent, for example, can alter the chemical potential of the protein so that the driving force for diffusion is diminished. This might provide additional time for the molecules at the surface to bind properly and produce a more ordered crystal. Contaminants which compete for binding sites on the crystal surface can inhibit growth, especially when the contaminant hinders attachment of protein to the crystal. This process not only reduces the growth rate, but halts crystal growth when the surface is completely "poisoned" by the contaminant.

Our calculations indicate that none of the convective processes investigated here is strong enough to affect the growth of protein crystals. Nevertheless, some experimental evidence exists which seems to imply that buoyancy-driven flow influences crystal growth rates and quality. Pusey et al. [1] observed convection plumes rising from growing tetragonal lysozyme crystals and noted that the plume velocity was of the same order as that expected from scaling arguments, i.e. about 30 μm/s (cf. section 2). They then subjected small crystals (< 20 μm) to forced convection of the same strength and noted that the growth rate decreased monotonically with time after convection commenced. Although the long-term effect of convection is to reduce growth rates, they also reported an initial enhancement of crystal growth due to flow. No evidence has been presented which indicates the mechanism for this behavior.

On the molecular scale, recent work by De Lucas et al. [2] shows that crystals grown in microgravity aboard the space shuttle diffracted to higher resolution than those grown in the laboratory. They conducted eleven experiments and found that the internal order of crystals from the space experiment was greater than that of terrestrial crystals. Additionally, two crystals grew larger than any reported in ground-based experiments. In the absence of evidence to the contrary, they attributed these beneficial effects to the reduction of buoyancy-driven motion.

Given these conflicting results, the purpose of this paper is to present our analyses and provide a context to investigate other mechanisms. The presentation is organized as follows. First, we present order-of-magnitude analyses to assess the strength of shear forces arising from natural convection. These scale analyses are used to evaluate the possibility that shear might pull molecules from the surface, confer a preferred orientation on molecules near the surface, or denature the protein by altering the protein's structure. An analysis of the effects of mass transfer by diffusion is presented next. This is followed by an inquiry into the effect of salt rejection at the surface of the growing crystal. None of these mechanisms is found to have much effect on the growth processes. The final section is a more speculative discussion on the way convection might alter crystal growth in the presence of an inhibitor.

2. Effects of fluid flow on protein crystal growth

It has been suggested that the terminal size of the crystals could result from the effects of natural convection due to disruption of crystal bonds by hydrodynamic forces. Protein molecules are held in the crystal lattice by weak hydrogen bonds ($\Delta H = -3$ to -6 kcal/mol in vacuo) which are not well characterized [3]. If the force required to break the crystal bonds is comparable to that produced by the shear flow at the crystal surface, flow might remove protein molecules from the crystal. This situation is depicted schematically in fig. 1a. Because the shear stress at the surface increases with crystal size, this would act as a self-limiting process. An order of magnitude estimate of the viscous stress will indicate whether
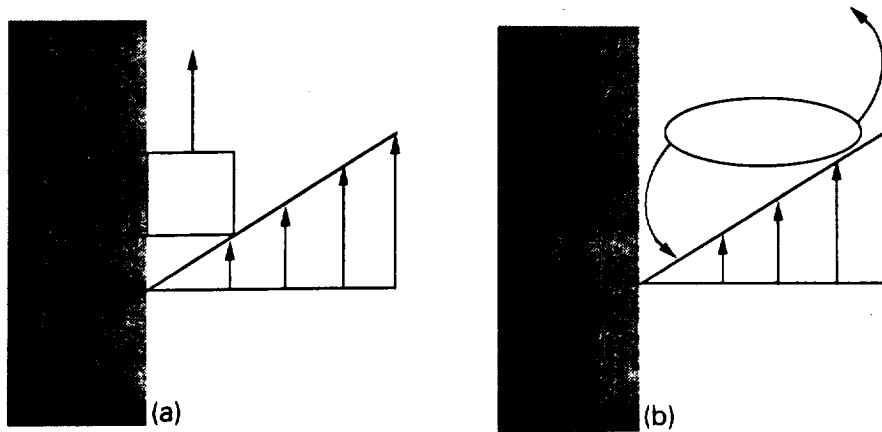
Fig. 1. Two mechanisms by which shear might disrupt protein crystal growth. (a) Shear flow removes protein molecule from crystal surface. (b) Shear flow imposes a preferred orientation on the molecule at the surface.

convective removal of molecules from the surface is a reasonable mechanism to halt crystal growth.

The shear stress at the surface is due to buoyancy driven natural convection around the growing crystal. This flow is caused by density differences between the fluid adjacent to the surface of the object and the bulk solution far from the crystal. The strength of the motion is characterized by the Grashof number [4], the ratio of the buoyancy force driving the motion to the viscous resistance. The Grashof number is defined as

$$Gr \equiv R^3 g \Delta \rho / \rho_\infty \nu^2, \qquad (2.1)$$

where g = gravitational acceleration, $\Delta \rho$ = density difference, ρ_∞ = bulk fluid density, ν = kinematic viscosity, and R = crystal radius. The ratio of the molecular transport coefficients for momentum and diffusion is the Schmidt number, $Sc = \nu/D$, where D = diffusion coefficient for the solute. For small Grashof numbers but large Schmidt numbers, the motion scales on the square root of the ratio of Grashof and Schmidt numbers due to the boundary layer structure of the flow [4].

For a 1 mm diameter spherical crystal in a 5% (w/v) lysozyme solution, we estimate that $\Delta \rho / \rho_\infty$ is roughly 0.002 (see section 3). This yields a Grashof number of about 2; the Schmidt number for lysozyme is 10^4. In a weak flow of this sort, the characteristic velocity, u_∞, equals (Gr/

$Sc)^{1/2} \nu/R$ and the shear rate, Γ, is u_∞/δ, with δ the boundary layer thickness [4]. Accordingly, the shear stress, τ, at the surface is given by

$$\tau = \mu \Gamma = \mu u_\infty / \delta, \qquad (2.2)$$

where μ is the fluid viscosity. Under the circumstances noted above, the characteristic velocity is 3×10^{-3} cm/s, δ is 8×10^{-3} cm, and the shear rate is about 0.36 s^{-1}. The shear stress acting on the crystal surface in a solution where $\mu = 1 \times 10^{-3}$ Pa s is approximately 3.6×10^{-4} Pa. If we take Fiddis et al.'s [5] approximation of the lysozyme molecule being a cube 30.9 Å on a side, then the shear force acting on a molecular at the surface is approximately 3.4×10^{-21} N.

In the spirit of our order of magnitude analysis, we compare the shear forces with intermolecular forces. In what follows, we examine the potential between molecules and make simplifying approximations which tend to underestimate the strength of the bonds. In order not to rule out the importance of fluid flow prematurely, we deliberately weaken our estimates of the bond strength. Nevertheless, our results indicate that even the weakest intermolecular bond is still thousands of times as strong as typical shear forces, indicating that this level of approximation is appropriate. If the strengths of the forces were commensurate, a more careful estimate would be required.

To provide a simple estimate, we approximate the interaction potential between any two atoms as a Lennard-Jones 6-12 potential with electrostatic interaction:

$$U = \frac{A}{r^6} + \frac{B}{r^{12}} + \frac{q_1 q_2}{4\pi\epsilon\epsilon_0 r}, \tag{2.3}$$

where A and B are constants for the particular bond of interest, q_1 and q_2 are the partial charges on the atoms in the bond, ϵ is the dielectric constant of the medium (water), ϵ_0 is permittivity of free space, and r is the separation between the atoms. Hagler et al. [6] determined the values of A, B, q_1 and q_2 for the bonds in amide crystals and found that the form of eq. (2.3) accounted adequately for the observed interactions. Rather than find the entire potential by performing a summation of eq. (2.3) over all the pairs on both molecules, we take the weakest interatomic bonding interaction as representative of the intermolecular bond. From the values of A, B, q_1 and q_2 reported by Hagler et al., the bond energies were calculated from the value of U_{min} at the equilibrium separation (where $F = -dU/dr = 0$) and the maximum attractive force was calculated by determining the force where $dF/dr = -d^2U/dr^2 = 0$. The weakest bond is that with the shallowest potential well having $U_{min} < 0$; i.e., metastable excited states with $U_{min} > 0$ are excluded. We computed bond energies for hypothetical bonds between each of the species listed by Hagler et al. [6] and chose the weakest. Since we seek a weak characteristic bond for this comparison, we do not limit our search to only those bonds which have been observed crystallographically.

The weakest bond determined in this manner is that between a non-carbonyl carbon and the amino hydrogen, having $U_{min} = -81$ J/mol and a breaking force of roughly $F = 8.3 \times 10^{-13}$ N/bond. The force generated by free convection is approximately eight orders of magnitude too small to break even this weak bond and thereby strip molecules from the crystal surface. The full intermolecular potential should yield a value of $U_{min} \approx \Delta H$ of crystallization; Howard et al. [7] report that ΔH of crystallization for tetragonal lysozyme crystals is -79 kJ/mol. Our estimate of the bond

strength is smaller than ΔH by a factor of 1000, yet the force required to break it is many orders of magnitude larger than the shear forces present due to natural convection.

Even though the shear stress cannot remove molecules from the surface, it might impart some preferred orientation to the molecules near the surface so that they are unable to find the proper alignment for addition to the crystal (fig. 1b). To test this hypothesis, we compare the characteristic rates of the processes: alignment by shear and randomization by rotational diffusion. The rate of alignment is comparable to the shear rate, Γ; the characteristic rotation rate is given by the rotational diffusion coefficient, $D_{rot} = kT/8\pi\mu R^3$, where R is the hydrodynamic radius of the protein [8]. The hydrodynamic radius of lysozyme is approximately 20 Å [8], giving $D_{rot} = 2 \times 10^7$ s^{-1},
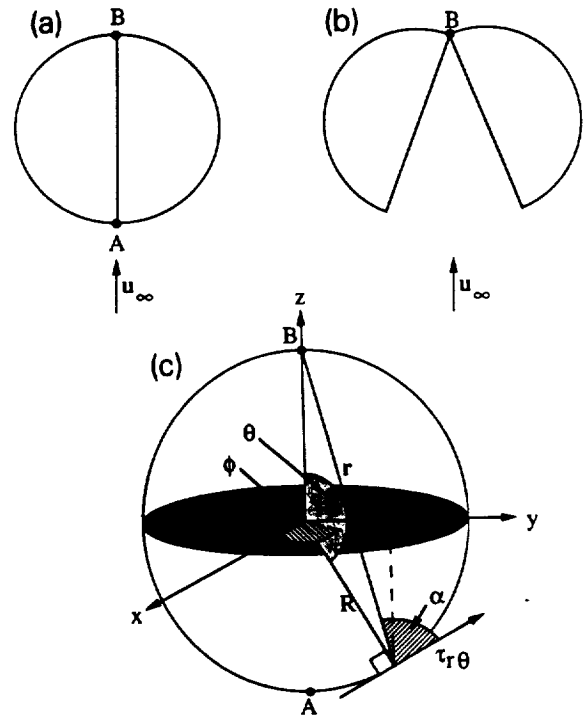

Fig. 2. Denaturation of protein molecule due to shear stress. (a) Protein in native conformation. Molecule is maintained in native state by a single hydrogen bond at A and is hinged at B. (b) Denatured protein molecule. After hydrogen bond is broken, both halves swing open. (c) Definition sketch for calculating force at point A due to shear stress.

while the shear rate is certainly less than 1 s^{-1}. The ratio of rotational and shear rates is therefore more than 10^7, indicating that randomization of the protein molecules occurs much faster than any orientation imposed by the shear flow.

Another possible explanation for slowing or halting of crystal growth is denaturation of protein by the shear field. The following model, suggested to us by W.B. Russel (Princeton University), was used to investigate the possibility of shear-induced denaturation. If the protein molecule must be in a particular conformation in order to bind to the crystal surface, crystal growth may be hindered if the shear stress changes the protein's conformation. For this analysis, consider a spherical protein molecule as shown in fig. 2a and assume that the molecule is maintained in this conformation by a single hydrogen bond placed at point A and is "hinged" at point B. If the shear forces on the molecule are sufficient to break the bond at A, the molecule will open up in the yz plane (fig. 2b) and the molecule might not bind to the surface. The force on the bond at A can be calculated by computing the torque about B due to creeping flow past the sphere and determining the equivalent force to place at A.

Over any differential area element on the molecular surface, the magnitude of the torque is given by

$$dT = r\left(\tau_{r\theta} R^2 \sin\theta \, d\theta \, d\phi\right) \sin\alpha, \qquad (2.4)$$

where r is the distance from point B to the area element, $\tau_{r\theta}$ is the shear stress acting on the protein surface in the θ direction, and θ, ϕ, and α are as shown in fig. 2c. Only the component in the $\pm x$ direction contributes to opening the hinge in the yz plane, however, so the appropriate expression for the x component of the torque is

$$dT_x = r\left(\tau_{r\theta} R^2 \sin\theta \, d\theta \, d\phi\right) \sin\alpha \sin\phi. \qquad (2.5)$$

From geometrical considerations, $\alpha = \theta/2$, and $r = \sqrt{R(1 - \cos\phi)}$, while the shear stress is related to the free stream velocity, u_∞, by $\tau_{r\theta} = (3\mu u_\infty/2R)\sin\theta$ [9]. Note that here R denotes the radius of the crystal and that we have supposed the molecule is held stationary in a uniform flow field of strength u_∞. If eq. (2.5) is integrated

over half a sphere ($0 \le \phi \le \pi$, $0 \le \theta \le \pi$), the $+x$ component of the torque is

$$T_{+x} = \frac{3R^2\mu u_\infty}{\sqrt{2}} \int_0^\pi \int_0^\pi \sin^2\theta \, (1 - \cos\theta)^{1/2}$$

$$\times \sin\frac{\theta}{2}\sin\phi \, d\phi \, d\theta = \frac{3\pi R^2\mu u_\infty}{2}. \qquad (2.6)$$

and the corresponding force is $3\pi R\mu u_\infty/4$. The force, F, on the hydrogen bond is twice the force due to flow around half the sphere,

$$F = 3\pi R\mu u_\infty/2. \qquad (2.7)$$

which must equal the breaking force of the hydrogen bond if the molecule is denatured.

According to our earlier calculations, the weakest bond has a breaking strength of 8.3×10^{-13} N. A velocity, u_∞, of approximately 9 cm/s is required to disrupt this bond. This velocity is more than three orders of magnitude greater than the free convection velocity estimated earlier, and is certainly greater than the velocity attained in the systems of interest. Furthermore, this is a worst case scenario since the weakest possible bond was chosen and only one hydrogen bond was permitted. In reality, other contributions would strengthen the bond.

These analyses indicate that viscous stresses due to natural convection are too weak to disrupt crystal growth by stripping molecules from the surface, orienting molecules at the surface, or denaturing the protein as it approaches the surface. Another way flow can influence protein crystal growth is by altering the mass transfer rate to the crystal surface, which we investigate next.

3. Mass transfer and protein crystal growth

The relative rates of mass transport and attachment kinetics determine the manner in which a crystal grows. Crystal growth can be thought of as occurring in two steps: (1) the molecule reaches the surface from the bulk solution and (2) the molecule is incorporated into the crystal. Two distinct growth regimes can be observed depending on which step is rate-limiting. When mass transport is rate-determining, molecules attach to

the surface as fast as they arrive and the region adjacent to the surface is depleted in protein relative to the bulk. At the other extreme, when attachment controls growth, mass transport maintains the protein concentration at the surface equal to the average protein concentration in solution. An expression for the the growth kinetics of tetragonal lysozyme crystals is available [10,11] so that we can perform a quasi-steady state analysis to determine when each step controls crystal growth.

At pH 4, 50 mg/ml NaCl, and 22°C, the (110) face was found to advance with a velocity, G, given by

$$G = k\left[(C_i - C_s)/C_s\right]^2,\tag{3.1}$$

where C_i is the mass concentration of protein at the interface, $C_s = 1.7$ mg/ml is the solubility mass concentration under these conditions, and $k = 1.46 \times 10^{-9}$ cm/s. In the analysis below, we take the crystal to be a sphere of radius R and equate G with the growth rate dR/dt. The crystal growth rate given by eq. (3.1) must also equal the volume flux to the crystal surface:

$$\frac{dR}{dt} = \frac{D}{C_x}\left.\frac{\partial C}{\partial r}\right|_R,\tag{3.2}$$

where $C_x = 725$ mg/ml is the mass concentration of protein in the crystal (corresponding to 50% solvent by volume [12]). The concentration gradient at the crystal surface can be expressed as the product of the concentration gradient which would obtain if diffusion were the only transport mechanism and a correction factor, Sh:

$$\left.\frac{\partial C}{\partial r}\right|_R = \frac{\partial C/\partial r\,|_R}{\partial C/\partial r\,|_{R,\mathrm{diff}\,n}}\left.\frac{\partial C}{\partial r}\right|_{R,\mathrm{diff}\,n} = \mathrm{Sh}\left.\frac{\partial C}{\partial r}\right|_{R,\mathrm{diff}\,n}.\tag{3.3}$$

Here Sh is the Sherwood number based on the crystal radius and is given by the Ranz–Marshall correlation [13]:

$$\mathrm{Sh} = 1 + 0.5\,\mathrm{Sc}^{1/3}\,\mathrm{Gr}^{1/4}.\tag{3.4}$$

The Sherwood number is the ratio of the actual mass transfer rate to the diffusion rate. The Schmidt number, Sc, and Grashof number, Gr,

were defined earlier. Note that the functional relation given here, $\mathrm{Sc}^{1/3}\mathrm{Gr}^{1/4}$, differs from that used earlier in connection with the shear rate and velocity. There is very little experimental data on mass transfer in free convection at low Grashof numbers but the Ranz–Marshall correlation encompasses that which is available.

When the crystal grows in a quasi-steady manner under diffusion control, the concentration gradient at the surface is given by

$$\left.\frac{\partial C}{\partial r}\right|_{R,\mathrm{diff}\,n} = \frac{C_x - C_i}{R}.\tag{3.5}$$

Equating the two expressions for crystal growth given in eqs. (3.1) and (3.2) and making use of eqs. (3.3)–(3.5) yields

$$K\left(\frac{C_i - C_s}{C_s}\right)^2 = \frac{C_x - C_i}{C_x}(1 + 0.5\,\mathrm{Sc}^{1/3}\,\mathrm{Gr}^{1/4}).\tag{3.6}$$

where $K = kR/D$. Eq. (3.6) can be solved for the interfacial concentration C_i as a function of crystal size. The resulting value of C_i is then substituted into eq. (3.1) to find the growth rate. When Gr = 0 (no buoyancy-driven flow), eq. (3.6) can be solved for C_i explicitly to yield

$$C_i = C_s\left\{-1 + 2K\frac{C_x}{C_s} + \left[1 + 4K\frac{C_x}{C_s}\left(\frac{C_x}{C_s} - 1\right)\right]^{1/2}\right\}$$

$$\times\left(2K\frac{C_x}{C_s}\right)^{-1}.\tag{3.7}$$

The interfacial concentrations calculated from eqs. (3.6) and (3.7) are shown in fig. 3a, while the corresponding growth rates are given in fig. 3b. We used the results shown in fig. 3a to estimate the scaled characteristic density difference, $\Delta\rho/\rho_x = 0.002$, used in section 1.

According to these results, the interfacial concentration is essentially equal to the bulk concentration over the entire size range studied by Pusey et al. [10,11]. A constant growth rate (broken lines), shows that natural convection is sufficient to maintain the surface concentration at the bulk level so that crystal growth is entirely kinetically controlled. If convection is suppressed (solid lines),
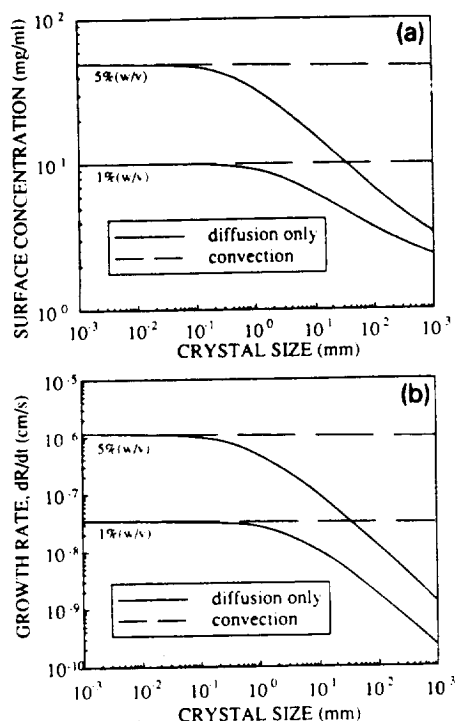
Fig. 3. Mass transfer effects on protein crystal size. (a) Interfacial concentration of lysozyme calculated from quasi-steady mass balance on growing crystal, eqs. (3.6) and (3.7). Solid lines are for diffusion only, broken lines include natural convection. (b) Crystal growth rate calculated from quasi-steady mass balance and growth rate expression given in eq. (3.1). All parameter values are taken from Pusey et al. [11].

the growth rate decreases as the crystal grows larger. For example, by the time a lysozyme crystal growing from a 5% (w/v) solution reaches 1 mm, its growth rate has slowed to approximately 25% of its initial value. Similar results can be seen for crystals grown from 1% (w/v) solution. A rough indication of the relative importance of mass transfer and kinetics can be obtained from the slope of the growth rate versus crystal size curve (fig. 3b). The slope is zero when interfacial kinetics are rate-limiting and approaches −1 in the diffusion-controlled limit. The curves in fig. 3b indicate that crystals grow under kinetically-controlled conditions until they reach approximately 100 μm irrespective of the mass transfer mechanism. These calculations agree well with those of Pusey and Naumann [10].

4. Salt rejection and protein crystal growth

There are at least two possible ways in which the rejection of salt (precipitating agent) at the interface may influence protein crystal growth: (i) a "blowing" velocity directed away from the crystal surface which slows transport of protein to the crystal; (ii) the alteration of the local protein solubility which reduces the driving force for diffusion. In the first case, the blowing would appear in the "crystallization" flow which arises from the diffusion of protein to the crystal surface [14]. This crystallization flow is related to the growth rate of the crystal, dR/dt, by

$$v_f = n \frac{dR}{dt} \left(1 - \frac{\rho_c}{\rho_f}\right), \qquad (4.1)$$

where v_f is the fluid velocity at the interface. n is the unit normal directed outward from the crystal surface, ρ_c is the crystal mass density and ρ_f is the fluid density at the interface. The crystallization flow is directed towards the crystal surface if $\rho_c > \rho_f$, and away from the crystal if $\rho_c < \rho_f$. Protein crystals are usually denser than the bulk fluid so the crystallization flow enhances mass transfer to the crystal surface. A straightforward calculation shows that the convection protein flux due to crystallization flow is approximately 1% of the diffusive flux for a spherical protein crystal and can be neglected without serious error.

The effect of variations in the local protein solubility can be estimated by considering the growth of a spherical protein crystal under diffusion control. Salt is rejected at the crystal surface and must diffuse to the bulk, producing a salt concentration gradient and corresponding gradient in the local solubility of the protein. In the diffusion limit, protein in the liquid at the crystal interface is at the solubility concentration and is in equilibrium with the protein in the crystal. The crystal form is reported to be insensitive to the salt concentration, so it may be reasonable to assume the chemical potential of the crystalline protein is independent of the salt concentration. The chemical potential of the protein in solution, however, is no longer directly proportional to its concentration because it depends on the con-

centration of other solutes. The salt concentration gradient due to rejection at the crystal interface alters the gradient in the protein's chemical potential with the result that the flux of protein to the crystal surface is less than the flux one would expect from examining the protein concentration gradient alone. We wish to establish how the salt gradient alters the protein flux to the crystal.

To set this out in mathematical form, we first express the flux of protein (species 1) in terms of its chemical potential [13]

$$j = -\frac{D_0}{kT} C_1 \nabla \mu_1, \tag{4.2}$$

where μ_1 is the chemical potential of the protein, D_0 = thermodynamic diffusion coefficient, and C_1 = molar concentration of protein. The chemical potential of the protein is given by

$$\mu_1 = \mu_1^\circ + kT \log x_1 \gamma_1, \tag{4.3}$$

where μ_1° = standard state chemical potential, x_1 = mole fraction of protein, and γ_1 = activity coefficient of the protein. Since the chemical potential of the protein at the solubility concentration is constant, it follows that

$$\mu_1^{sol} = \mu_1^\circ + kT \log x_1^{sol} \gamma_1^{sol} = \text{constant}.$$

The flux relation given by eq. (4.2) is unchanged by adding the gradient of a constant, so the flux can also be expressed as

$$j = -\frac{D_0}{kT} C_1 \nabla(\mu_1 - \mu_1^{sol})$$

$$= -D_0 C_1 \nabla \log\left(\frac{x_1 \gamma_1}{x_1^{sol} \gamma_1^{sol}}\right). \tag{4.4}$$

One form for the activity coefficient is [15]

$$\gamma_1 = \gamma_1^\infty \exp(-Kx_1), \tag{4.5}$$

where γ_1^∞ is the activity coefficient of protein in the limit of an infinitely dilute solution. If K is a constant independent of salt concentration and γ_1^∞ varies with salt concentration, then the chemical potential of the dissolved protein can be written in terms of the local γ_1^∞:

$$\mu_1 = \mu_1^0 + kT \log[x_1 \gamma_1^\infty \exp(-Kx_1)], \tag{4.6}$$

where

$$\gamma_1^\infty \sim \exp(Kx^{sol})/x_1^{sol}. \tag{4.7}$$

Although this manner of adjusting γ_1^∞ to satisfy the solubility constraints is ad hoc, it makes the mathematics somewhat simpler by implicitly absorbing the salt dependence into x_1^{sol} so that substitution of eqs. (4.5), (4.6) and (4.7) into eq. (4.4) gives the flux as

$$j = -D_0 C_1 \nabla \log\left(\frac{x_1}{x_1^{sol}} \exp[-K(x_1 - x_1^{sol})]\right). \tag{4.8}$$

A quasi-steady mass balance around a growing spherical crystal yields

$$\left(R^2 \frac{dR}{dt}\right) C_x$$

$$= r^2 D_0 C_1 \frac{d}{dr} \log\left(\frac{x_1}{x_1^{sol}} \exp[-K(x_1 - x_1^{sol})]\right), \tag{4.9}$$

where C_x is the molar concentration of protein in the crystal. If the following dimensionless variables based on a reference length R_0 are introduced:

$$\lambda = \frac{R}{R_0}, \quad z = \frac{R}{r} = \frac{R_0 \lambda}{r}, \quad \tau = \frac{tD_0}{R_0^2}. \tag{4.10}$$

the mass balance becomes

$$x_1 \frac{d}{dz} \log\left(\frac{x_1}{x_1^{sol}} \exp[-K(x_1 - x_1^{sol})]\right) = -\text{Pe}\frac{C_x}{C_T}, \tag{4.11}$$

where the Peclet number,

$$\text{Pe} = \lambda \frac{d\lambda}{d\tau} = \frac{R}{D_0} \frac{dR}{dt}. \tag{4.12}$$

can be considered a scaled crystal growth velocity. Eq. (4.11) was obtained by approximating the protein concentration, C_1, by the relation $C_1 = C_T x_1$, and taking C_T to be 55M. Transforming the equation from an expression for the activity into a

differential equation for the mole fraction of protein yields:

$$\frac{dx_1}{dz} = -\left[\text{Pe}\frac{C_x}{C_T} + \left(Kx_1 - \frac{x_1}{x_1^{sol}} \right)\frac{dx_1^{sol}}{dz} \right]$$

$$\times (1 - Kx_1)^{-1}. \tag{4.13}$$

Note that the reciprocal relation between z and r in eq. (4.10) means that z tends to zero as we move away from the crystal.

The salt concentration was calculated from the quasi-steady diffusion profile:

$$C_{salt} = C_{salt.bulk} + \Delta C_{salt} z, \tag{4.14}$$

where $C_{salt.bulk} = 50$ mg/ml, and $\Delta C_{salt} = C_{salt.surf} - C_{salt.bulk}$. The solubility was assumed to obey the expression [16]:

$$x_1^{sol} = \alpha \exp(-\beta C_{salt}), \tag{4.15}$$

where α and β are empirical parameters. Combining eqs. (4.14) and (4.15) gives x_1^{sol} as a function of position:

$$x_1^{sol} = x_{1.bulk}^{sol} \exp(-\beta \Delta C_{salt} z). \tag{4.16}$$

Substituting eq. (4.16) into (4.13) yields

$$\frac{dx_1}{dz} = -\left(\text{Pe}\frac{C_x}{C_T} - \beta \Delta C_{salt}[Kx_{1.bulk}^{sol} \right.$$

$$\left. \times \exp(-\beta \Delta C_{salt} z) - 1] x_1 \right)(1 - Kx_1)^{-1}, \tag{4.17}$$

a differential equation that can be integrated numerically from the crystal surface ($z = 1$, $x_1 = x_{1.surf}^{sol}$) to "infinity" ($z = 0$, $x_1 = x_{1.bulk}$). The resulting value of $x_{1.bulk}$ may then be used to calculate the expected growth rate due to diffusion in a uniform salt concentration field, viz.

$$\text{Pe}_{nom} = \frac{C_T}{C_x}\left(x_{1.bulk} - x_{1.bulk}^{sol} \right), \tag{4.18}$$

and the ratio of the actual and nominal growth rates can be determined as a function of system properties.

For a dilute protein solution, $Kx_1 \ll 1$ [15], and this term can be neglected in the denominator of

eq. (4.17). In addition, neglecting the first term in square brackets in the numerator provides an upper bound on the effect of salt rejection on the diffusion rate. In this case, eq. (4.17) can be integrated analytically to yield

$$x_1 = x_{1.bulk}^{sol} \exp(-\beta \Delta C_{salt} z)$$

$$- \frac{\text{Pe}}{\beta \Delta C_{salt}}\{ 1 - \exp[-\beta \Delta C_{salt}(z - 1)] \}. \tag{4.19}$$

The value of $x_{1.bulk}$ obtained from eq. (4.19) can be substituted into (4.18) to obtain

$$\text{Pe} = \frac{\beta \Delta C_{salt}}{\exp(\beta \Delta C_{salt}) - 1}\text{Pe}_{nom}. \tag{4.20}$$

Although the form of the relation between the nominal Peclet number and the actual Peclet number has been established, the apparent reduction in diffusion rate depends on ΔC_{salt}, which has not yet been determined. Recall that the quasi-steady salt concentration profile, eq. (4.14), was used to obtain eq. (4.20) but the surface concentration was left unspecified. A mass balance on the salt rejected at the crystal surface yields:

$$\frac{dR}{dt}(1 - s)C_{salt.surf} = -D_{salt}\frac{\partial C_{salt}}{\partial r}\bigg|_R, \tag{4.21}$$

where $s =$ segregation coefficient of the salt ($C_{salt.crystal}/C_{salt.surf}$); $0 \leq s \leq 1$. In terms of the dimensionless variables introduced in eq. (4.10) and using eq. (4.14), eq. (4.21) reduces to

$$\text{Pe}\frac{D_0}{D_{salt}}(1 - s)C_{salt.surf} = C_{salt.surf} - C_{salt.bulk}, \tag{4.22}$$

so that

$$\Delta C_{salt} = C_{salt.surf} - C_{salt.bulk}$$

$$= C_{salt.bulk}\frac{\text{Pe}(D_0/D_{salt})(1 - s)}{1 - \text{Pe}(D_0/D_{salt})(1 - s)}. \tag{4.23}$$

For proteins, $D_0/D_{salt} \approx 10^{-1}$, and typical Peclet numbers for lysozyme crystals are less than 10^{-1}. The maximum concentration difference occurs when $s = 0$ (total segregation of the salt), in which case $\Delta C_{salt} \leq 10^{-2} C_{salt.bulk}$. At a bulk con-

centration of 50 mg/ml NaCl, this gives $\Delta C_{salt} \leq$ 0.5 mg/ml. For crystals to be diffusion limited once they reach 10 μm in size (compared with 100 μm as shown in fig. 3), β should be approximately 7.2 ml/mg. Reported values of lysozyme solubility put the value of β close to 10^{-1} ml/mg [7,17]. Thus, $Pe \approx 0.98\ Pe_{nom}$, and salt rejection cannot reduce the diffusion rate to the point where crystal growth is no longer kinetically controlled.

5. Contaminants and convection

In most circumstances, convection promotes crystal growth by enhancing mass transfer to the crystal surface. However, the presence of a species which attaches itself to the surface and inhibits protein binding could retard growth. Suppose that, in the absence of convection, inhibitor molecules are delivered to the surface by diffusion and bound there at a certain rate. If the binding rate is low compared to diffusion, the inhibitor concentration near the surface will be high and the rate of inhibition is kin. ly controlled. Individual binding sites are oc ied by inhibitor molecules by the crystal continues to grow because successive additions of protein near the inhibited site overlay the inhibitor, producing fresh surface with new attachment sites. The growth process is only slightly retarded because protein addition keeps ahead of inhibition.

As the crystal grows, diffusion proceeds at a slower pace (cf. fig. 3). Four possibilities exist:
(i) both the growth and inhibition processes remain kinetically controlled;
(ii) the protein attachment process remains kinetically controlled while the rate of inhibition slows due to the slower rate of diffusion;
(iii) the protein attachment process becomes diffusion controlled but the rate of inhibition remains kinetically controlled;
(iv) both processes become diffusion controlled.

In case (ii), the effects of the inhibitor species diminish with time and growth continues unabated in the absence of convection. Convection would replenish the region near the surface and increase the rate at which the inhibitor poisons further growth. In case (iii), the growth rate de-

creases without convection, so convection diminishes the effects of the inhibitor. The effects of convection in case (iv) would depend on the relative rates of transport and the degree to which they are altered by convection. In situations (ii) and (iv) above, enhancing the rate of inhibitor transfer by convection would poison the surface faster and diminish crystal growth. Case (ii) is consistent with the retardation of growth observed by Pusey et al. [1].

6. Conclusions

The search for better protein crystals has drawn crystallographers into the realm of fluid mechanics and mass transfer. Forces arising from fluid flow have been suspected of interfering with the normal growth of protein crystals by breaking the hydrogen bonds which both hold the molecule in the crystal lattice and maintain the protein in its native conformation. Our analyses indicate shear forces are several orders of magnitude smaller than those required to break a single intramolecular hydrogen bond, and as much as eight orders of magnitude too small to strip molecules from the surface of growing crystals. Another scale analysis reveals that the protein's orientation is randomized through rotational diffusion approximately 10^7 times as fast as shear can impose a preferred orientation. We find no hint that buoyancy driven convection mechanically alters the state of the protein near the crystal surface.

Calculations from a quasi-steady model delineate the approximate size where crystal growth changes regimes from kinetic control to diffusion control. All crystals start in the kinetic regime, and remain there until they reach the transition size, which is approximately 70–100 μm for hen egg white lysozyme. Unless diffusion is substantially slower than expected, defects caused by improper attachment will have formed before convective mass transfer is significant. The reduction in protein diffusion rate due to counter-diffusion of precipitating agent is insufficient to reduce the transition size appreciably. The mechanisms discussed here fail to explain why growth retardation is observed in the presence of convection.

One possible mechanism by which convection may play a role is the transport of a second, "contaminant" species which competes for attachment to the crystal. Several scenarios are possible. For example, when the contaminant attaches faster than the protein, it is preferentially depleted from solution near the surface so that its concentration falls below its bulk value. This makes attachment of protein more competitive and favors crystal growth. Convection, which brings fresh solution in contact with the crystal, effectively returns the contaminant concentration to its bulk value and reduces crystal size below its diffusion-limited size. The presence of contaminant is conjecture, but it provides a simple mechanism by which convection can hinder crystal growth, and is consistent with observations.

Acknowledgements

References

[1] M. Pusey, W. Witherow and R. Naumann, J. Crystal Growth 90 (1988) 105.

[2] L.J. DeLucas, C.G. Smith, H.W. Smith, S. Vijay-Kumar, S.E. Senadhi, S.E. Ealick, D.C. Carter, R.S. Snyder, P.C. Weber, F.R. Salemme, D.H. Ohlendorf, H.M. Einspahr, L.L. Clancy, M.A. Navia, B.M. McKeever, T.L. Nagabhushan, G. Nelson, A. McPherson, S. Koszelak, G. Taylor, D. Stammers, K. Powell, G. Darby and C.E. Bugg, Science 246 (1989) 651.

[3] T.E. Creighton, Proteins: Structure and Molecular Principles (Freeman, New York, 1983).

[4] S. Ostrach, Ann. Rev. Fluid Mech. 14 (1982) 313.

[5] R.W. Fiddis, R.A. Longman and P.D. Calvert, J. Chem. Soc. Faraday Trans. 75 (1979) 2753.

[6] A.T. Hagler, E. Huler and S. Lifson, J. Am. Chem. Soc. 96 (1974) 5319.

[7] S.B. Howard, P.J. Twigg, J.K. Baird and E.J. Meehan, J. Crystal Growth 90 (1988) 94.

[8] C. Tanford, Physical Chemistry of Macromolecules (Wiley, New York, 1961).

[9] R.B. Bird, W.E. Stewart and E.N. Lightfoot, Transport Phenomena (Wiley, New York, 1960).

[10] M. Pusey and R. Naumann, J. Crystal Growth 76 (1986) 593.

[11] M.L. Pusey, R.S. Snyder and R. Naumann, J. Biol. Chem. 261 (1986) 6524.

[12] B.W. Matthews, J. Mol. Biol. 33 (1968) 491.

[13] E.L. Cussler, Diffusion (Cambridge University Press, London, 1984).

[14] W.R. Wilcox, J. Crystal Growth 12 (1972) 93.

[15] P.G. Debenedetti and S.K. Kumar, AIChE J. 32 (1986) 1253.

[16] G. Feher and Z. Kam, Methods Enzymol. 114 (1985) 77.

[17] M. Ataka and S. Tanaka, Bioploymers 25 (1986) 337.

Electrostatic Interactions Between a Protein Molecule and a Charged Surface:
Part I: Development and Testing of a Computational Method

M. L. Grant[1] & D. A. Saville

Department of Chemical Engineering
Princeton University
Princeton, NJ 08544

[1]Now at Exxon Production Research Co. Houston TX.

Abstract

The behavior of colloidal scale systems is often controlled by electrostatic particle-particle and particle-surface interactions. Examples include the electrostatic stabilization of suspensions of charged particles and surface adsorption of protein molecules in chromatography. Previous studies have dealt almost exclusively with particles having a nearly uniform surface charge density, but such analyses are inadequate for the complicated charge distributions on biological macromolecules. A boundary element method (BEM) was developed to study the interaction between a spherical particle with a nonuniform surface charge density and a large, uniformly charged surface. Our calculations show that the effect of a nonuniform particle charge distribution can be dramatic. The technique has also been used to study the interaction of a globular protein with a surface; the results of this study will be described in Part II.

1. Introduction

Interactions between electrically charged bodies and surfaces are determined by the arrangement of the objects' charged groups. Many cases have been analyzed wherein the charge distribution is uniform or has azimuthal symmetry. In systems of synthetic latex particles, for instance, the charge distribution is fairly uniform and these are excellent approximations. Particle aggregation and particle-surface adsorption can be elucidated with models based on uniform surface charge distributions. But, when the objects are nonuniformly charged their behavior is more difficult to explain and the models are correspondingly more complicated. Biological macromolecules, which may have extremely complex charge distributions, often exhibit counter-intuitive behavior. The enzymatic activity of copper zinc superoxide dismutase is a case in point.

Superoxide dismutase (SOD) is reported to be a homodimer of molecular weight 32,000 with a net valence of –4 [1]; its substrate, the superoxide radical, has a valence of –1. At first glance it appears that the enzyme's activity should be limited by electrostatic repulsion between like charges as the substrate approaches the enzyme. One might also expect the enzymatic activity to increase with ionic strength as the electrostatic repulsion is screened by counterions. Experimental data contradict both notions: the enzyme activity is close to that calculated from the Brownian collision rate for uncharged particles of similar size and *decreases* with added salt [1].

Crystallographic studies of SOD reveal that a group of positively charged residues around the active site guide the superoxide. Cudd and Fridovich[1] chemically modified the residues near the active site and measured enzyme activity as a function of salt concentration. A 90% drop in enzyme activity at an ionic strength of zero was observed when arginine 141 was neutralized and the activity still decreased with ionic strength. Neutralization of 7 or 8 lysine residues reduced the reaction rate by approximately 80% but reversed the trend with ionic strength. Cudd and Fridovich concluded that the lysines are responsible for long-range steering while arginine provides local orientation of the incoming molecule near the active site. Calculations of the electrostatic potential near SOD [2,3] and Brownian dynamics simulations [4-7] have largely confirmed this interpretation.

Klapper *et al.* [3] employed a finite-difference method to solve the linearized Poisson-Boltzmann equation in the region surrounding SOD. Charged groups were placed at their crystallographically measured coordinates and the boundary between the interior of the molecule and the bulk solution was defined to be the solvent-accessible surface. This calculation, the first to assign different dielectric constants to the protein molecule ($\varepsilon_1 = 2$) and the solution ($\varepsilon_2 = 80$), showed that the surface charge distribution

3

and shape of the enzyme create a large "target" of positive potential which attracts the negatively charged substrate. As ionic strength increases, the effective target area is reduced while repulsion from the negatively charged region decreases; the former effect dominates, accounting for the trend in enzyme activity. Good agreement with experiment was obtained only with the two-dielectric model.

Subsequent versions of this technique can now handle the nonlinear Poisson-Boltzmann equation. However, computational requirements rise rapidly with the resolution of the finite difference grid. These finite difference calculations are typically performed with grid spacing scaled so the molecule occupies 50 - 75% of the domain [8]. Such scaling is adequate when the substrate is small compared with the enzyme and can be treated as a point charge. Treating interactions between molecules (or molecules and macroscopic bodies) by this technique appears difficult or infeasible at present.

Anisotropic charge distributions clearly have a substantial effect on the behavior of macromolecules, but current finite difference techniques are not completely satisfactory for protein-surface interactions. The model developed here uses a boundary element technique to circumvent some of the difficulties. In Part I, the technique is described and its utility demonstrated using, as an example, a sphere with a charged cap. The presentation begins with a discussion of the mathematical structure of the problem. Next, the formulation and implementation of a boundary element method created to treat a sphere with fixed, nonuniform surface charge density, is explained. The boundary element code is then used to solve two test problems to establish its accuracy. Finally, we study a sphere with a charged cap interacting with an insulated plate to assess the significance of charge inhomogeneity. Part II of the series describes the interaction between a lysozyme molecule and a charged surface.

2. Mathematical Structure of the Electrostatics Problem

Figure 1 depicts the particle-surface system. The electrostatic potential is a solution of the linearized Debye-Hückel equation [9]:

$$\text{region 1 (molecule):} \quad \nabla^2 \psi_1 = 0 \tag{1}$$

$$\text{region 2 (solution):} \quad \nabla^2 \psi_2 = \kappa^2 \psi_2 \tag{2}$$

where $\kappa^2 = 2n_b z^2 e^2 / \varepsilon_o \varepsilon_2 kT$ for a z-z electrolyte; n_b = bulk ion number density, e = elementary charge, ε_o = permittivity of free space, k = Boltzmann's constant, and T = absolute temperature. The boundary conditions at the surface of the particle are the continuity

of potential,

$$\psi_1 = \psi_2 \qquad (3)$$

and the jump in electric displacement,

$$\varepsilon_1 \nabla \psi_1 \cdot \mathbf{n}_1 + \varepsilon_2 \nabla \psi_2 \cdot \mathbf{n}_2 = \frac{\sigma}{\varepsilon_o} \qquad (4).$$

Note that $\mathbf{n}_1$ and $\mathbf{n}_2$ point *out* of their respective regions. The boundary conditions are:

$$\text{at} \qquad z = 0: \quad \frac{\partial \psi_2}{\partial z} = -\frac{\sigma_x}{\varepsilon_o \varepsilon_2} \qquad (5)$$

and

$$\text{as} \qquad z \to \infty: \quad \psi_2 \to 0 \qquad (6).$$

If we scale all the lengths on the particle radius, a, and write the equations in terms of the dimensionless potential, $u = \psi/\psi_o$, the problem becomes:

$$\text{region 1:} \qquad \nabla^2 u_1 = 0 \qquad (7)$$

$$\text{region 2:} \qquad \nabla^2 u_2 = (a\kappa)^2 u_2 \qquad (8)$$

$$\text{sphere surface:} \quad \begin{cases} u_1 = u_2 & (9) \\ \varepsilon_1 \nabla u_1 \cdot \mathbf{n}_1 + \varepsilon_2 \nabla u_2 \cdot \mathbf{n}_2 = \sigma^* & (10) \end{cases}$$

$$z = 0: \quad \frac{\partial u_2}{\partial z} = -\frac{\sigma_x^*}{\varepsilon_2} \qquad (11)$$

$$z \to \infty: \quad u_2 \to 0 \qquad (12).$$

The reference quantities for potential and surface charge are $\psi_o = kT/e$ and $\sigma_o = \varepsilon_o \psi_o/a$.

The solution of the problem specified by equations (7) - (12) is complicated, but its linearity allows it to be split into readily-solved subproblems as shown in Figure 2. First we divide the problem into two separate problems: (i) a charged sphere near an insulated flat plate and (ii) a charged plate with an uncharged sphere. Since the potential of problem (i) is identical to that produced by the charged sphere and its mirror image [10-12], we denote it u^{ss} (i.e., sphere-sphere); the potential in problem (ii) is u^{sp}, the sphere-plate potential. The total potential is their sum

5

$$u = u^{ss} + u^{sp} \qquad (13).$$

The equations for the sphere-sphere problem are:

region 1: $\qquad \nabla^2 u_1^{ss} = 0 \qquad (14)$

region 2: $\qquad \nabla^2 u_2^{ss} = (a\kappa)^2 u_2^{ss} \qquad (15)$

sphere surface: $\begin{cases} u_1^{ss} = u_2^{ss} & (16) \\[2mm] \varepsilon_1 \nabla u_1^{ss} \cdot \mathbf{n}_1 + \varepsilon_2 \nabla u_2^{ss} \cdot \mathbf{n}_2 = \sigma^* & (17) \end{cases}$

$z = 0: \qquad \dfrac{\partial u_2^{ss}}{\partial z} = 0 \qquad (18)$

$z \to \infty: \qquad u_2^{ss} \to 0 \qquad (19),$

while the sphere-plate potential satisfies:

region 1: $\qquad \nabla^2 u_1^{sp} = 0 \qquad (20)$

region 2: $\qquad \nabla^2 u_2^{sp} = (a\kappa)^2 u_2^{sp} \qquad (21)$

sphere surface: $\begin{cases} u_1^{sp} = u_2^{sp} & (22) \\[2mm] \varepsilon_1 \nabla u_1^{sp} \cdot \mathbf{n}_1 + \varepsilon_2 \nabla u_2^{sp} \cdot \mathbf{n}_2 = 0 & (23) \end{cases}$

$z = 0: \qquad \dfrac{\partial u_2^{sp}}{\partial z} = -\dfrac{\sigma_x^*}{\varepsilon_2} \qquad (24)$

$z \to \infty: \qquad u_2^{sp} \to 0 \qquad (25).$

u^{ss} can be obtained using a boundary element technique. A solution for u^{sp} is more difficult because the boundary condition at $z = 0$ is not easily satisfied by the method of images. Instead, we further divide the sphere-plate problem, viz.,

$$u^{sp} = u^{fp} + u^r \qquad (26)$$

where u^{fp} is the potential due to the charged plate in the absence of the sphere, and u^r is the "remainder" potential. The flat plate potential is

$$u^{fp} = \frac{\sigma_x^*}{\varepsilon_2 \, a\kappa} e^{-a\kappa z} \tag{27}$$

When u^{fp} is subtracted from u^{sp}, we obtain:

region 1:

$$\nabla^2 u_1^r = -(a\kappa)^2 u^{fp} = -\rho^* \tag{28}$$

region 2:

$$\nabla^2 u_2^r = (a\kappa)^2 u_2^r \tag{29}$$

sphere surface:
$$\begin{cases} u_1^r = u_2^r & (30) \\ \varepsilon_1 \, \nabla u_1^r \cdot \mathbf{n}_1 + \varepsilon_2 \, \nabla u_2^r \cdot \mathbf{n}_2 = -(\varepsilon_1 - \varepsilon_2) \, \nabla u^{fp} \cdot \mathbf{n}_1 & (31) \end{cases}$$

$$z = 0: \quad \frac{\partial u_2^r}{\partial z} = 0 \tag{32}$$

$$z \rightarrow \infty: \quad u_2^r \rightarrow 0 \tag{33}.$$

In this problem the sphere contains a known charge density, $\rho^* = (a\kappa)^2 u^{fp}$. The fixed charge density is scaled on $\rho_o = \varepsilon_o \psi_o / a^2$. Since the potential produced by the two mirror image spheres satisfies the boundary conditions (30) and (32), u^r can be obtained from the boundary element technique used to find u^{ss}. The full solution is the sum of the three potentials.

We are also interested in the electrostatic potential *energy* and its dependence on particle-surface separation. This energy, or interaction potential, is defined in terms of the work performed to bring two bodies to a particular configuration from some reference state[13]. When performed isothermally and reversibly, the free energy change for the system can be expressed in terms of the work required to assemble all the charges from infinity [14,15]:

$$\Delta G_{elec} = \int_\Omega dV \int_0^{\rho^f} \psi \, d\rho^f \tag{34},$$

Here Ω denotes the volume of the system and the f superscript indicates a fixed charge density (not subject to thermal randomization). When the charge density is proportional to the potential (as is the case for solutions of the linearized Poisson-Boltzmann equation) and all the fixed charges reside on the surfaces of the system, equation (34) simplifies to [14-16]

$$\Delta G_{elec} = \frac{1}{2} \int_\Gamma \sigma \psi \, dA \tag{35}.$$

Γ represents all the surfaces of the system and σ is the fixed surface charge.

The change in free energy can be divided into two parts:

$$\Delta G_{elec} = \Delta G_{elec}^{\infty} + \Phi_{elec}(r) \qquad (36),$$

where ΔG_{elec}^{∞} is the change in free energy required to "charge up" the molecule and plate at infinite separation, and $\Phi_{elec}(r)$ is the change in free energy as the molecule and plate are brought together. In terms of scaled electrostatic variables,

$$\frac{\Phi_{elec}(d)}{\varepsilon_0 \psi_0^2 a} = \frac{1}{2} \int_\Gamma \sigma^* [u(d) - u(\infty)] dA \qquad (37).$$

Here, d = gap (in particle radii) between the plate and the surface of the sphere (see Figure 1), $u(d)$ = potential when the particle and plate are separated by d, and $u(\infty)$ = potential when particle is infinitely far from plate; dA is dimensionless.

3. Boundary Element Formulation

The starting point for the boundary element formulation is the differential equation:

$$\nabla^2 u - (a\kappa)^2 u = -\rho^* \qquad (38),$$

where ρ^* is a *fixed* charge density. Solutions of equation (38) describe the potential in the electrolyte (region 2) when $\rho^* = 0$, in region 1 of the "remainder" problem when $a\kappa = 0$, and in region 1 of the sphere-sphere problem when both $a\kappa$ and $\rho^* = 0$. The fundamental solution (Green's function) of the homogeneous form of equation (38) is:

$$u^* = \frac{1}{4\pi} \frac{e^{-a\kappa r}}{r} \qquad (39),$$

where r is measured from the "source" point x_0 (i.e., $r = |x - x_0|$). The differential equation can be converted into an integral equation using standard manipulations [11] to yield:

$$c\, u(x_0) + \int_\Gamma u(\nabla u^* \cdot n) dA = \int_\Gamma u^* (\nabla u \cdot n) dA + \int_\Omega \rho^* u^* dV \qquad (40),$$

where:

$$c = \begin{cases} 1, & x_o \text{ in } \Omega \\ \frac{1}{2}, & x_o \text{ in } \Gamma \\ 0, & \text{otherwise} \end{cases} \qquad (41).$$

An attractive feature of the boundary integral expression is that computations in the infinite domain are unnecessary; the integral over Ω is performed only when there is a distribution of fixed charges in the domain. This formulation greatly reduces the amount of computation needed to obtain a numerical solution.

To convert the integral equation into a form suitable for numerical computation, the boundary of the system is divided into N elements, denoted as Γ_j. The integrals over Γ in equation (40) are equivalent to the sum of integrals over all the elements:

$$c\, u(x_o) + \sum_{j=1}^{N} \int_{\Gamma_j} u\,(\nabla u^* \cdot n)\, dA = \sum_{j=1}^{N} \int_{\Gamma_j} u^* (\nabla u \cdot n)\, dA + \int_{\Omega} \rho^* u^* dV \qquad (42).$$

In the notation of Brebbia et al. [11], equation (42) reads:

$$c\, u(x_o) + \sum_{j=1}^{N} \int_{\Gamma_j} u\, q^* dA = \sum_{j=1}^{N} \int_{\Gamma_j} u^* q\, dA + \int_{\Omega} \rho^* u^* dV \qquad (43),$$

where $q = \nabla u \cdot n$, $q^* = \nabla u^* \cdot n$, and $u^* = $ fundamental solution centered at x_o. For points in the domain, equation (43) expresses the potential as the sum of a single-layer distribution of strength q, a double-layer distribution of strength u, and a particular solution given by the volume integral.

In the "constant element" approximation, each element has uniform values of potential u_j and normal flux, q_j, associated with the node (x_j) of the element. Applying (43) at each node yields N equations of the form:

$$\frac{1}{2} u_i + \sum_{j=1}^{N} u_j \int_{\Gamma_j} q_i^* dA = \sum_{j=1}^{N} q_j \int_{\Gamma_j} u_i^* dA + u_i^P \qquad (44),$$

where $u_i = $ potential at node i, $u_j = $ potential of element j, $q_j = $ normal flux through element j, u_i^* and q_i^* are the potential and normal flux due to the fundamental solution placed at x_i, and u_i^P is the potential at node i produced by the distribution of fixed charges; $c = 1/2$ because each node lies in the surface. Writing

$$G_{ij} = \int_{\Gamma_j} u_i^* \, dA \qquad \hat{H}_{ij} = \int_{\Gamma_j} q_i^* \, dA \qquad (45)$$

allows us to express equation (44) in matrix form:

$$HU = GQ + U^P \qquad (46)$$

where

$$H_{ij} = \begin{cases} \hat{H}_{ij} + \dfrac{1}{2} \ , \ i = j \\[2em] \hat{H}_{ij} \ , \ i \neq j \end{cases} \qquad (47).$$

If there are N elements on the spheres, equation (46) is a system of N equations in $2N$ unknowns (N $u's$ and N $q's$) for each domain, the interior of the sphere (region 1) and the exterior (region 2). When the equations for both regions are combined, we obtain $2N$ equations and $2N$ constraints (boundary conditions). N of the boundary conditions govern the continuity of potential at the surface ($u_j^1 = u_j^2$), while the others specify the jump in the normal derivative caused by the local surface charge density ($\varepsilon_1 q_j^1 + \varepsilon_2 q_j^2 = \sigma_j^*$).

Evaluation of the boundary integrals requires integration of the fundamental solution, u^*, and its normal derivative, q^*, over each surface element. In addition to the surface integrals, the "remainder" problem requires a volume integral to determine the particular solution produced by the fixed charge density in the sphere. The details of these calculations are described by Grant [17].

4. Boundary Element Geometry

The surface of the sphere is divided into spherical triangular elements (Figure 3), each with constant values of surface charge density, surface potential, and normal flux. Each edge of an element is the intersection of the sphere's surface with the plane containing both vertices and the origin of the sphere (the arc of the great circle connecting the vertices). The location of a node is determined by calculating the location of the element's centroid and projecting the ray from the sphere's origin through the centroid to the surface.

The pattern for the initial (coarse) discretization of the sphere is based on either a regular octahedron (8 equilateral triangular faces) or an icosahedron (20 equilateral triangular faces) circumscribed by the unit sphere. The vertices of the polyhedron are the vertices of the corresponding spherical triangular elements on the sphere's surface. The inscribed

polyhedron is oriented so that vertices of the polyhedron lie at the north and south poles of the sphere and the prime meridian (0° longitude) coincides with the boundary between two of the elements having the north pole as a common vertex. The two coarse discretizations and their "surface maps" (latitude and longitude) are shown in Figure 4. The discretization is refined by either converting each node into a vertex to form three smaller elements or connecting the midpoint of the longest edge with the opposing vertex to form two elements.

The orientation of the sphere must be defined in preparation for discussion of situations where there is a nonuniform charge distribution. For a given separation the electrostatic interaction energy of the system depends only on which point on the sphere lies closest to the plate. (This is a consequence of the mirror symmetry about the plane $z = 0$, which implies that a rotation of the spheres about the line of centers will not alter the interaction potential.) In the sphere's coordinate system defined in Figure 4, the latitude, α ($-90° \leq \alpha \leq +90°$) and longitude, β ($-180° \leq \beta \leq +180°$), specify the location of this point and, therefore, the orientation of the sphere (Figure 5). An orientation of (α, β) indicates that the point on the sphere with latitude α and longitude β is closest to the plate.

Once the nodal potentials and fluxes have been calculated, the charging integrals must be computed. The charging work for the sphere is evaluated using the formula:

$$\frac{\Phi_{elec}^{sphere}(s)}{\varepsilon_0 \psi_0^2} = \frac{1}{2} \int_{A_{sphere}} \sigma^* u \, dA \approx \frac{1}{2} \sum_{j=1}^{N} \sigma_j^* u_j A_j \tag{48}.$$

where u = the total electrostatic potential. The coefficients in the summation are the charge density, potential, and area of each element; the summation formula reflects the constant element approximation. A similar approximation is applied to the plate.

First the boundary element method (BEM) was used to solve two simple problems with uniform charge to assess its accuracy. Then the significance of nonuniform charge distributions was studied with a relatively simple configuration.

5. Applications of the Boundary Element Method

In section 2, we split the full problem into two subproblems: the sphere-sphere problem and the sphere-plate problem (see Figure 2). We now apply the BEM to an example of each to check its accuracy.

A Sphere-Sphere Problem

The first problem involves two uniformly charged spheres (see Figure 6). For $\varepsilon_1 = \varepsilon_2 = \sigma^* = 1$, the dimensionless surface potential at infinite separation is $u^\infty = (1 + a\kappa)^{-1}$.

Φ_{elec} was calculated as a function of distance from the plate and compared with the results from the linear superposition approximation [9,14]:

$$\frac{\Phi_{elec}^{LSA}(s)}{\varepsilon_o \psi_o^2 a} = \frac{4\pi}{(1+a\kappa)^2} \frac{e^{-2a\kappa(s-1)}}{2s} = \frac{4\pi}{(1+a\kappa)^2} \frac{e^{-2a\kappa d}}{2s} \qquad (49).$$

Results for $a\kappa = 0.1$ and 1 are shown in Figure 7, while calculations for $a\kappa = 5$ are presented in Figure 8. In each case, the $\hat{z}$-axis of the sphere's coordinate system (see Figure 4) is coincident with the line of centers. Calculations with $N = 8, 24, 48$, and 96 are based on an initial octahedron discretization while the results for $N = 20$ and 60 are based on the icosahedron. The BEM calculations agree well with the LSA for dimensionless gaps $d \geq (a\kappa)^{-1}$. For instance, BEM calculations with 96 elements are within 1% of the LSA for $d \geq 0$ when $a\kappa = 0.1$, for $d > 0.05$ when $a\kappa = 1$, and for $d > 0.11$ when $a\kappa = 5$. For $d \sim a$, the relative error in the BEM calculations is approximately 10^{-4}. At smaller separations (especially at contact), the linear superposition approximation is not valid [9,18], but convergence can be studied by comparing the computed values of Φ_{elec} with a reasonable upper bound.

At high ionic strengths (large $a\kappa$), the calculated energy is sensitive to the location of the node nearest the plane $z = 0$, since the surface potential decreases rapidly with increasing z. With the constant element approximation, the potential of the entire element is that of the node, so if the node is relatively far from (α, β), the element's contribution to the charging work is underestimated. The "nearest node effect" can be removed by rotating the sphere so that a node is closest to the image sphere. The potential is then correct to within the accuracy of the boundary element method, but the charging work is overestimated because the infinitesimal area over which it obtains is exaggerated by the finite area of the element. Φ_{elec} was calculated at contact for several discretizations and the results plotted in Figure 8b. The calculated energies converge to the same value irrespective of orientation.

The relatively slow convergence for this test problem reveals a shortcoming of the constant element approximation, viz., the length scale of the discretization must be smaller than κ^{-1} for good accuracy. In the case of uniform spheres with $a\kappa = 5$, a 240 element discretization produces an answer within 2% of the "converged" value at contact. When the charge distribution is nonuniform or the ionic strength higher, the discretization must be further refined to achieve comparable accuracy.

A Sphere-Plate Problem

As shown in Figure 2, the sphere-plate problem describes the interaction of a uniformly charged plate and an uncharged dielectric sphere. Here the force on the particle is

proportional to $-\nabla(\mathbf{E \cdot E}) = -\nabla E^2$, where $\mathbf{E}$ is the electric field vector [19]. The electrostatic energy of the system is therefore proportional to E^2. Except near contact, the electric field experienced by the sphere is approximately that created by the flat plate potential, u^{fp}. As given in Equation (27), the electric field produced by the flat plate is proportional to $\exp(-a\kappa d)$, so the potential energy is proportional to $\exp(-2a\kappa d)$. We analyzed the case where $\varepsilon_1 = 2$, $\varepsilon_2 = 78.54$, $a\kappa = 5$, and $\sigma_x^* = 100$ using 240 elements. The expected exponential decay is reproduced in the BEM calculations shown in Figure 9.

Spherical Particles with Charged Caps

The effects of a nonuniform charge distribution are illustrated using a charged "cap" covering 25% of the particle's surface while the remainder of the sphere is uncharged. The scaled surface charge density of $\sigma^* \approx 358$ over the cap is based on a net charge of $+10.5e$ spread uniformly over a sphere 16.48Å in radius. These values are appropriate for the idealized representation of hen egg white lysozyme which will be discussed in Part II. The initial discretization for the cap studies is an icosahedron with five elements spanning the charged cap covering the particle's north pole.

The orientation angle α, was varied from $+90°$ to $-90°$ in steps of $45°$; β was fixed at $+90°$. The calculated value of Φ_{elec} based on 240 elements is shown in Figure 10 as a function of orientation and separation for $a\kappa = 5$ and 10. The most striking feature of these calculations is that a rotation of $90°$ can easily change Φ_{elec} by a factor of more than 60. The relative difference between $\alpha = +90°$ and $\alpha = +45°$ for $a\kappa = 10$ is smaller than for $a\kappa = 5$, reflecting the stronger screening for $a\kappa = 10$.

Computations for spheres with charged caps are subject to convergence problems similar to those encountered with uniform spheres. The electrostatic interaction energy for $\alpha = +90°$ should be larger than for any other orientation because a larger area of the charged caps can interact. The boundary element method results at contact, however, are still dominated by the sensitivity to node placement described above. With 240 elements, the node spacing is just close enough at $a\kappa = 5$ to ensure that $\Phi_{elec}(+90°) > \Phi_{elec}(+45°)$, although that is not true for the derivative of Φ_{elec}. For $a\kappa = 10$, 240 elements are insufficient to place the potential energies in the proper ranking for all separations. A series of calculations with sequentially refined grids shows a consistent reduction in the size of this discrepancy, indicating it is a numerical artifact.

6. Summary and Discussion

In preparation for studying the interaction potential for a protein molecule and a charged surface, we developed a boundary element method to calculate the electrostatic

13

potential. The use of the linearized Poisson-Boltzmann equation in the electrolyte region permits us to divide the complete problem into three subproblems (sphere-sphere, flat plate, and "remainder") that can be solved independently to obtain the full potential. A consistent solution of Laplace's equation inside the sphere is implicitly obtained to satisfy the continuity of potential and jump in electric displacement at the surface of the sphere.

Electrostatic free energies calculated from the boundary element method agree closely with those predicted from the linear superposition approximation when the particles are not too close. The finite size of the elements introduces some numerical "orientation" effects which decrease with further refinement of the mesh. Similar calculations for an uncharged sphere - charged plate system also reproduce the expected behavior. Calculations with a nonuniform charge distribution show that the free energy depends strongly on orientation. Such orientation effects can play important roles in protein adsorption or crystal growth. Results for a nonuniformly charged protein are reported in Part II.

References

(1) Cudd, A.; Fridovich, I. *J. Biol. Chem.* **1982**, 257, 11443-11447.

(2) Getzoff, E. D.; Tainer, J. A. ; Weiner, P. K; Kollman, P. A.; Richardson, J. S.; Richardson, D. C. *Nature.* **1983**, 306, 287-290.

(3) Klapper, I.; Hagstrom,R.; Fine,R; Sharp. K; Honig, B. *Proteins: Structure, Function, and Genetics.* **1986**, 1, 47-59.

(4) Allison, S. A.; McCammon, J. A. *J. Phys. Chem.* **1985**, 89, 1072-1074.

(5) Ganti, G.; McCammon,J. A.; Allison, S. A. *J. Phys. Chem.* **1989**, 89, 3899-3902.

(6) Allison, S. A.; Northrup, S. H.; McCammon, J. A. *Biophys. J.* **986**, 49, 167-175.

(7) Northrup, S. H; Allison, S. A.; McCammon, J. A. *J. Chem. Phys.* **1984**, 80, 1517-1524.

(8) Sharp, K. *J. Computational Chem.* **1991**, 12, 454-468.

(9) Russel, W. B.; Saville, D. A.; Schowalter, W. R. *Colloidal Dispersions.* Cambridge: Cambridge University Press, **1989**.

(10) Jackson, J. D. *Classical Electrodynamics, 2d ed.* New York: Wiley, **1975**.

(11) Brebbbia, C. A.; Telles, J. C. F.; Wrobel, L. C. *Boundary Element Techniques.* Berlin: Springer-Verlag, **1984**.

(12) Kellogg, O. D. *Foundations of Potential Theory.* New York: Murray, **1929**.

(13) Israelachvili, J. N. *Intermolecular and Surface Forces.* Orlando: Academic Press, **1985**.

(14) Verwey, E. J. W.; Overbeek, J. Th. G. *Theory of the Stability of Lyophobic Colloids.* New York: Elsevier, **1948**.

(15) Sharp, K. A.; Honig, B. *J. Phys. Chem.* **1990**, 94, 7684-7692.

(16) Davis, M. E.; McCammon, J. A.. *J. Computational Chem.* **1990**, 11, 401-409.

(17) Grant, M. L. *Protein Crystal Growth: The Influence of Colloidal Interactions and Fluid Motion*. PhD Thesis, 223 pp., Princeton University **1992**.

(18) Krozel, J. W.; Saville, D. A. *J. Colloid Interface Science* **1992**, 150, 365-373.

(19) Lorrain, P.; Corson, D. R. *Electromagnetic Fields and Waves 2d ed*. San Francisco: W. H. Freeman, **1970**.

Figure 1: Definition Sketch.

Lengths are scaled by the particle radius, a, and surface charge densities by $\sigma_0 = \varepsilon_0 \psi_0/a$.

Figure 2: Decomposition into subproblems.

(top) The potential produced by a nonuniformly charged sphere near an uncharged insulated wall is equivalent to a charged particle interacting with its mirror image, u^{ss}. The mirror image is obtained by reflecting the original particle across the plane $z = 0$.

(bottom) The potential produced by an uncharged sphere near a uniformly charged infinite plate, u^{sp}, can be written as the sum of the potential of a uniformly charged flat plate (u^{fp}) and a "remainder" (u^r). The fixed volume and surface charge densities shown in the figure are the result of subtracting u^{fp} from u^{sp}.

Figure 3: A spherical triangle element on the sphere.

Vertices are identified by circled numbers; edges are numbered sequentially as the perimeter of the element is traversed. The centroid of the element lies inside the sphere but is projected onto the surface to locate the node of the element.

Figure 4: Boundary element discretization of the sphere's surface.

The boundaries of the elements have been drawn on the surface of the sphere; the axes shown define the sphere's internal coordinate system and show the orientation of the discretization. The corresponding 2-dimensional projection ("surface map") of the discretization is also shown. Locations on the surface are identified by latitude and longitude. The nodes are plotted as filled circles. (a) $N = 8$. (b) $N = 20$.

Figure 5: Orientation of the sphere.

The orientation of the sphere is defined by the angles α and β (latitude and longitude) which identify the point on the sphere closest to the plane $z = 0$. The figure shows an example where $\alpha < 0$. The line of centers of the two spheres is an axis of rotational symmetry. The octants have been identified by letters and their reflections are indicated by primes to illustrate the mirror symmetry about the plane $z = 0$.

Figure 6: Definition sketch for the two sphere problem.

Figure 7: Electrostatic free energy for two uniformly charged spheres with $\sigma^* = \varepsilon_1 = \varepsilon_2 = 1$.

Solid line is the linear superposition approximation. Plot symbols denote number of elements on the sphere: ■ 8, ● 24, ▲ 48, ◆ 96, □ 20, O 60. On the scale of the figure these results are almost indistinguishable.

Figure 8: Electrostatic free energy for two uniformly charged spheres for $a\kappa = 5$ and $\sigma^* = \varepsilon_1 = \varepsilon_2 = 1$.

    (a) Φ_{elec} as a function of separation. Solid line is the linear superposition approximation. Plot symbols denote number of elements on the sphere: ■ 8, ● 24, ▲ 48, ◆ 96, □ 20, ○ 60.

    (b) Φ_{elec} at contact as a function of the number of elements on the sphere. Maximum values were calculated with a node closest point to the image sphere. Plot symbols: ■ Φ_{elec}, ● Φ_{elec}^{max}.

Figure 9: Electrostatic free energy for a charged plate and an uncharged sphere.

    In this system, the potential decays as $\exp(-2a\kappa d)$ except near the plate. The line shows the expected slope. $\sigma_x = 100$, $\varepsilon_1=1$, $\varepsilon_2=78.5$.

Figure 10: Electrostatic free energy for two image spheres with charged caps.

    Uniform charge density of $\sigma^* = 358$ is applied to a spherical cap centered at the particle's "north pole" ($\alpha = +90$) and covering 25% of the surface; the remainder of the sphere is uncharged. Dielectric constants are $\varepsilon_1 = 1$ and $\varepsilon_2 = 78.5$; $\beta = +90°$. Each symbol represents a different angle α. Plot symbols: ■ +90°, ● +45°, ▲ 0°, ◆ −45°, □ −90°. (a) $a\kappa=5$. (b) $a\kappa = 10$.

Figure 1

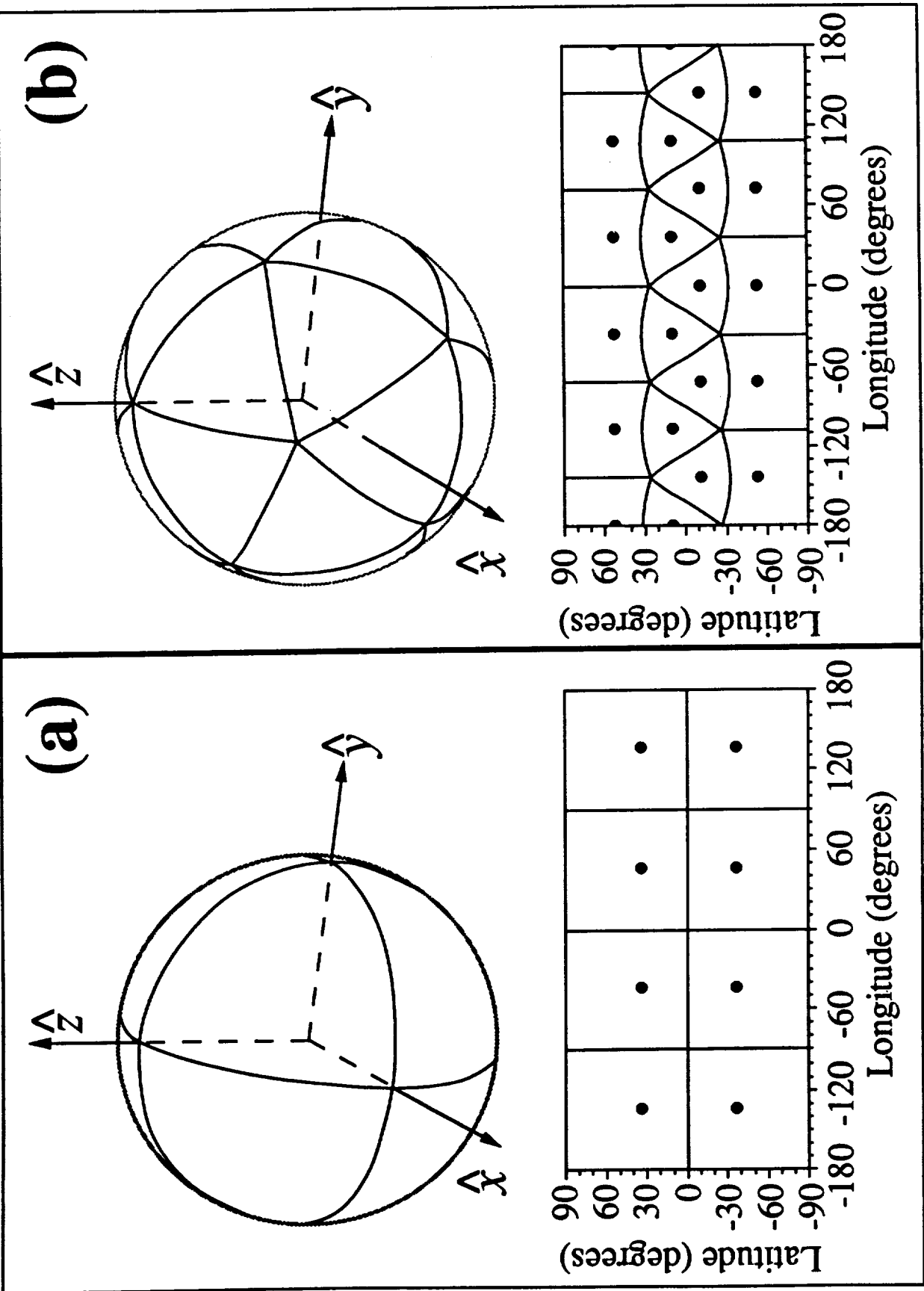sphere-sphere

sphere-sphere $\nabla u \cdot \mathbf{n} = 0$ σ^*

remainder

flat plate u^{fp} z σ_x^*

sphere-plate $\sigma^* = 0$ z σ_x^*

Figure 2

node

edge 2

centroid

edge 1

edge 3

②

①

③

③

(a)

(b)

A

$\hat{z}$

C

$\hat{x}$

B

β

α

D

$\hat{y}$

z

z = 0

D'

C'

B'

A'

Figure 5

Fig. 6

6

$a\kappa = 1$

$\dfrac{\Phi_{elec}}{\varepsilon_o \psi_o^2 a}$

gap half-width, d

$a\kappa = 0.1$

$\dfrac{\Phi_{elec}}{\varepsilon_o \psi_o^2 a}$

gap half-width, d

⑦

Figure

(b) number of elements, N
$\dfrac{\Phi_{elec}}{\varepsilon_0 \psi_0^2 a}$

(a) gap half-width, d
$\dfrac{\Phi_{elec}}{\varepsilon_0 \psi_0^2 a}$

plate-particle separation, d

$\dfrac{\Phi_{elec}}{\varepsilon_0\psi_0^2 a}$

Figure 9

$a\kappa = 10$

$\dfrac{\Phi_{elec}}{\varepsilon_o \psi_o^2 a}$

gap half-width, d

$a\kappa = 5$

$\dfrac{\Phi_{elec}}{\varepsilon_o \psi_o^2 a}$

gap half-width, d
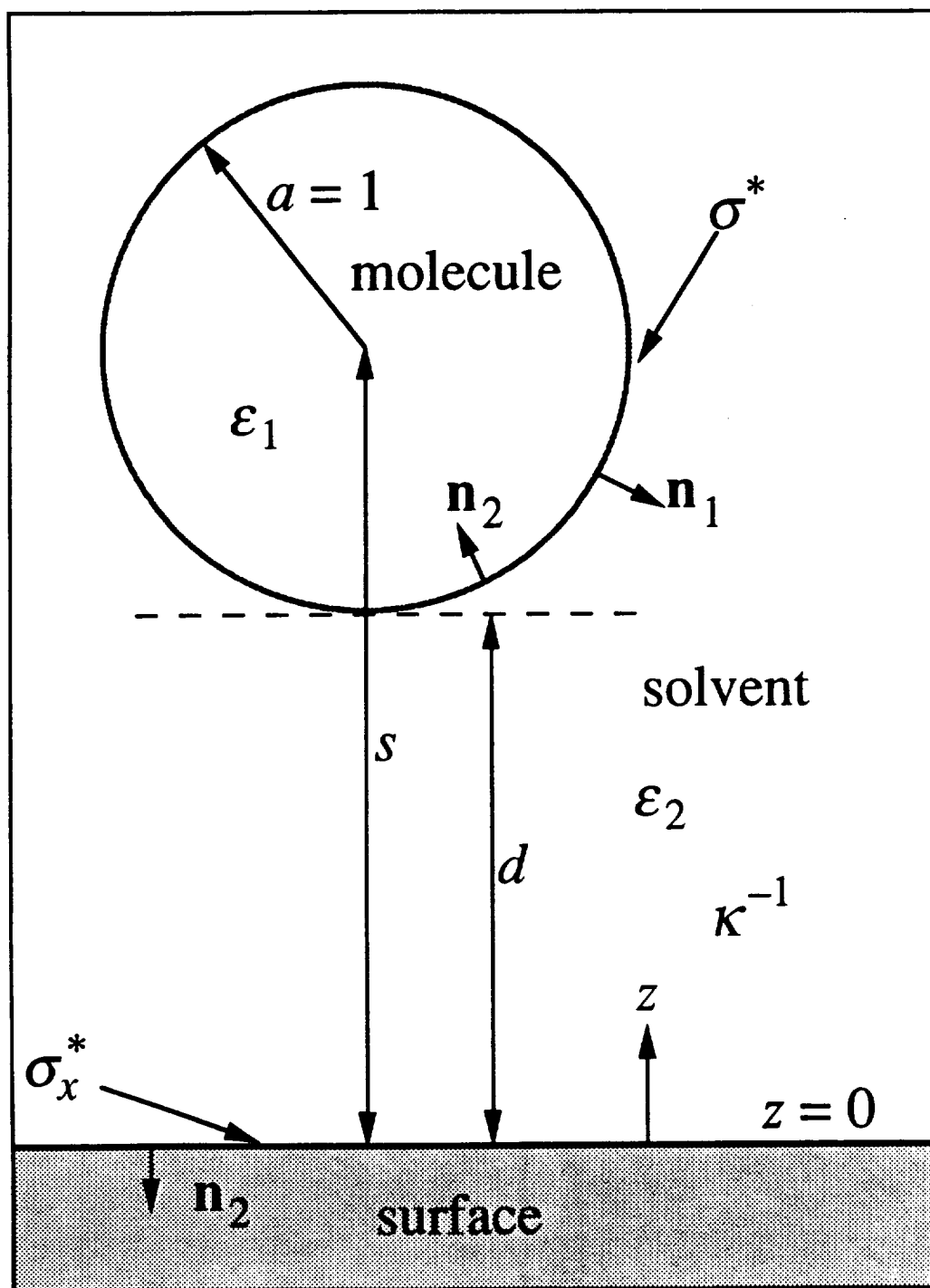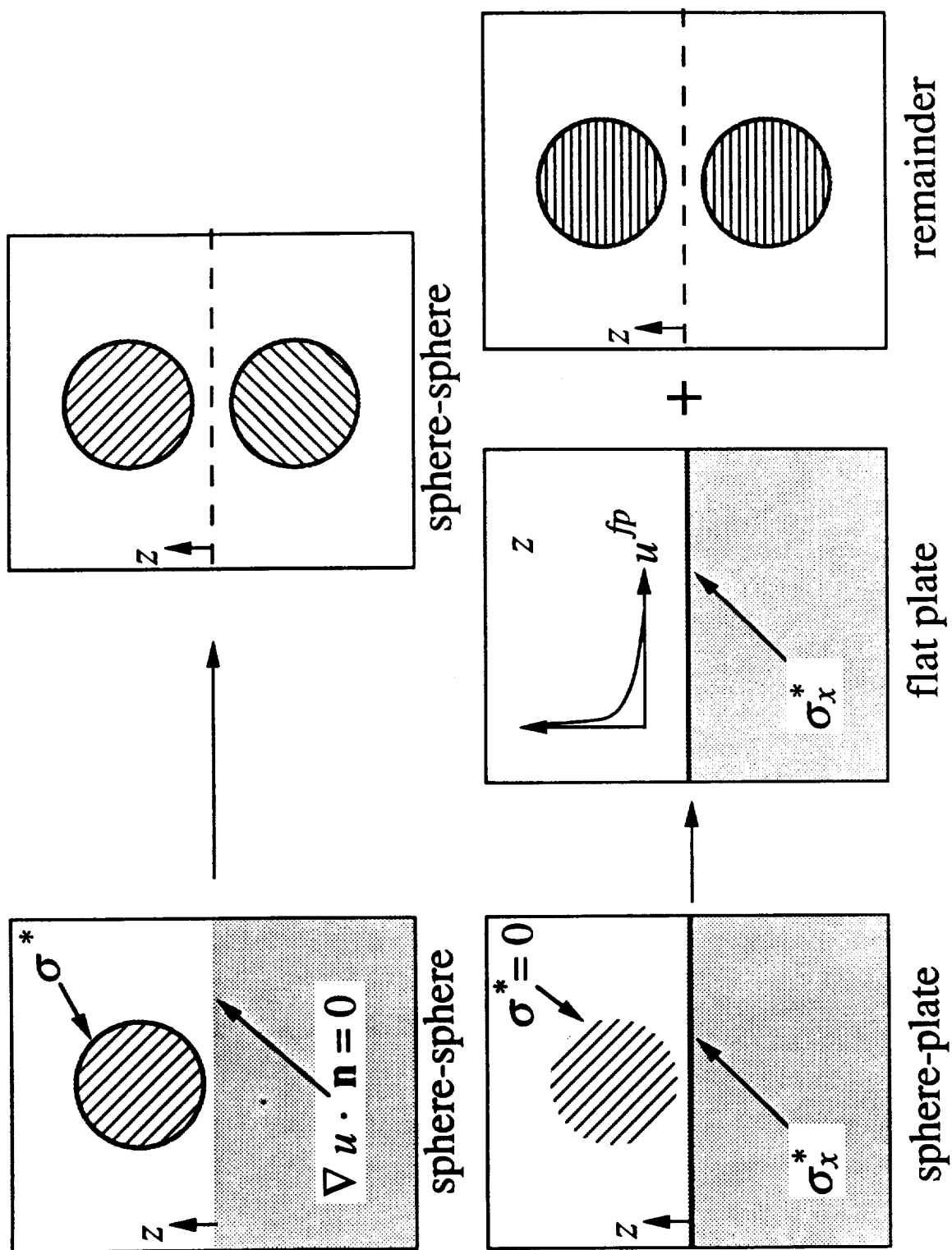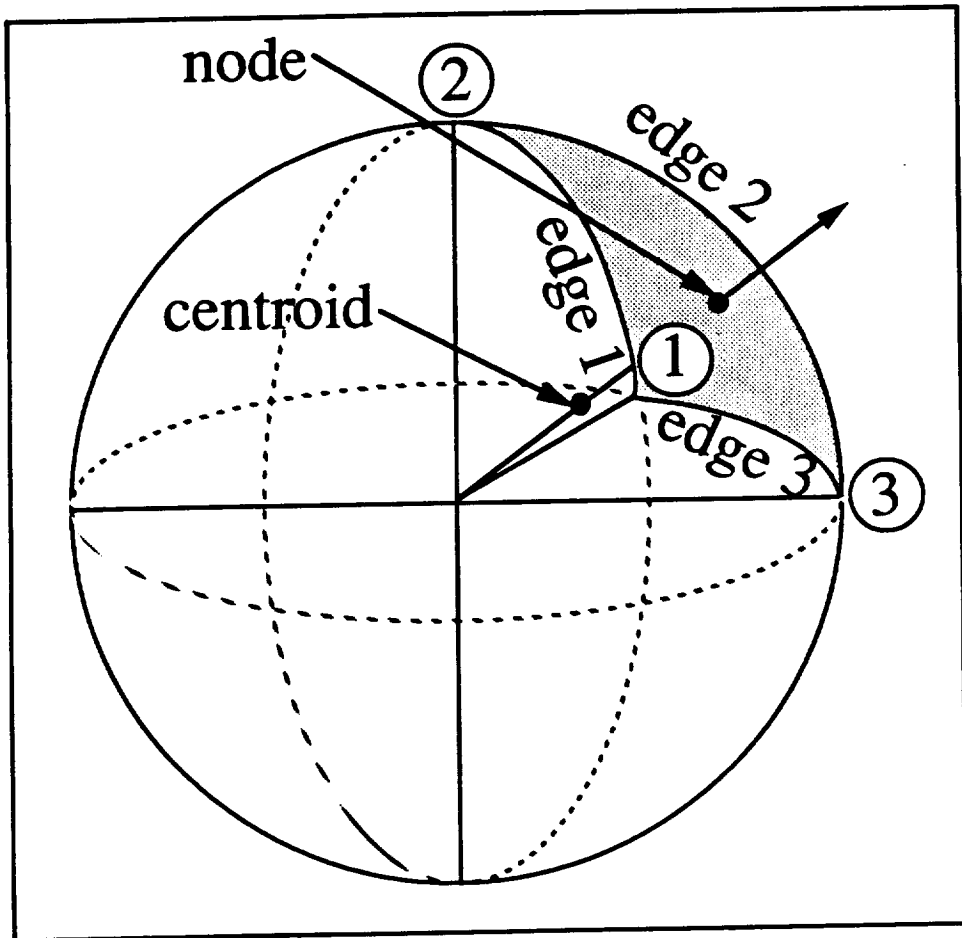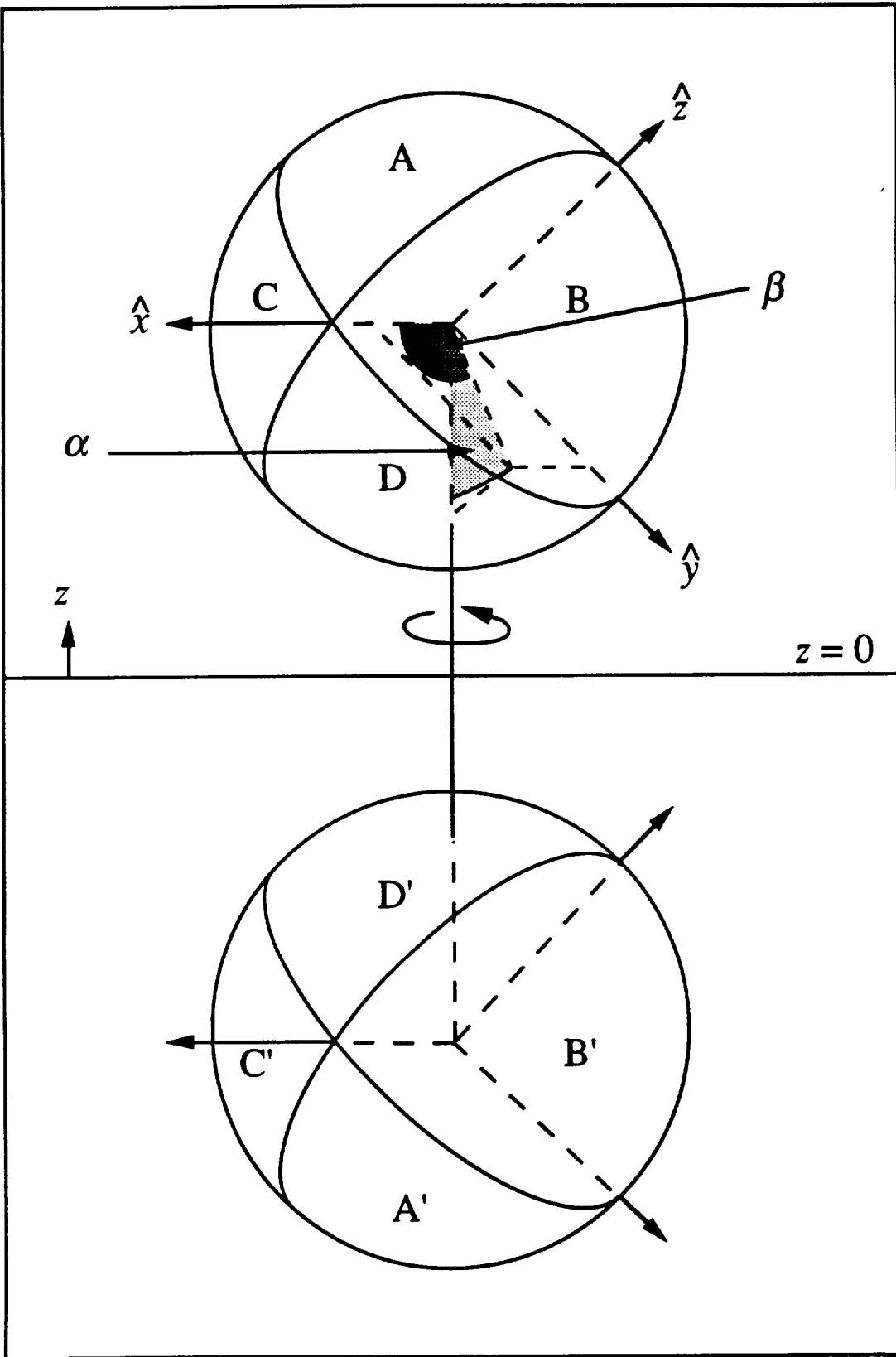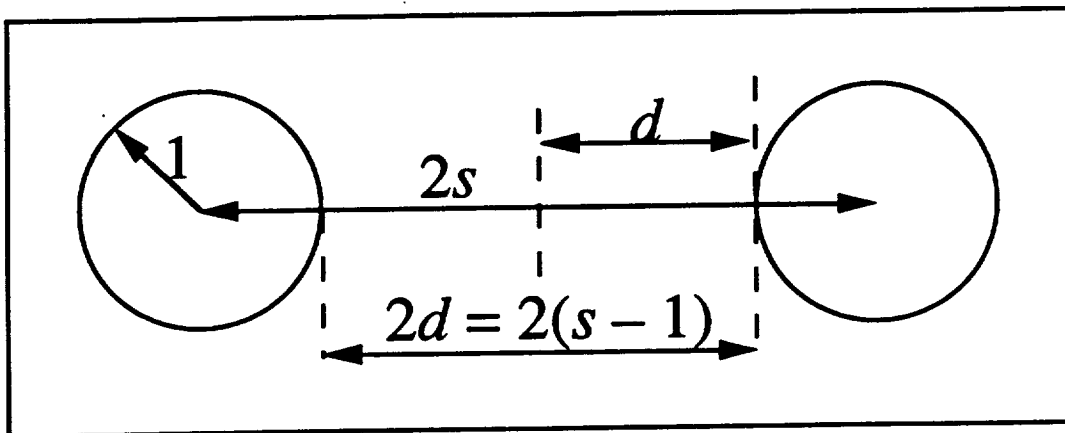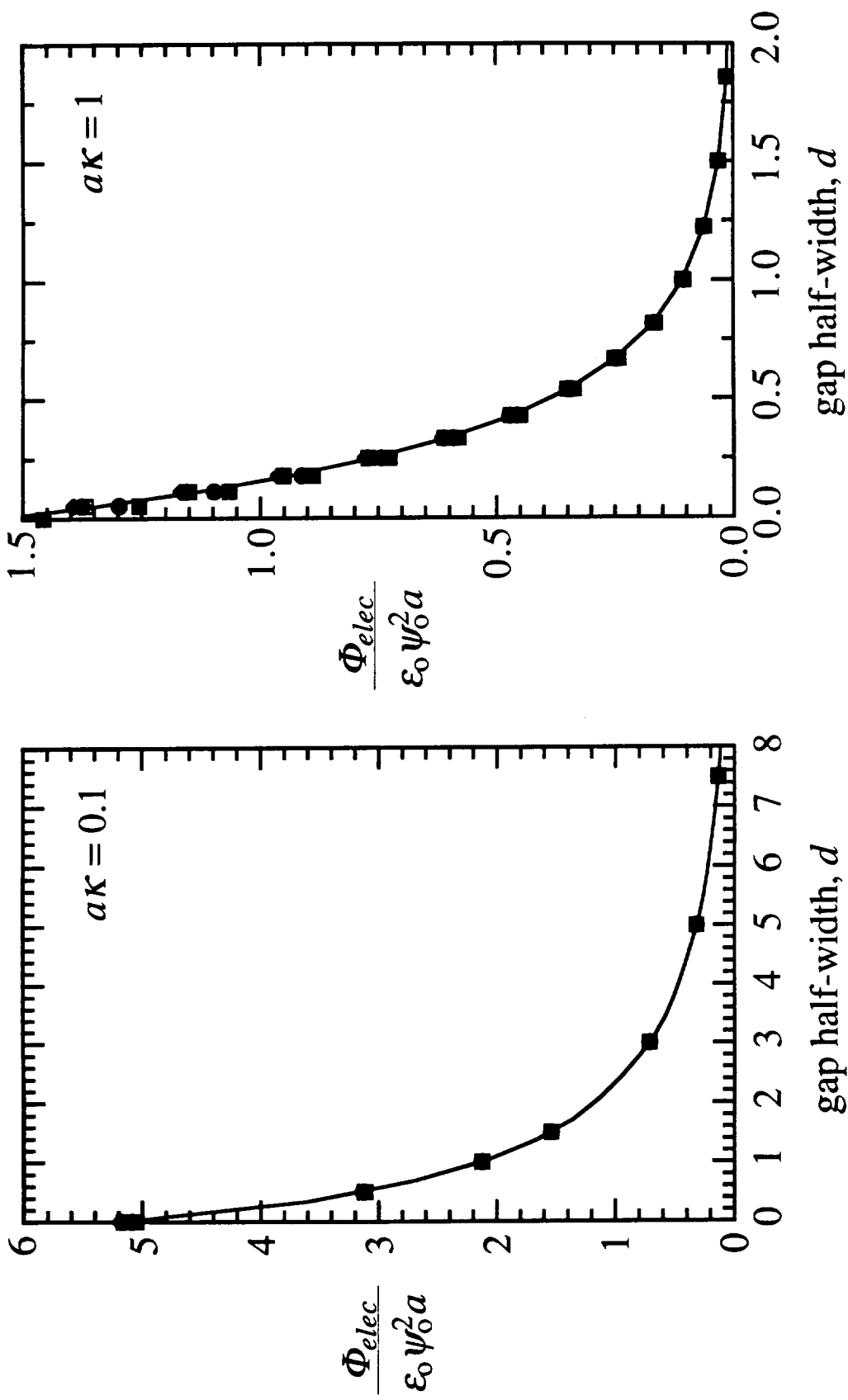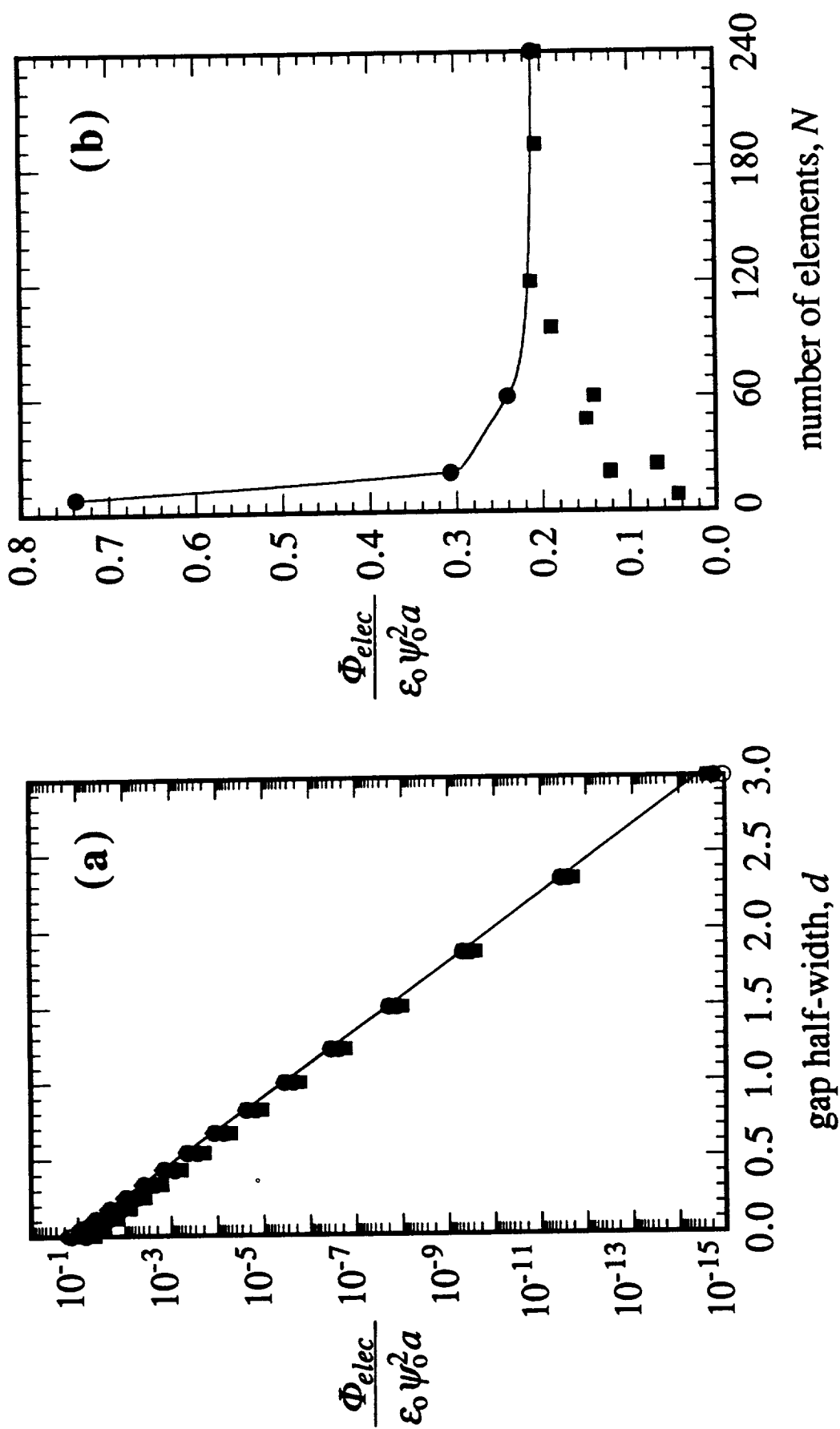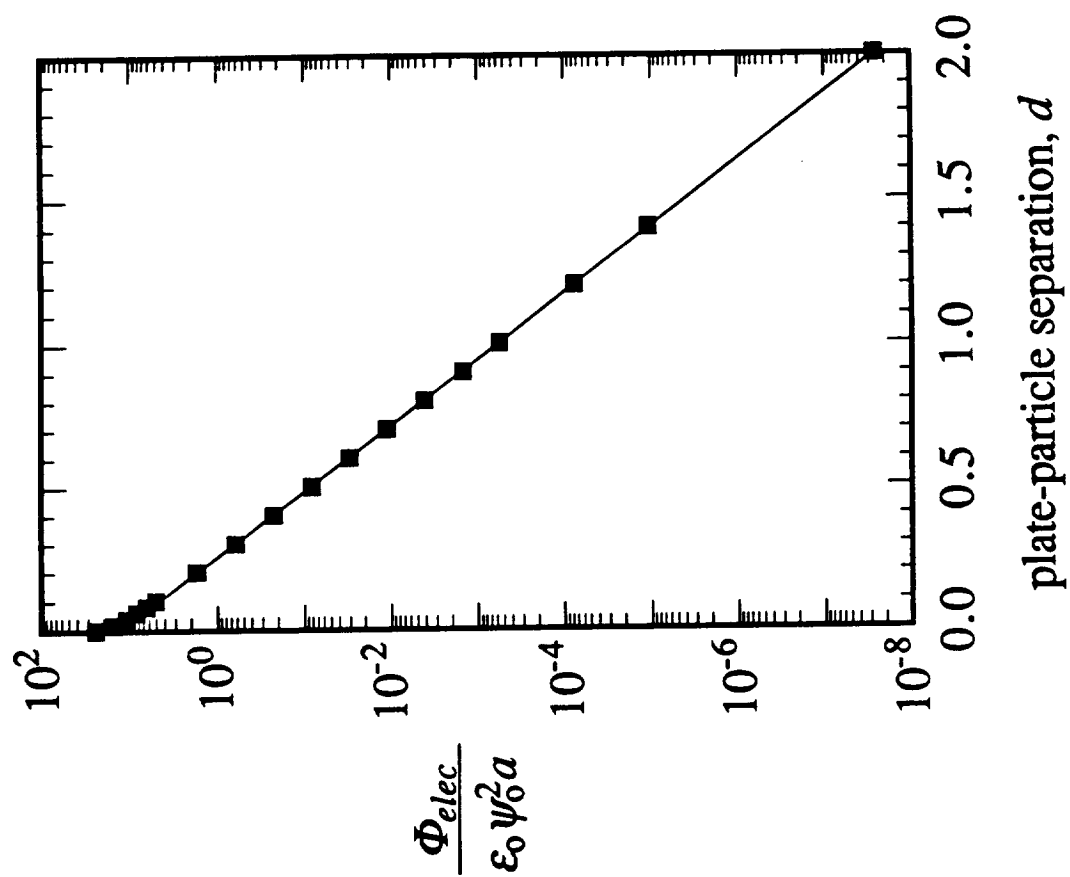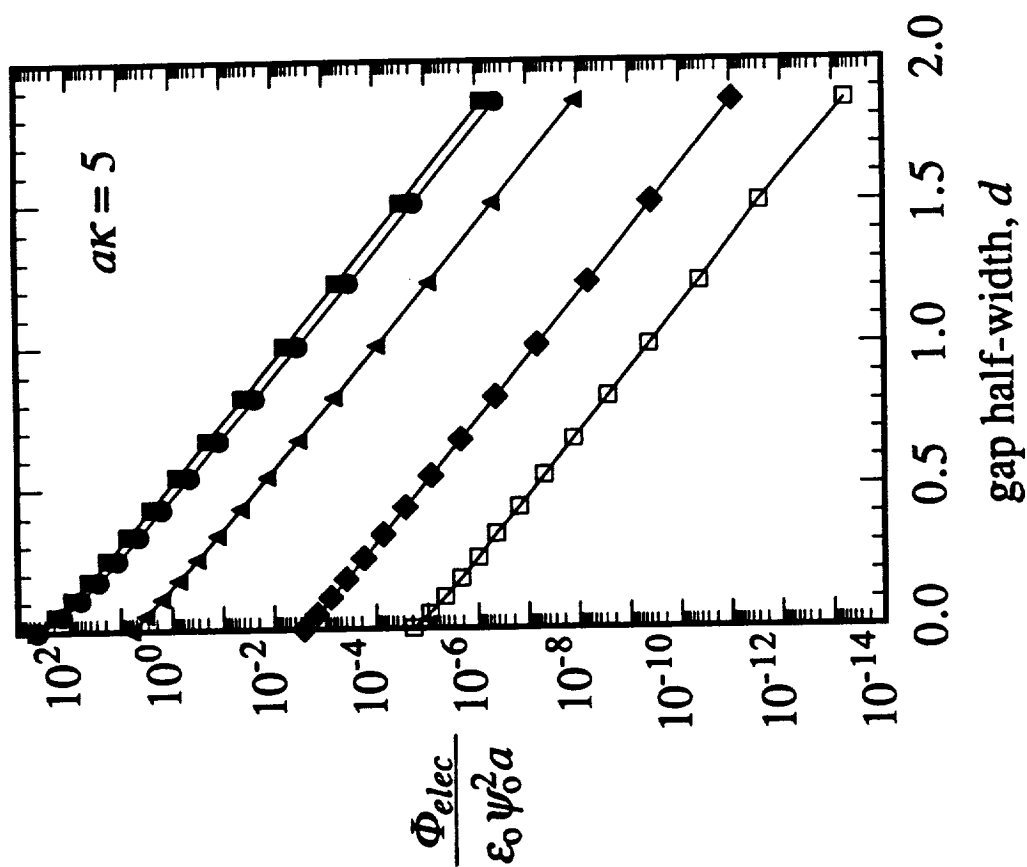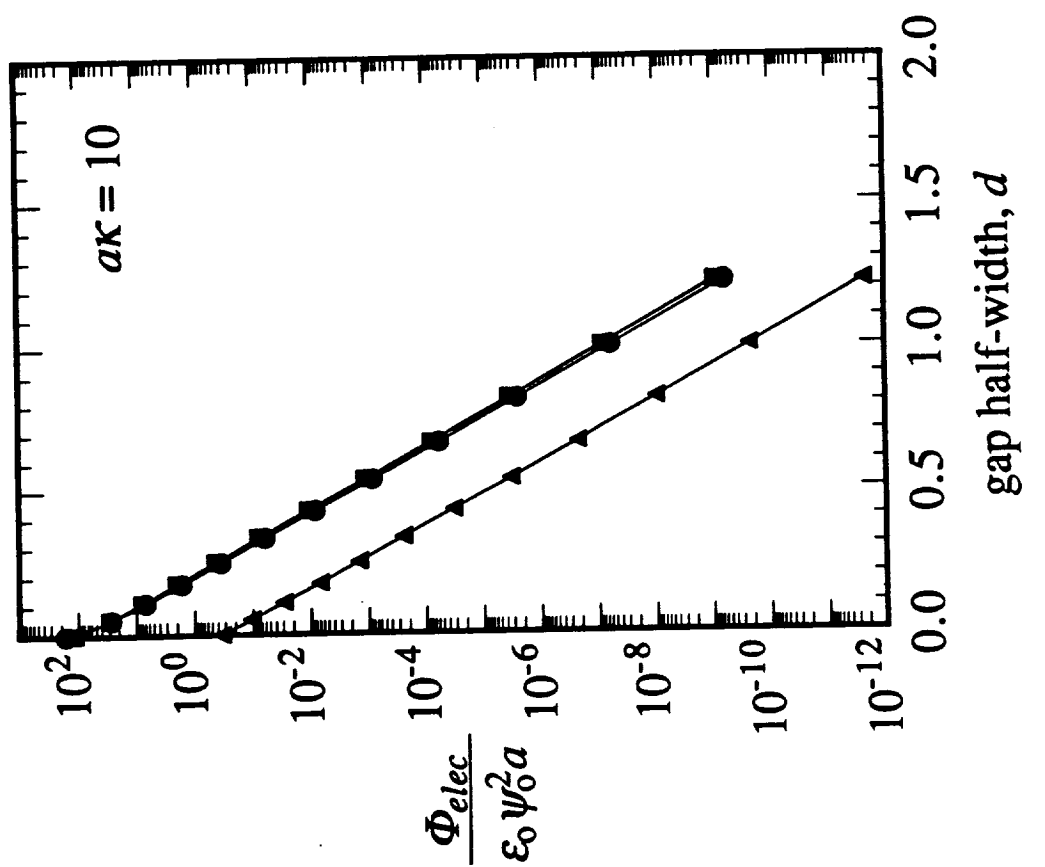
Figure

Electrostatic Interaction Between a Protein Molecule and a Charged Surface:

Part II: The Free Energy of a Lysozyme Molecule Near a Flat Plate

M. L. Grant[1] & D. A. Saville

Department of Chemical Engineering
Princeton University
Princeton NJ 08544

---

[1]Now at Exxon Production Research Company, Houston, Texas

Abstract

A boundary element method (BEM) was employed to calculate the interaction potential for a protein molecule and a uniformly charged flat plate. The protein molecule was treated as a sphere with a dielectric constant of 2 and the protein charge distribution represented by patches of charge on the sphere surface. The interaction potential was computed as a function of orientation and an angle-averaged potential calculated. As expected, there are a large number of local minima in the potential at contact. The angle-averaged free energy is close to the free energy of a uniformly charged sphere having the same net charge as the protein molecule when the plate surface charge density is modest sized. When the plate is highly charged, the free energy of the protein system can be as much as 10 kT lower than the uniform sphere. Even larger differences are expected if the plate's charge distribution is as heterogeneous as the molecule's.

1. Introduction

In this paper, we describe the results of calculations of the interaction energy between a protein molecule and a charged surface (a flat plate) using the boundary integral technique described in Part I. The interaction energy depends on the separation and orientation of the two bodies and is the reversible work done against both electrostatic and dispersion or van der Waals forces. Our objective is to calculate the free energy of the interaction, taking account of the nonuniform charge distribution on a representative protein molecule and ascertain how it is reflected in the "adsorption" energy for a flat surface. That surface might be a protein crystal, if one is interested in protein crystallization; another solid body, if the application is to a separation process such as chromatography; or simply another protein covered surface. To mimic the behavior of a typical protein we use data on the globular protein lysozyme.

The assumptions used to simplify the calculations are listed in Table 1. First, the two interactions are presumed additive; this is the cornerstone of the Derjaguin-Landau-Verwey-Overbeek (DLVO) theory and is justified by numerous observations[1-3]. Dispersion forces are modeled using an "effective" Hamaker constant, A_{eff}. Frequency spectra for a material's dielectric behavior are required for a detailed calculation using the Lifshitz theory [1] so, in the absence of such data for proteins, we take A_{eff} as given. We assess the relative importance of dispersion forces by varying A_{eff} but neglect effects due to restructuring of the solvent, e.g., hydration forces.

Next, linearization of the Poisson-Boltzmann equation simplifies the electrostatics problem. The linearization is consistent with the low net charge on the molecule and, moreover, allows us to readily assess the significance of nonuniform charge distributions in protein-surface interactions. The average surface potential of lysozyme in 1M NaCl in water ($\varepsilon_2 = 80$) is about 16 mV based on a net valence of +10.5 at pH 4.7 [4] and a hydrodynamic radius of 20Å [5]. Since the linearization is valid for potentials up to approximately 100 mV [1], it is more than adequate except when the particle and surface are almost in contact.

The disparate sizes of the molecule and surface justify the treatment of the surface as a semi-infinite region with a surface charge. For an ionic strength of 1M, κ^{-1}, the Debye length, is approximately 3Å. Exponential decay of the potential limits the range of the electrostatic forces to about $5\kappa^{-1}$ (15 Å) so a molecule approaching a surface may not "sense" it until it is roughly 15Å away. Nevertheless, the use of a uniformly charged flat plate to represent the surface is one of the more severe assumptions because the scale of the roughness and charge heterogeneity of most surfaces are the same as those of the molecule. Although we recognize the limitations of this approximation, the intricacies caused by such effects are beyond the scope of our calculations. To some extent, the effect of a nonuniform surface charge

distribution can be estimated by calculating the electrostatic potential energy for different amounts of (uniform) surface charge, σ_x, since mobile ions in solution screen the influence of all but a small portion of the surface. Nevertheless, detailed calculations which take account of the structure of the surface charge will eventually be needed to appreciate the subtleties of adsorption.

Table 1

Assumptions Employed in Studying Molecule-Surface Interactions.

The electrostatic and dispersion (van der Waals) potentials are additive.

The dispersion potential is independent of molecular orientation.

The effective Hamaker constant, A_{eff}, is independent of separation.

The linearized Poisson-Boltzmann equation governs the electrostatics.

The surface can be treated as semi-infinite region with a uniform surface charge density, σ_x.

The protein molecule can be treated as a sphere.

The charge of the protein molecule can be represented by a surface charge distribution.

The interior of the protein molecule has a dielectric constant of 2.

The main reason for treating the protein molecule as a sphere is simplicity. Crystallographic data indicate that most globular proteins are roughly spherical and a table of 20 proteins of known structure [6] shows that the ratio of maximum to minimum dimensions is seldom greater than 2. Hen egg white lysozyme is variously described as being an ellipsoid of dimensions 23Å × 28Å × 40Å [4], or 30Å × 30Å × 45Å [6], or 30Å × 30Å × 45Å "with a wedge-shaped piece removed" [7]. All these are consistent with a spherical approximation and a hydrodynamic radius of approximately 20Å [5].

Charged residues are almost invariably found at the surface of the protein molecule, where they can interact with the polar water molecules [6,7]. Researchers who use finite difference methods [8-11] model the charge distribution with point charges lying just inside the surface of the protein that is accessible to a "probe sphere", e.g., a water molecule 1.4Å in radius [6,9]. We represented the protein's charge using a smoothed surface charge distribution to facilitate implementation of the boundary element method. The method for translating the

charge distribution obtained from X-ray crystallography into a surface charge distribution will be described in section 2.

Hydrophobic residues and side chains tend to be buried in the interior of the molecule, at least when the molecule is soluble in water [6,7]. Calculations of packing density give values around 0.75 [6,7], indicating that the interior is relatively uniform. Free water is generally absent from the interior, although molecules such as lysozyme and α-chymotrypsin seem to have cavities or holes which are presumed to contain solvent [7]. Water molecules can be detected in the interior of some protein molecules and appear to be intrinsic features of protein structure [6]. Thus the dielectric constant in the interior of the molecule is often taken to be in the range between 2 and 4 [12-16]. Dao-pin et al. [11] calculated the electrostatically induced shift in pK_a for two systems as a sensitivity check and found the shift was insensitive to values chosen in the range $2 \leq \varepsilon_1 \leq 8$, except at low ionic strength.

The purpose of these approximations is to simplify the problem so it can be solved while preserving its essential features. Results for a molecule with an anisotropic charge distribution can then be compared with those for a uniformly charged molecule and differences in behavior ascribed to the anisotropic particle charge. The level of approximation employed here is appropriate for such an investigation.

2. Idealization of the Lysozyme Molecule

The thrust of the study is to describe those features of the electrostatic interaction which derive from anisotropic surface charge distributions. Rather than create completely artificial distributions, the charge distribution of lysozyme was used.

As noted earlier, hen egg white lysozyme is an oblong molecule. The approximate coordinates of its charged groups (taken from crystallographic data for the tetragonal space group at 1.4M NaCl in 0.02M sodium acetate buffer at pH 4.7) are listed in Table 2 [4]. We assume that all the charged groups lie on a spherical surface and seek the location and size of the sheath which comes closest to all the charged groups. The sphere is defined by the location of its origin (x_o, y_o, z_o) and its radius, a. One method for obtaining the best-fit sphere is to find the location of the origin such that the lengths of radii from the origin to the charges,

$$R_i = \left[(x_i - x_o)^2 + (y_i - y_o)^2 + (z_i - z_o)^2\right]^{1/2} \tag{1},$$

have minimum scatter about the mean value $\bar{R} = a$. We performed such a calculation using the method of random descent with a final step size of 0.01Å. In the coordinate system specified in Table 2, the best-fit sphere is located at $(-1.67, 20.91, 17.91)$ and has a radius of 16.48Å. These compare favorably with the center of mass $(-1.08, 20.00, 18.35)$ determined by inspection [4] and the hydrodynamic radius of approximately 20Å [5]. The location of charge i

was projected onto the surface of the sphere using the radius vector $\mathbf{R}_i$; the surface charge distribution is diagrammed in Figure 1.

Table 2

Coordinates of charged groups in tetragonal hen egg white lysozyme.

Number	Residue	Type	Charge	X	Y	Z
1	1	N-terminus	+1	3.28	10.16	10.35
2	1	lys	+1	−3.80	10.48	8.18
3	5	arg	+1	−6.31	24.40	2.84
4	13	lys	+1	−17.40	21.25	11.10
5	14	arg	+1	−12.20	9.25	14.63
6	15	his	+0.5	−9.67	11.01	17.86
7	18	asp	−1	−14.73	24.29	14.83
8	21	arg	+1	−11.82	23.93	29.27
9	33	lys	+1	3.17	23.88	5.62
10	35	glu	−1	4.38	24.84	18.14
11	45	arg	+1	18.46	15.42	23.99
12	48	asp	−1	14.17	22.91	29.22
13	52	asp	−1	8.98	21.08	22.43
14	61	arg	+1	13.02	20.81	31.91
15	66	asp	−1	11.50	12.56	27.61
16	68	arg	+1	16.16	12.96	24.25
17	73	arg	+1	1.83	16.91	39.96
18	87	asp	−1	−5.45	7.45	16.81
19	96	lys	+1	−11.68	16.57	22.82
20	97	lys	+1	−5.50	14.40	30.09
21	101	asp	−1	−2.00	24.43	32.74
22	112	arg	+1	5.25	33.64	23.22
23	114	arg	+1	6.61	30.51	10.82
24	116 °	lys	+1	−1.79	36.55	22.86
25	125	arg	+1	−10.80	31.20	−1.00
26	128	arg	+1	−18.86	17.79	0.09
27	129	C-terminus	−1	−17.14	21.78	6.41

If the charged groups on the surface are represented as point charges, the potential in their immediate neighborhood is too high for the linearized Poisson-Boltzmann equation to apply. Instead, we employ the method of "local averaging" to create a patchwork of charge smooth enough to ensure that the governing equations remain valid but "lumpy" enough to exhibit behavior unique to anisotropically charged proteins. Local averaging is often used to make continuum approximations of discrete phenomena. Here the averaging is done by centering a spherical cap at the point of interest and summing the point charges which lie within the cap. The local charge density is the net charge within the cap divided by the area of the cap, A_{sample}. A specific charge contributes to the local charge density when the distance (r_i) from the point of interest to charge i is less than r_{sample} (see Figure 2). The local charge density is:

$$\sigma = \frac{1}{A_{sample}} \sum_{i=1}^{N} Q_i H\left(r_{sample} - r_i\right) \tag{2},$$

where Q_i = charge of group i, and $H(\cdot)$ is the Heaviside step function. The sampling radius is given by $r_{sample} = a\sqrt{2(1 - \cos\theta)}$; the sampling area is $A_{sample} = \pi r_{sample}^2$. Maps of the local surface charge density derived for lysozyme are shown in Figure 3 for sample areas of 300, 200, and 100 Å^2. The surface area of the model lysozyme molecule, A_{sphere}, is approximately 3400 Å^2, so the charge density maps shown in Figure 3 correspond to sample areas ranging from about 9% to 3% of the molecule's surface. Note, however, that mapping the sphere's surface as a rectangle distorts the distribution. The degree of heterogeneity and the size of its effect are controlled by the choice of A_{sample}. As an extreme example, setting the $A_{sample} = A_{sphere}$ produces a uniformly charged particle with the same net charge as the model sphere.

A_{sample} has a lower bound below which the model no longer applies. This bound derives from the limits of applicability of the linearized Poisson-Boltzmann equation, approximately 100 mV (a dimensionless potential of 4 when scaled on kT/e). For an isolated sphere with a uniform scaled surface charge density, σ^*, the scaled surface potential, u^∞, is $\sigma^*/[\varepsilon_2(1 + a\kappa)]$. Surface charge densities greater than about $4\varepsilon_2(1 + a\kappa)$ would place the system outside the range of validity of the linearized Poisson-Boltzmann equation. Therefore, if the net charge within the sampling area is Q, the corresponding restriction on A_{sample} is:

$$A_{sample} > \frac{Qa}{4\varepsilon_0\varepsilon_2\psi_0(1 + ak)} \tag{3}.$$

5

To smear a proton charge ($Q = 1.6\times10^{-19}$ C) on a particle with $a = 16.48$Å, $\varepsilon_2 = 80$ (water) and $a\kappa = 5$ (ionic strength approximately 1M) requires a *minimum* sampling area of 60 Å^2. Our calculations are based on a sampling area of 100 Å^2.

Once a smooth charge distribution available, it must be translated into a form consistent with the boundary element formulation wherein each element has uniform potential and charge. The (constant) charge density, σ_j, assigned to an element is calculated by averaging over the area of the element, A_j:

$$\sigma_j = \frac{1}{A_j} \int_{A_j} \sigma \, dA \qquad (4).$$

This method of computing σ_j introduces the length scale of the discretization into the problem. The larger of A_{sample} and A_j determines the length scale of the patchiness. Surface charge density maps shown in Figure 4 show how the charge distribution in Figure 3c is approximated by successive refinements of the original icosahedral discretization (Part I). The discretized charge distribution shown in Figure 4d retains much of the general character exhibited by the smoothed charge distribution in Figure 3c, although the range of surface charge densities in Figure 4d is slightly smaller because of the additional averaging described by equation (4).

Several layers of approximation have been employed to create a realistic model of a protein molecule. The choice of sampling area is dictated by the linearization of the governing equation. The idealization of the molecule as a sphere and the corresponding mapping of the charged groups reflect a desire to keep the problem as simple as possible. Despite these simplifications the resulting surface charge distribution appears able to capture the essential features of the electrostatic phenomena.

3. Interaction Energy Between a Lysozyme Molecule and a Surface

Once the protein charge distribution is established, the boundary element technique can be used to calculate the sphere-plate electrostatic interaction energy as a function of separation and orientation (cf. Part I). However, the electrostatic free energy for an uncharged surface is always repulsive because charges on the sphere nearest the plate dominate the interaction. The effect of charge anisotropy can be seen in Figure 5, where we compare the electrostatic free energy at contact with an uncharged plate (Figure 5a) with the charge distribution (Figure 5b). When the surface charge density on the plate is raised to $\sigma_x^* = 500$ (230 Å^2 per charge), the repulsion is greatly increased (Figure 5c). Differences between various orientations are

enormous, reflecting variations in charge density around the sphere. According to these calculations there are a large number of local free energy minima with similar energies.

In some orientations, the calculated electrostatic surface potential can be 10 kT/e or larger at contact and would seem to violate the low potential assumption used to linearize the Poisson-Boltzmann equation. However, as the particle moves away from the flat surface, the potential decreases rapidly into the range where linearization is valid. Hence, although there is some uncertainty in the value of Φ_{elec} near contact, the results appear consistent with those calculated at small non-zero separations. This shortcoming is inherent in any model which employs the linearized Poisson-Boltzmann equation to describe the electrostatics.

In Part I, we discussed how the energy of a given orientation depends on the charge distribution on the nearest surfaces. When the plate is charged, orientations offering similarly charged surfaces suffer an increase in free energy while the free energies of orientations presenting oppositely charged surfaces are reduced, relative to their interaction with an uncharged plate. As we have just seen, energies between different orientations can be quite large. The "average" behavior of anisotropically charged and uniformly charged spheres is also of interest since rotary Brownian motion enables a molecule to sample many orientations. Therefore, we compare the orientation-averaged interaction potential with, e.g., the potential for a uniformly charged molecule having the same net charge. The proper orientation average is [17-19]:

$$\frac{\langle \Phi_{elec}(d) \rangle}{kT} = -\ln\left\{ \frac{1}{4\pi} \int\limits_{4\pi} \exp\left[-\frac{\Phi_{elec}(d,\Omega)}{kT} \right] d\Omega \right\}, \tag{5}$$

with the orientation defined in terms of the solid angle Ω. Using the constant element approximation, the integral over all solid angles can be replaced by a sum over the elements on the sphere:

$$\frac{\langle \Phi_{elec}(d) \rangle}{kT} = -\ln\left\{ \frac{1}{4\pi} \sum_{j=1}^{N} A_j \exp\left[-\frac{\Phi_{elec}(d,\alpha_j,\beta_j)}{kT} \right] \right\}. \tag{6}$$

Here A_j is the area of element j on the unit sphere and the coordinates (α_j, β_j) of node j define the orientation of the sphere (cf. Part I). The significance of the nonuniform charge distribution can be determined by comparing the angle-averaged interaction potential defined by equation (6) with that for the uniformly charged particle.

7

The angle-averaged interaction potential for the 240 element discretization of lysozyme is shown in Figure 6, along with results for the uniformly charged sphere ($\Phi_{elec}^{uniform}$) and lysozyme orientations having the maximum (Φ_{elec}^{max}) and minimum (Φ_{elec}^{min}) electrostatic potential energy. The arithmetic average potential energy ($\overline{\Phi}_{elec}$) is also shown. Note the large differences between the maximum, minimum and angle-averaged potentials. The relative ranking of $\langle\Phi_{elec}\rangle$, $\overline{\Phi}_{elec}$, and $\Phi_{elec}^{uniform}$ at small separations is obscured in Figure 6, so the results are replotted in Figure 7. At high surface charge densities, the angle-averaged potential lies below $\overline{\Phi}_{elec}$ and $\Phi_{elec}^{uniform}$, as expected, because the Boltzmann weighting favors lower potential energy orientations.

An important feature of these electrostatic free energy curves is the weak electrostatic repulsion at these charge densities (less than 6 kT when $\sigma_x^* = 500$, i.e., with approximately 230 Å^2 per charge). In addition, the difference in free energy (2 kT or less at these conditions) between the uniformly charged and angle-averaged molecules is relatively small. Each conclusion is consistent with the modest charge on the molecule and the surface.

To see how the electrostatic effects contribute to the total interaction we can add the effect of the van der Waals or dispersion potential. The dispersion potential for a (spherical) macroscopic body and a (spherical) molecule is [1,3,18]:

$$\Phi_{vdw} = -\frac{A_{eff}}{6}\left[\frac{2R}{2(R+1)d+d^2} + \frac{2R}{4R+2(R+1)d+d^2}\right.$$
$$\left. + \ln\frac{2(R+1)d+d^2}{4R+2(R+1)d+d^2}\right]$$

(7),

where R = radius of the macroscopic body and d = separation (gap) between the surfaces and the molecule; all lengths have been scaled by the particle radius. For cases of interest here, $R \gg 1$ and Φ_{vdw} at small d is insensitive to the exact value of R; a value of $R = 10^6$ was used for all calculations.

If the molecule and surface were pure hydrocarbon bodies interacting through water, A_{eff} would be about 1 kT at 300K [18]. Measurements of dispersion forces with lysozyme indicate values for A_{eff} in the range of 1 - 2 kT at room temperature [20,21]. In the study of protein crystallization, there is a sizable uncertainty in the value of A_{eff} because the crystal is approximately 50% solvent by volume [22]. There may be a similar uncertainty in the study of protein adsorption on a protein-covered surface. A naive estimate would take A_{eff} as roughly half the value for pure hydrocarbons, in which case the balance between van der Waals

attraction and electrostatic repulsion is as shown in Figure 8. The sensitivity of the barrier height to A_{eff}, is shown in Figure 9. At values of A_{eff} as low as 0.1 kT, the angle-averaged potential still peaks at only 2 kT (not shown in Figure 9).

Until now attention has focused on plate charge densities of modest size. Local "charge densities" on protein covered surfaces may be much larger . The surface potentials on an isolated lysozyme molecule provide some guidance in selecting the range of interest. For $a\kappa =$ 5, local surface potentials on an isolated lysozyme molecule range from +3.91 (+100 mV) to –2.44 (–63 mV); the equivalent surface charge densities on the plate are 1600 (72 Å^2 per charge) and –1000 (116 Å^2 per charge). Surface charge densities of this magnitude cause dramatic changes in the electrostatic free energy at contact (Figure 10). Figure 11 depicts the way the angle-averaged interaction potential varies with distance in these two cases.

4. Summary and Discussion

A simplified model of molecule-surface interactions was developed to take account of charge anisotropy on a protein molecule using a boundary element method (BEM). The BEM employs a linearized equation for the electrostatics, which allows the problem to be divided into subproblems that can be solved separately to obtain the total electrostatic potential. The nonuniform charge distribution on the protein molecule is represented by a set of surface elements of differing charge densities. Smooth surfaces and simple geometries are assumed for mathematical convenience. Electrostatic free energies calculated from the boundary element method for two uniformly charged spheres agree well with those given by the linear superposition approximation.

Interaction free energies (electrostatic and dispersion potentials) for the molecule-surface system in different orientations are calculated from the isothermal reversible work required to bring the two bodies into a given configuration. Different orientations have substantially different interaction energies. Free energies for different orientations were angle-averaged to obtain an "average potential." At moderate plate surface charge densities, the potentials of the angle-averaged molecule and a uniformly charged sphere having the same net charge are similar. In both cases, the electrostatic and dispersion terms nearly balance; the free energy maxima are correspondingly small (about 3 kT).

As σ_x^* increases to about 1000 (approximately 100 Å^2 per charge), large differences between the model lysozyme molecule and the uniformly charged sphere appear. The electrostatic free energy of uniformly charged particles can exceed the molecule's free energy by 10 kT at contact (see Figure 10). Dispersion forces, which dominate near the plate, reduce the difference somewhat, but the differences in the free energy maxima for the two systems are significant.

9

The nature of the plate's surface controls the behavior of the molecule near contact and this is where our model lacks rigor. The approximation of a moderate, uniform surface charge density on the plate clearly becomes less appropriate as the molecule approaches the plate. Instead, the highly charged patches on both the molecule and the surface interact, so differences in free energy as the molecule rotates and moves parallel to the surface should be similar to those shown in Figure 11. These results, although not definitive, clearly demonstrate the need to account for nonuninform charge distributions when modeling protein-surface interactions. The boundary element method provides a means to study the effects of charge heterogeneities on the adsorption of biological macromolecules.

Acknowledgments

References

(1)   Russel, W. B.; Saville, D. A.; Schowalter, W. R. *Colloidal Dispersions*. Cambridge: Cambridge University Press, **1989**.

(2)   Verwey, E. J. W.; Overbeek, J. Th. G. *Theory of the Stability of Lyophobic Colloids*. New York: Elsevier, **1948**.

(3)   Hiemenz, P. C. *Principles of Colloid and Surface Chemistry*. New York: Marcel Dekker, **1977**.

(4)   Smith, C. D. *Personal communication*. The structure of the lysozyme as recorded in the Brookhaven data bank was displayed on screen for visual inspection. Coordinates reported are estimates of the center of mass of the charged groups on the molecule.

(5)   Tanford, C. *Physical Chemistry of Macromolecules*. New York: Wiley, **1961**.

(6)   Creighton, T. E. *Proteins: Structures and Molecular Properties*. New York: W. H. Freeman and Company, **1983**.

(7)   Cantor, C. R. and P. R. Schimmel. *Biophysical Chemistry Part 1*. San Francisco: W. H. Freeman and Company, **1980**.

(8)   Klapper, I.; Hagstrom, R; Fine, R.; Sharp, K.; Honig, B. *Proteins: Structure, Function, and Genetics*. **1986**, 1, 47-59.

(9)   Gilson, M. K.; Sharp, K.; Honig, B. *J. Computational Chem*. **1987**, 9, 327-335.

(10) Nicholls, A.; Honig, B. *J. Computational Chem*. **1991**,12, 435-445.

(11) Dao-pin, S., D.-I. Liao, and S. J. Remington. *Proc. Natl. Acad. Sci. USA*. **1989**, 86, 5361-5365.

(12) Sharp, K. A.; Honig, B. *Ann. Rev. Biophys. Biophys. Chem*. **1990**, 19, 301-332.

(13) Davis, M. E.; McCammon, J. A. *J. Computational Chem*. **1990**, 11, 401-409.

(14) Gilson, M. K.; Honig, B. *Biopolymers*. **1986**, 25, 2097-2119.

(15) Gilson, M. K.; Honig, B. *Proteins: Structure, Function, and Genetics*. **1988**, 4, 7-18.

(16) Yoon, B. J.;Lenhoff, A. M. *J. Computational Chem*. **1990**, 11, 1080-1086.

(17) McQuarrie, D. A. *Statistical Mechanics*. New York: Harper and Row, **1976**.

(18) Israelachvili, J. N. *Intermolecular and Surface Forces*. Orlando: Academic Press, **1985**.

(19) Bett, K. E.,; Rowlinson, J. S; Saville, G. *Thermodynamics for Chemical Engineers*. Cambridge, MA: MIT Press, **1975**.

(20) Parsegian, V. A. *Ann. Rev. Biophys. and Bioeng*. **1973**, 2, 221-255.

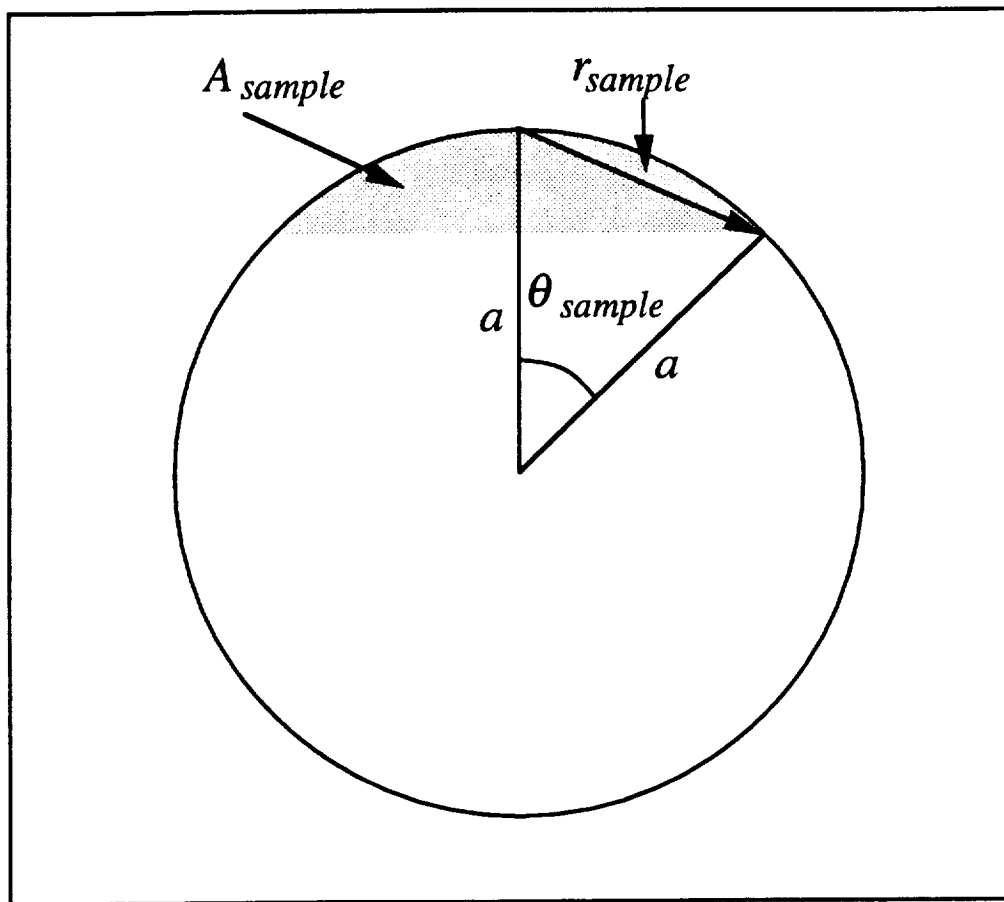(21) Parsegian, V. A.; Brenner, S. A. *Nature*. **1976**, 259, 632-635.

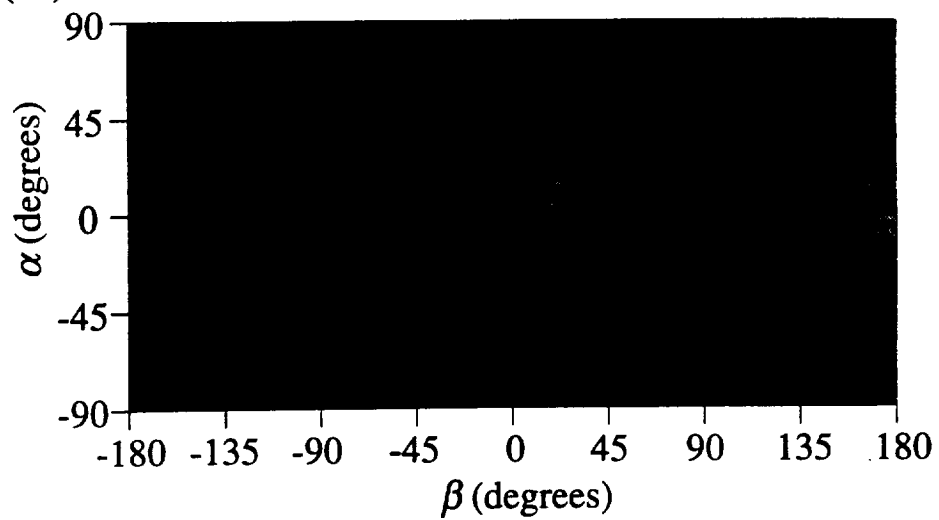(22) Matthews, B. W. *J. Mol. Biol.* **1968**, 33, 491-497.

FIGURE CAPTIONS

Figure 1. A map of the surface charge distribution for an idealized lysozyme sphere. Symbols: ■ +1; ● −1; ▲ +1/2. All charges given in units of the proton charge $(1.6 \times 10^{-19} \text{ C})$

Figure 2. Sampling area and radius. Charged groups lying within the shaded area contribute to the local charge density.

Figure 3. Local (smoothed) charge density on the surface for different averaging areas. The lysozyme sphere has a surface area of approximately 3400 Å^2 and in the figure charge densities are scaled by $\sigma_o \approx 1.4 \times 10^{-2} \mu\text{C/cm}^2$. Scaled charge densities are shown for sampling areas of: (a) 300 Å^2 (b) 200 Å^2 (c) 100 Å^2. The legend at the bottom of the figure shows the charge level.

Figure 4. Constant element approximation for the surface charge density. Various representations of the charge density on the model lysozyme molecule based on a 100 Å^2 averaging area (Figure 3c). Charge densities are scaled by $\sigma_o \approx 1.4 \times 10^{-2} \mu\text{C/cm}^2$. (a) 20 elements. (b) 60 elements. (c) 120 elements. (d) 240 elements.

Figure 5. A comparison of the electrostatic free energy at contact and the surface charge distribution for $a\kappa = 5$. The results at contact are shown for the 240 element discretization. Free energies are scaled by kT; charge density scaled by $\sigma_o \approx 1.4 \times 10^{-2} \mu\text{C/cm}^2$. (a) Φ_{elec} when $\sigma_x^* = 0$. (b) scaled charge density. (c) Φ_{elec} when $\sigma_x^* = 500$.

Figure 6. Comparison of maximum and minimum electrostatic free energies with several averages for lysozyme when $a\kappa = 5$. Symbols: ■ Φ_{elec}^{max}; ● Φ_{elec}^{min}; ▲ $\Phi_{elec}^{uniform}$; □ $\overline{\Phi}_{elec}$; ○ $\langle \Phi_{elec} \rangle$.

Figure 7. Electrostatic free energies near contact Symbols: ▲ $\Phi_{elec}^{uniform}$; □ $\overline{\Phi}_{elec}$; ○ $\langle \Phi_{elec} \rangle$.

Figure 8. The combined interaction potential between a charged sphere and a surface for different surface charge densities; $a\kappa = 5$, $A_{eff} = 0.5\ kT$. Symbols indicate the surface charge density on the plate, σ_x^*: ○ 0; □ 100; ◇ 200; △ 300; ● 400; ■ 500.

Figure 9. The combined interaction potential between a charged sphere and a surface for different Hamaker constants; $a\kappa = 5$, $\sigma_x^* = 500$. The Hamaker constants are: ○ 0; □ 0.5 kT; ◇ 1 kT.

Figure 10. Angle-averaged electrostatic free energy at contact as a function of the surface charge density. The solid curve represents the model lysozyme molecule while the dashed curve is the uniformly charged sphere with the same net charge.

Figure 11. Angle-averaged lysozyme interaction potentials for $a\kappa = 5$. The solid curves correspond to $A_{eff} = 0.5\ kT$ and the dashed curves represent $A_{eff} = 0$. The plot symbols represent the surface charge density on the plate, σ_x^*: O 1600 (72 Å^2 per charge); □ −1000 (116 Å^2 per charge).
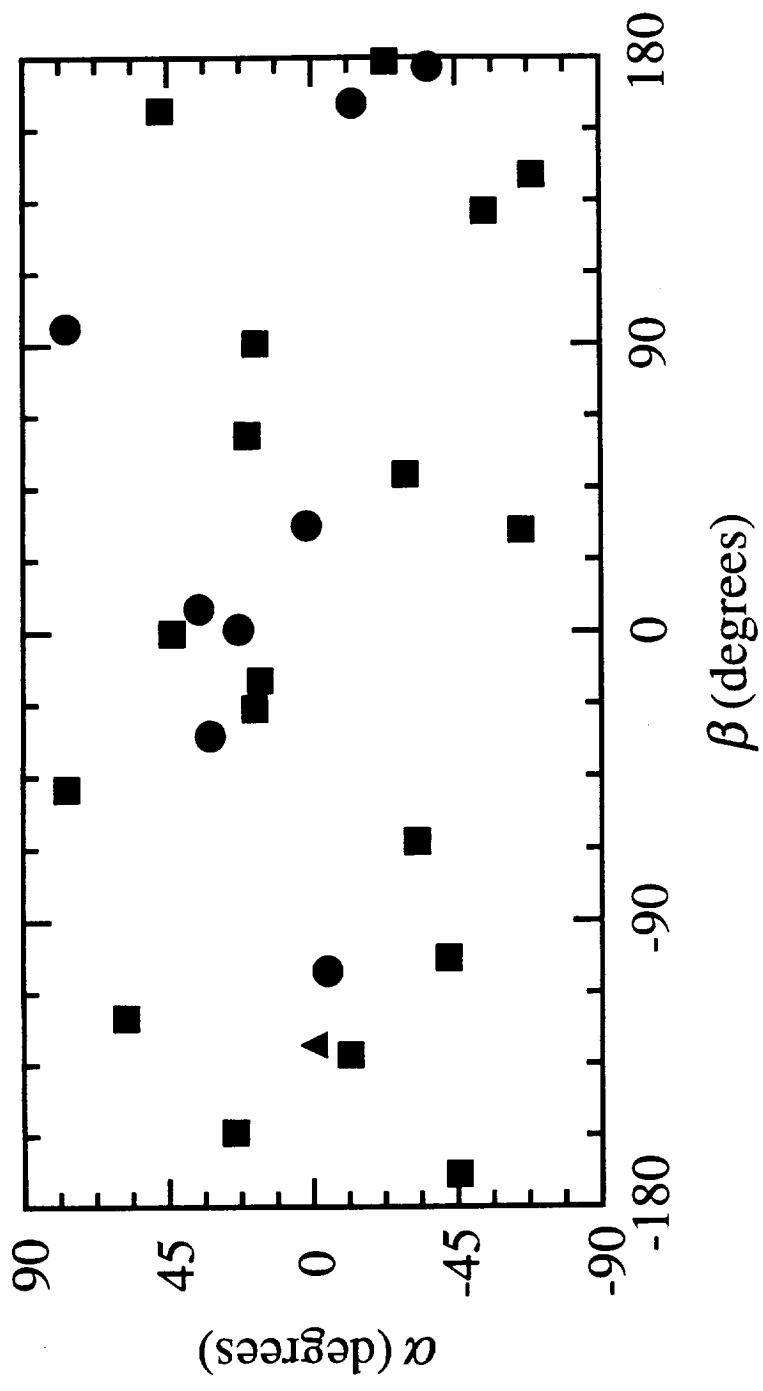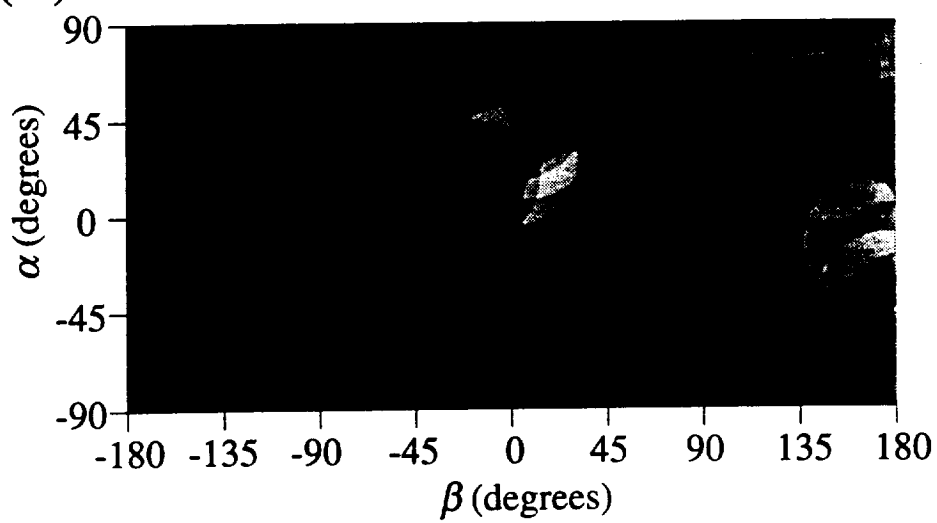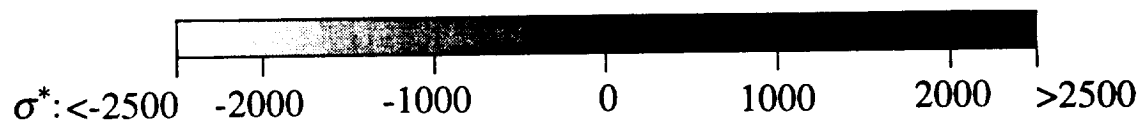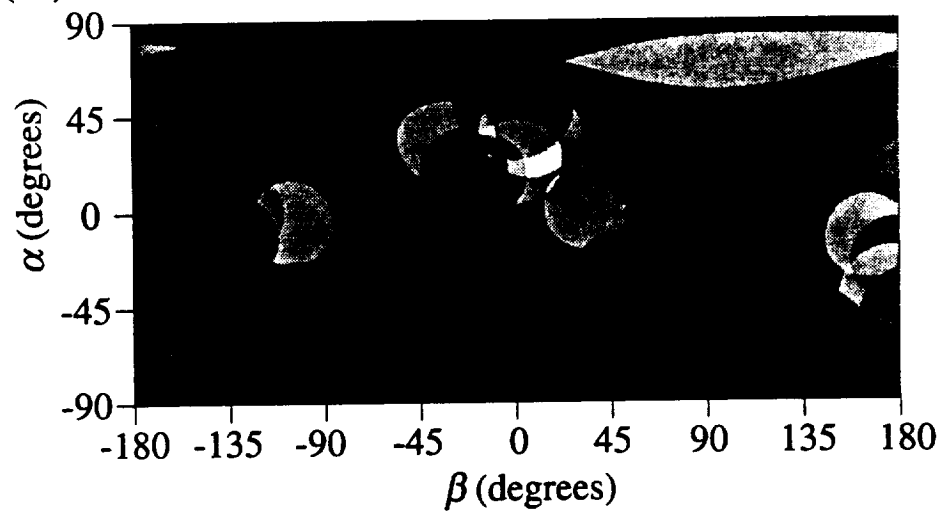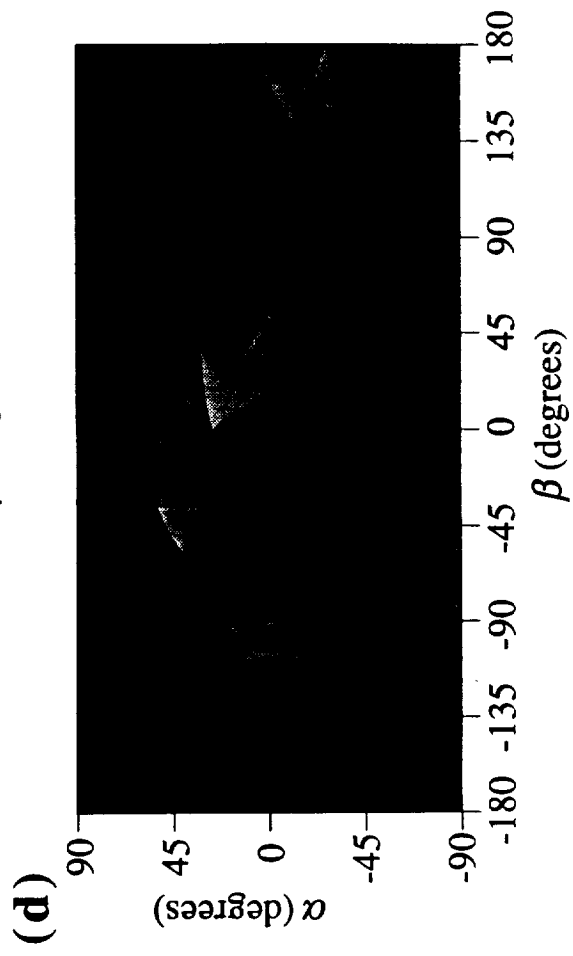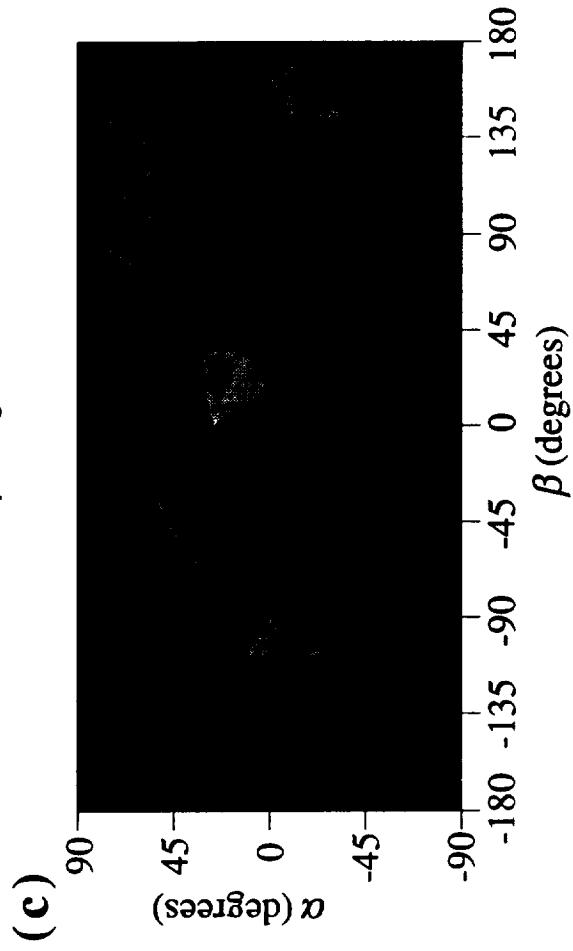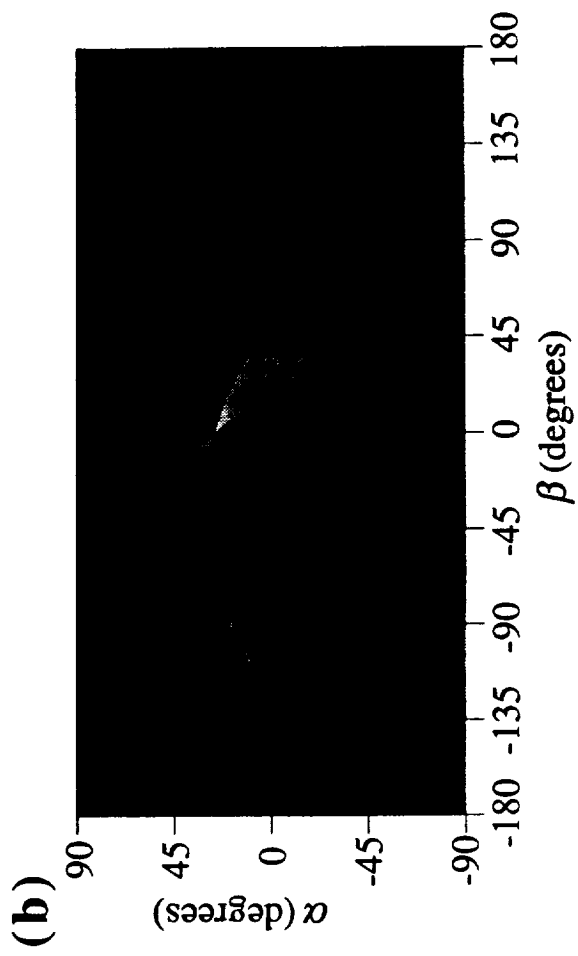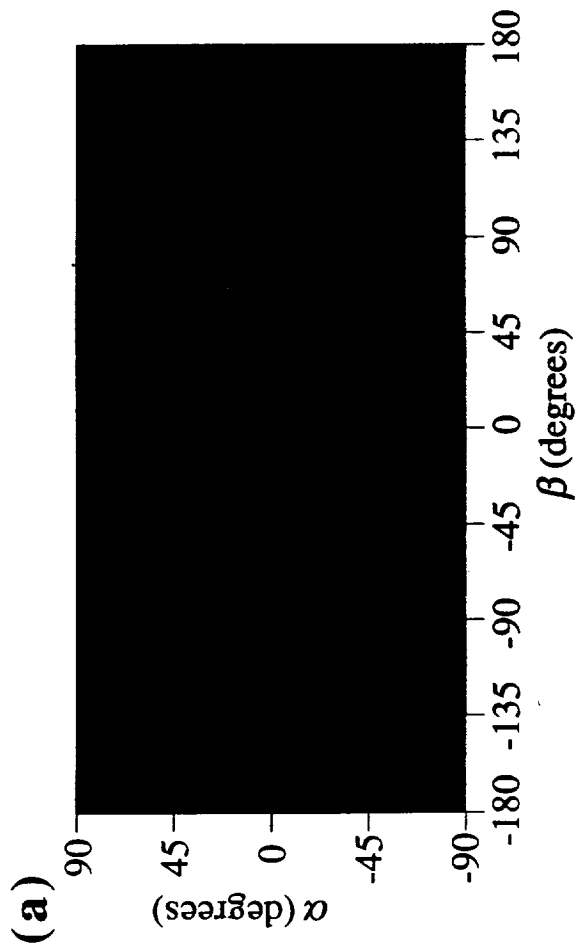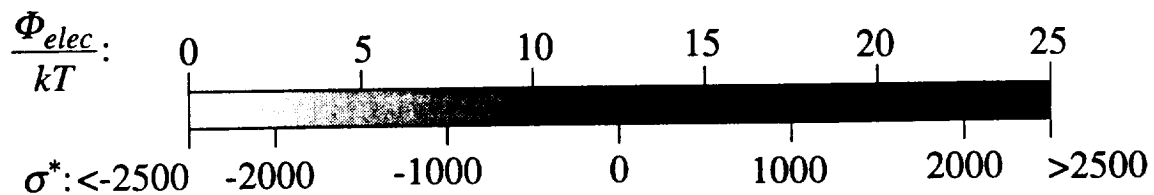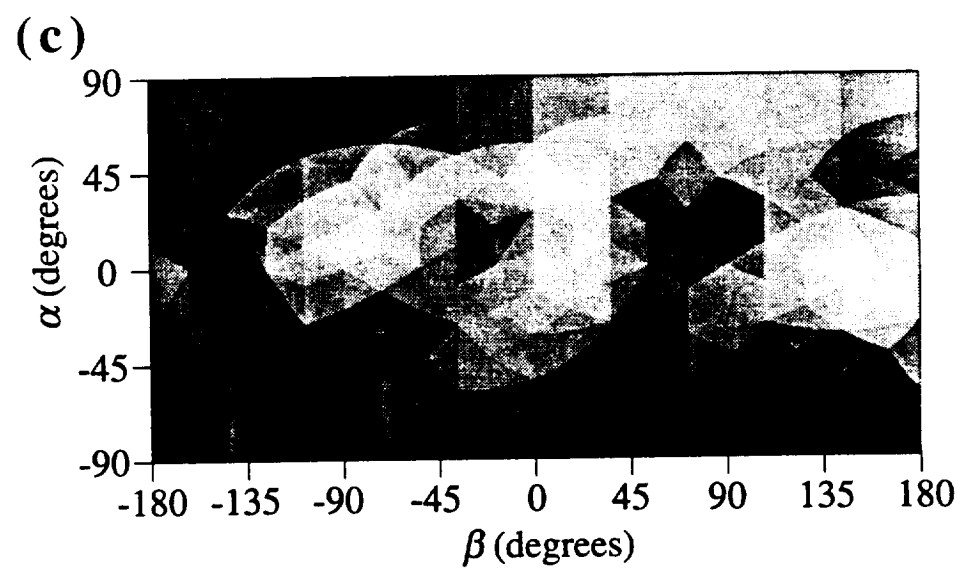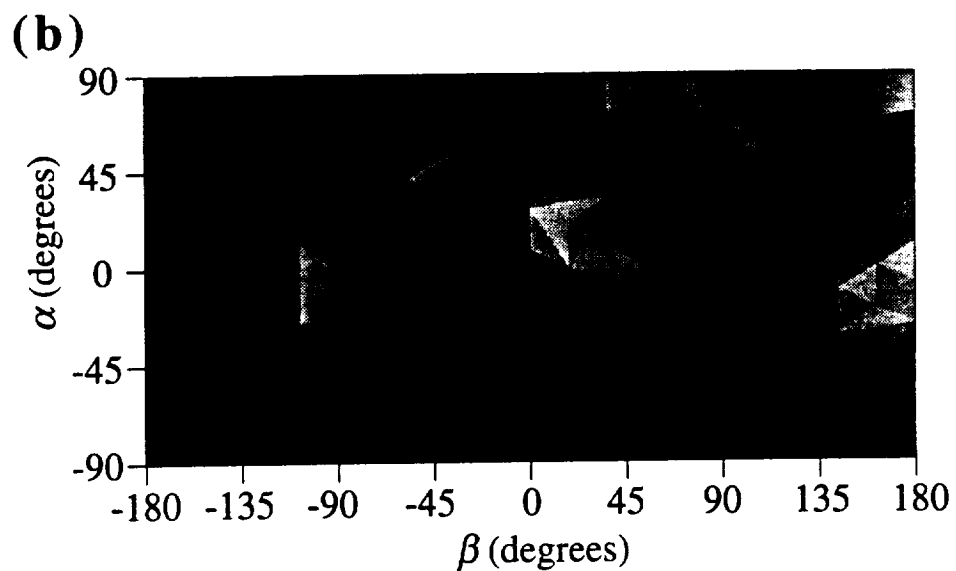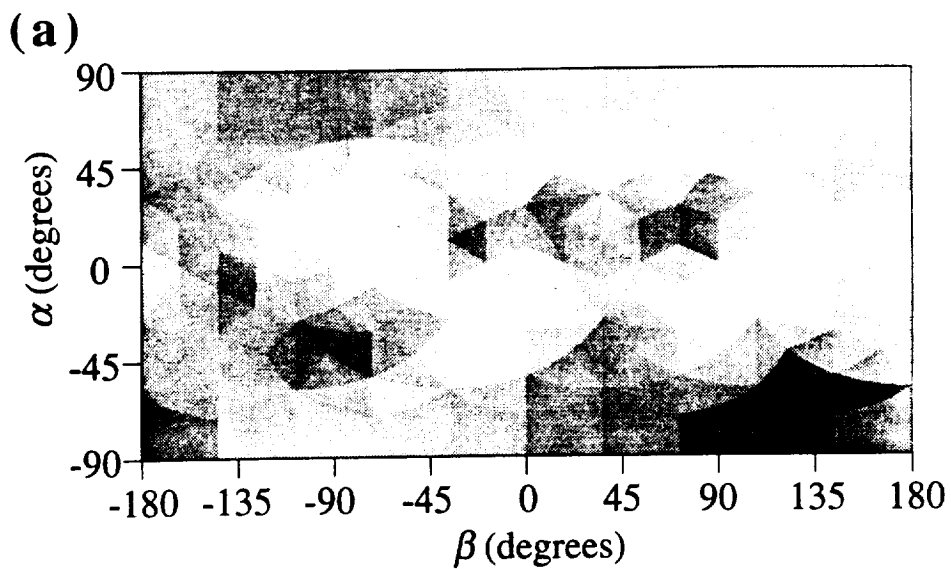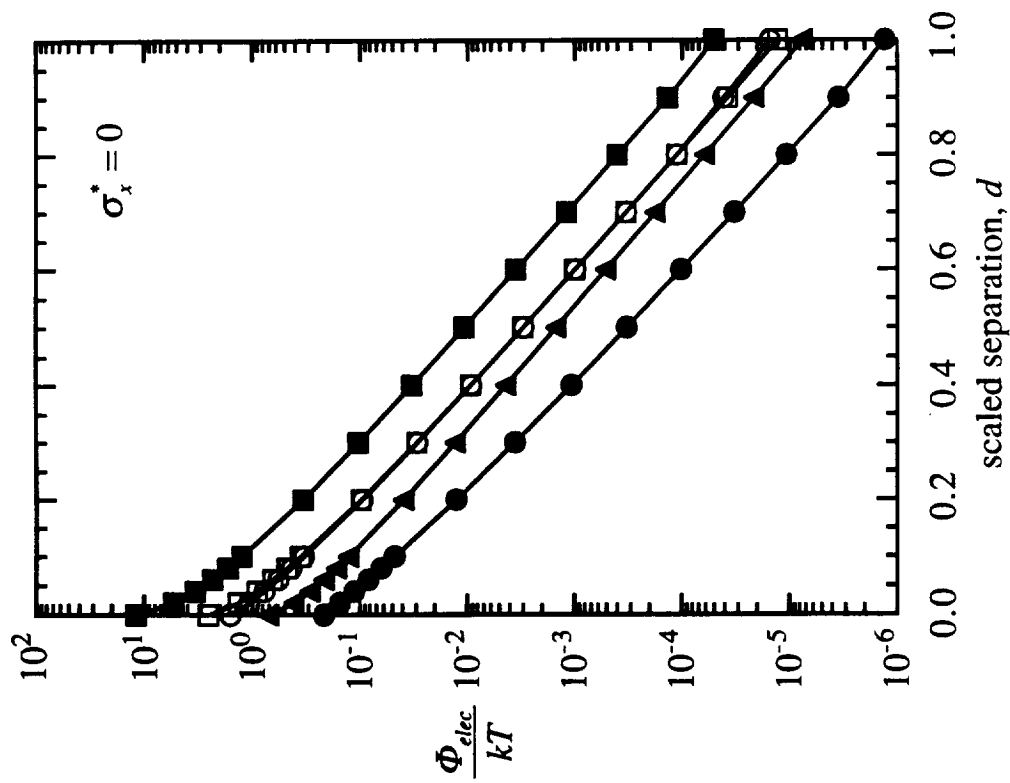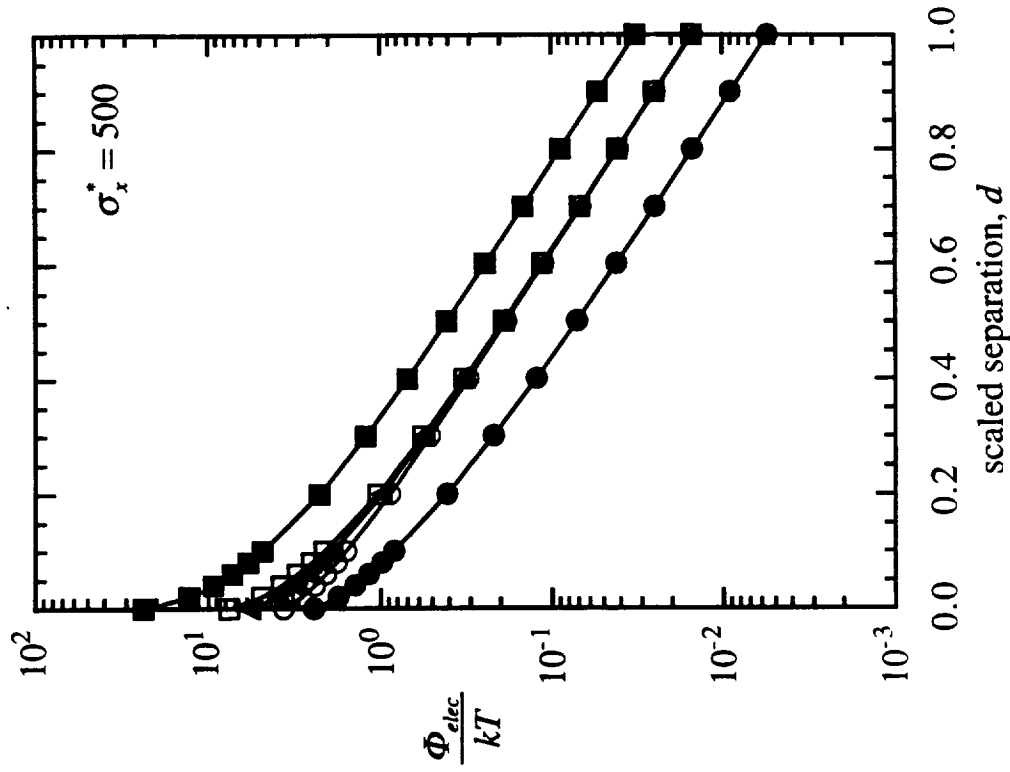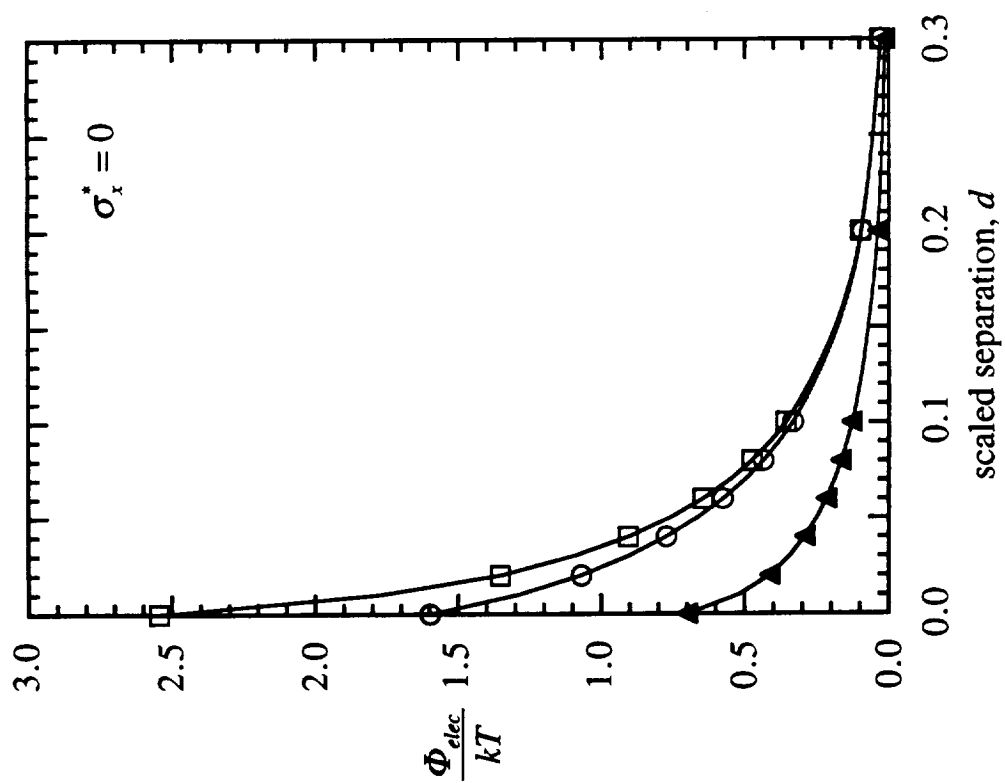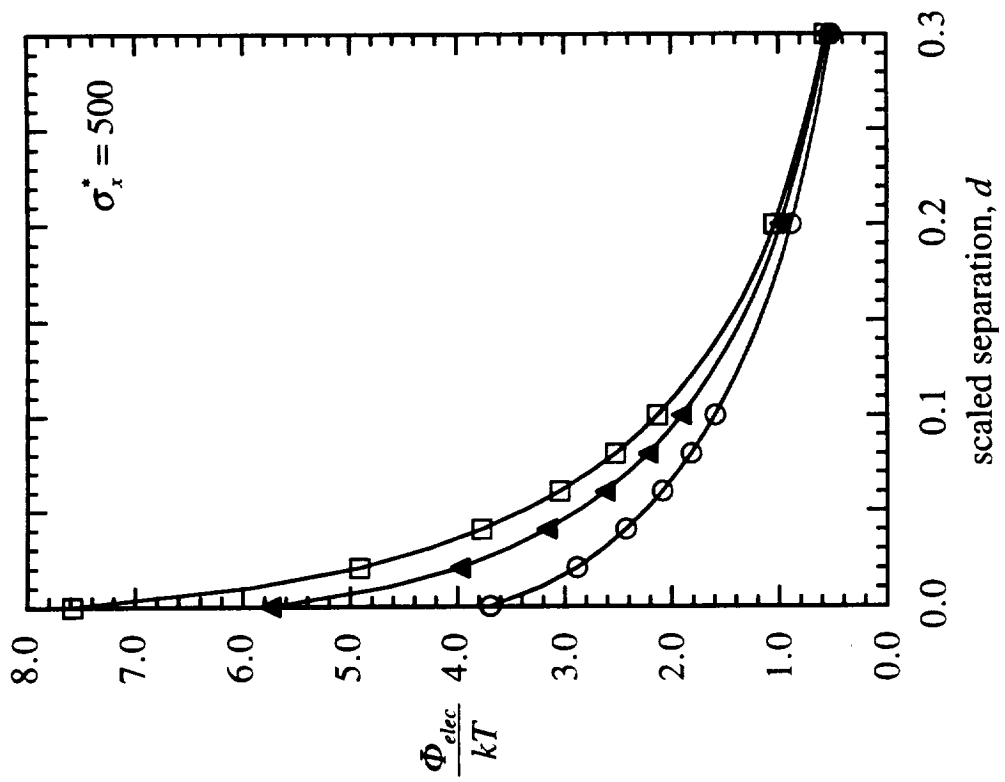
A_{sample} r_{sample}

a θ_{sample}

a

(a)

(b)

(c)

σ^*: <-2500   -2000   -1000   0   1000   2000   >2500

③

(a)

(b)

(c)

(d)

σ^*: <-2500   -2500   -2000   -1000   0   1000   2000   >2500

α (degrees): 90   45   0   -45   -90

β (degrees): -180   -135   -90   -45   0   45   90   135   180

(a)

(b)

(c)

$$\frac{\Phi_{elec}}{kT}:$$

0   5   10   15   20   25

σ^*: <-2500   -2000   -1000   0   1000   2000   >2500

⑤

Figure 6

$\dfrac{\Phi_{elec}}{kT}$

$\sigma_x^* = 0$

$\sigma_x^* = 500$

scaled separation, d

Figure 2

uniformly charged sphere

model lysozyme molecule

⑨

$$\frac{\langle \Phi_{elec} \rangle}{kT}$$

plate charge density, σ_x^*

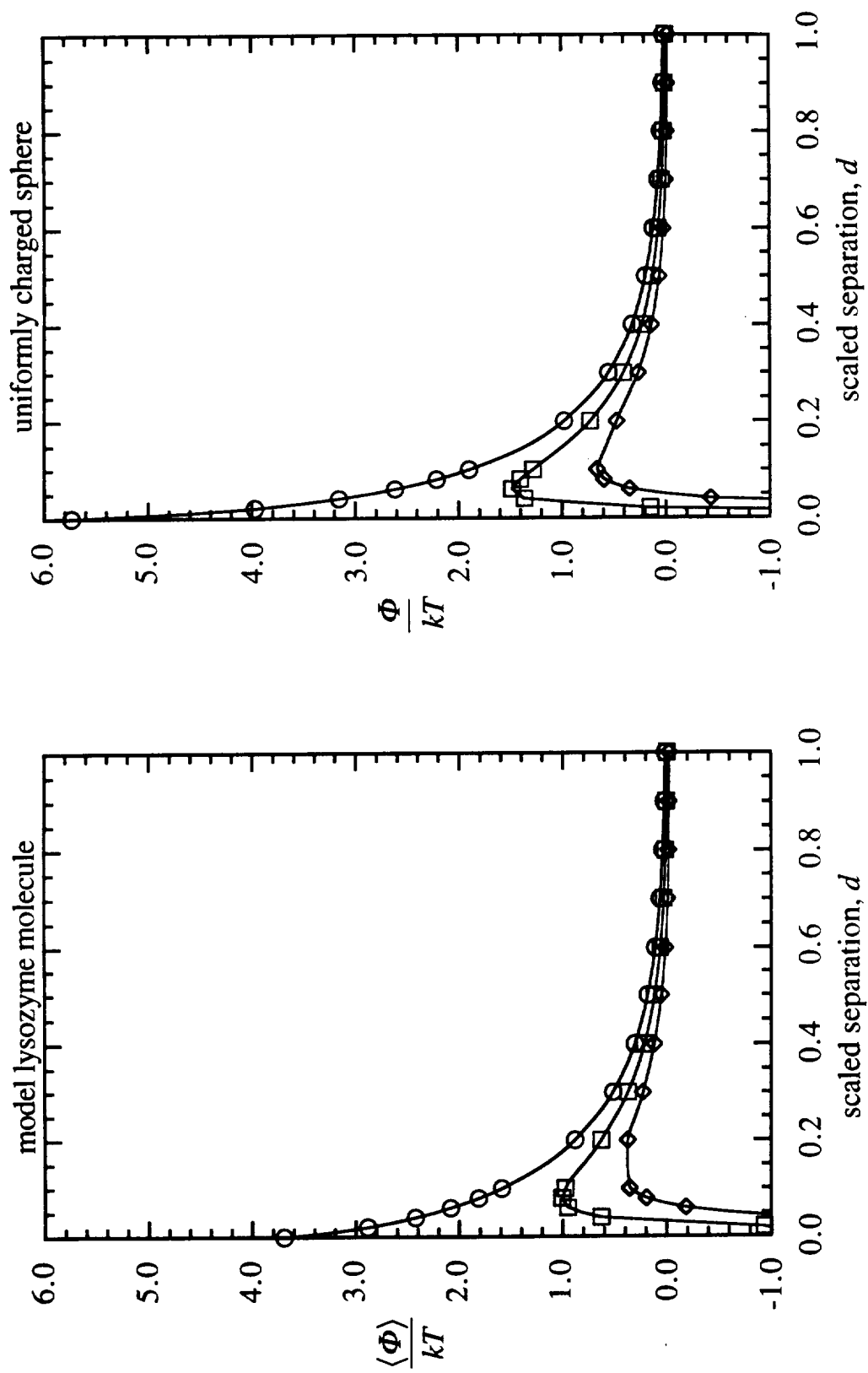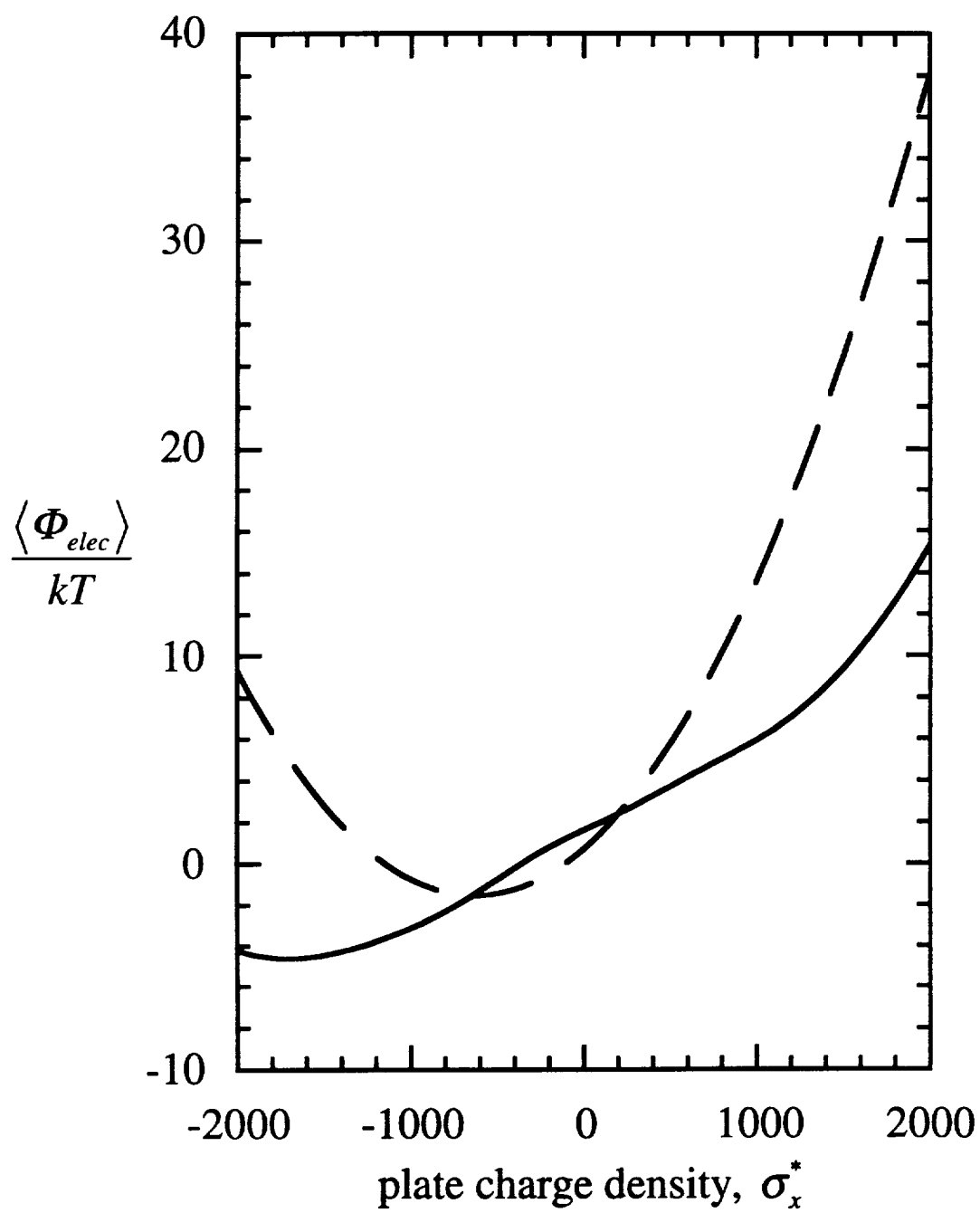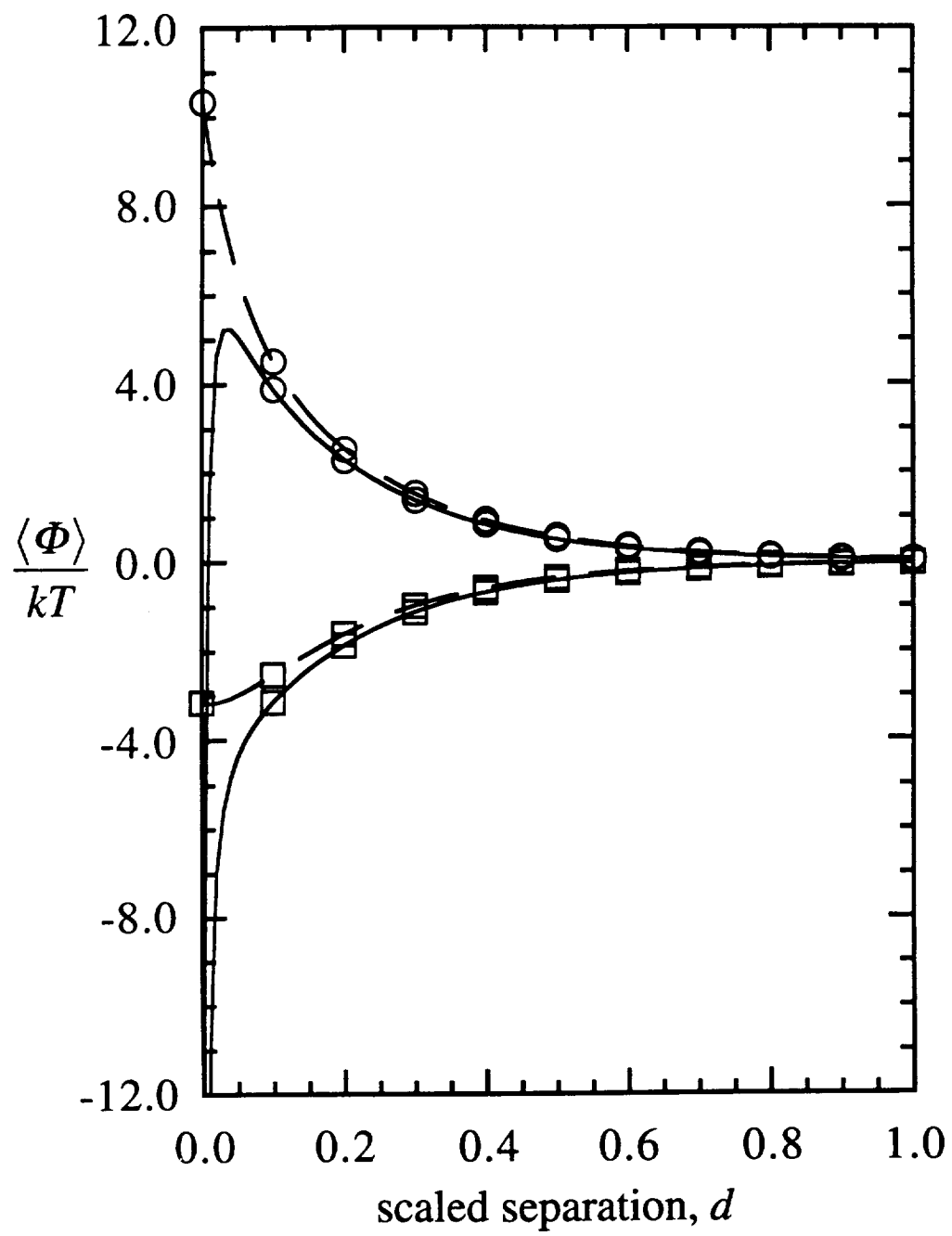Figure showing $\langle\Phi\rangle/kT$ versus scaled separation, d.
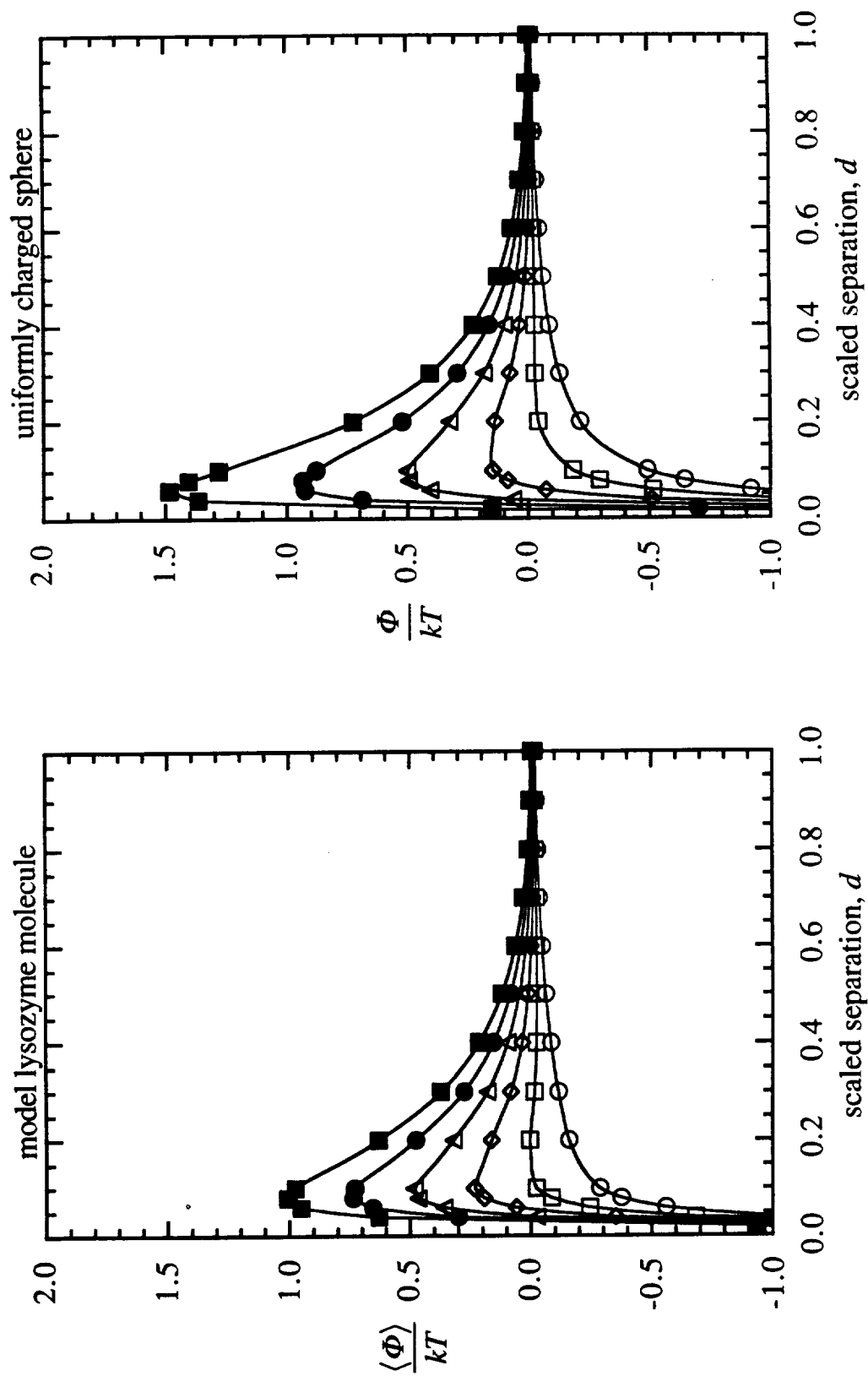
PROTEIN CRYSTAL GROWTH: THE INFLUENCE OF COLLOIDAL

INTERACTIONS AND FLUID MOTION

MARSHALL L. GRANT

A DISSERTATION

PRESENTED TO THE FACULTY

OF PRINCETON UNIVERSITY

IN CANDIDACY FOR THE DEGREE

OF DOCTOR OF PHILOSOPHY

RECOMMENDED FOR ACCEPTANCE

BY THE DEPARTMENT OF

CHEMICAL ENGINEERING

JANUARY 1992

ABSTRACT

The three dimensional structure of biological macromolecules is determined from X-ray diffraction studies of large, well ordered crystals. Many proteins, however, form crystals too small or too disordered to diffract well. Two findings suggest buoyancy-driven natural convection may affect protein crystal growth: (i) crystals grown in microgravity are reported to diffract better than crystals grown in the laboratory and (ii) crystals subjected to weak forced convection slow their growth. Reasons for this behavior are unknown.

In this work, digital microscopy was used to measure growth rates of tetragonal crystals of hen egg white lysozyme; the size range covered was 50 - 325 μm. The growth rate distribution of crystals grown under nominally quiescent consitions was compared statistically with that of crystals exposed to forced convection of approximately 50 μm/s. In both cases, the sample standard deviation and sample mean were proportional; relative standard deviations of both groups were approximately equal. The shape of the distributions did not change with time during the experiment (3 - 10 days), implying that flow effects, if any, act on all crystals irrespective of growth rate or size. Natural convection is present even under nominally quiescent conditions, but growth rates for quiescent crystals remained constant over the size range 156 - 322 μm. At the 99% confidence level, no evidence was found to suggest natural convection retards crystal growth. These results agree with previously published quasi-steady mass balances on growing protein crystals.

Colloidal interactions of a uniformly charged crystal with a spherical molecule having a patchy surface charge distribution were computed. Calculations of the angle-averaged interaction potential show the balance between electrostatic repulsion and dispersive attraction is sensitive to the effective surface charge on the crystal and the effective Hamaker constant; neither quantity is known with certainty. Nevertheless, it

appears that colloidal forces reduce the protein flux to the crystal only slightly, suggesting that the rate-limiting step in protein crystal growth occurs once the molecule has reached the surface. These results, coupled with the experimental findings, indicate mass transport from bulk solution does not limit protein crystal growth.

ACKNOWLEDGEMENTS

Kelly, Charlton Shen, Larry Rosen and Brenda Belkin to know they are appreciated. It was always a pleasure to visit with Sean and Susan Montgomery. I would particularly like to thank Frank and Jenny Torres for all the evenings we spent animatedly discussing everything in the world (or so it seemed). Special thanks to James Baygents, who helped me over some of the rough spots.

University housing policy and my own reluctance to find a new apartment combined to leave me homeless for the month of August, 1989; Lynda Sharkey and her family opened their home to me. I will always be grateful to them. George Allen, my friend and confidant, helped me put graduate school in perspective. Thank you.

For three years, I was an active member of the East Windsor Township Rescue Squad, District 1. I admire all the volunteer members of the squad and thank them for the opportunity to help. I still appreciate the hospitality of Kay Oestreich and her husband Curt (the men's auxiliary), who let me stay with them when I was on call.

TABLE OF CONTENTS

LIST OF FIGURES

LIST OF TABLES

CHAPTER 1

The Art and Science of Protein Crystal Growth

1.1 Introduction

A fundamental axiom of biochemistry declares that the structure of biological macromolecules reflects their function. If the role of the molecule can be determined through some sort of assay and the relevant structures identified, a synthetic molecule can be designed to mimic the original molecule. This is the basis of "rational drug design" [1]. X-ray diffraction studies of protein crystals (or crystals of other biological macromolecules such as DNA) provide the knowledge of the macromolecular structure required for such endeavors.

Crystallographic techniques are now sufficiently developed so that the rate-limiting step in protein structure determination is the growth of suitable crystals [2-5]. Protein crystals are grown from aqueous solutions containing protein, buffer, and precipitating agent (often salt or an organic solvent). Given a newly isolated protein, it is often a painstaking process of trial and error to find conditions which produce any crystals, let alone crystals large enough and sufficiently well ordered to diffract X-rays to high resolution [2,6-8]. Crystallographers may have only small amounts of material with which to work and do not have time to perform the exhaustive experiments needed to establish the phase diagram for each protein. Any finding or technique that reduces the time needed to obtain protein structures would be welcomed by crystallographers.

Many of the difficulties of growing good protein crystals have been attributed to buoyancy-driven natural convection, although the mechanism by which fluid flow inhibits crystal growth remains a matter of conjecture. In particular, convection is suspected of mechanically disrupting the bonds holding the molecules to the crystal surface [5], disturbing the homogeneous deposition of protein on the crystal [9], or perturbing the molecular packing in the crystal [10]. Others, on the basis of a simple model of colloidal

1

interactions between molecule and crystal, have suggested that the small terminal size of protein crystals results from a poor choice of crystal growth conditions [11]. Our intent is to examine the roles of transport phenomena, colloidal forces, and attachment kinetics in protein crystal growth. Studies of these subjects are incorporated into a single framework by interpreting the results in terms of the relative rates of transport and attachment.

Experimental studies were used to investigate possible flow effects on protein crystal growth. Quasi-steady mass balances on growing lysozyme crystals in the presence of natural convection [5,12,13], for instance, predict crystal growth is entirely kinetically controlled. Any systematic deviation from this behavior would imply some important process has been omitted. The predictions of quasi-steady model had not been tested until now because all studies of flow effects and growth kinetics were performed on small crystals which should be significantly affected by fluid flow. The long-term crystal growth studies described in Chapters 2 and 3 are the first in which crystals larger than 100 μm were measured. Although these experiments do not settle the issue of flow effects, they suggest alternative hypotheses which had not been considered.

Of primary importance is the result that lysozyme crystals 150 - 300 μm in size do not slow their growth in the presence of natural convection. Over this size range, at least, the rates of attachment and transport appear unaffected by the presence of buoyancy-driven flow. Three additional findings of the experiments are: (i) there may be a long initial downward transient in crystal growth rate before the system reaches steady-state, (ii) distributions of growth rate and size are extremely broad, and (iii) size and growth rate distributions are similar irrespective of the presence of forced convection.

The colloidal interaction between crystal and molecule consists of electrostatic and dispersive contributions. If there is a net repulsion between the crystal and molecules in solution, the rate of transport to the surface is diminished [14]. In this context, addition of the molecule to the crystal consists of three steps in series: (i) transport from bulk solution

2

to the vicinity of the surface, (ii) climbing a free energy barrier to reach the surface, and (iii) suitable surface kinetics to fit into the crystal lattice. Note that in the previous analysis, steps (ii) and (iii) were lumped together into the growth kinetics. In Chapter 4, the colloidal interaction potential was calculated for a simplified model of lysozyme crystal systems including some effects of the molecule's nonuniform charge distribution. In agreement with the current experimental findings, as well as the predictions of quasi-steady mass balances, transport from bulk solution does not seem to control protein crystal growth.

In this opening chapter, general background on the nature of protein crystals and their growth is presented. A critical review of previous crystal growth studies is given, as well as a discussion of hypotheses about the unusual behavior of protein systems. In particular, the possible effect of convection on protein crystal growth is examined in detail. The evidence is often contradictory, and it is difficult to interpret all the claims and findings. The behavior of protein crystal systems is then discussed in terms of interactions between molecules in solution and macroscopic bodies. Next, in Chapter 2, is a description of the crystal growth experiment intended to test for convective effects. A technique developed for estimating the size and orientation of three-dimensional objects based on two-dimensional projections (digitized images) is also presented. Chapter 3 is a thorough statistical analysis of the crystal growth measurements from the experiment described in Chapter 2. Emphasis is placed on the sources of variance within each experiment that produce a wide range of behavior from what are nominally uniform populations.

Chapter 4 begins with a description of the interaction potential between protein molecules and protein crystals. The electrostatic contribution to the interaction potential is calculated from a combined numerical and analytical solution for the electrostatic potential produced by a nonuniformly charged protein molecule and a crystal with a constant uniform surface charge. The numerical solution was obtained by a boundary element

3

method, the details of which are described. Finally, the total interaction potential is calculated by adding the dispersive potential with the angle-averaged electrostatic potential and the effect of nonuniform charge effects are discussed. Recommendations for future work, both experimental and computational, are presented in Chapter 5.

1.2 The Nature of Protein Crystals

Compared with ideal inorganic or "small molecule" crystals, protein crystals have an open structure with channels of solvent [4]. Solvent content ranges from 27% to 65% of the crystal volume, with values of 40% - 50% being most common [15]. Protein molecules are thought to be held in place in the crystal lattice by hydrogen bonds [2], which are relatively weak ($\Delta H \approx -3$ to -6 kcal/mol *in vacuo* [16] compared with O(100 kcal/mol) for covalent bonds [17]). The loose structure of the crystal and weak bonding allow the molecule to crystallize without a radical change in conformation [2,16], which is why X-ray diffraction can be used to study the relationship between structure and function. Evidence that the molecule's structure is not greatly altered upon crystallization comes largely from assays that show enzymes retain their activity in the crystal state [16].

The weak bonding in the protein crystal and the complexity of the molecules combine to give proteins an almost legendary reputation for sensitivity and fragility. In a list of 21 variables influencing macromolecule crystallization given by McPherson [6], two items stand out in particular: vibration and sound (#13) and gravity, gradients and convection (#21). Some of the difficulty of protein crystal growth can be attributed to the stochastic nature of nucleation and growth. Small perturbations of a highly metastable state can disturb nucleation and produce a rapid amorphous precipitation of the protein. The nonspecific nature of the crystal bonds, which produces several local solubility minima, is at least partly responsible for the reported polymorphism of macromolecular crystals; McPherson [6] shows a photograph in which two different crystal forms of yeast phenylalanine tRNA grow from the same solution.

4

The resolution at which a molecule's structure can be determined depends on how well the crystal diffracts. A typical X-ray study requires crystals which are sufficiently large ($\sim$ 1 mm^3 in volume) and reasonably well ordered. Few proteins readily form crystals which are suitable for X-ray analysis, although many precipitate as fine crystals or amorphous solids. Occasionally, large crystals form but the crystal packing is too disordered to diffract well [2]. Some studies [18,19] suggested that proteins may have a limiting size beyond which they cannot grow. This "cessation of growth" phenomenon has become firmly entrenched in the protein crystal growth literature. More recent studies have been performed in which careful control of conditions produced crystals significantly larger than the previously reported terminal size [11,20].

At least in the past, there was a tendency on the part of protein crystal growers to attribute all the quirkiness of the protein systems on the extreme sensitivity of the molecule. It was common, in fact, for protein crystallographers to deny theories of crystal growth developed by small molecule crystal growers could be applied at all to biological macromolecules [4]. Now, however, most protein crystallographers realize that a better understanding of the underlying processes of crystal growth can reduce the time and effort needed to grow crystals and solve the molecular structure. The structure, after all, is the goal of the crystallographers.

1.3 Physico-chemical Description of Protein Crystal Systems

A survey of the protein crystal growth literature shows how difficult it can be to characterize protein solutions. (Since most protein crystal growth studies have been performed on hen egg white lysozyme, the discussions of protein behavior in this text are based on lysozyme. Characteristics of other globular proteins are expected to be qualitatively similar.) Physical properties such as size, density and diffusion coefficient appear to be relatively consistent among different researchers [21-23] but thermodynamic properties such as solubilities display much more variation. Consider the solubility of

5

lysozyme at 20°C, pH 4 and a NaCl concentration of 50 mg/ml: Fiddis et al. [24] report a value of 3.5 mg/ml while Howard et al. [10] report 6 mg/ml. Pusey et al. [5] report a solubility of only 1.7 mg/ml at 22°C and Feher and Kam [19] measured a value of 5.0 mg/ml at 20°C and pH 4.2. The proliferation of conditions for growth studies is another complication which must be considered when comparing the results of different workers.

There is also some uncertainty in the state of aggregation of the protein molecules in solution. Sophianopoulos and Van Holde [25] found evidence that dimers are the dominant form of lysozyme in the pH range 5 - 9; Bruzzesi et al. [26] employed light scattering and sedimentation experiments to observe a reversible association of lysozyme at pH > 4.5. At pH 6.8 and protein concentrations greater than about 20 mg/ml, oligomers larger than dimers seem prevalent; at pH 4.3, however, lysozyme appears to be mostly monomeric even up to protein concentrations of 50 mg/ml [26].

Dynamic light scattering has also been used to study aggregation in protein systems. Kam and coworkers [18,19] looked at the power spectrum of light scattered from lysozyme solutions in an attempt to assay possible crystallization conditions quickly. By using the linewidth of the power spectrum to fit the parameters in their aggregation model, they could discriminate between conditions known to produce crystals and those known to form amorphous precipitate. Although their technique is adequate for measuring large qualitative differences between conditions, it cannot be used to determine the state of aggregation in the system. Sample calculations [27] show that the linewidth is sensitive to the size of the "average" scatterer, but is unable to resolve the exact form of the size distribution. For now, the degree of association in lysozyme solutions remains an interesting but unresolved issue.

The formation and shape of oligomers may affect the crystal growth process. If, for example, crystal growth occurs by addition of monomer, a high degree of association effectively depletes the population of growth units in solution. Not only might the rate of transport to the surface be altered, but crystal growth could be controlled by the rate of

6

oligomer dissociation. On the other hand, if crystal growth occurs by addition of associated protein molecules, the shape and complexity of the growth unit might determine the intrinsic attachment rate. Salemme et al. [28] analyzed intermolecular contacts in the monoclinic, triclinic, and tetragonal forms of hen egg white lysozyme and found a common molecular "chain" in all of them despite the difference in crystal packing. They hypothesized that such chain formation is related to crystal nucleation and growth. As in many of the other questions about protein crystal growth, available data are simply inadequate to identify the growth unit.

By now, the reader will appreciate some of the complexity of protein systems and the confusion surrounding the interpretation of crystallization behavior. Until recently, the emphasis was on structure determination from a small population of crystals; even though the underlying phenomena were not well understood, crystallographers were able to refine conditions repeatedly until they grew enough crystals to solve the structure. Since the mid-1980s, protein crystallographers have become more interested in systematizing protein crystal growth and have have begun an interdisciplinary effort to characterize protein crystal systems [4]. The prognosis for the future is encouraging, but the interpretation of current results remains clouded.

1.4 Previous Protein Crystal Growth Studies

The driving force for crystallization of species i from solution can be written in terms of the difference in the chemical potential of species i in solution, $\mu_i = \mu_i^o + kT \ln (\gamma_i x_i)$, and in the crystal, $\mu_i^{xtal} = \mu_i^o + kT \ln \left(\gamma_i^{sol} x_i^{sol} \right)$. Here, μ_i^o = standard state chemical potential of species i, k = Boltzmann's constant, T = absolute temperature, γ_i = activity coefficient and x_i = mole fraction of species i; the superscript "sol" denotes solubility values. The chemical potential of solute in solution exceeds that in the crystal by an amount

$$\Delta \mu_i = \mu_i - \mu_i^{xtal} = kT \ln \left(\gamma_i x_i / \gamma_i^{sol} x_i^{sol} \right) \tag{1.1},$$

7

which is normally taken to be the driving force for crystallization [29]. Equation (1.1) is strictly valid when the crystal is large enough that surface effects are negligible compared with bulk effects. When x_i is small, the term in parentheses is written approximately as $\gamma_i C_i / \gamma_i^{sol} C_i^{sol}$. Researchers studying small molecule crystal growth usually invoke the ideal solution approximation ($\gamma_i = 1$) because solute concentrations are low and the necessary thermodynamic data are unavailable [29,30]. If the conditions are further restricted to small relative supersaturations, the logarithm in (1.1) can be expanded in terms of the relative supersaturation to give $\left(C_i - C_i^{sol}\right) / C_i^{sol}$ to first order.

In contrast with inorganic (small molecule) crystal growth, theoretical studies of crystal growth mechanisms are scarce, so a hybrid approach is often taken. Crystal growth rates are measured and fitted to models borrowed from inorganic crystal growth. Researchers often draw conclusions about growth mechanisms based on agreement with the functional form of the growth rate dependence, without regard to the possibility that grossly different mechanisms can sometimes predict the same behavior [4]. In other cases, growth rate expressions are fit in a wholly empirical fashion with no attempt to explain the underlying process. A popular method is to fit growth rates to a power-law in the relative supersaturation, even though this is not entirely consistent with the logarithmic driving force described by (1.1). The review of protein crystal growth studies given below, although brief, covers most of the extant work.

Pioneering work on protein crystal growth was done by Schlichtkrull in the 1950s. Working with insulin crystals up to 100 μm in size, he determined that the face growth rate (the rate at which a crystal face advances along its normal, sometimes called the linear growth rate because it is related to the change in the linear dimension of the crystal) was proportional to $(C - C_{final})^2$, where the reported C_{final} could be as much as six times the solubility [31]. In a subsequent study in which seed crystals were grown from solution containing India ink and later transferred to a clear solution, Schlichtkrull found that only three of the six crystal faces were advancing [32]. Seed crystals were seen clearly in the

8

corners of the final crystals. The anisotropic growth of insulin crystals was ascribed to a corresponding anisotropy in the unit cell which somehow prevented deposition of protein molecules from solution. Population balances on the crystals indicated crystal nucleation was highly heterogeneous and increased with crystal surface area as well as the liquid-vapor interfacial area of the solution [31].

Pusey and coworkers [5,12] performed a similar empirical study on the post-nucleation growth of the {110} faces of tetragonal hen egg white lysozyme crystals from solution. They found a dependence on the square of the relative supersaturation. The fourfold symmetry of the tetragonal crystal form makes all four {110} faces equivalent, so that anisotropic growth was neither expected nor detected. Pusey *et al.* were primarily concerned with the relative importance of material transport and attachment kinetics in controlling protein crystal growth (see section 1.5 for a detailed discussion). No size-dependent growth was observed for the size range (up to 70 μm) used in the study. Calculations based on their results indicate that even in the absence of convective transport, lysozyme crystal growth is kinetically controlled until the crystals are at least 100 μm in size.

Fiddis *et al.* [24] measured the growth of tetragonal lysozyme crystals up to about 50 μm in size and compared their measurements with predictions from several models of inorganic crystal growth. As might be expected from the discussion above, the thermodynamic driving force in Equation (1.1) was simplified with the ideal solution assumption. Growth rates were compared with those expected from models in which growth was controlled by the rates of: diffusive transport, convective transport, addition to a uniformly rough surface, addition to a screw dislocation, and nucleation of new surface layers. In agreement with Pusey and coworkers [5,12], the kinetics were found to be rate-limiting over the size range studied. The data agreed best with the model based on surface nucleation kinetics. Fiddis compared Schlichtkrull's results for insulin [31] with the surface nucleation model and found reasonable agreement; the cessation of growth at

concentrations above the solubility was reported to be consistent with a surface nucleation mechanism.

Durbin and Feher [33] applied the same crystal growth models to their measurements as did Fiddis *et al*. In contrast, however, Durbin and Feher claimed none of the models describe the data. The models were rejected on the basis of condition-dependent variations in parameters which, according to the models, were supposed to be constants. An empirical power-law fit of the growth rate dependence on relative supersaturation gave exponents in the range 2.0 - 3.9. At protein concentrations greater than 20 mg/ml, secondary nucleation forced them to measure crystal growth from unstirred solutions. Under these circumstances, they obtained constant crystal growth rates for crystals smaller than 50 μm which diminished with increasing crystal size; they attributed this behavior to protein depletion of the solution. At moderate protein concentrations, crystals grew at the same rate whether in quiescent conditions or in the presence of forced convection of about 150 μm/s. Durbin and Feher noticed that equivalent crystal faces grew at unequal rates at low supersaturations but not at high supersaturations; they decided that the unequal growth was driven by some type of defect and that some other mechanism was dominant at higher supersaturations. In addition, they noted that crystals exposed to low supersaturations for several days exhibited a "patchiness" in their growth: protein molecules seemed to attach to isolated locations on the surface and were unequally etched when placed in unsaturated protein solutions.

A more detailed study of crystal surfaces was performed later by Durbin and Feher [34] using freeze-etch electron microscopy. They were able to identify surface features which resemble the step trains, growth spirals, and growth islands described in theoretical studies of crystal growth. At relative supersaturations larger than about 3 (protein concentration of approximately 10 mg/ml based on a reported solubility of 3.5 mg/ml at 24°C, pH 4.6, 50 mg/ml NaCl), growth islands were distributed more or less uniformly over the crystal surfaces; at lower supersaturations, the formation of new layers seemed

10

confined to selected regions on the surface. Durbin and Feher interpreted this behavior at low supersaturations in terms of a competition between deposition of lysozyme and some unknown contaminant that poisons the surface for further growth. Their observations are consistent with their earlier work [33] and may be related to the "cessation of growth" phenomenon [18,19] which has become part of the protein crystal growth lore.

The profusion of crystal growth models and interpretations follows from the uncertainties in the physico-chemical properties discussed in the previous section. Although the conflicting results of extant crystal growth studies make it difficult to form a clear picture of the phenomena, characterization of the surface by freeze-etch electron microscopy [34] may help identify crystal growth mechanisms. Until now, protein crystallographers felt that the complexity of protein systems defied quantitative description based on models of inorganic crystal growth [4]. By showing the qualitative similarity between the surfaces of protein crystals and inorganic crystals, the work of Durbin and Feher suggests that better crystals require a deeper understanding of the state of the protein system.

1.5 Effects of Convection on Protein Crystal Growth

Flow effects might have remained of only incidental interest to protein crystal growers if not for some preliminary experiments performed aboard Spacelab 1 [35]. Littke and John [35] reported the growth of lysozyme crystals in orbit with linear dimensions approximately ten times those grown in the laboratory with the same equipment. Related work performed by Bugg and coworkers [3,36] also suggested some sort of flow effect. The major shortcoming of these first experiments is the small sample populations from which the researchers draw their conclusions. More extensive experiments have been conducted with mixed results. Erdmann *et al.* [37] launched a series of 101 experiments aboard a Chinese Long March CZ-2C rocket and compared the diffraction resolution of space-grown crystals with controls grown in the laboratory. They found that although

some proteins grew larger and diffracted better than the controls, overall quality was below that of crystals grown under optimal conditions in the laboratory. De Lucas et al. [10], on the other hand, found that at least three proteins (γ-interferon D^1, porcine elastase and isocitrate lyase) grown aboard the U. S. space shuttle were larger and diffracted better than any crystals grown in the laboratory.

Three general mechanisms have been proposed by which fluid flow could interfere with the growth of large, well ordered crystals: (i) convective transport of protein to the crystal surface could overwhelm the attachment kinetics and produce poor quality crystals, (ii) forces produced by the flowing fluid could mechanically disrupt the orderly deposition of protein molecules on the surface, and (iii) convection has some other effect which inhibits crystal growth. Each of these mechanisms has been offered to account for the small, poorly diffracting crystals with which protein crystallographers must often contend. We examine each of them in turn.

The crystal growth studies of Pusey, Snyder, and Naumann [5] and Pusey and Naumann [12] were discussed briefly in the previous section. Their main purpose was to estimate the relative importance of importance of solute transport and interfacial kinetics in controlling protein crystal growth. Pusey *et al.* performed a quasi-steady mass balance on the growing tetragonal lysozyme crystal to compute the growth rate as a function of crystal size for various protein concentrations at 22°C, pH 4.0 and 50 mg/ml NaCl. They modeled the growth process as two steps: (i) transport of the solute to the interface and (ii) attachment to the surface. Solute transport was treated as the diffusion of protein from a well mixed bulk solution to the interface across a boundary layer of thickness $\delta = L (Sc\ Gr)^{-1/4}$. Here, L = characteristic length of the crystal, Sc = Schmidt number v/D, and Gr = Grashof number $L^3 \beta g/v^2$; v = kinematic viscosity of the solution, D = diffusion coefficient of the solute, β = scaled density difference between fluid at the interface and the bulk fluid $(\rho_i - \rho_\infty)/\rho_\infty$, and g = acceleration of gravity.

12

The quasi-steady growth rates calculated by Pusey *et al.* [5,12] clearly indicate that even in the absence of convective transport, lysozyme crystal growth is kinetically limited until crystals reach sizes of at least 10 μm. Grant and Saville [13] equated the crystal growth rate calculated from Pusey's kinetic expression with the flux predicted by the Ranz-Marshall correlation for mass transfer to a growing sphere and reached essentially the same conclusion except that the transition from kinetic to diffusion control is expected to occur at crystal sizes larger than 100 μm. Diffusion is not expected to really limit crystal growth until the crystal is significantly larger than the typical 1 mm size used in X-ray diffraction studies. In practice, then, protein crystals appear to be kinetically controlled during most of their growth.

The relative fragility of the hydrogen bonds which maintain the molecule's tertiary structure and hold the molecule in the crystal has led some researchers to suggest that shear stresses produced by buoyancy-driven flow may somehow disrupt the molecule's structure or strip it from the surface of a growing crystal. Grant and Saville [13] used an order of magnitude analysis to show that characteristic velocity of the convective plume, U, should scale as

$$U \sim \left(\frac{Gr}{Sc}\right)^{1/2} \frac{v}{R} \qquad (1.2),$$

where R = radius of the (assumed) spherical crystal. This is the same scaling derived by Ostrach [38], Rosenberger [4], and Pusey, Witherow and Naumann [9]. Thus, the boundary layer thickness scales as

$$\delta = (Gr\,Sc)^{-1/4}\,R \qquad (1.3),$$

so the characteristic shear stress is given by:

$$\tau \sim \mu \frac{U}{\delta} \sim \mu \left(\frac{Gr^{1/2}}{Sc^{1/2}} \frac{v}{R}\right)\left(\frac{Gr^{1/4}\,Sc^{1/4}}{R}\right) \sim \frac{\mu v}{R^2}\left(\frac{Gr^3}{Sc}\right)^{1/4} \sim R^{1/4} \qquad (1.4),$$

where μ = solution viscosity. Typical Schmidt numbers for proteins are on the order of 10^4 while estimates of the Grashof number for a growing lysozyme crystal are about 2

13

[13]. The characteristic velocity under these conditions is $U \approx 30$ μm/s, in good agreement with the velocities measured by Pusey *et al.* [9]. This scale analysis shows that shear stresses produced by buoyancy-driven flow are small and are only weakly dependent on crystal size.

Grant and Saville [13] then compared forces calculated from a simple model of nonspecific interatomic bonding with the shear forces estimated above in order to assess the likelihood that molecules and crystals could be disrupted by free convection. The representative nonspecific bond had a strength of 81 J/mol, compared with a typical hydrogen bond (> 12 kJ/mol *in vacuo* [16]) and the magnitude of ΔH of crystallization of tetragonal lysozyme (70 - 80 kJ/mol [20,39]). Shear forces were found to be three orders of magnitude too small to break the molecule's internal hydrogen bonds and almost eight orders of magnitude too weak to strip molecules from the crystal surface. Another order of magnitude analysis compared the rates at which the orientation of the molecule is imposed by the shear flow and randomized by rotary diffusion; randomization occurs approximately 10^7 times as fast as the shear flow can orient the molecule. These simple calculations provide no evidence that buoyancy-driven convection can mechanically alter the state of the molecule near the crystal surface; nor do they suggest that a low gravity environment would be beneficial for protein crystal growth.

Despite the absence of an obvious mechanism, other observations do suggest that crystal orientation and flow environment may affect protein crystal growth [9,40]. Broom *et al.* [40] noted that crystals of human serum albumin, which form plates approximately 0.5 mm × 0.5 mm × 0.05 mm (length × width × thickness) when one of the large faces is occluded, could be grown almost twice as thick if one of the narrow faces were occluded. They chose to interpret the change in aspect ratio with orientation in terms of a combination of convective and surface occlusion effects. Note, however, that the crystal's thickness is determined by the rate at which the large faces advance. When both large faces are exposed to supersaturated solution, as when one of the small faces is occluded, both large faces can

14

advance. If this interpretation is correct, there is no need to invoke convection because a doubling of the thickness is a natural consequence of crystal orientation alone.

Pusey, Witherow, and Naumann [9] measured the velocity of the convective plume produced by growing lysozyme crystals and obtained values in the range 5 - 50 μm/s depending on crystal size and bulk protein concentration. These values are in reasonable agreement with the characteristic velocity calculated from Equation (1.2). Pusey *et al.* conducted a series of growth experiments in which crystals smaller than 50 μm were exposed to forced convection comparable to the free convection velocities they measured. They report that growth rates were initially consistent with kinetic expressions derived from quiescent crystal studies but started to fall within 2 hours. Furthermore, growth rates after 8 - 20 hours were only 5 - 10% of the initial growth rates. The reduction in growth rate began at shorter times as the strength of convection was increased [M. L. Pusey, personal communication]. Pusey *et al.* interpreted their results as tentative support for the hypothesis that convection was responsible for "cessation of growth."

One puzzling result of these convection experiments is an apparent enhancement of the crystal growth rate in the presence of convection. This transient enhancement is inconsistent with the notion that small crystals grow under kinetic control (as suggested by the absence of any size dependent growth in small crystals at short times). One possible explanation for this unusual behavior lies in the nature of the experimental system: conditions in the supersaturated bulk protein solution are *extremely* difficult to control. Protein tends to come out of solution whenever possible by: deposition on the face of a growing crystal, secondary nucleation ("showering") of new crystals, or amorphous precipitation as a stringy floc. Secondary crystals and amorphous precipitates, both of which were reported by Pusey *et al.*, compete for protein with the crystals under observation and could significantly reduce the measured crystal growth rate by depleting the bulk solution. In fact, this hypothesis was actually suggested by Pusey and coworkers

in an earlier study [5] to explain some apparent discrepancies in the work done by Fiddis *et al.* [24].

A second hypothesis was suggested by Grant and Saville [13], who posited the existence of a high molecular weight contaminant which somehow "poisons" the surface against further addition of protein to the crystal. If deposition of the contaminant is favored over the desired protein, the contaminant concentration is reduced near the crystal surface and protein addition is favored. Convection effectively raises the surface concentration of contaminant to the bulk value by bringing in fresh solution, thereby retarding crystal growth. The identity of the contaminant (if any) is unknown, but oligomers of protein could fill the role.

In brief, the case for convective effects in protein crystal growth remains ambiguous. Order of magnitude calculations of a characteristic shear force provide no evidence that buoyancy-driven flow mechanically disrupts the bonds that hold the moleucle in the crystal lattice or maintain native structure of the protein [13]. Similar calculations based on measured crystal growth kinetics reveal that protein crystals grow under kinetically-controlled conditions until they are approximately 100 μm in size. Nevertheless, crystals grown aboard the U. S. space shuttle are reported to diffract X-rays to higher resolution than control crystals grown in the laboratory [10]. Crystals grown under forced convection slow their growth [9], but the interpretation of this behavior remains elusive. These somewhat conflicting results prompted our investigation into possible flow effects, as described in Chapters 2 and 3.

1.6 The Search for Crystallization Conditions

Finding suitable crystallization conditions can be the most time consuming step in a structure determination. A balance must be struck between the demand for relatively rapid crystal growth (high supersaturations) and the need to limit the number of competing nuclei (low supersaturations). In a typical scenario, an array of possible crystallizing conditions

16

is tested simultaneously using microliter quantities of protein solution [2]. Subsequent trials are spent refining conditions to produce a few satisfactory crystals. Heidner [41] examined crystal number density as a function of protein concentration and supersaturation. The nucleation rate of rabbit muscle aldolase crystals was reported to depend on total protein concentration, C, and not the supersaturation as expected from thermodynamic arguments. Growth rates, in contrast, were dependent on supersaturation. These results led Heidner to suggest dilute but highly supersaturated solutions would be optimal for rapid growth of only a few crystals.

Rosenberger and Meehan [42] suggested exploiting the different functional dependences of nucleation and growth to create a small number of primary crystals in one concentration regime and then reduce the supersaturation to maintain steady growth and reduce secondary nucleation. The novel aspect of their suggestion (at least for protein crystal growers) was the use of a programmed temperature history to alter the protein solubility. Controlling solubility in this way is a marked change from the usual practice of changing the ionic strength of the solution. Effective use of such a technique requires knowledge of the dependence of solubility on temperature - exactly the fundamental data which are scarce and not always reliable (see section 1.3).

In a different approach, Young et al. [11] examined the selection of crystallization conditions in terms of the interaction potentials between protein crystals and protein molecules in solution. As the reader might expect, these interactions are poorly understood. The behavior of protein crystal systems can, in principle, be described in terms of the electrostatic and dispersion (van der Waals) potentials between protein molecules and crystals. The case examined by Young was that of protein molecules (spheres) with a constant surface potential interacting with a crystal (flat plate) also at constant potential. At the current level of understanding, the approximation of the crystal as a flat plate is reasonable since the crystal is typically 10^5 - 10^6 times as large as the molecule and faceted. They claim that optimal conditions for crystal growth are those

where the sphere-sphere potential is more repulsive (presents a higher barrier to aggregation) than the sphere-plate potential; the sphere-plate potential should have a moderate to low energy barrier to promote attachment of molecules to the surface.

Young and coworkers focused most of their attention on the role of ionic strength on reducing the electrostatic repulsion between similarly charged bodies. Their working hypothesis, that salt rejection by growing protein crystals eventually raises the ionic strength of the solution above the critical electrolyte concentration and induces rapid coagulation, was based on a sudden increase in turbidity of a protein solution (30 mg/ml lysozyme, 50 mg/ml NaCl, pH 4.0, 17°C) upon addition of a single seed crystal. In a subsequent experiment, they placed comparable seed crystals in solutions with various NaCl concentrations and noted that significant crystal growth occurred for NaCl concentrations between 30 mg/ml and 50 mg/ml. They suggest that electrostatic repulsion at low ionic strength is too strong to permit crystal growth, while protein in solution is depleted by rapid coagulation at high ionic strength.

Rapid coagulation is a regime in which colloidal particles experience no repulsion and coagulate as soon as they come in contact [14]. If 50 mg/ml NaCl is above the critical flocculation concentration, rapid coagulation of the protein molecules should be observed even in the absence of the seed crystal. In addition, Young's argument would suggest that crystal growth would be impossible at salt concentrations significantly greater than 50 mg/ml (0.85 M). Nevertheless, crystallographic data for hen egg white lysozyme grown from a solution of 1.4M NaCl [C. D. Smith, personal communication] indicate a much larger value for the critical flocculation concentration. Excursions in local salt concentration larger than a few percent of the bulk concentration can be excluded on the basis of a quasi-steady model of salt rejection by a growing lysozyme crystal [13].

The main contribution of the work by Young *et al.* was to set out the problem of protein crystal growth in a form familiar to colloid scientists. Properties which determine the interaction potentials of molecules with crystals and other molecules are the surface

potentials on the molecule and crystal (which need not be the same), the ionic strength of the solution, and the strength of the dispersive attraction. The surface potential is determined by the distribution of charged groups which, because they are determined by acid-base equilibria, are pH dependent. The nonuniform (fixed) charge distribution on the surface of the molecule introduces a major complication into the analysis of protein systems compared with the simpler "regular" colloidal systems. Until now, no work has been done which is applicable to the current situation. The effects of the charge distribution on enzyme activity has been studied, however, and is presented in the following section.

1.7 Effects of Nonuniform Charge Distribution

Nonuniform charge distributions on biological macromolecules can produce superficially counter-intuitive behavior. The enzymatic activity of copper, zinc superoxide dismutase is a case in point. Superoxide dismutase (SOD) is reported to be a homodimer of molecular weight 32,000 with a net valence of -4 [43]; its substrate, the superoxide radical ($\cdot O_2^-$) has valence -1. An initial inspection might suggest that the activity of the enzyme would be limited by repulsion of the like charges as the substrate approaches the enzyme. One might also expect the enzymatic activity to increase with ionic strength as the repulsion is diminished by counterion screening. Experimental findings contradict both these hypotheses: the enzyme activity is close to that calculated from the Brownian collision rate for uncharged particles of similar size and decreases with added salt [43].

Crystallographic studies of SOD revealed a group of positively charged residues around the active site which guide the superoxide. Cudd and Fridovich [43] chemically modified the residues near the active site and measured enzyme activity as a function of salt concentration. A 90% drop in enzyme activity was observed when arginine 141 was neutralized, and the activity still decreased with ionic strength. A similar neutralization of 7

19

- 8 lysine residues reduced the reaction rate by approximately 80% but reversed the trend with ionic strength. It was concluded that lysines are responsible for long-range steering while the arginine provides local orientation of the incoming molecule near the active site.

Getzoff *et al.* [44] calculated the electrostatic potential near SOD by treating the charged groups as point charges. Her results indicate that the electric field produced by SOD's charge distribution channels the negatively charged substrate into the active site, and that certain residues have particularly large effects on the field direction. The criterion for assigning relative significance was the size of the change in the average E-field vector in the active site channel. By this standard, arg 141, the neutralization of which changes the average direction of the electric field by approximately 20° at short distances from the active site, is the most important single residue. Glu 131 and lys 134 contribute significantly to the E-field direction at ranges greater than about 8Å.

Several workers have used Brownian dynamics to estimate the importance of electrostatic steering in the activity of SOD [45-47]; the electrostatic forces in these simulations were calculated by treating the charged groups as point charges in a uniform dielectric medium ($\varepsilon = 78$) with no added salt. The protein dimer was modeled as a sphere approximately 30Å in radius with two reactive caps at the poles (the caps covered about 10°). The 76 charged groups of SOD have been variously approximated as: (i) a single charge in the center of the dimer, (ii) 5 charges which reproduce the monopole, dipole and quadrupole moments of the charge distribution observed crystallographically, (iii) 76 point charges, and (iv) 2196 partial charges on all non-hydrogen atoms in the dimer. Allison and McCammon [45] showed that including the dipole and quadrupole moments of the molecule increased the reaction rate by 40% ~~increase~~ compared with the monopole alone. X They also found that the reaction rate for the charged species was 40% that expected for uncharged particles. They attributed the small difference in rates to the small potential energy barrier ($\leq$ 1 kT at contact) which the incoming superoxide radical must overcome in

order to reach the enzyme surface. The calculated reaction rates for models (ii), (iii) and (iv) were approximately the same [46,47]. When the Debye-Hückel expression for the potential was used to simulate the effect of salt, the reaction rate reached a maximum at an ionic strength of approximately 0.03M [45].

In 1986, Klapper *et al.* [48] employed a finite-difference method to solve the linearized Poisson-Boltzmann equation in the vicinity of SOD. Charged groups were placed at their crystallographically measured coordinates and the boundary between the interior of the molecule and the bulk solution was defined to be the solvent-accesible surface. Points inside the molecule were assigned $\varepsilon_1 = 2$; those outside, $\varepsilon_2 = 80$. Electrically charged groups were represented by fractional charges assigned to the eight nearest grid points. Klapper's calculations showed that the surface charge distribution and molecular shape of the enzyme combine to create a large "target" area of positive potential to attract the negatively charged substrate. As ionic strength increases, repulsion from the negatively charged region decreases at the same time the effective target area is reduced; the latter effect dominates the former, accounting for the trend in enzyme activity.

Subsequent versions of this technique can now handle the nonlinear Poisson-Boltzmann equation. One limitation of the finite element method, however, is that computer memory requirements rise rapidly as the resolution of the finite difference grid is increased. These finite difference calculations are typically performed with grid spacing scaled so the molecule occupies 50 - 75% of the domain [49]. Such scaling is adequate when the substrate is small enough compared with the enzyme that it can be treated as a point charge, but the interactions between molecules (or molecules and macroscopic bodies) are infeasible.

Brownian dynamics simulations of the association between cytochrome *c* and cytochrome *c* peroxidase were performed by Northrup *et al.* [50]. They modeled the proteins as spheres with embedded charges to reproduce the monopole and dipole moments of the molecules calculated from the crystallographic locations of the charged groups. The

most significant finding was a reaction rate enhancement of an order of magnitude resulting from mutual alignment of the enzymes by their large dipole moments (300D - 500D). Virtually no work has been published on the interaction of charged proteins with macroscopic objects (such as crystals); this situation is addressed in the study described in Chapter 4.

1.8 Present Work

For reasons outlined earlier, the research in this project is divided between an experimental study on the effect of forced convection on protein crystal growth (Chapters 2 and 3) and a theoretical study of the interaction potential between crystals and protein molecules in solution (Chapter 4). The former is a response to hypotheses about the role of buoyancy-driven natural convection in protein crystal growth [9,10,35,37,40], while the latter is intended to describe some of the complex interactions experienced by protein molecules near the crystal surface.

There is a certain amount of ambiguity in the results of the crystal growth experiments. Differences in experimental conditions restrict most of the analysis to trends within a given experiment instead of a comparison of flow and quiescent experiments. Certain theoretical predictions of crystal growth behavior can be tested, however, and some possible mechanisms can be ruled out in this manner. Mass transport does not seem to limit crystal growth under the conditions studied, so future research may be better spent exploring other phenomena of crystal growth. A comparable level of uncertainty pervades the calculation of interaction potentials, but again transport from the bulk does not seem crucial. In conjunction with the experimental findings, the results suggest that a study of processes occurring near the crystal surface.may be worthwhile.

References

[1] Goodford, P. J. *J. Medicinal Chem.* **27** (1984) 557-564.

[2] McPherson, A. *Preparation and Analysis of Protein Crystals.* New York: Wiley, 1982.

[3] Kolata, G. *Science.* **229** (1985) 370-371.

[4] Rosenberger, F. *J. Crystal Growth.* **76** (1986) 618-636.

[5] Pusey, M. L., R. S. Snyder and R. Naumann. *J. Biol. Chem.* **261** (1986) 6524-6529.

[6] McPherson, A. *Meth. Enzymology.* **114** (1985) 112-120.

[7] Sweet, R. M. *Meth. Enzymology.* **114** (1985) 19-46.

[8] Leberman, R. *Science.* **230** (985) 374-375.

[9] Pusey, M., W. Witherow and R. Naumann. *J. Crystal Growth.* **90** (1988) 105-111.

[10] DeLucas, L. J., C. D. Smith, H. W. Smith, S. Vijay-Kumar, S. E. Senadhi, S. E. Ealick, D. C. Carter, R. S. Snyder, P. C. Weber, F. R. Salemme, D. H. Ohlendorf, H. M. Einspahr, L. L. Clancy, M. A. Navia, B. M. McKeever, T. L. Nagabhushan, G. Nelson, A. McPherson, S. Koszelak, G. Taylor, D. Stammers, K. Powell, G. Darby and C. E. Bugg. *Science.* **246** (1989) 651-654.

[11] Young, C. C., R. C. De Mattei, R. S. Feigelson and W. A. Tiller. *J. Crystal Growth.* **90** (1988) 79-85.

[12] Pusey, M. and R. Naumann. *J. Crystal Growth.* **76** (1986) 593-599.

[13] Grant, M. L. and D. A. Saville. *J. Crystal Growth.* **108** (1991) 8-18.

[14] Hiemenz, P. C. *Principles of Colloid and Surface Chemistry.* New York: Marcel Dekker, 1977.

[15] Matthews, B. W. *J. Mol. Biol.* **33** (1968) 491-497.

[16] Creighton, T. E. *Proteins: Structures and Molecular Properties.* New York: W. H. Freeman and Company, 1983.

[17] Israelachvili, J. N. *Intermolecular and Surface Forces.* Orlando: Academic Press, 1985.

[18] Kam, Z., H. B. Shore and G. Feher. *J Mol. Biol.* **123** (1978) 539-555.

[19] Feher, G. and Z. Kam. *Meth. Enzymology.* **114** (1985) 77-112.

[20] Howard, S. B., P. J. Twigg, J. K. Baird and E. J. Meehan. *J. Crystal Growth.* **90** (1988) 94-104.

[21] Tanford, C. *Physical Chemistry of Macromolecules.* New York: Wiley, 1961.

[22] Sophianopoulos, A. J., C. K. Rhodes, D. N. Holcomb and K. E. Van Holde. *J. Biol. Chem.* **237** (1962) 1107-1112.

[23] Dubin, S. B., N. A. Clark and G. B. Benedek. *J. Chem. Phys.* **54** (1971) 5158-5164.

[24] Fiddis, R. W., R. A. Longman and P. D. Calvert. *J. Chem. Soc. Faraday Trans.* **75** (1979) 2753-2761.

[25] Sophianopoulos, A. J. and K. E. Van Holde. *J. Biol. Chem.* **239** (1964) 2516-2524.

[26] Bruzzesi, M. R., E. Chiancone and E. Antonini. *Biochemistry.* **4** (1965) 1796-1800.

[27] Grant, M. L. and D. A. Saville. Paper presented at Joe Wheeler Conference on Protein Crystal Growth. Rogersville, AL: May 11-14, 1987.

[28] Salemme, F. R., L. Genieser, B. C. Finzel, R. M. Hilmer and J. J. Wendoloski. *J. Crystal Growth.* **90** (1988) 273-282.

[29] Ohara, M. and R. C. Reid. *Modeling Crystal Growth Rates from Solution.* Englewood Cliffs, NJ: Prentice-Hall, 1973.

[30] Bennema, P. and G. H. Gilmer. in *Crystal Growth: An Introduction.* ed. P. Hartman. New York: American Elsevier, 1973.

[31] Schlichtkrull, J. *Acta. Chem. Scand.* **11** (1957) 439-460.

[32] Schlichtkrull, J. *Acta. Chem. Scand.* **11** (1957) 484-486.

[33] Durbin, S. D. and G. Feher. *J. Crystal Growth.* **76** (1986) 583-592.

[34] Durbin, S. D. and G. Feher. *J. Mol. Biol.* **212** (1990) 763-774.

[35] Littke, W. and C. John. *Science.* **225** (1984) 203-204.

[36] Naumann, R. J., R. S. Snyder, C. E. Bugg, L. J. De Lucas and F. L. Suddath. *Science.* **230** (1985) 375-376.

[37] Erdmann, V. A., C. Lippmann, C. Betzel, Z. Dauter, K. Wilson, R. Hilgenfeld, J. Hoven, A. Liesum, W. Saenger, A. Müller-Fahrnow, W. Hinrichs, M. Düvel, G. E. Schulz, C. W. Müller, H. G. Wittmann, A. Yonath, G. Weber, K. Stegen and A. Plaas-Link. *FEBS Letters.* **259** (1989) 194-198.

[38] Ostrach, S. *Ann. Rev. Fluid Mech.* **14** (1982) 313-345.

[39] Ataka, M. and M. Asai. *J. Crystal Growth.* **90** (1988) 86-93.

[40] Broom, M. B. H., W. K. Witherow, R. S. Snyder and D. C. Carter. *J. Crystal Growth.* **90** (1988) 130-135.

[41] Heidner, E. *J. Crystal Growth.* **44** (1978) 139-144.

[42] Rosenberger, F. and E. J. Meehan. *J. Crystal Growth.* **90** (1988) 74-78.

[43] Cudd, A. and I. Fridovich. *J. Biol. Chem.* **257** (1982) 11443-11447.

[44] Getzoff, E. D., J. A. Tainer, P. K. Weiner, P. A. Kollman, J. S. Richardson and D. C. Richardson. *Nature.* **306** (1983) 287-290.

[45] Allison, S. A. and J. A. McCammon. *J. Phys. Chem.* **89** (1985) 1072-1074.

[46] Ganti, G., J. A. McCammon and S. A. Allison. *J. Phys. Chem.* **89** (1985) 3899-3902.

[47] Allison, S. A., S. H. Northrup and J. A. McCammon. *Biophys. J.* **49** (1986) 167-175.

[48] Klapper, I., R. Hagstrom, R. Fine, K. Sharp and B. Honig. *Proteins: Structure,, Function, and Genetics.* **1** (1986) 47-59.

[49] Sharp, K. *J. Computational Chem.* **12** (1991) 454-468.

[50] Northrup, S. H., J. C. L. Reynolds, C. M. Miller, K. J. Forrest and J. O. Boles. *J. Am. Chem. Soc.* **108** (1986) 8162-8170.

CHAPTER 2

Description of Protein Crystal Growth Experiments

2.1 Introduction

The conflicting reports of experimentally observed effects of convection on protein crystal growth [1,2], coupled with the negative findings of order-of-magnitude calculations of proposed disruptive mechanisms [3], prompted this experimental investigation into the existence and magnitude of flow effects. An examination of published results showed no data on crystals significantly larger than 100 μm, precisely the range where transport effects, if any, would become manifest [3]. A series of studies was planned to establish the baseline behavior of large (> 100 μm) lysozyme crystals, both in the presence and absence of forced convection.

This chapter can be divided into two parts: (i) the history of the experiment's purpose and procedure, and (ii) the methods developed to analyze digital images of a growing crystal and estimate the size and orientation of the three-dimensional crystal. Although the final experimental set-up is similar to that used by other researchers [2,4-6], it was originally quite different. Most of the changes in the experiment were made in response to difficulties in sample preparation. Some of the difficulties in growing lysozyme crystals which can be used for growth studies are discussed at some length below.

The analysis of crystal images is considerably more routine than growing the crystals. The geometric information contained in a picture of a crystal can, with certain assumptions, be reduced to list of crystal vertex locations for quantitative analysis. The construction of three-dimensional ideal analogues for a given crystal image allows crystals in almost any orientation to be studied. Given the difficulties associated with producing isolated single crystals, and the need to measure many crystals to establish baseline behavior, even a slight increase in the fraction of usable crystals is a boon to investigators.

Nevertheless, some crystals are extremely difficult to interpret and cannot be measured with these techniques.

The intent here is to trace the evolution of the crystal growth experiment before describing the final system. Sample preparation and experimental procedure are then decribed, followed by the results of measurements of effluent fluid taken from the growth cell. The geometry of an ideal tetragonal lysozyme crystal is then presented in order to set the stage for interpreting the digital images. Ideal analogues are compared with the raw images, and limitations of the method are discussed. Finally, some additional observations are presented before concluding.

2.2 Evolution of the Crystal Growth Experiment

The goal of these experiments was to measure the growth rates of single crystals over a much larger size range than had been done before. By continuing measurements into the 100 μm – 1 mm size range, the experiment would provide baseline information on the long-term behavior of protein crystals, especially the reported cessation of growth [7]. If such a phenomenon were observed, the manner in which growth stopped would provide clues to the responsible mechanism. Furthermore, the extent to which convection contributes to growth cessation could also be evaluated by comparing the rates at which crystals grew in the presence of forced convection and in its absence.

As originally conceived, the experiment called for size measurements of isolated crystals growing on a "sting," a glass fiber approximately 50 μm in diameter, well away from the walls of the growth cell. Crystals on a surface probably grow differently from isolated crystals in solution, so the sting was proposed as a means of reducing the effect of the substrate by reducing the area of contact. The sting was suspended from above and mounted on microtranslators to allow xyz translations of the fiber, as well as rotation about the z axis. Crystals growing anywhere on the fiber could be selected for observation; orientation effects could be studied by selecting suitably oriented crystals. The microscope

27

was placed on a rotary table so that simulated stereo observations of a given crystal could be made from two angles for three-dimensional modeling. When convective effects were studied, crystals could be positioned in the midst of the bulk flow, which would be easier to characterize than the region near the walls. The flow field experienced by the crystals would, presumably, be less influenced by the fiber than by the cell walls, at least near the base of the fiber.

This approach was eventually abandoned because the strict requirements imposed by the experiment could not be satisfied regularly. It was sometimes difficult to obtain satisfactory images of the crystals for several reasons. The lensing effect of the curved fiber produced a bright halo which obscured the edges of the crystal. The crystal positioning scheme, which permitted observation of any crystal on the sting, also hindered development of an optical train which could consistently produce clear images of the crystal. The relative positioning of illuminator, microscope, fiber, and crystal changed from crystal to crystal and required a great deal of adjustment between measurements. In addition, the fibers swayed when immersed in solution and this motion was more pronounced as fiber length increased. This motion may have resulted from building vibration and/or weak convection in the growth cell. The digitizing board used to capture images requires 1/30 of a second to record an image, and the vibration frequency was such that pictures were too blurry to interpret, even when using microscope objectives as weak as 10X.

Since measurements were to be made on only a few crystals during any one experiment, fast growth was required in order to build up a statistically significant sample in a reasonable time. Unfortunately, small particles of protein formed quickly from the highly supersaturated solution and scattered light, making the solution too murky to see the crystals on the glass fiber. The turbidity of the solution could have been reduced by using lower protein concentrations, but experimental requirements placed a premium on rapid crystal growth (high protein concentration). The contradictory requirements of quick

growth and a clear optical path between the sting and the front cell wall could not be resolved, and this approach was abandoned.

2.3 Control of Crystal Nucleation

The most serious difficulty encountered during this project was consistently nucleating single crystals which were sufficiently separated from their neighbors for use in growth experiments. Although sample preparation was standardized as much as possible, results were inconsistent. Early exploratory experiments in which lysozyme powder (as received) was dissolved in warm buffer at a concentration of 100 mg/ml, diluted with an equal volume of 100 mg/ml NaCl solution in buffer, and transferred to vials made of soda-lime glass, were uniformly successful. In this context, success was judged as the formation and growth of relatively large (> 100 μm) crystals which could easily be distinguished from their neighbors. These initial successes were not readily transferred to a system where size measurements could be made.

The most common result was a cluster of many small crystals which grew into a single mass. Discussions with protein crystallographers revealed that batch-to-batch variation due to trace contaminants is a common phenomenon in protein crystal growth. Durbin and Feher [2], for instance, used SDS-PAGE electrophoresis to detect the presence of some sort of contaminant in the lysozyme supplied by their vendor. Similar measurements performed here found no evidence of contaminants, either in samples prepared from lysozyme powder as purchased or in protein solutions which had sat in the laboratory for two months. Nevertheless, several procedural changes were made in order to reduce possible interference by extraneous, undetected species. Protein was dissolved in buffer at room temperature to reduce the possibility of thermal denaturation which might increase the variability in the experiment. The dissolved protein was then dialyzed against buffer in hopes of removing low molecular weight contaminants that might denature the protein or act as nucleation sites. The new procedure did not consistently increase the

number of suitable crystals. Filtering and centrifugation of the protein solutions produced comparable results.

A screening was performed to assess the effects of each preparation step and the role of the substrate on the size and number of lysozyme crystals. A large batch of protein solution was prepared by dissolving the protein powder (as supplied) in buffer. Samples of solution (as dissolved) were diluted with 100 mg/ml NaCl in buffer and transferred to vials of various types of glass, some of which contained stings of different glasses. The remainder of the protein solution was divided into smaller portions which received different treatments. The most elaborate treatment sequence was dialysis, centrifugation, and filtration; other portions were treated with only one of the three methods. Samples were removed after each step in the process, diluted with an equal volume of 100 mg/ml NaCl in buffer, and transferred to the vials. No obvious qualitative differences among the cleaning treatments could be discerned; crystals formed regardless of treatment history. The nature of the substrate, however, did affect the size and number of lysozyme crystals.

Some measure of control was gained by adjusting the concentration of protein in the solution from which crystals were nucleated. The nucleation rate had been reported to be a function only of protein concentration and not supersaturation [8]. A reduction in protein concentration reduced the number of crystals while increasing the fraction of usable crystals. The clarity of the optical path also improved. Crystal growth rates were so sharply reduced as a result of the lower protein concentration, however, that it was no longer feasible to study only a few crystals per experiment. The experiment was modified to observe crystals growing on the cell walls so that reasonable sample populations could be measured in a single experiment. Although the new experiment relaxed the requirements set forth earlier, obtaining crystals which could be used for the experiment remained haphazard.

2.4 Sample Preparation

The procedure detailed here produced the crystals measured during the experiments. No statement is made about the reliability of the method. There is a significant stochastic quality to crystal growth, even in well characterized systems. Protein systems, which are not well characterized, show even greater variability.

Two liters of buffer (pH 4) were prepared by dissolving 20.0 g of fused anhydrous sodium acetate (FW 82.03, Fisher) and 50 ml glacial acetic acid (Fisher) in deionized water and diluting to the mark in a volumetric flask. Twenty-five grams of lysozyme powder (L-6876, Sigma, grade 1, 3X crystallized, dialyzed and lyophilized) were dissolved in buffer to form 1 liter of solution. One liter of precipitant solution was prepared by dissolving 100.0 g of NaCl in buffer. A triple beam balance was used for all weighings; the uncertainty in each value is ± 0.05 g.

Some white floc-like material formed during dissolution or shortly thereafter; more formed while the solution was stored for use. In addition, the protein solution was slightly turbid. Both the protein and precipitant solutions were pumped through a prefilter (AP15, Millipore) to remove foreign matter and extremely large aggregates of protein. The protein solution, which contained no visible floc strands and was markedly clearer after this step, was loaded into the feed reservoir for use in the experiment. The solutions were not cleaned further because each cleaning step removed some protein and experience had shown that elaborate cleaning procedures have only a marginal effect on crystal formation.

2.5 Apparatus

A schematic diagram of the crystal growth experiment is shown in Figure 2-1. A two-channel syringe pump (Harvard Apparatus) supplied feed solutions at room temperature to the reservoirs in the constant temperature recirculating bath (RMS-6, Lauda). Glass cold traps having a capacity of approximately 85 ml were used as reservoirs. The solution entering the reservoir displaced fluid that had already equilibrated

31
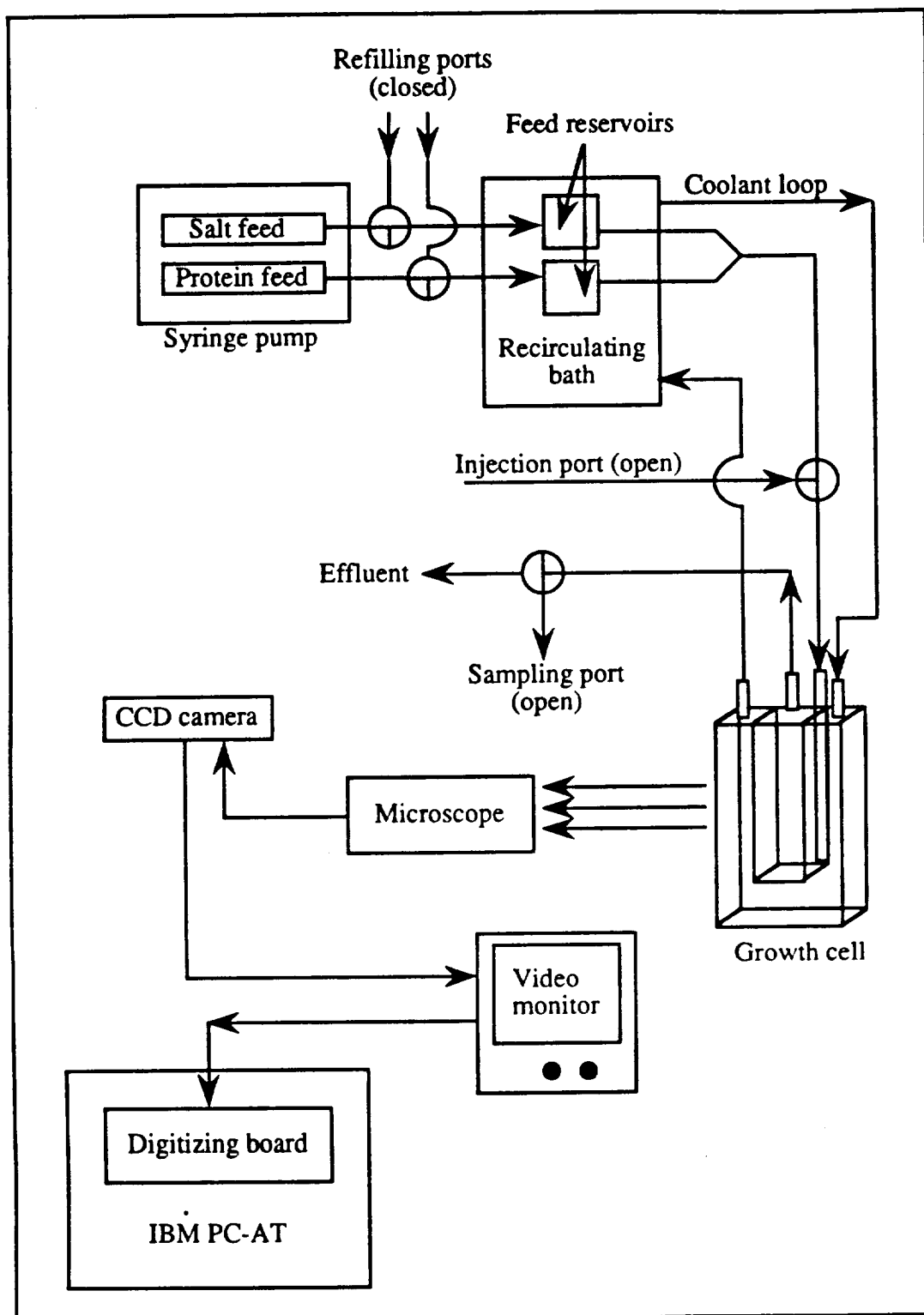
Figure 2-1: Schematic diagram of protein crystal growth experiment.

with the bath. After leaving the reservoirs, the fluids flowed through approximately 110 cm of 0.16 cm (1/16") ID Tygon tubing before merging in a "Y." An additional 40 cm of 0.32 cm (1/8") ID Tygon tubing connected the "Y" with the cell entrance. Total hold-up in the feed lines was estimated to be 2.1 ml of each solution upstream of the merge and 3.3 ml of mixed solution downstream. The effluent flowed through approximately 30 cm of 0.32 cm ID tubing before reaching the sample port, where it could be diverted down a final 45 cm of 0.32 cm tubing for collection in scintillation vials for later analysis. The volume of effluent in the lines between the cell exit and sample collection point was approximately 6.1 ml. All tubing was flushed with several hundred milliliters of deionized water prior to the expeiment.

Crystals were grown in a fused quartz spectrophotometer cell (type 66-Q, Uvonics) with a water jacket. The dimensions of the growth chamber were 0.4 cm × 1.0 cm × 3.8 cm (width × depth × height). Feed solution entered the cell in the lower right rear corner of the cell (as viewed from the microscope) and effluent departed at the rear top center. The horizontal and vertical position of the cell could be adjusted with a rack and pinion which was, in turn, mounted on a translation stage. The range of travel permitted observation of all but the bottommost few millimeters of the cell. See Figure 2-2 for a picture of the cell/microscope assembly.

A Mitutoyo Finescope FS 50 microscope was used to inspect the growing crystals. The microscope was custom-mounted horizontally so it could be used to examine crystals growing on vertical surfaces. The microscope could be rotated about the cell because it was mounted on a rotary table, a holdover from the design of the original experiment. For this experiment, the angle was not changed after the initial alignment. Observations were made using transmitted light provided by a fiber-optic ring light (series 180 Fiber-Lite, Dolan-Jenner) positioned behind the growth cell; the only illumination control was brightness.
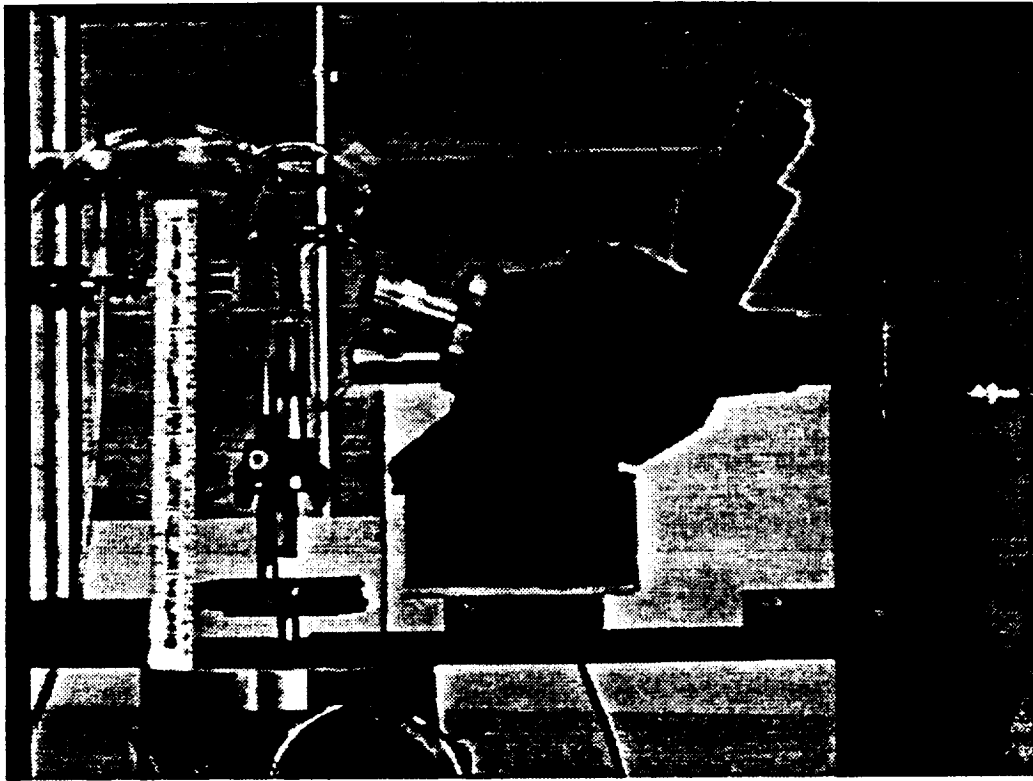
Figure 2-2: Crystal growth cell/microscope assembly.

Video images, which were produced by a Sanyo VDC 3800 charge-coupled television (CCTV) camera were displayed on an Hitachi Denshi VM-920 monitor for framing and focusing. Suitable images could be captured by a Matrox PIP-640B frame grabber which was installed in an IBM PC-AT. Image files were copied to magnetic tape for long-term storage. Captured images were displayed on a Mitsubishi HF 1400 rgb monitor for analysis. A Mouse Systems mouse was installed on the PC-AT to provide cursor control when measuring crystals. Measurement software, which consisted of calls to Matrox-supplied "primitive" routines and mouse driver routines, was written by the author.

2.6 Procedure

A highly supersaturated slug of protein solution was injected into the growth cell, where it remained until crystals could be observed on the side of the cell. The cell was flushed with fresh growth solution at lower supersaturation prior to digitizing the initial pictures of the crystals. For the quiescent experiment, the initial slug was prepared by slowly adding NaCl to the stock protein feed solution until the solution became cloudy. The salt concentration of the slug was approximately 100 mg/ml (0.5 g NaCl added to 5 ml of protein feed solution). Crystals were first clearly observed after approximately 4 hours. Repetition of this procedure for the flow experiment produced many highly crowded crystals which seemed likely to grow into large masses. Slug preparation was modified to reduce the number of nuclei formed rapidly and to relieve crowding. The final procedure was to mix 6 ml of protein feed solution with 5 ml of buffer solution saturated with NaCl. The mixture was injected into the cell as before. Crystals were observed after 75 – 80 minutes, at which time the forced convection was started. The volumetric flow rate was approximately 1.87 ± 0.04 μl/s, corresponding to an average velocity of 46.7 ± 0.9 μm/s based on the 0.4 cm² cross-sectional area of the growth cell.

During the first digitizing pass, crystals were included for study based on two criteria: they had to be visible through the 10X objective of the microscope and sufficiently isolated that they would not impinge on each other early in the experiment. The wall of the growth cell was surveyed in a "switchback" pattern progressing from one corner of the cell to the diagonally opposing corner. Quiescent crystals were inspected starting in the upper left corner while the search for flow crystals began in the lower right corner. Subsequent imaging passes through the crystals followed the same sequence established during the initial pass.

Numbers were assigned to each image in the order they were added to the sample population. Image files were named according to the date and order in which they were

made. The names of all crystal images start with "X," followed by the date (year-month-day) and a suffix indicating the order in the sequence; for example, X900512.002 was the second picture taken on 12 May 1990. After capturing an image, the file name, time, and microscope objective used were written onto the stored image so that this information could not be accidentally separated from the image. Each crystal was named according to the experiment and frame in which it appeared. Thus, crystal XQ008001 was the first crystal measured in the eighth picture of the quiescent experiment and XF033002 was the second crystal in the 33rd frame of the flow experiment. When more than one crystal appeared in a picture, the order of selection was arbitrary. Crystals appearing in more than one picture were named according to the frame in which the measurements were made. These naming conventions were violated occasionally when crystal measurements were repeated; successive attempts were treated like measurements of additional crystals, although only one set of measurements was included in the analysis. A crystal's name provides some information about its position: crystals at the end of the sampling sequence were at the top or bottom of the cell; crystals with sequential names were nearer than those with widely differing names.

Samples of effluent were collected at least once a day so that conditions in the growth cell could be determined *ex post facto*. Samples from the quiescent experiment were obtained by opening the sample port and flushing the cell and lines with enough fresh solution to displace the fluid originally in the cell into a scintillation vial. Flow samples were taken by opening the sample port to allow the forced convection to flush the effluent line; collection started after a reasonable time had passed. Flow samples probably tracked cell conditions better than the quiescent samples because the feed to the collection vial was continuous, while quiescent sampling was a sporadic event. A small aliquot (approximately 0.5 ml) of the supernatant was removed by pipet and diluted to 10 ml in a volumetric flask for later measurement. The dilution was necessary to make the solution unsaturated and to put the ultraviolet absorbance by the protein into an easily measured

36

range. Measurements of pH, sodium concentration, and protein concentration were made on all samples collected in both experiments. The sampling was intended primarily as a check for serious problems since, in light of the relatively slow growth rates previously reported [4-6], these values were not expected to vary greatly over the course of the experiment. No correction was possible, even if real-time measurements had been made, because no active control was in effect.

During the quiescent experiment, fresh feed solution was introduced to the cell in order to maintain a constant protein concentration. This was usually done at the same time the samples were taken so that excessive solution was not required. There was no rigid schedule for replacing the solution since the concentration was not expected to change rapidly. As a result, the volume of fresh solution infused each time was not closely measured. The infused volumes were, however, slightly larger at the beginning than at the end. Drifts in protein concentration were not expected to be significant during the flow experiment.

The syringes in the pump were refilled whenever the volume in each fell below approximately 10 ml. This caused no disruption during the quiescent experiment since the pump was normally off, but the forced convection was interrupted briefly to resupply the syringes. The procedure was to turn off the pump, open the refilling port, and infuse fresh solution with loaded syringes. The syringe pump was set to a higher speed and air was bled from the lines through the refilling port. The refilling port was closed, the pump speed reset, and the experiment resumed.

2.7 Measurements of Samples

The pH of the stored samples was measured using an EA 940 expandable ion analyzer (Orion Research, Inc.) with pH and reference electrodes (MI-405, MI-409) obtained from Microelectrodes, Inc. After calibration with two standards (pH 4.00 and pH 7.00, Fisher), measurements were taken in random sequence. Instrument drift required a

one-point recalibration after every 5 - 7 samples; pH 4.00 standards were used. A two-point calibration was performed after 24 samples had been measured. The pH of samples from the quiescent experiment was 4.02 ± 0.04, while flow samples had pH 3.99 ± 0.03. The reported uncertainties are the unbiased estimates of the population standard deviations.

The samples were diluted by an additional factor of 1:5 prior to measuring sodium concentration. A sodium-selective electrode (MI-420, Microelectrodes, Inc) and the EA 940 ion analyzer were used. A 10,000 ppm sodium stock solution was prepared by diluting 100 ml of a 10% sodium standard (Orion Research, Inc.) to 1 liter in a volumetric flask. Calibration standards with 100, 250, and 500 ppm added sodium were prepared by adding appropriate amounts of 10,000 ppm stock solution to 10 ml of sodium acetate/acetic acid buffer and diluting to 1 liter in volumetric flasks. These standards had approximately the same background sodium and hydronium concentrations as the diluted samples. The corrections for background signal caused by the buffer and for instrument drift are described in Appendix A. NaCl concentrations of quiescent samples were measured at 52.1 ± 5.8 mg/ml ; after an initial upward transient, flow samples contained 51.7 ± 4.9 mg/ml NaCl.

Protein concentration was determined from UV absorbance at 280 nm based on a value of $A_{280\ nm}^{1\%(w/v)}$ = 26.35 ± 0.13 for a 1 cm light path [9]; 1%(w/v) = 10 mg/ml. Measured effluent stream protein concentrations are plotted in Figure 2-3. Measurements were made in duplicate using a Beckman DU 64 spectrophotometer and the average value was reported after correcting for dilution. The largest deviation from the mean was 0.15 mg/ml and the standard deviation for all measurements was less than 0.05 mg/ml. In each experiment, there is an interval over which the protein concentration is constant within statistical error at the 95% confidence level. These intervals are marked by double-headed arrows in Figure 2-3. The sample mean and 95% confidence limits of the measurements are also shown.

38
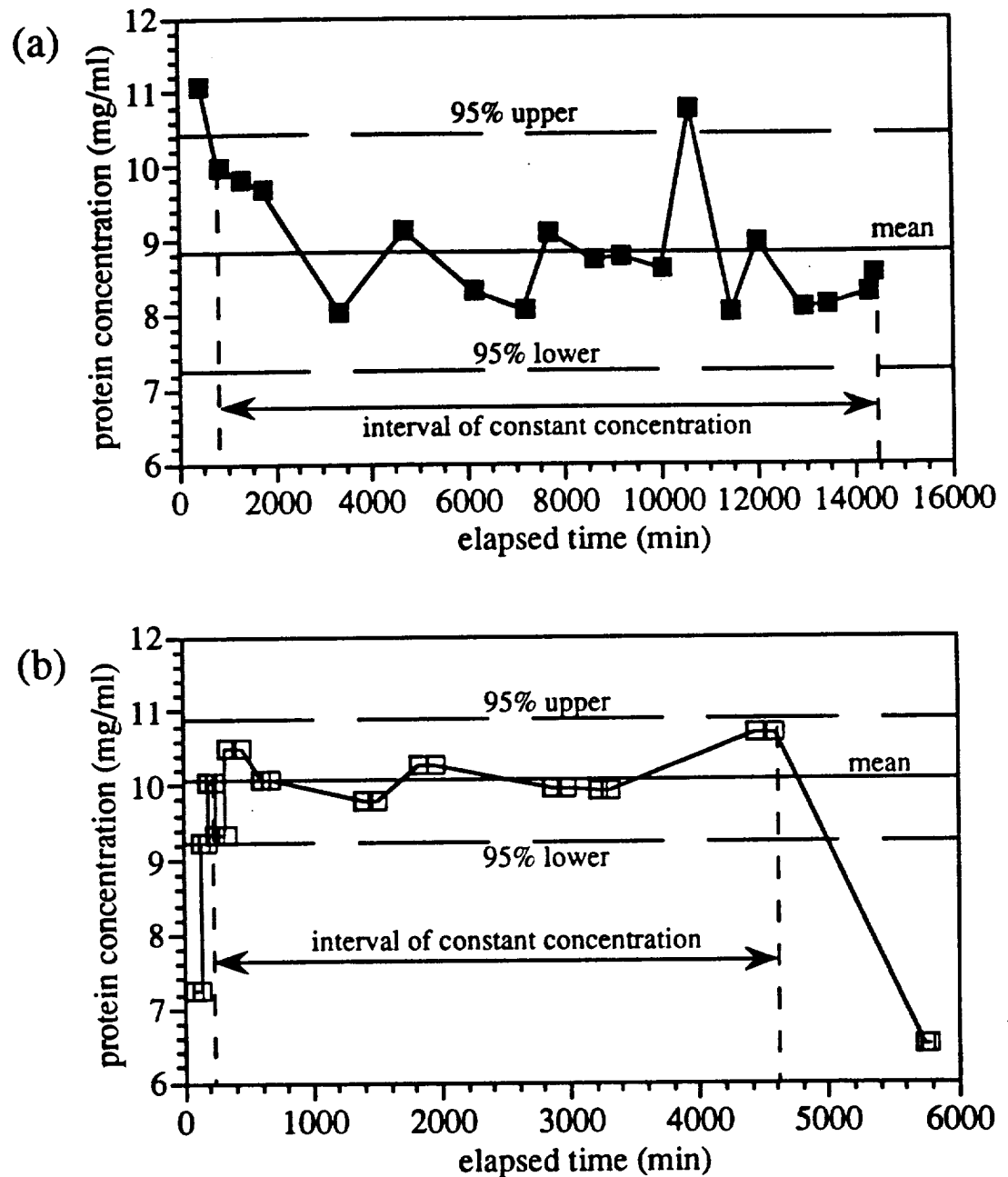
Figure 2-3: Protein concentration in growth cell effluent solution.
The interval of constant concentration is determined from a linear regression of protein concentration as a function of elapsed time. The calculated slope is not statistically different from zero at the 95% confidence level. The mean protein concentration and 95% confidence limits are marked on the figure.
(a) Quiescent experiment. (b) Flow experiment.

The initial concentration during the quiescent experiment was initially 11.07 mg/ml and decreased to 8.84 mg/ml. In contrast, the protein concentration in the effluent from the flow experiment was initially 7.24 mg/ml, climbed quickly to 10.06 mg/ml, and remained constant until the pump failed after 4600 min had elapsed. Prior to the flow experiment, the system was flushed with large amounts of deionized water, so the initial transient in effluent protein concentration may record the reintroduction of protein solution into the system. The longer, downward transient in the quiescent experiment may reflect the gradual depletion of the highly supersaturated nucleation slug and its displacement by the less supersaturated growth solution. Although the variations in protein concentration may not seem large, a strong concentration dependence is implied by empirical growth rate expressions of the form $(C - C^{sol})^n$. With values of n reported in the range 2 - 4 [2,4,5] and the large range of reported solubilities (3.5 mg/ml [6] to 6 mg/ml [10]), crystal growth rates could change drastically during the experiment. In the statistical analysis of the experiments (chapter 3), the different trends in the two experiments prevent a direct comparison of the results.

The formation of a floc-like network of filaments (Figure 2-4) was observed in both experiments. During the quiescent experiment, the filaments formed a layer along the left wall of the cell; filaments were observed in the lower middle region of the cell in the flow experiment. The presence of such strands has been reported before in experiments performed at similar protein concentrations [1].

Figure 2-4: Floc-like structure formed during protein crystal growth experiments.

2.8 Geometry of Tetragonal Lysozyme Crystals

The shape, or habit, of an ideal tetragonal crystal is a right rectangular bipyramidal prism (Figure 2-5a) in which the pyramidal caps are formed by the {101} faces (parallelograms) and the sides of the "box" are formed by the hexagonal {110} faces. In the figure, the faces have been made opaque to enhance the three-dimensional effect. The line connecting the tips of the pyramids is designated the z axis (denoted $\hat{z}$) of the crystal; lines from the centroid of the crystal normal to the hexagonal faces define the x and y axes $(\hat{x},\hat{y})$. As a result of the symmetry in the crystal habit, the selection of top and bottom is arbitrary. Similarly, the assignment of $\hat{x}$ (or $\hat{y}$) unit vector is also arbitrary. The coordinate system defined by $(\hat{x},\hat{y},\hat{z})$ is the "standard" coordinate system, which will be used for all measurements. Various dimensions are defined in Figure 2-5b, which shows the crystal in Figure 2-5a with transparent faces. The overall height, H_{xtal}, of the crystal is the distance between apices, while the face height, H_f, measures the separation between top and bottom pyramidal caps. L_{101}, the distance between parallel {101} faces, is simply related to H_{xtal} by $L_{101} = H_{xtal} \cos \beta$. The {110} dimension, L_{110}, is the distance between parallel hexagonal faces of the crystal. The angle, β, between the $\hat{z}$ axis and the normals to the {101} faces was measured to be 24° 10′ [11], which is relatively close to the theoretical

41

Figure 2-5: Ideal tetragonal crystal of hen egg white lysozyme.
(a) Sketch showing standard coordinate system. Only visible lines are shown.
(b) Definition sketch identifying key crystal dimensions and angles. Hidden lines are shown.

value of 25° 36´ calculated from unit cell dimensions reported by Palmer, Ballantyne and Galvin [12]. All calculations were performed using the theoretical value.

Some additional reference points on the crystal are required for clear analysis. Each of the 18 vertices on the crystals is labeled as shown in Figure 2-6. Vertex A is always at the top (in the standard coordinate frame), while vertex R is at the bottom. Vertices, A, B, D, N, P, and R all lie in the $\hat{x}\hat{z}$ plane, while vertices A, C, E, O, Q, and R are contained in the $\hat{y}\hat{z}$ plane. The 12 faces of the crystal, and the vertices defining them, are defined as in Table 2-1. The 28 edges formed by the intersection of the faces have five distinct slopes and are grouped accordingly (Table 2-2).

Table 2-1

Crystal face nomenclature for tetragonal lysozyme crystals.

Face	Type	Vertices	Face	Type	Vertices
1	{101}	A,B,G,C	7	{110}	D,H,L,P,M,I
2	{101}	A,C,H,D	8	{110}	E,I,M,Q,J,F
3	{101}	A,D,I,E,	9	{101}	R,N,K,O
4	{101}	A,E,F,B	10	{101}	R,O,L,P
5	{110}	B,F,J,N,K,G	11	{101}	R,P,M,Q
6	{110}	C,G,K,O,L,H	12	{101}	R,Q,J,N

The aspect ratio and orientation can give lysozyme crystals appearances which are significantly different from that of the crystal in Figure 2-5; some examples are shown in Figure 2-7. For descriptive purposes, the aspect ratio is defined to be:

$$\varepsilon_H = \frac{H_{xtal}}{L_{110}}$$ (2.1),

where the subscript H denotes it is based on H_{xtal}. The aspect ratio could also have been based on L_{101}:
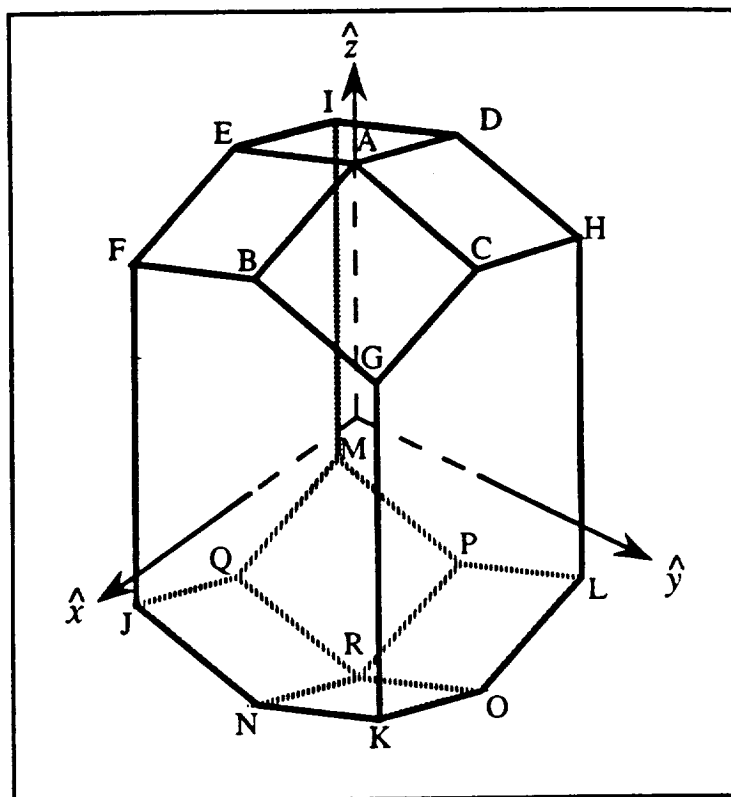
Figure 2-6: Vertex nomenclature.

Table 2-2

Edge classification for tetragonal lysozyme crystals.

Type	Edges
1	AB,CG,EF,LO,MQ,PR
2	AC,BG,DH,JN,MP,QR
3	AD,CH,EI,JQ,KO,NR
4	AE,BF,DI,KN,LP,OR
5	FJ,GK,HL,IM

44

$$\varepsilon_L = \frac{L_{101}}{L_{110}} \qquad\qquad (2.2).$$

Each definition has its advantages: ε_H conveys a better sense of the geometry of the crystal because maximum and minimum dimensions are included, while ε_L is a direct measure of the relative growth of {101} and {110} faces. The choice is a matter of personal preference since the two are related by a factor of $\cos \beta$, and they differ from each other by less than 10%. In Figure 2-7, the crystals lie at some orientation with respect to the "laboratory" coordinate frame, which is a right-handed coordinate system with the xy plane in the page (+x axis pointing to the right, +y axis pointing up) and the +z axis pointing out of the page towards the reader. The angles reported in Figure 2-7 are those describing the directions of the $\hat{x}$ and $\hat{z}$ axes of the crystals in the laboratory frame described above. The back wall of the cell, which slices through the crystal, can give crystals a decidedly odd appearance (Figure 2-8).

2.9 Interpretation of Digital Images

When the experiment became a study of crystals growing on a wall instead of a sting, the full three-dimensional reconstruction of the growing crystal was no longer possible. Some general estimate of crystal size was required since the growth rates of single faces could not be measured. An obvious choice was the projected area of the crystal as it grew: each observable growing face made a contribution to the projected area of the crystal, and some orientation-averaged growth rate could be obtained from measurements of the time rate of change of the crystal's area. This method of analysis, however, required that the orientation distribution of the quiescent crystals closely resemble that of the flow crystals, a hope which was quickly extinguished by a cursory inspection of the first twenty crystals from each experiment.

Nevertheless, if the geometry of the crystals grown during the experiments is relatively close to ideal, two-dimensional projections (images) of the crystals can be used to

45

construct a "best-fit" ideal crystal. Dimensions of the ideal crystal, in turn, provide estimates of the actual crystal size for assessing the effects of convection on crystal growth.
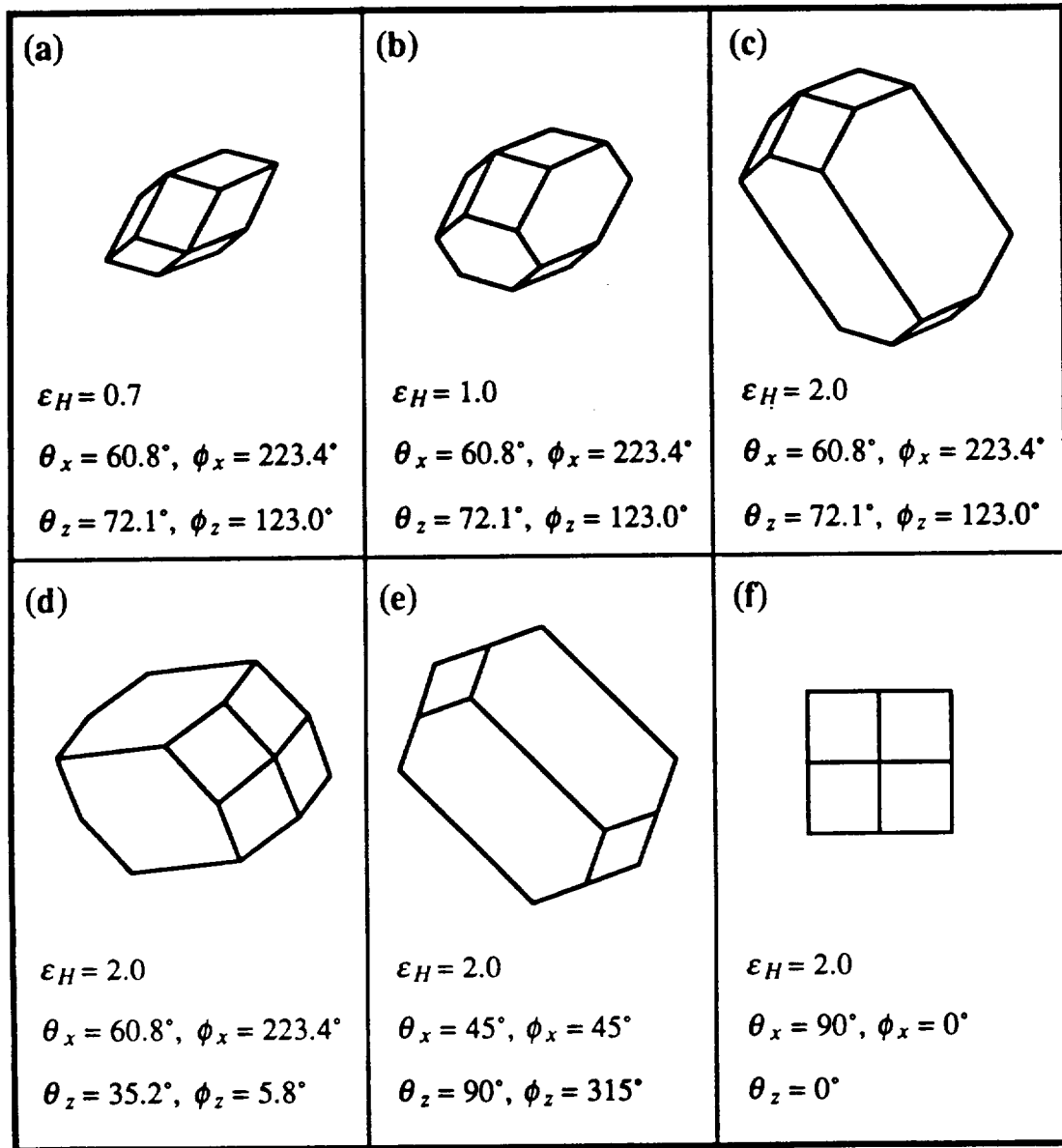
Figure 2-7: Effects of aspect ratio and orientation on crystal appearance.
    (a-c) Crystals have same orientation but aspect ratio increases from left to right.
    (c-f) Crystals are the same size but their orientations are different.

From the outset, this was recognized as an extrapolation from the data; no claim was made that the dimensions calculated from this method were correct, or even unique, only that the

46

projections of the ideal crystals were close to those of the real crystals. In previous work [2,4-6], the effect of orientation on the apparent size of crystals was either neglected entirely or reduced by selecting crystals oriented "cleanly" with respect to the optics. By explicitly accounting for differing orientations, the restrictions on suitable crystals were relaxed and the potential sample pool was increased.
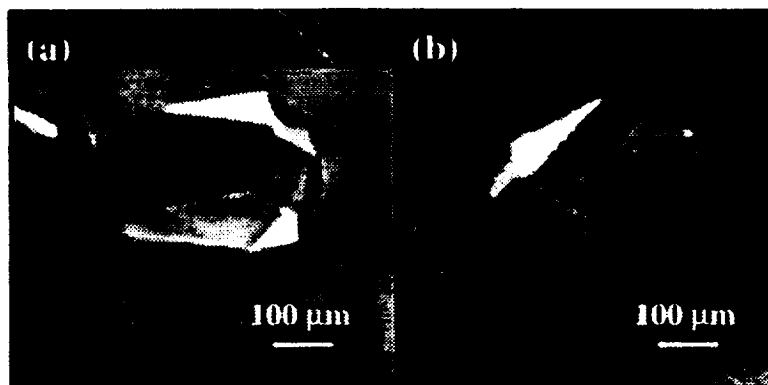
Figure 2-8: Growth of crystals on rear wall of cell.
Only one pyramidal cap is visible on these crystals. The rear wall slices through the crystals at an arbitrary angle, so the edges of the crystal in contact with the wall do not satisfy ideal geometry.

The measurement programs described here were written in Microsoft C 5.0 on the IBM PC-AT used for the experiments. The intent was to reduce the 307.2 kilobytes required for each picture (640 horixzontal pixels × 480 vertical pixels) to a list of coordinates which could be analyzed by separate programs written in FORTRAN on an IBM 3081 mainframe computer. Although tedious and sometimes confusing in practice, the measurement procedure was straightforward in theory. All pictures of a given crystal were "previewed" in order to determine whether the vertices were sufficiently recognizable that an ideal crystal could be mentally superimposed. A crystal was removed from further study if its orientation could not be estimated, it was hopelessly crowded, could not be well focused, or combinations of the above. Examples of crystals which could not be interpreted are given in Figure 2-9. Crowding by neighbors (Figure 2-10) and walls (Figure 2-11) did not always interefere with interpretation. In Figure 2-10a, what appears

47

to be the upper crystal of the contacting pair is actually an amalgam of at least two crystals; the lower crystal seems to present a {110} face, but the vertices could not be located clearly. In contrast, the crystal pair in Figure 2-10b could be easily distinguished despite their marked interpenetration. In Figure 2-10c one crystal seems to be above the second, which can be seen through the first. Figure 2-10a is from the quiescent experiment, while the crystals in Figure 2-10b-c are from the flow experiment. The presence of the side wall of the cell did not always prevent measurements of crystals, as demonstrated by crystal XF015001 (Figure 2-11).

If the crystal could be identified clearly, vertices were marked in a sequence consistent with the model crystal shown in Figure 2-6. Only visible vertices were marked; hidden vertices were omitted. Computer programs written to calculate best-fit ideal crystals required that the "upper" pyramidal cap be included in all measurements, so crystals with only one visible apex were marked as though they pointed upward. When vertices of both caps were visible, the choice of top and bottom was arbitrary.

When the visible vertices in each picture of a given crystal had been marked, the information was written to a disk file. The information included in this data file was: a character string identifying the image file from which the crystal was selected, the elapsed time from an arbitrary zero, the power of the objective used to take the picture, and the list of coordinates including a status identifier. The status identifier of vertex i, δ_i, was an integer acting as a binary switch to indicate whether the vertex was marked; $\delta_i = 1$ when the vertex was visible and 0 when the vertex was hidden. When the file was written to disk, the logical coordinate system of the digitizing board and mouse driver (origin in upper left corner, x increasing to the right, y increasing downward) was converted to the "laboratory" coordinate frame (origin in upper left, x increasing to the right, y increasing upward). Note that in the laboratory coordinate system, the crystal was digitized from directly above ($z \rightarrow \infty$). After each frame had been measured, the operator could enter relevant comments about the crystal. These comments, along with a copy of the information described above,

were written into a "log" file for later inspection. The duplication was also a safeguard against accidental loss of the data file.
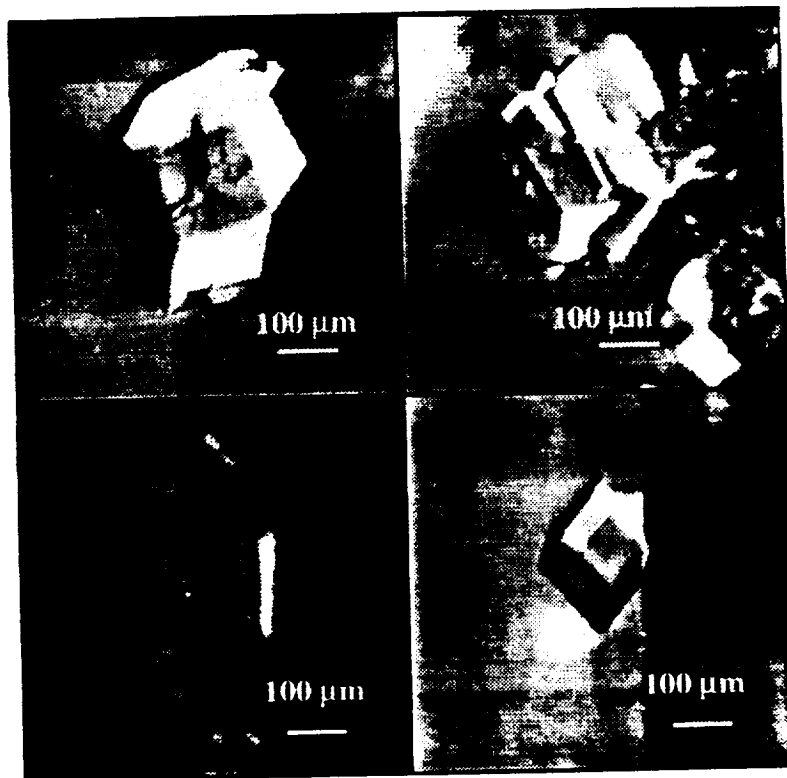
Figure 2-9: Examples of uninterpretable crystals.
Vertices corresponding to those of the ideal crystal cannot be identified on these crystals. The bias introduced by omitting uninterpretable crystals is unknown.

2.10 Determination of Crystal Orientation

The method for determining the orientation and size of lysozyme crystals is presented in this section (orientation) and section 2.11 (crystal size). The author developed the technique based on the geometry of the ideal lysozyme crystal without reference to the work of others. The approximate nature of the estimates has already been mentioned (§2.9) and limitations of the method are discussed below (§2.12). The software was tested by comparing calculated orientations and dimensions with the known values used to generate two dimensional projections of ideal crystals; calculated dimensions were usually within a few percent of the known values except when crystal orientation made "depth

perception" inaccurate. The accuracy of the estimates for real crystals can be determined only when the true dimensions of the crystal are known. Of course, if the actual dimensions were known, there would be no need for the technique.

All the necessary information to determine the orientation of an ideal crystal is contained in the angles of the edges, of which there are only five distinct types (see Table 2-2). This information can be represented by a "stencil" constructed by drawing unit vectors at the appropriate angles from a common origin. An example of such a stencil and its normalized projection onto the xy plane of the laboratory coordinate system is shown in Figure 2-12. The angles between vectors in the two-dimensional projection depend on the stencil's orientation, as can be seen by comparing Figures 2-12 and 2-13. Assigning an orientation to a given crystal in the experiment is a matter of finding the stencil orientation which most closely approximates the measured angles.

The main assumption underlying the calculations is that the images are orthographic projections of ideal crystals. Under the assumption of orthography, parallel edges of the crystal would also be parallel in the image. Normally, pictures violate this approximation only when the depth of field is large enough that perspective effects become significant. In this work, there were no gross violations of this approximation because the back wall of the cell prevented crystals from growing away from the microscope and the limited focal depth of the microscope restricted observation to those crystal which did not show obvious foreshortening. A second assumption is that the orientation of the crystal did not change during the experiment so that all measurements could be pooled to obtain a single orientation for the crystal. Since the crystals were anchored to the walls of the cell, this assumption seems reasonable.

Estimates of crystal orientation are made by the program ANGLE based on the coordinates supplied in the data file. After reading the status and coordinates of all vertices in each picture of a given crystal, ANGLE determines which of the 28 edges appear in the image by multiplying the status indicators of the two points defining the edge. If the edge

is present in the image, its type is identified, and the vector describing the edge is normalized. Thus, the angle of the edge is represented by a two-dimensional unit vector having the same slope as the measured edge. Measurements of the same type of edge are grouped by adding the point corresponding to the x and y components of the resulting unit vector to any previous measurements. A pooled estimate for the angle of a given 2-D stencil edge is obtained from the slope of the line connecting the origin of the stencil to the centroid of all measurements for that edge. Data for the crystal XF014001 are used for illustration (Figure 2-14a).
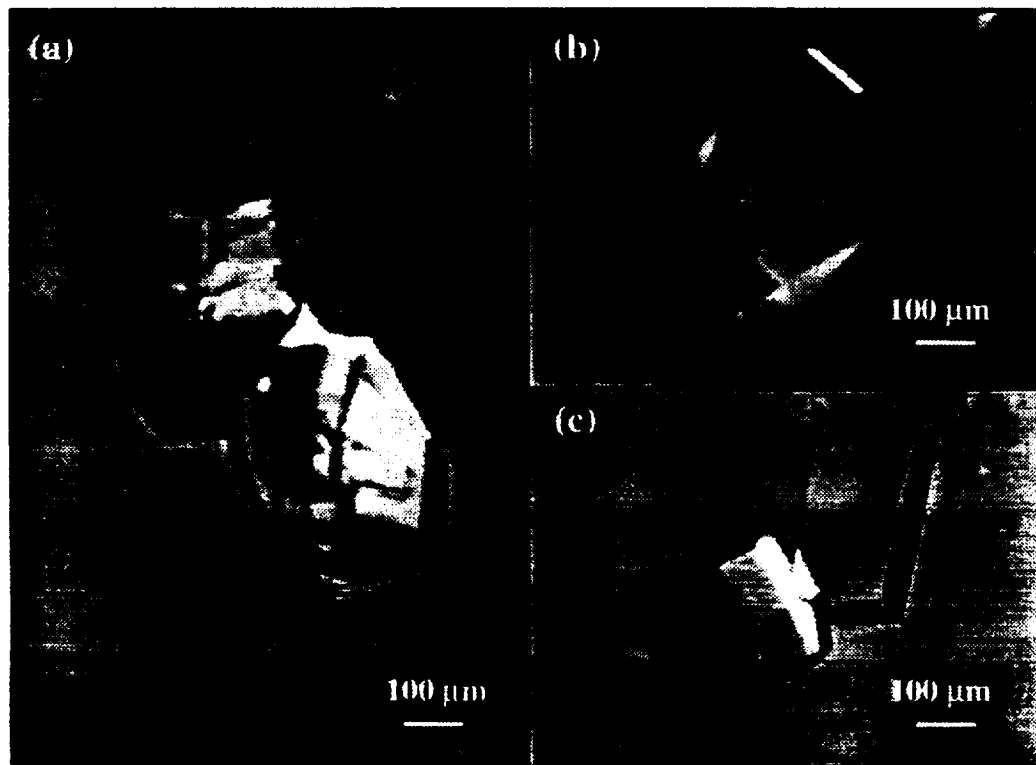
Figure 2-10: Influence of crystal contact on interpretation.
(a) The crystals in contact do not display recognizable vertices. The upper crystal of the pair is actually two crystals which had grown together earlier.
(b) These crystals, although intergrown, retain their identities and can be measured.
(c) Crystal on the right appears to be closer to the microscope than the other. Both crystals can be measured.
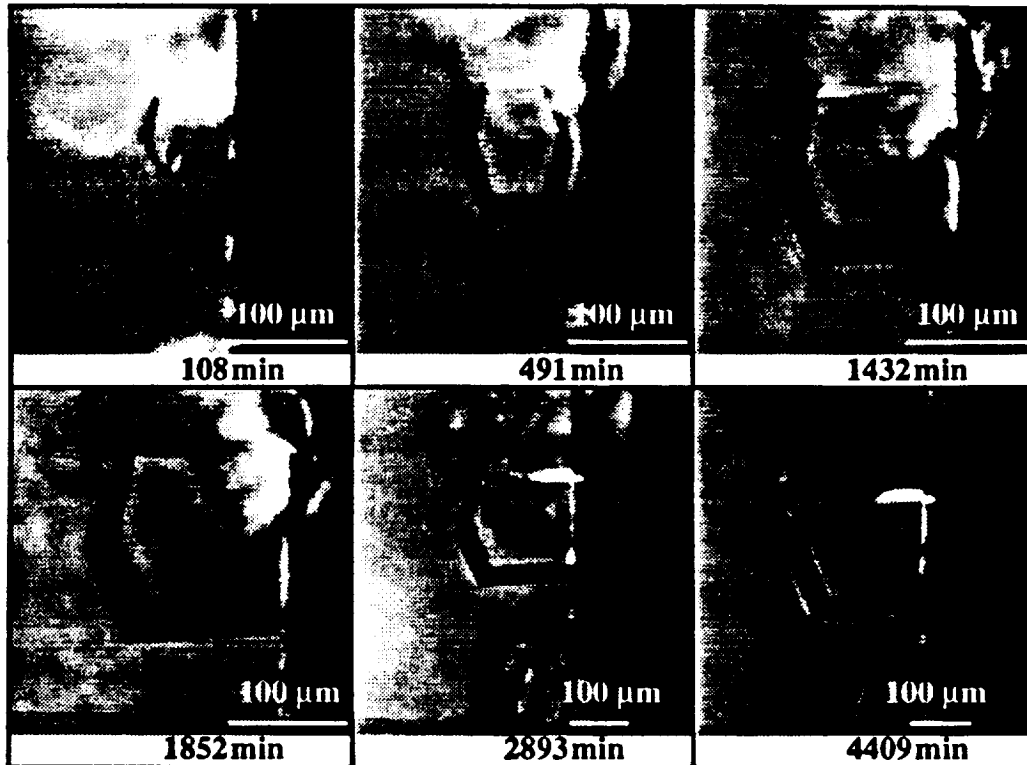
Figure 2-11: Time series for crystal XF015001.
Vertices on this crystal were easily identified, so it could be measured despite its contact with the right hand wall of the growth cell.

The centroid method for determining the average slope was chosen because it is simple and robust. The major drawback of the method is that each measurement is weighted equally, even though the relative uncertainties in measurement are larger for short lines than for long ones. Other methods for calculating average edge angles were not investigated because the accuracy of the measurments did not warrant further refinements. Assigning relative weights for each type of edge is a related issue. Equal weighting for each edge type present in the image was rejected because the relative freqency of occurrence could vary widely. The confidence limits of the "average" or characteristic angle are expected to shrink as the sample population increases. Greater weight should be attached to those edges with more measurements. An analogy with least-squares analysis of pooled experimental data [13] might suggest that the relative weight for each edge should be
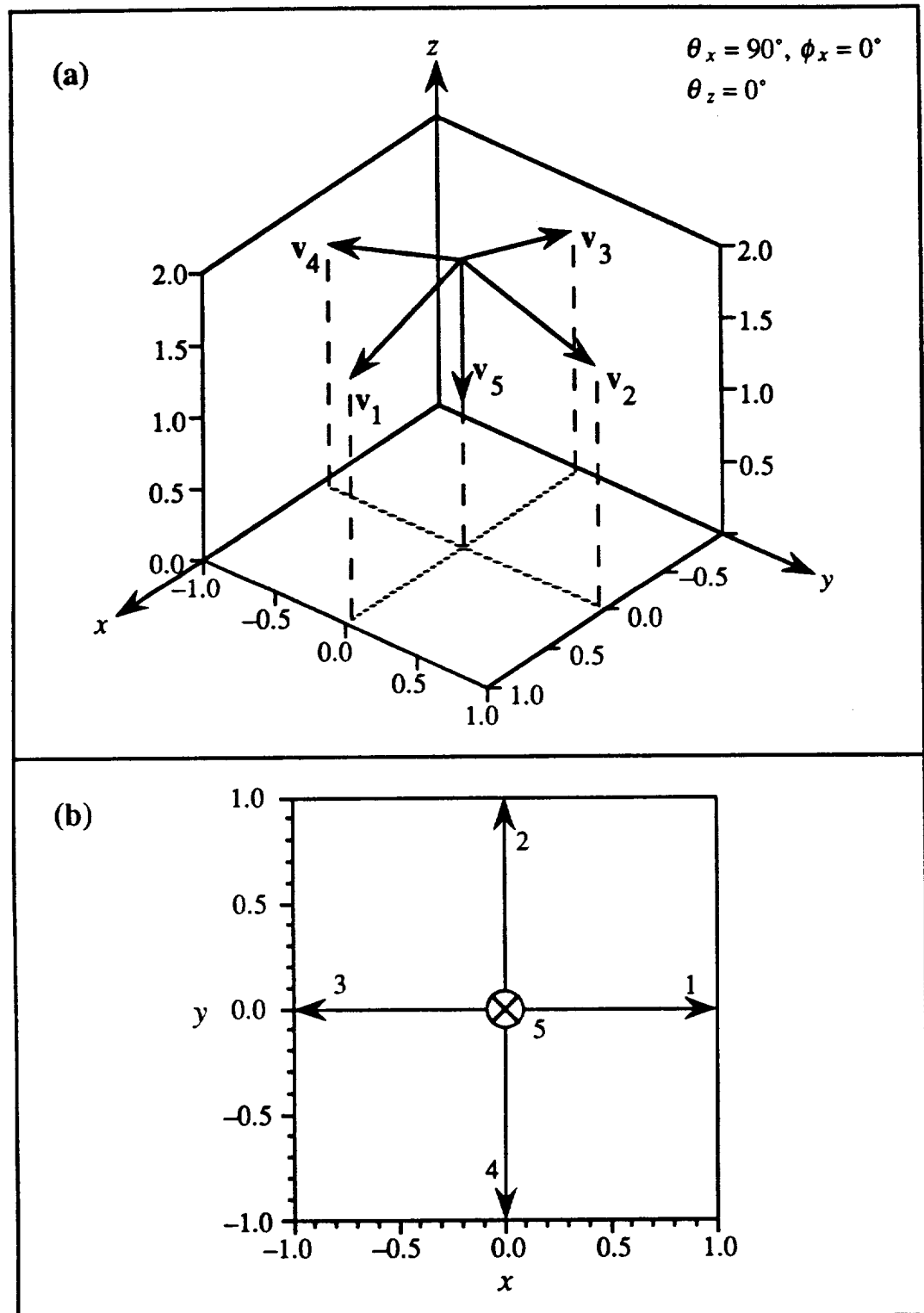
Figure 2-12: Orientation stencil when standard coordinate frame is aligned with laboratory frame.

(a) 3-D stencil. (b) Normalized 2-D projection onto *xy* plane.
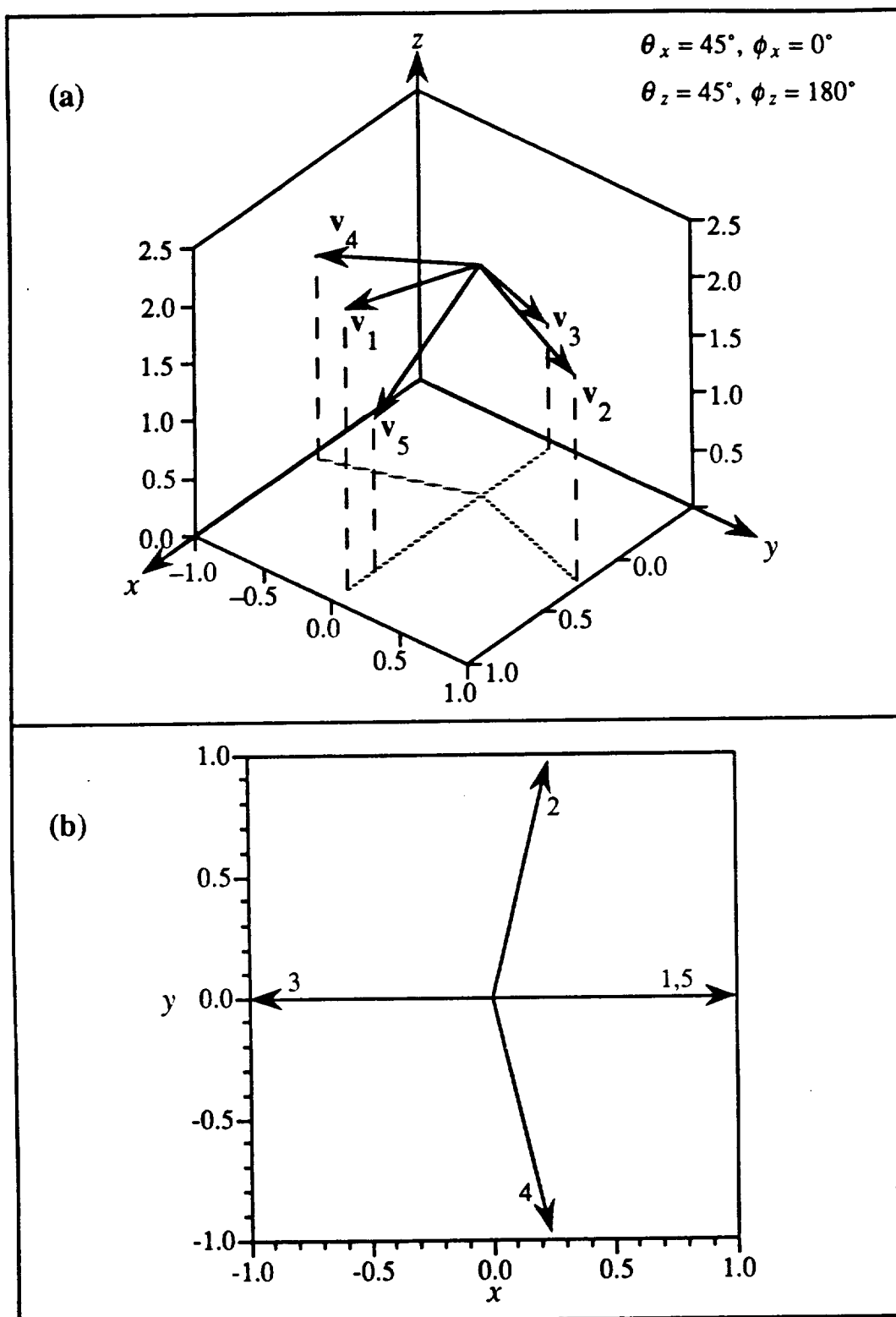
Figure 2-13: Orientation stencil when standard coordinate frame is rotated 45° about the ŷ axis through the stencil origin.
(a) 3-D stencil. (b) Normalized 2-D projection onto *xy* plane.
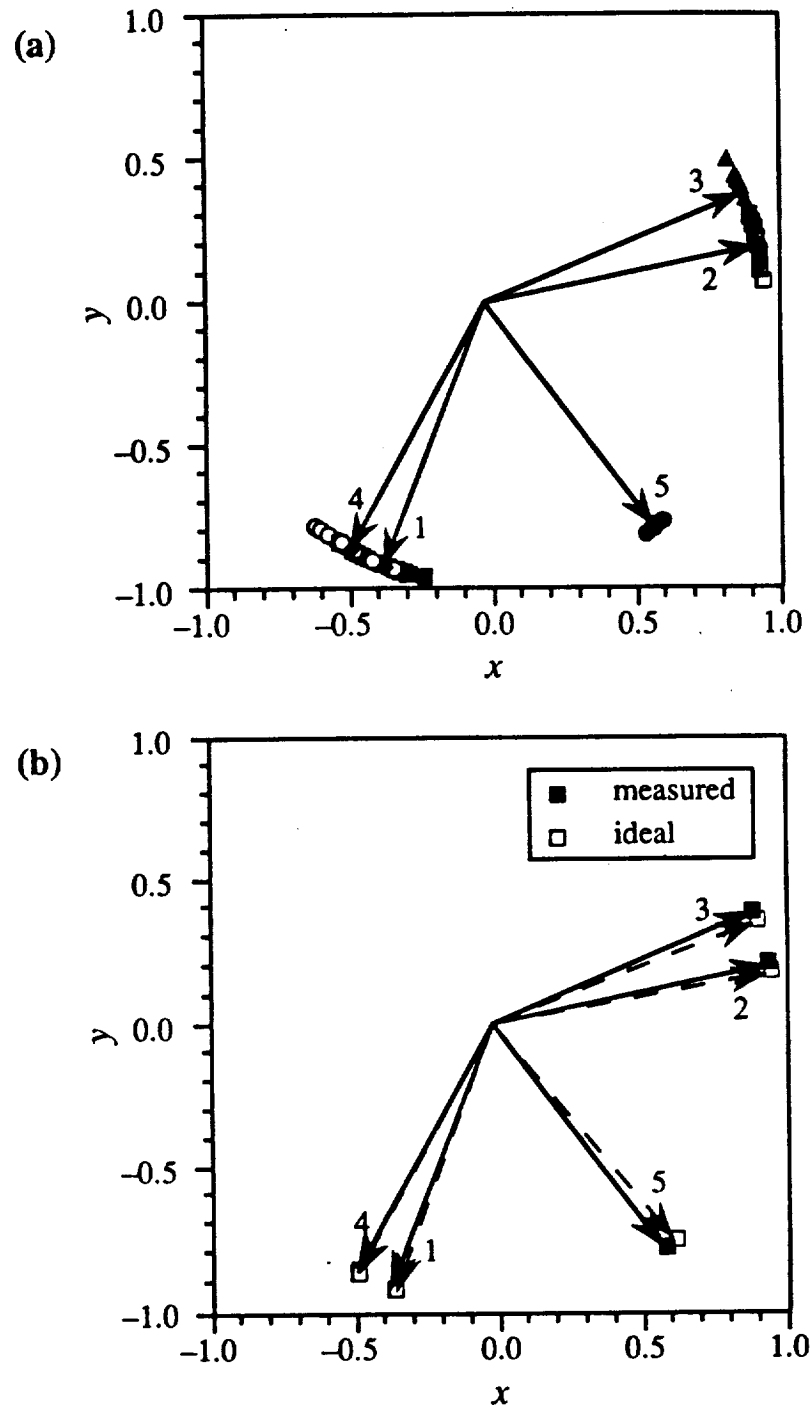
Figure 2-14: Orientation stencils for crystal XF014001.

(a) Points are measurements of edge angles. Arrows represent "average" angles determined by connecting stencil origin with centroid of measurements for each type of edge as indicated.

(b) Measured average edge angles are compared with "ideal" best-fit stencil projection. Solid lines are measured values; dashed lines are best-fits.

inversely proportional to its sample variance. When only one measurement is available for a given edge, however, the sample variance is undefined. Instead, the relative weight of edge k was taken to be the relative frequency of its measurements: $w_k = n_k/N$, where w_k = weight of edge k, n_k = number of measurements of edges of type k, and N = total number of measurements for a given crystal. This method reflects the greater confidence resulting from larger sample sizes, although not in a fashion rigorously supported by statistical reasoning. This weighting was chosen largely because it is simple and reasonable.

Two-dimensional projections of the ideal stencil, such as those in Figures 2-12 and 2-13, are compared with the measured angles to determine the orientation of the crystal. The orientation of the crystal is taken to be the same as that of the stencil which best describes all the measured angles. The selection criterion is the minimization of the objective function:

$$G_1(\theta_x,\phi_x,\theta_z,\phi_z) = \left[F(\theta_x,\phi_x,\theta_z,\phi_z) + \sum_{k=1}^{5} \delta_k\, w_k\, \gamma_k^2 \right] \qquad (2.3),$$

where

$$\delta_k = \begin{cases} 1, \text{ if at least one edge of type k is present} \\ 0, \text{ otherwise} \end{cases} \qquad (2.4),$$

w_k is the relative weighting of edge k, γ_k is the angle between the measured and ideal projections of edge k, and $F(\theta_x,\phi_x,\theta_z,\phi_z)$ is an empirical "avoidance" function to prevent orientations in which the normals to {101} faces lie in the xy plane of the laboratory coordinate system.

In certain cases tested during the development of the analysis programs, the calculated dimensions of the crystal were extremely sensitive to the orientation of the {101} faces. When the planes of the {101} faces were nearly orthogonal to the xy plane, slight variations in orientation could produce a tenfold change in calculated size. The avoidance function was introduced during this stage in the development in order to reduce the erratic behavior of the calculated crystal dimensions. The avoidance function is

56

$$F(\theta_x, \phi_x, \theta_z, \phi_z) = \sum_{j=1}^{4} exp\left(-5000\ n_{j,z}^2\right) \qquad (2.5),$$

where $n_{j,z}$ = z component of the normal to face j. The function has a steep decay, falling to 1% of its maximum when the angle between the normal and the plane is ± 0.03 radian (1.7°). A difference of 2° is small when compared with the estimated accuracy of the measurements, but makes a large difference in providing consistent size results for L_{101}. Subsequent changes in the methods of computing crystal sizes diminished the need for an avoidance function, but its presence in Equation (2.3) acts as insurance against a poorly selected dta set. In this work, the effect of F is negligible in most cases, since orientations with small angles between the {101} normals and the xy plane were rare. Typical values of G_1 are less than 0.05 for almost all crystals, with many crystals giving values of $G_1 <$ 10^{-4}. In a few cases, the assigned orientation is relatively close to forbidden; the maximum value of G_1 is approximately 0.05, which would indicate a {101} normal within 0.02 radian (1.4°) of the xy plane.

The search for a suitable orientation begins by aligning the standard coordinate frame $(\hat{x}, \hat{y}, \hat{z})$ with the laboratory frame (x,y,z) and placing the ideal 3-D stencil at the origin of the laboratory frame. An initial value of G_1 is calculated for this starting orientation. The ideal stencil is "rocked" 0.1 radian (approximately 5.7°) about the laboratory y axis in each direction and G_1 is evaluated for both potential orientations. In what is basically the method of random descent, a new orientation is accepted only if it produces a new minimum value of G_1. The stencil is then rocked about the laboratory x axis, G_1 is calculated for both possible orientations, and a decision is made to accept or reject the new orientations. The process is repeated for rotation about the z axis, to complete the sequence. Rotations about each of the axes in the laboratory frame are repeated cyclically until a local minimum is reached. This coarse position is used as a starting point for a finer search (step size 0.05 radian), which in turn sets up a final search using a step size of 0.01 radian. The global minimum is found by repeating the entire

procedure starting from all initial orientations in which vector 5 is aligned with each coordinate axis. The best-fit stencil is compared with the measured angles for crystal XF014001 in Figure 2-14b

2.11 Calculation of Ideal Crystal Dimensions

The method used to determine the dimensions of ideal crystals, unsurprisingly, depends heavily on knowledge of the crystal geometry and the estimated orientation discussed above. As long as the five unit vectors ($v_1 - v_5$) are related to their standard stencil counterparts ($\hat{v}_1 - \hat{v}_5$) through a simple rotation about the stencil origin, the coordinates of each vertex of the ideal crystal in any coordinate system can be written in terms of the vector from the origin to vertex A (denoted p_1), the appropriately rotated stencil unit vectors, and crystal dimensions (Table 2-3). Note that use has been made of the relation $H_{xtal} = H_f + 2\alpha L_{110}$, where $\alpha = 2(\hat{z}_A - \hat{z}_B)/L_{110} = 2(\hat{z}_1 - \hat{z}_2)/L_{110}$ reflects the pitch of the {101} faces in the pyramidal caps. Henceforth, vertices will be designated by the numbers given in Table 2-3 instead of by letters. Although inspection of the equivalent vectors in Table 2-3 shows that a full description of the location and shape of an ideal crystal is contained in only five variables (the three components of p_1, L_{110}, and H_f), only four of these variables can be used to fit the projected image: x_1, y_1, L_{110}, and H_f. These variables are defined to be, respectively, the four unknowns of interest, $s_1 - s_4$. When the following notation is introduced:

$$P_{x, i, j} = \frac{\partial x_i}{\partial s_j} \quad , \quad P_{y, i, j} = \frac{\partial y_i}{\partial s_j} \tag{2.6},$$

the coordinates (x_i, y_i) of vertex i can be written in terms of s_j as:

$$x_i = \sum_{j=1}^{4} P_{x, i, j} s_j \quad , \quad y_i = \sum_{j=1}^{4} P_{y, i, j} s_j \tag{2.7}.$$

Table 2-3

Position of vertices in arbitrary coordinate system.

Vertex	Number	Equivalent vector
A	1	$\mathbf{p}_1$
B	2	$\mathbf{p}_2 = \mathbf{p}_1 + \frac{1}{2}\mathbf{v}_1 L_{110}$
C	3	$\mathbf{p}_3 = \mathbf{p}_1 + \frac{1}{2}\mathbf{v}_2 L_{110}$
D	4	$\mathbf{p}_4 = \mathbf{p}_1 + \frac{1}{2}\mathbf{v}_3 L_{110}$
E	5	$\mathbf{p}_5 = \mathbf{p}_1 + \frac{1}{2}\mathbf{v}_4 L_{110}$
F	6	$\mathbf{p}_6 = \mathbf{p}_1 + \frac{1}{2}(\mathbf{v}_1 + \mathbf{v}_4) L_{110}$
G	7	$\mathbf{p}_7 = \mathbf{p}_1 + \frac{1}{2}(\mathbf{v}_1 + \mathbf{v}_2) L_{110}$
H	8	$\mathbf{p}_8 = \mathbf{p}_1 + \frac{1}{2}(\mathbf{v}_2 + \mathbf{v}_3) L_{110}$
I	9	$\mathbf{p}_9 = \mathbf{p}_1 + \frac{1}{2}(\mathbf{v}_3 + \mathbf{v}_4) L_{110}$
J	10	$\mathbf{p}_{10} = \mathbf{p}_1 + \frac{1}{2}(\mathbf{v}_1 + \mathbf{v}_4) L_{110} + \mathbf{v}_5 H_f$
K	11	$\mathbf{p}_{11} = \mathbf{p}_1 + \frac{1}{2}(\mathbf{v}_1 + \mathbf{v}_2) L_{110} + \mathbf{v}_5 H_f$
L	12	$\mathbf{p}_{12} = \mathbf{p}_1 + \frac{1}{2}(\mathbf{v}_2 + \mathbf{v}_3) L_{110} + \mathbf{v}_5 H_f$
M	13	$\mathbf{p}_{13} = \mathbf{p}_1 + \frac{1}{2}(\mathbf{v}_3 + \mathbf{v}_4) L_{110} + \mathbf{v}_5 H_f$
N	14	$\mathbf{p}_{14} = \mathbf{p}_1 + \frac{1}{2}(\mathbf{v}_1 + \alpha\,\mathbf{v}_5) L_{110} + \mathbf{v}_5 H_f$
O	15	$\mathbf{p}_{15} = \mathbf{p}_1 + \frac{1}{2}(\mathbf{v}_2 + \alpha\,\mathbf{v}_5) L_{110} + \mathbf{v}_5 H_f$
P	16	$\mathbf{p}_{16} = \mathbf{p}_1 + \frac{1}{2}(\mathbf{v}_3 + \alpha\,\mathbf{v}_5) L_{110} + \mathbf{v}_5 H_f$
Q	17	$\mathbf{p}_{17} = \mathbf{p}_1 + \frac{1}{2}(\mathbf{v}_4 + \alpha\,\mathbf{v}_5) L_{110} + \mathbf{v}_5 H_f$
R	18	$\mathbf{p}_{18} = \mathbf{p}_1 + 2\,\alpha\,\mathbf{v}_5 L_{110} + \mathbf{v}_5 H_f$

Once an orientation has been assigned to the crystal and the stencil unit vectors have been rotated accordingly, an ideal crystal is superimposed on the image so that its vertices are as close as possible to the measured vertices. Vertices are placed in order to minimize the objective function:

$$G_2 = \sum_{i=1}^{18} \delta_i \left[(\tilde{x}_i - x_i)^2 + (\tilde{y}_i - y_i)^2 \right] \qquad (2.8),$$

where $(\tilde{x}_i, \tilde{y}_i)$ denotes the measured coordinates of vertex i, while the coordinates of the corresponding ideal analogue are (x_i, y_i). The presence of vertex i in the measured data set is indicated by the value of δ_i:

$$\delta_i = \begin{cases} 1, \text{ if vertex } i \text{ is present} \\ 0, \text{ otherwise} \end{cases} \qquad (2.9).$$

A direct substitution of Equations (2.7) into Equation (2.8) casts the objective function into a form which is amenable to a linear least-squares minimization:

$$G_2 = \sum_{i=1}^{18} \delta_i \left[\left(\tilde{x}_i - \sum_{j=1}^{4} P_{i,1,j} \, s_j \right)^2 + \left(\tilde{y}_i - \sum_{j=1}^{4} P_{i,2,j} \, s_j \right)^2 \right] \qquad (2.10).$$

The four normal equations arising from partial differentiation with respect to each of the s_j can be solved in matrix form:

$$\mathbf{A} \, \mathbf{S} = \mathbf{B} \qquad (2.11),$$

where

$$A_{j,k} = \sum_{i=1}^{18} \delta_i \left(P_{i,1,j} \, P_{i,1,k} + P_{i,2,j} \, P_{i,2,k} \right) \qquad (2.12)$$

and

$$B_j = \sum_{i=1}^{18} \delta_i \left(\tilde{x}_i \, P_{i,1,j} + \tilde{y}_i \, P_{i,2,j} \right) \qquad (2.13).$$

In the event that the data set lacks sufficient information to determine H_f, it is simply omitted. **A** is then a 3×3 matrix, while **S** and **B** become 3×1 column vectors.

60

When Equation (2.11) has been solved for S by the FORTRAN program IDEAL3D, the coordinates of all the vertices of the ideal crystal can be calculated (provided that all four s_j could be determined). Again, the example of crystal XF014001 is used to compare the raw images with the ideal analogues (Figure 2-15). L_{101} and L_{110} for XF014001 are plotted against elapsed time in Figure 2-16. The time series of crystals XQ005002 and XQ023001 are shown in Figures 2-17 and 2-18; orientation measurements and calculations are compared in Figure 2-19, while the calculated dimensions are shown in Figure 2-20. L_{101} was not calculated for either of these crystals because no points in the lower pyramidal cap had been measured. The entire process is summarized for crystals XQ002001 and XQ002002 in Figure 2-21, where the raw image, vertex markings, and best-fit ideal crystal are displayed in successive panels.

2.12 Limitations of the Ideal Crystal Approximation

There are two levels of approximation in the analysis: (i) marking the vertices in a manner consistent with ideal geometry, and (ii) the calculation of the dimensions of the ideal analogue. The effect of each is shown Figure 2-22, where the raw images, vertex markings, and ideal crystals are compared for four different crystals. Symmetry constraints of the ideal crystal result in a slight displacement of the best-fit vertices from the marked vertices, although this displacement is small in most cases. The situation shown in the bottom row of Figure 2-22 (crystal XQ023001) is common: the {101} face in the lower left is significantly smaller than the others, reflecting a faster growth rate. Compared with the ideal crystal, crystal XQ023001 has an extra vertex which cannot be interpreted in the current scheme. In most cases like this, the apex of the pyramid was marked along the edge connecting the two vertices so that the calculated value of L_{110} characterized the overall dimensions of the crystal reasonably well. In this particular case, the vertices at the corners of the small {101} face were not marked because the angles of the resulting

61
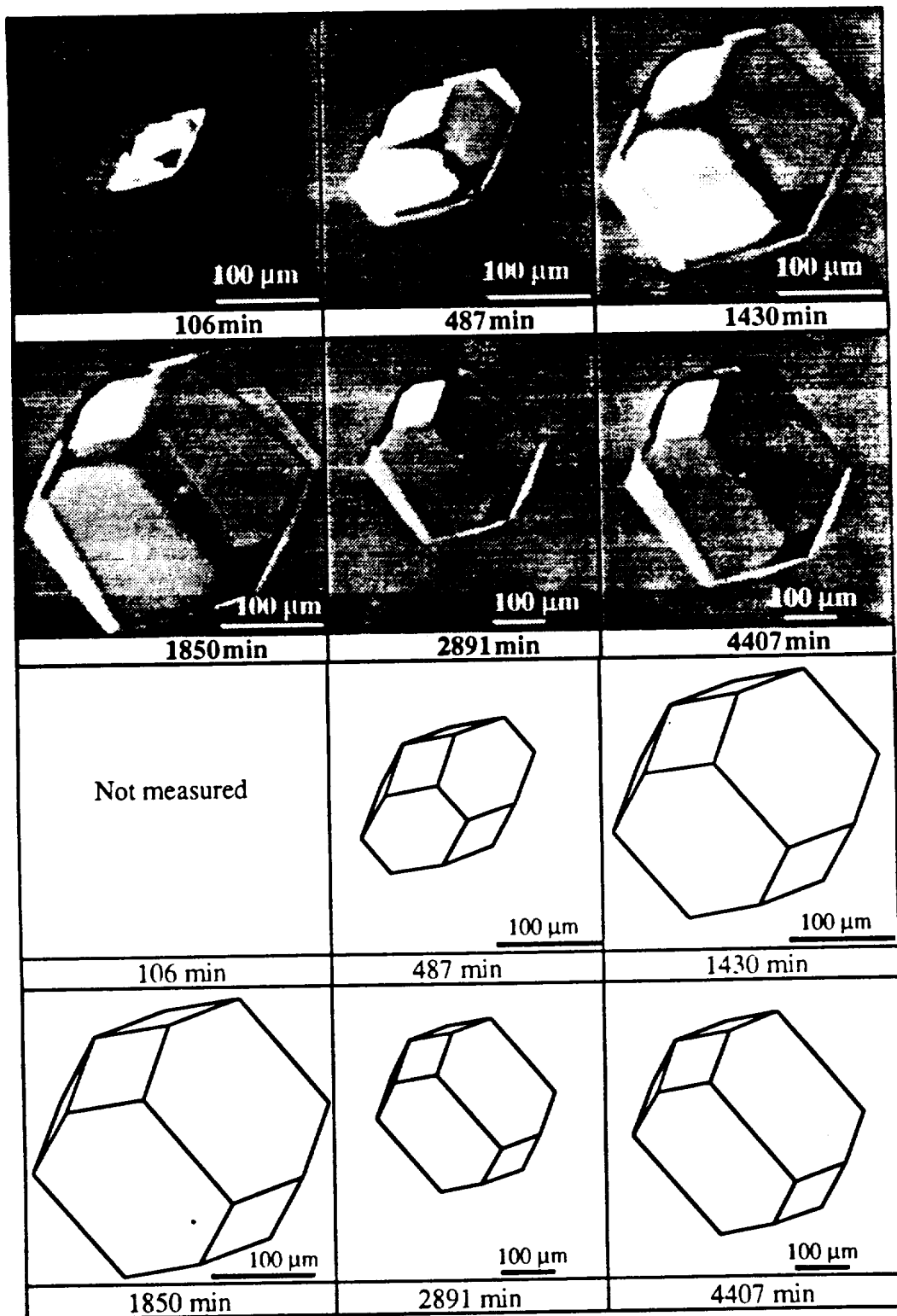
Figure 2-15: Comparison of crystal XF014001 and ideal analogue.
(upper half) Digitized images of crystal XF014001 taken during experiment.
(lower half) Ideal analogues calculated to same scale as actual images.
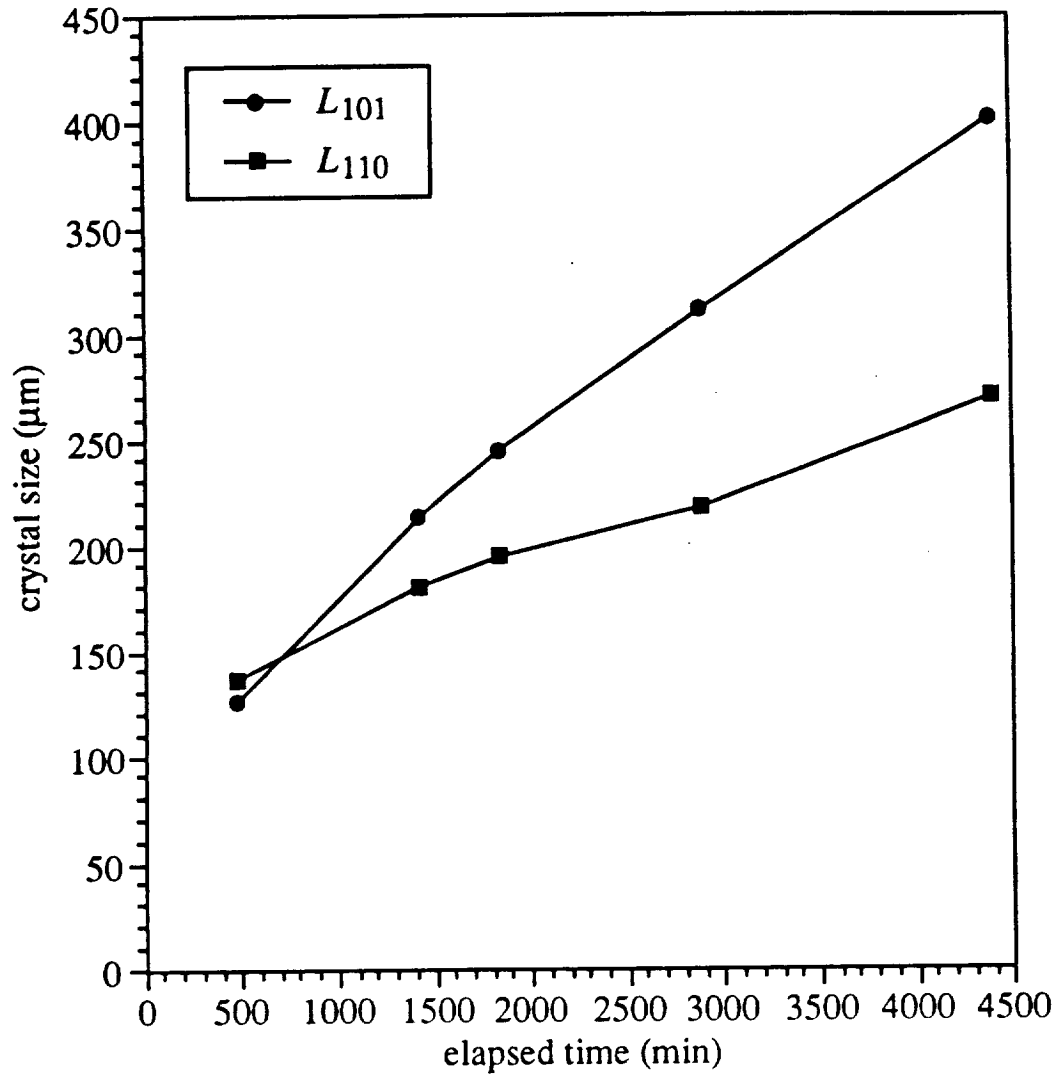
Figure 2-16: Calculated dimensions of crystal XF014001.

edges might introduce a large error in the calculated fits. In Figure 2-23, the effect of approximation (ii) is isolated; the asymmetry is caused primarily by unequal {110} growth rates. Clearly, image analysis requires some judgment on the part of the researcher.

A crystal's appearance can change as a result of asymmetric growth of equivalent faces. The time series for crystal XQ033002 demonstrates the apparent disappearance of {101} faces over the course of the experiment (Figure 2-24). The requirement that all
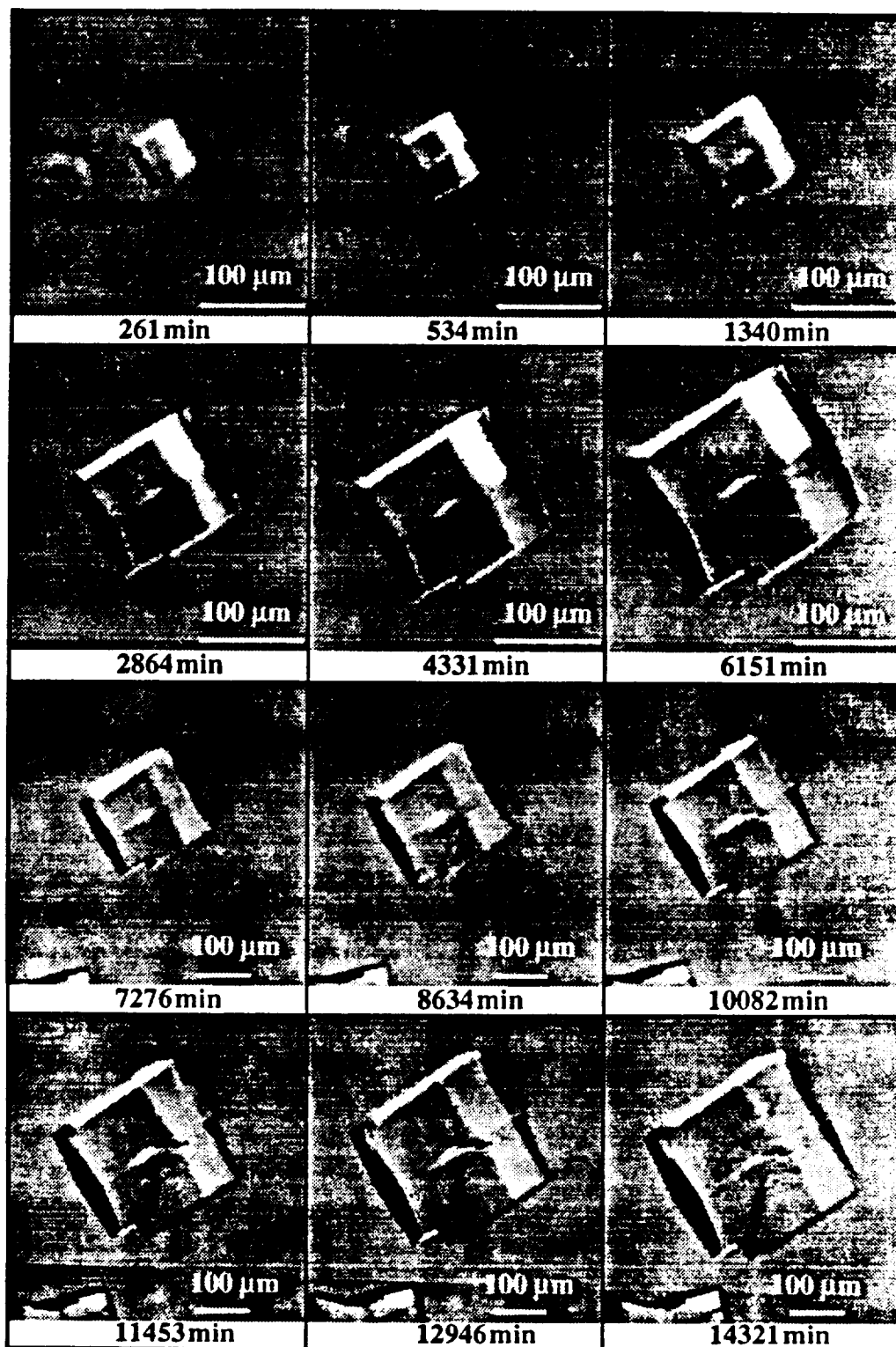
Figure 2-17: Time series for crystal XQ005002.
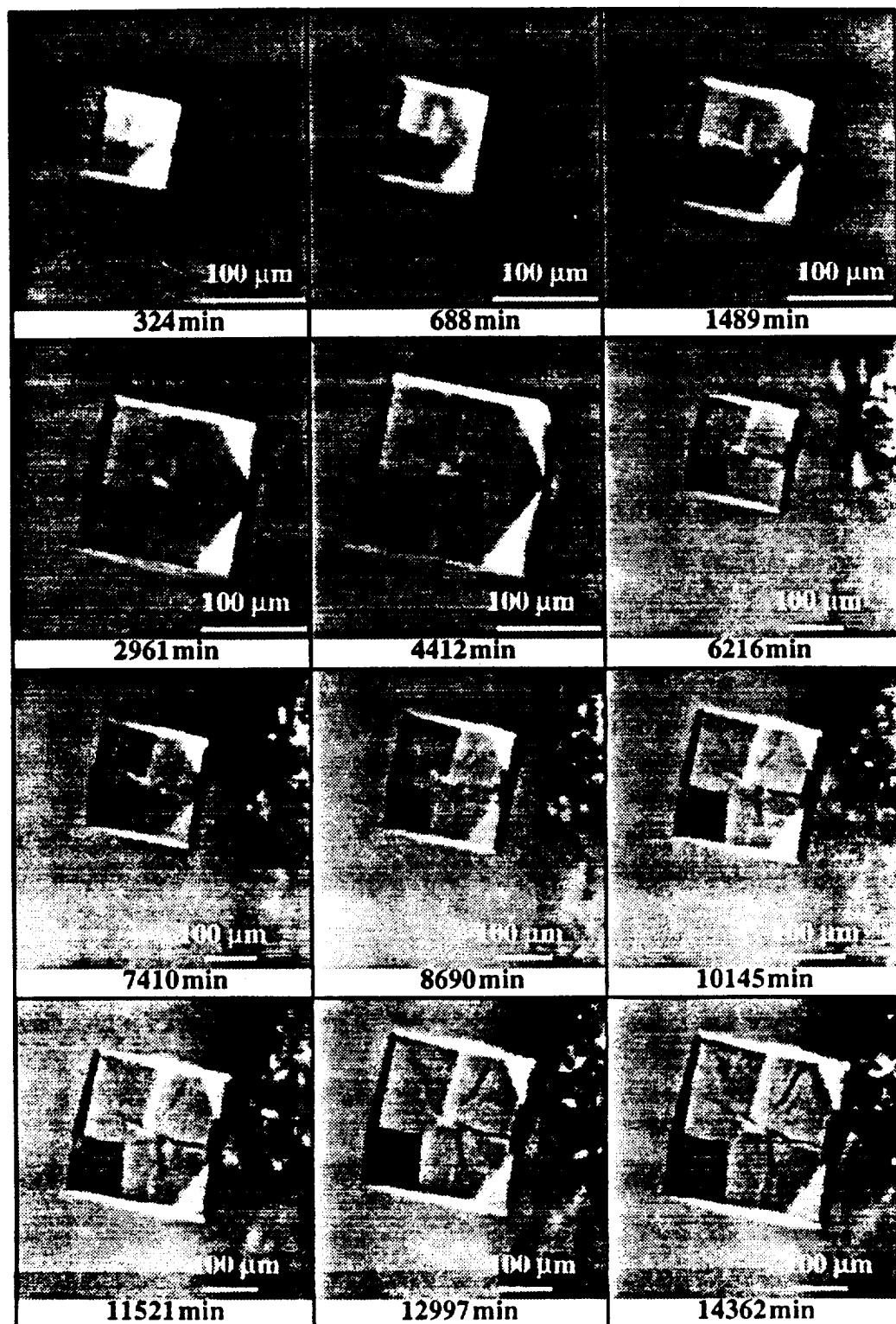
Figure 2-18: Time series for crystal XQ023001.
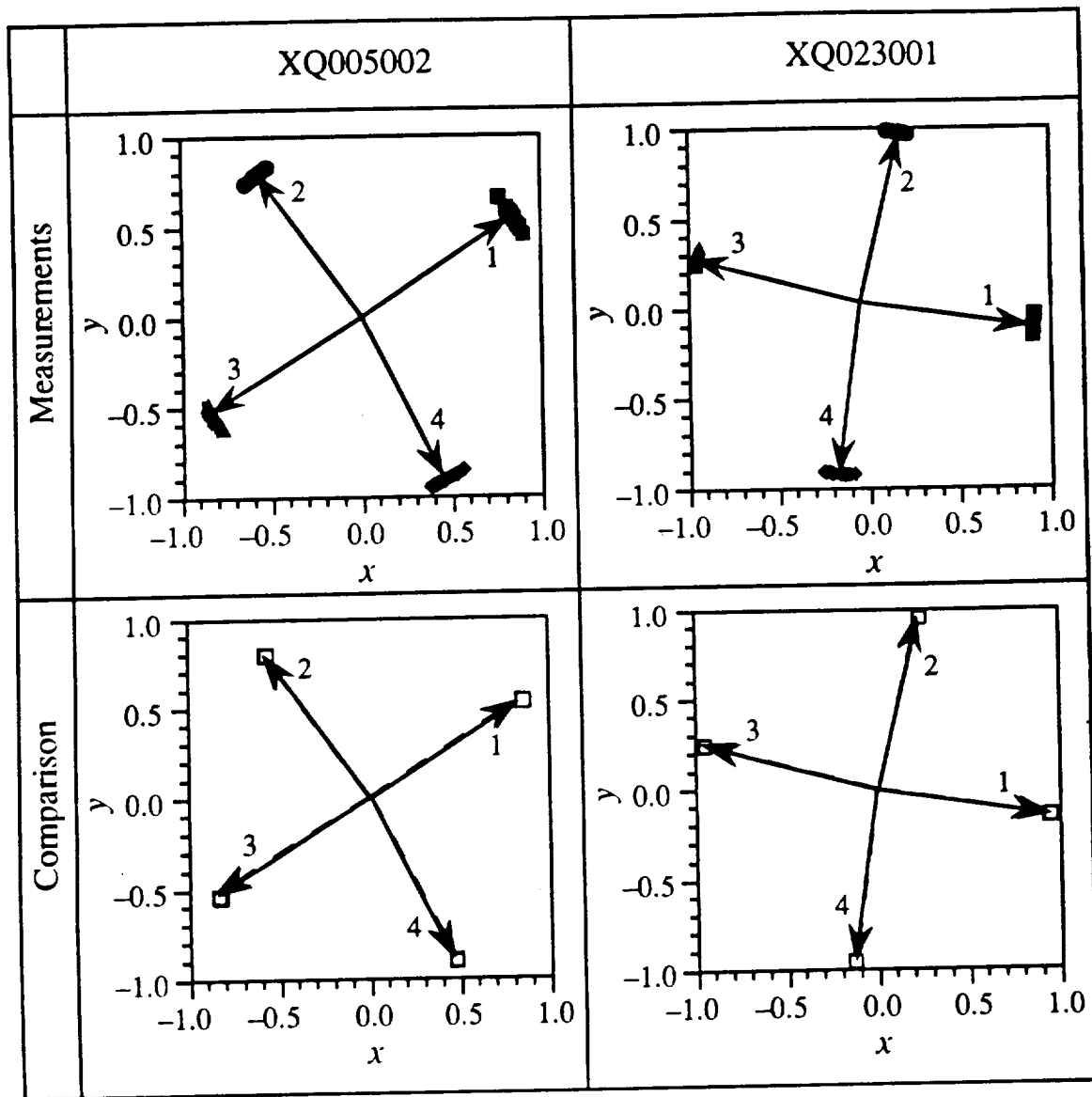
Figure 2-19: Comparison of measured and ideal edge angles for crystals
XQ005002 and XQ023001.
(top row) Arrows are drawn from stencil origin to centroid for each edge.
(bottom row) Measured stencil points (■) and ideal stencil (□) are
coincident.

pictures be marked consistently sometimes produces questionable vertex placements, as

illustrated by comparing the measurements and calculations of XQ033002 at two diferent

times (Figure 2-25). Two interpretations, differing in the angle between the hexagonal face

and the xy plane, are possible. Early pictures favor a steeper pitch, while later images

suggest the {110} face is almost parallel to the back wall of the cell. Without a full stereo view, it is extremely difficult to determine which is correct.
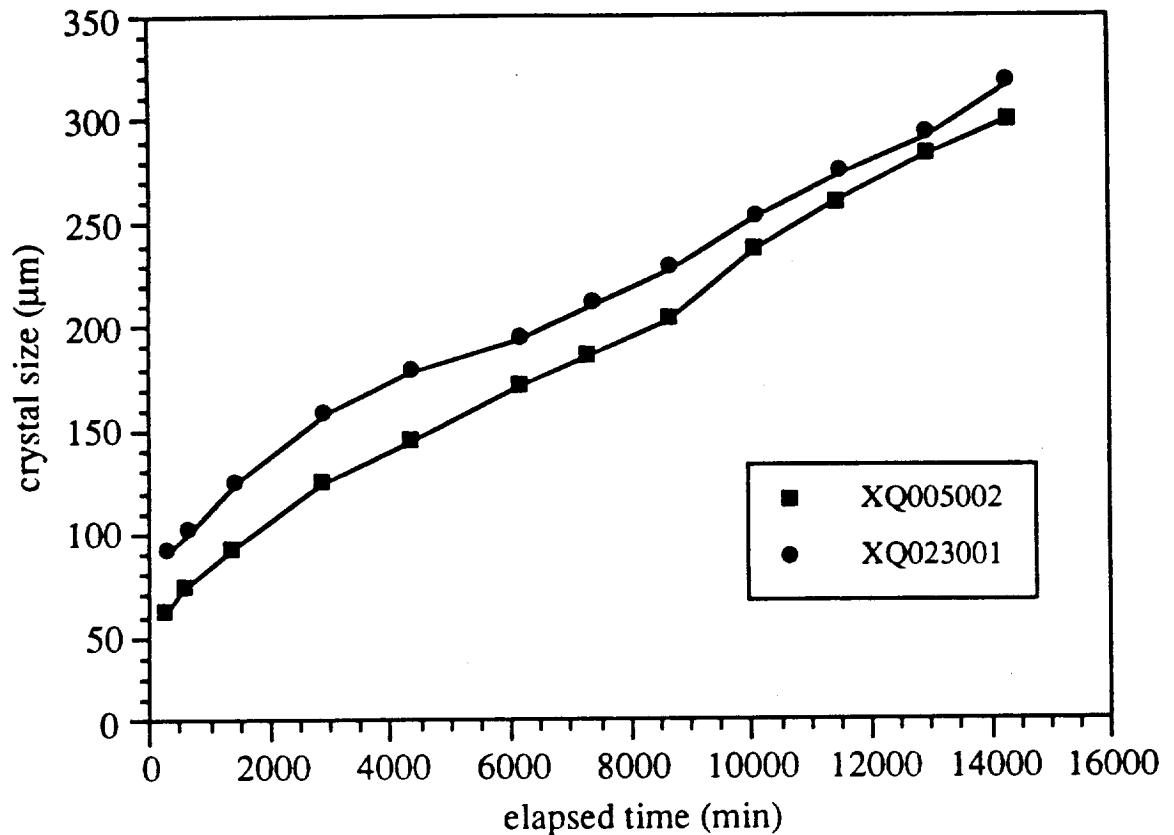
Figure 2-20: Calculated {110} dimensions for crystals XQ005002 and XQ023001.

It is reassuring that inaccurate measurements produce inaccurate results which are easy to detect. This point is made emphatically in Figure 2-26, which compares measurements of XQ033001 at two different times. Crystals XQ033001 and XQ033002 were selected for inspection because their calculated growth rates seemed to be inconsistent from one interval to the next. In some cases, measurements of L_{101} indicated shrinkage, a phenomenon not expected in a supersaturated solution; no calculated shrinkage of L_{110} was found. Some of the uncertainty arises from "depth perception" problems discussed briefly in section 2.10 in conjunction with the empirical avoidance function
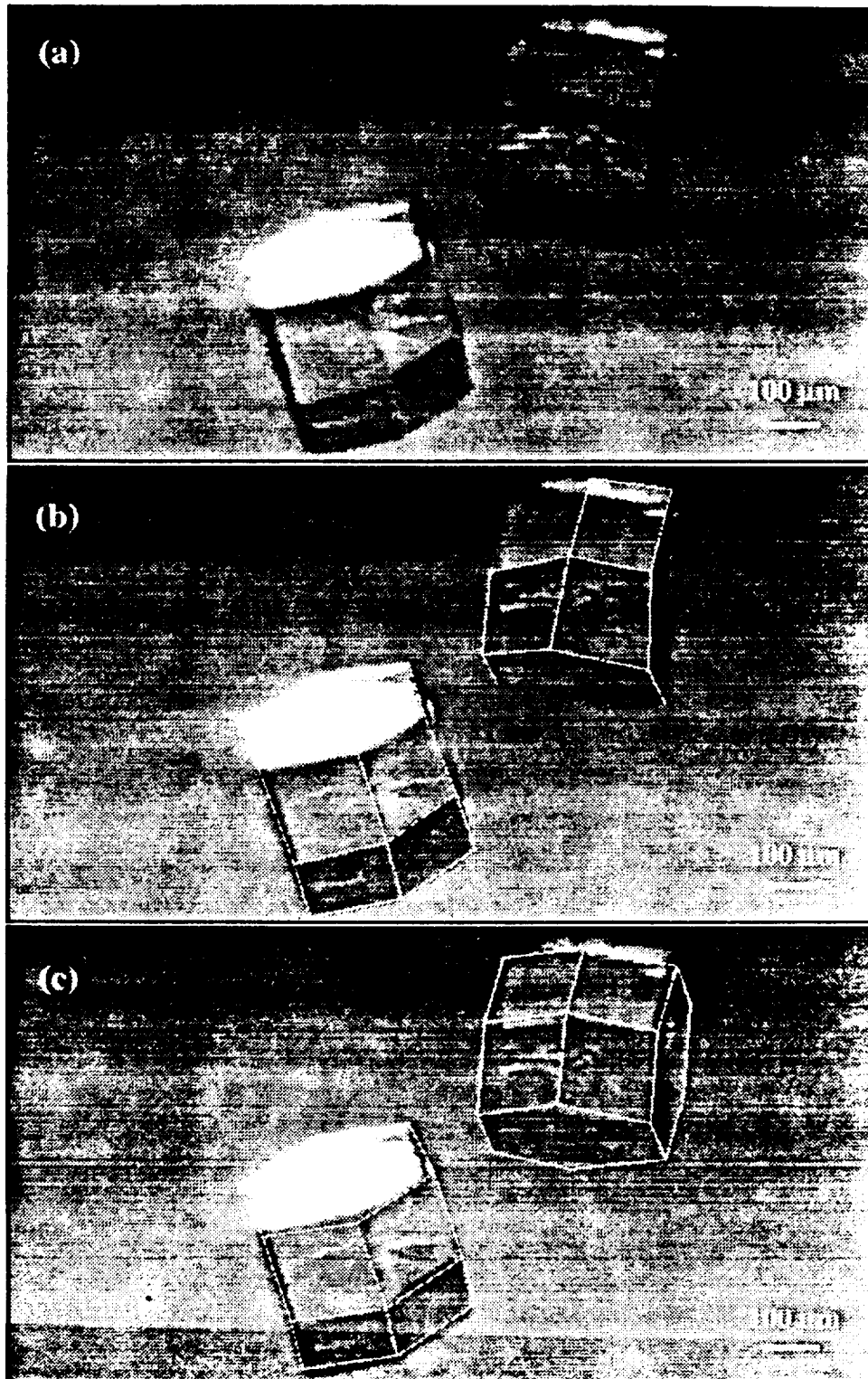
Figure 2-21: Summary of measurement steps for crystals XQ002001 and XQ002002.

(a) As digitzed. (b) As marked. (c) Ideal best-fit analogue.

Figure 2-22: Summary of measurement steps for four different crystals.
(top row) XF014001. (second row) XF050001.
(third row) XQ005002. (bottom row) XQ023001.
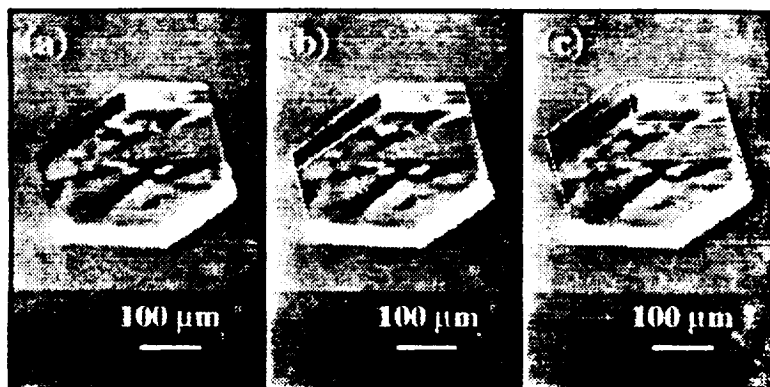
Figure 2-23: Ideal analogue of an asymmetric crystal.
The {110} face on the left grew faster than the one on the right, producing the asymmetric morphology shown.
(a) As digitized. (b) As marked. (c) Ideal best-fit analogue.

[Equation (2.5)]. Note, however, that the calculated L_{110} is relatively close to the apparent size of the crystal in Figures 2-25 and 2-26. The robustness of L_{110} permitted the use of all measurements in the statistical analyses of chapter 3; L_{101} was not included because there were fewer measurements (particularly of quiescent crystals) and they were less reliable.

2.13 Additional Observations

There is a great range in appearance of lysozyme crystals. Some, like those shown in Figures 2-11, 2-15, 2-17 and 2-18, are easy to interpret. Others, like XQ033002 (Figure 2-24) seem to change their appearance and have no clear interpretation. Quiescent crystals seem to have more internal defects than crystals subjected to convection. In Figure 2-22, for instance, compare the flow crystals in the top two rows with the quiescent crystals in the bottom two rows. These are not isolated instances; most crystals from the flow experiment are easier to interpret and measure than comparable quiescent crystals. On the whole, quiescent crystals exhibit more incomplete layers and missing corners than do flow crystals. The development of a heavily defect-laden quiescent crystal is shown in Figure 2-27. No comparably flawed flow crystal was found during the experiment.

70
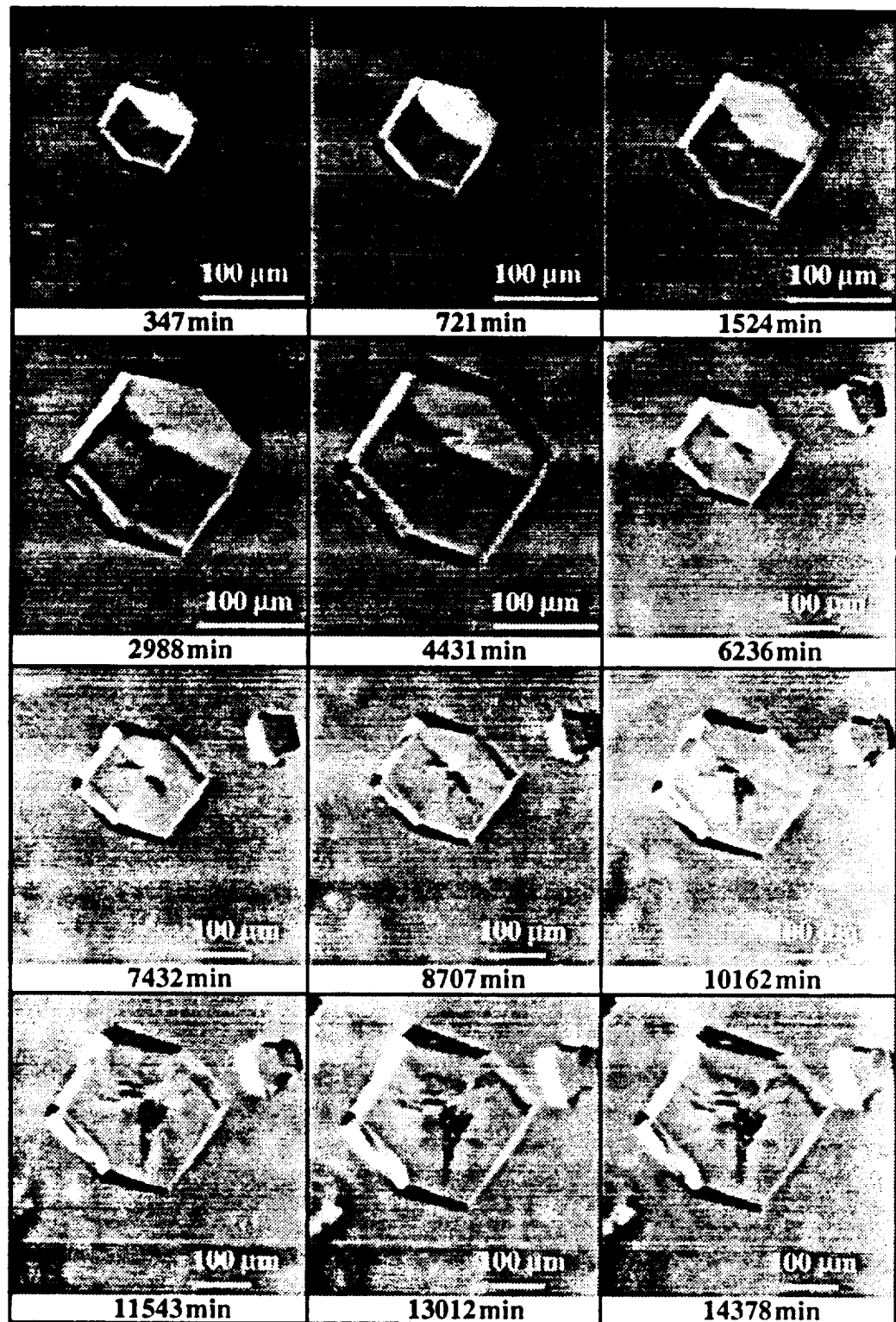
Figure 2-24: Time series for crystal XQ033002.

As digitized	As marked	Ideal best-fit
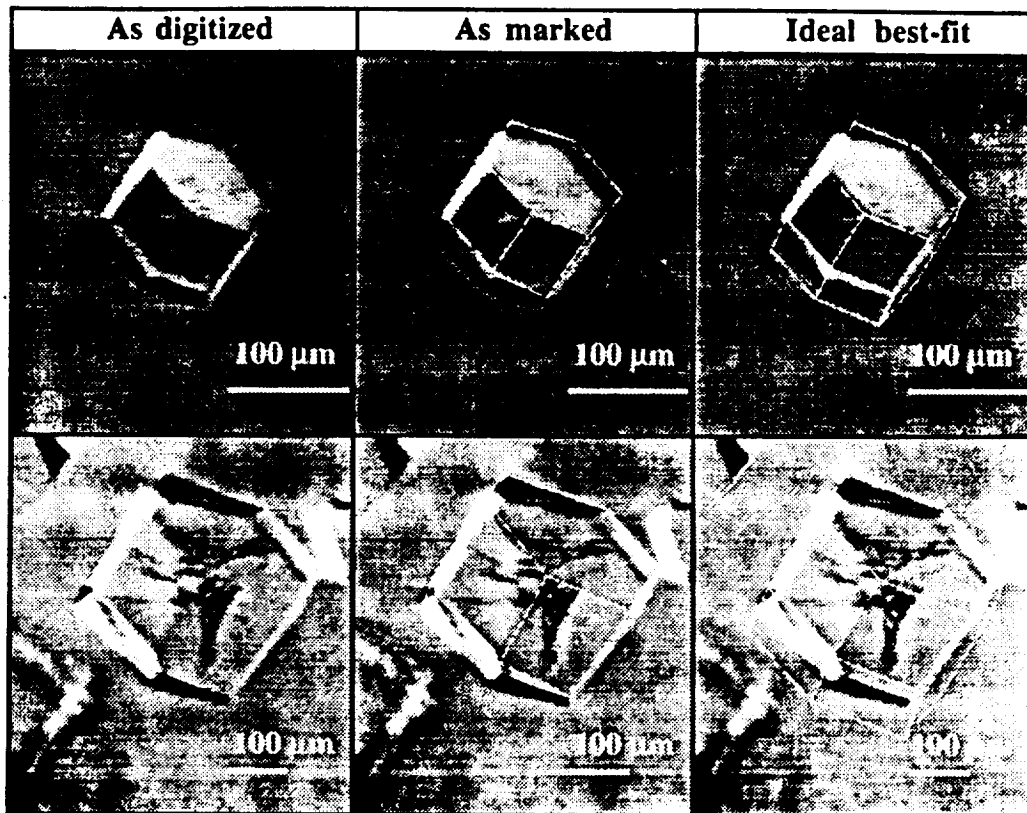
Figure 2-25: Change in the appearance of crystal XQ033002 with time.

The requirement that the crystal be marked consistently is not always easily met. The distance between parallel {110} faces still seems reasonable despite the uncertainty in orientation.

(top) 1524 minutes. (bottom) 14378 minutes.

Crystals exhibiting growth over only parts of a surface were unexpected (Figures 2-28 and 2-29). Durbin and Feher [2] reported that when a crystal had been aged in an unstirred solution for 51 days and then placed in a supersaturated solution, rapid growth resumed only in isolated locations on the surface. When they repeated the experiment with a crystal several days old, growth resumed uniformly over the surface. Although it is difficult to judge the height of the growth layers from their figures, the length scale of the growth "patchiness" (approximately 5 - 10 μm) is somewhat finer than that observed in this work (~ 30 - 100 μm). Additionally, Durbin and Feher reported that the surfaces filled in, albeit imperfectly, after approximately 30 minutes. In the case of crystal XQ041001

As digitized	As marked	Ideal best-fit
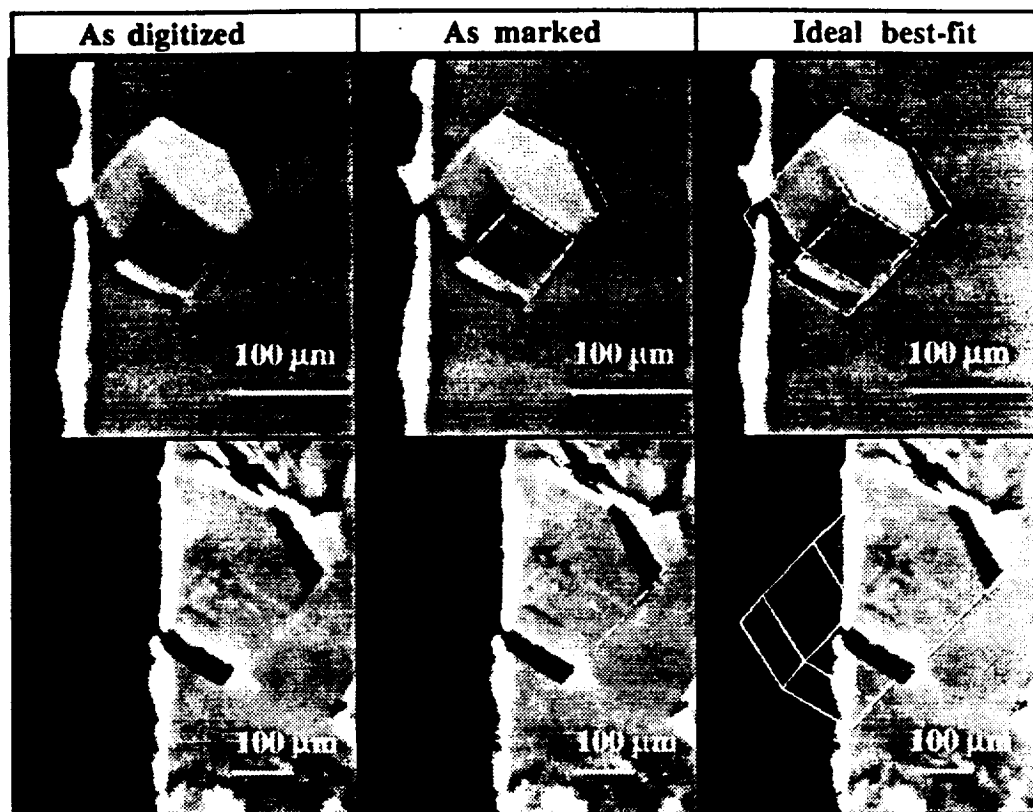
Figure 2-26: Change in appearance of crystal XQ033001 with time.
There is uncertainty in the orientation of the crystal. The best-fit placement of the pyramid is seriously in error, but the distance between {110} faces appears close.
(top) 1524 minutes. (bottom) 14378 minutes.

(Figure 2-28), the discontinuity in height was easily visible under a 5X microscope objective and required four days to fill in the surface. Durbin and Feher suggested that this partial inactivation of the crystal surface could be related to the cessation of growth which had been reported earlier [7]. Certainly, the crystals in this study continued to grow despite an apparent spatial variation in growth rate. The net effect of this observation is to add another item to the overwhelmingly long list of questions about protein crystal growth.
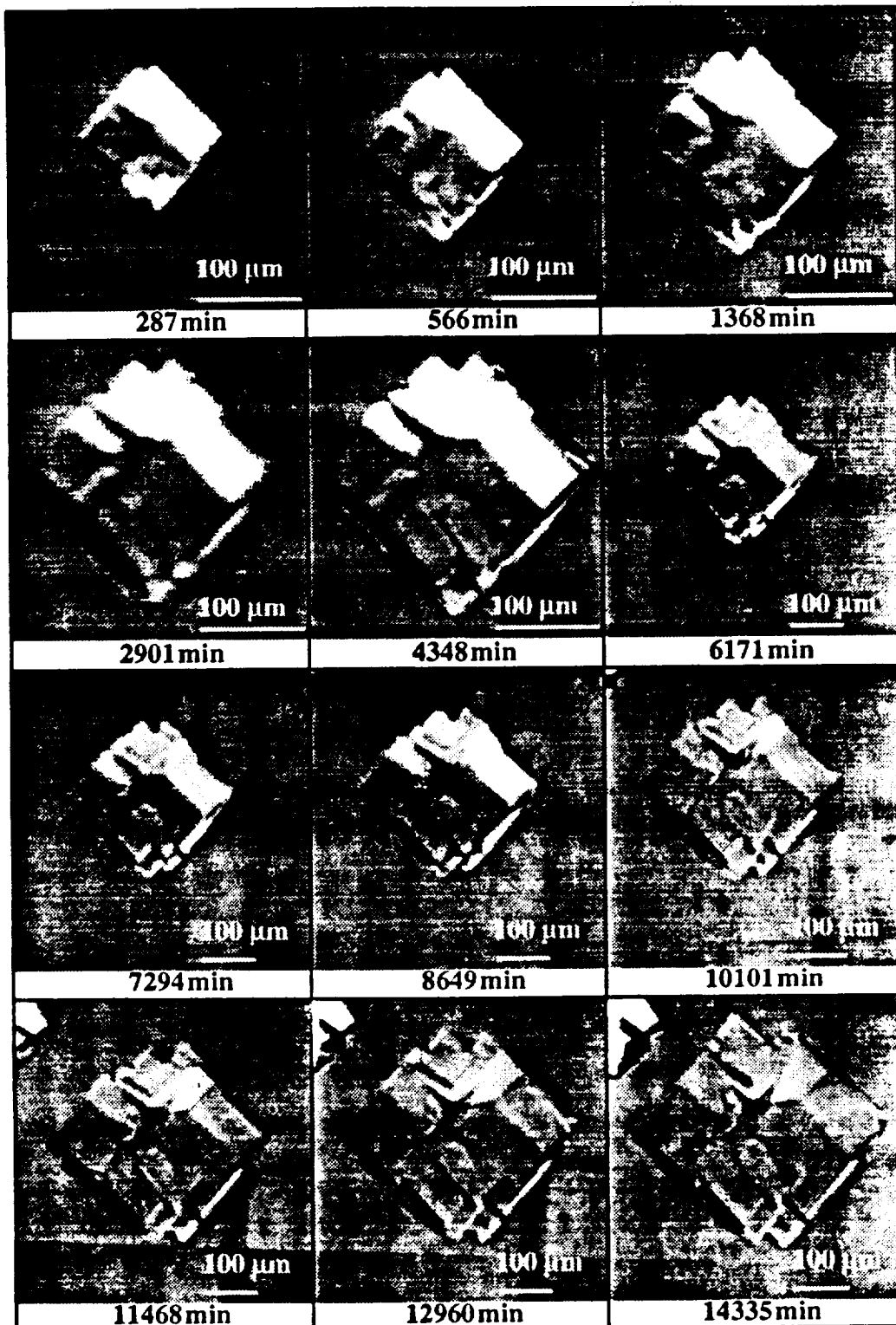
Figure 2-27: Time series for crystal XQ014001.
Crystal displays a large number of terraces which may be incomplete layers.
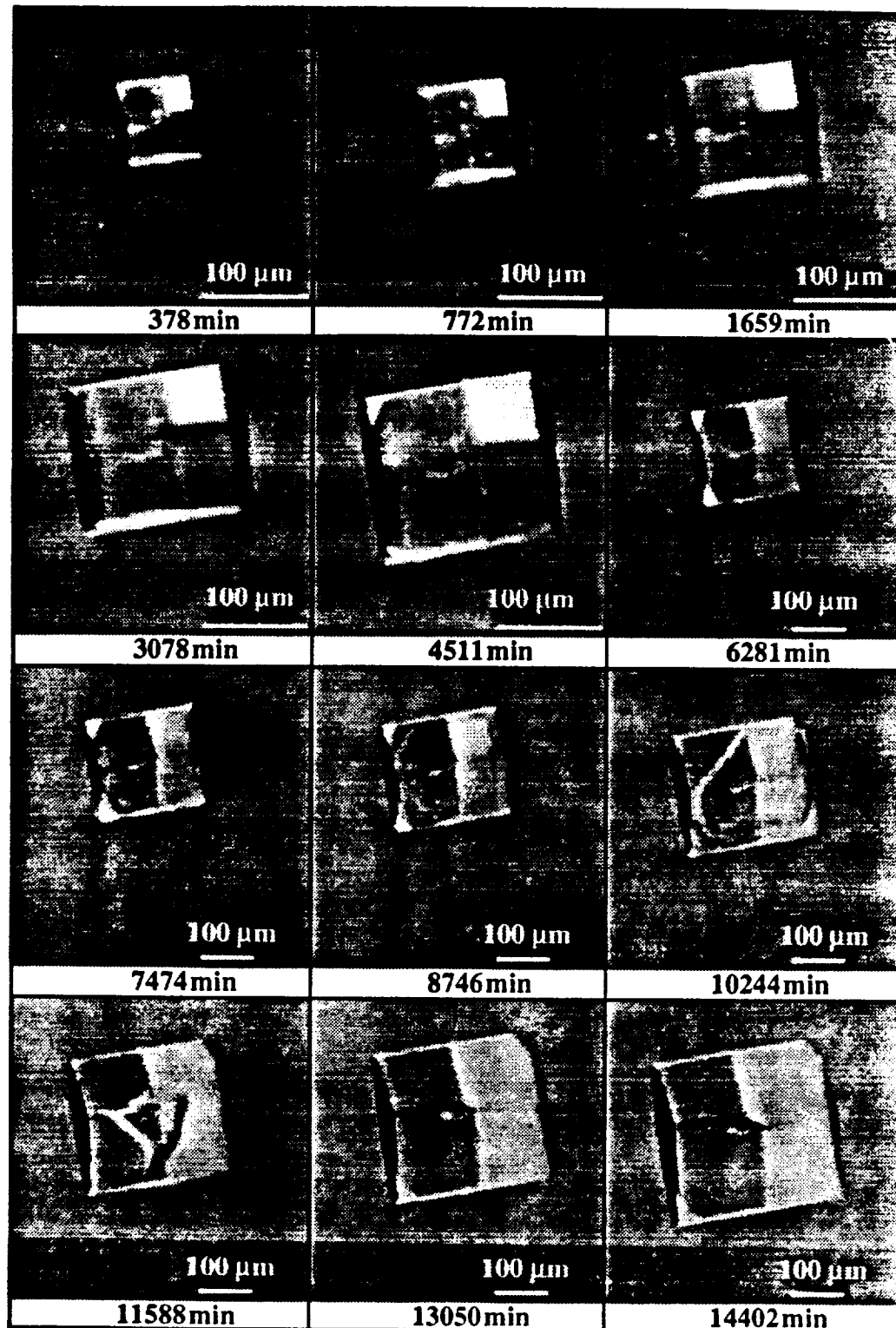
Figure 2-28: Time series for crystal XQ041001.
Shading suggests the presence of incomplete layers starting at 7474 minutes. The surface has filled in by 13050 minutes. The face in the upper left quadrant seems to have grown faster than the other {101} faces.
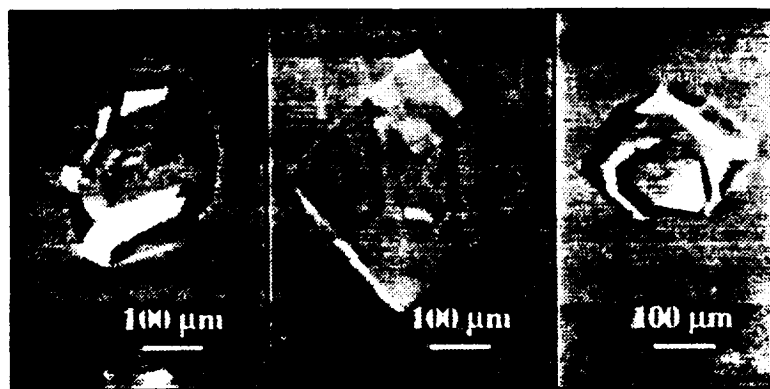
Figure 2-29: Several quiescent crystals with incomplete layers.

2.14 Summary

The growth of isolated single crystals remains largely a matter of chance. The original design of the experiment imposed strict requirements on the clarity of the optical path, crystal density, and protein concentration. In the end, these requirements could not be satisfied simultaneously and the initial approach was abandoned. The experiment was then altered so that it was similar to earlier reported experiments [2,4-6]. Batch-to-batch variations plagued the experiments throughout, although efforts were made to clean the protein to obtain a uniform starting material. No cause for the irreproducibility was determined. Crystals grown from a single batch of protein solution provided all the data for this work.

A method was developed to estimate the size and orientation of growing tetragonal crystals of hen egg white lysozyme. The method relies on the assumption that digitized images of the crystals are orthographic projections of an ideal crystal onto a plane. The angles of the crystal's edges are measured by recording the coordinates of all the visible vertices. The crystal is assumed to have the same orientation as the ideal crystal which minimizes the sum of the squares of the angles between the measured edges and projections of the ideal edges. The size of the crystal is taken the be the same as that of the "best-fit" ideal crystal which can be superimposed on the measured crystal. The accuracy of the

76

method cannot be determined without calibration against objects of known dimensions, but inspection of the superimposed ideal crystals shows that the ideal dimensions are in reasonable agreement with the raw images. Furthermore, they seem to be internally consistent.

The method allows crystals in any orientation to be measured, which significantly relaxes the requirements imposed in previous work [2,6] and increases the potential sample size. The method produces its best results when the measured crystals are close to ideal, but the {110} dimension is robust even when the crystal is highly asymmetric; the robustness of L_{110} holds even when there is a large uncertainty in the placement of vertices. L_{101}, in contrast, seems highly sensitive to the calculated orientation. The major advantage of the method, its ability to estimate dimensions of a three-dimensional object from a two-dimensional image, is also its major limitation: the symmetry constraints of the ideal crystal preclude measurement of variations in growth rates among equivalent faces. At the conditions used in this work (lysozyme concentration $\approx$ 10 mg/ml, 50 mg/ml NaCl, pH 4), asymmetrical growth of {101} faces was prevalent. A full stereo view is required to obtain single face growth rates.

References

[1] Pusey, M., W. Witherow and R. Naumann. *J. Crystal Growth.* **90** (1988) 105-111.

[2] Durbin, S. D. and G. Feher. *J. Crystal Growth.* **76** (1986) 583-592.

[3] Grant, M. L. and D. A. Saville. *J. Crystal Growth.* **108** (1991) 8-18.

[4] Pusey, M. L. and R. Naumann. *J. Crystal Growth* **76** (1986) 593-599.

[5] Pusey, M. L., R. S. Snyder and R. Naumann. *J. Biol. Chem.* **261** (1986) 6524-6529.

[6] Fiddis, R. W., R. A. Longman and P. D. Calvert. *J. Chem. Soc. Faraday Trans.* **75** (1979) 2753-2761.

[7] Kam, Z., H. B. Shore, and G. Feher. *J. Mol. Biol.* **123** (1978) 539-555.

[8] Heidner, E. *J. Crystal Growth.* **44** (1978) 139-144.

[9] Sophianopoulos, A. J., C. K. Rhodes, D. N. Holcomb and K. E. Van Holde. *J. Biol. Chem.* **237** (1962) 1107-1112.

[10] Howard, S. B., P. J. Twigg, J. K. Baird and E. J. Meehan. *J. Crystal Growth.* **90** (1988) 94-104.

[11] Cervelle, B., F. Cesbron, J. Berthou and P. Jolles. *Acta. Cryst.* **A30** (1974) 645-648.

[12] Palmer, K. J., M. Ballantyne and J. A. Galvin. *J. Am. Chem. Soc.* **70** (1948) 906-908.

[13] Brunk, H. D. *An Introduction to Mathematical Statistics 2d ed.* Waltham, MA: Blaisdell, 1965.

CHAPTER 3

Analysis of Experimental Results

3.1 Introduction

Crystal growth experiments provide data on crystal size as a function of time; the time derivative of crystal size is the growth rate. Statistical analysis of growth rates as a function of time can be used to determine whether there is a trend. A downward trend in growth rate is a necessary, but not sufficient, condition to infer that flow has an inhibitory role in protein crystal growth. Other phenomena, such as changes in the local environment, may cause crystals to slow their growth over time. Under ideal conditions, flow effects would be assessed by comparing crystal growth from two experiments differing only in whether or not crystals were subjected to forced convection. As discussed in Chapter 2, conditions in the two experiments were not identical, so differences in crystal growth behavior between the two experiments cannot be attributed entirely to flow without first assessing the effects of these other variables. The drift in protein concentration during the quiescent experiment and the shorter duration of the flow experiment are the two main differences which cloud interpretation of the results. The effect of sampling bias must also be investigated as a source of differences in behavior between the two experiments.

A series of statistical tests is applied to the distributions of sample size and growth rate obtained from the experiment. Trends in these measurements are compared with those expected from some of the mechanisms proposed to explain apparent convective effects on protein crystal growth. Based on the trends in growth rate, for instance, a simple competition between mass transfer and attachment kinetics is ruled out. The crystal populations within each experiment exhibit a large degree of heterogeneity in their growth rates, and the latter part of the analysis is a search for the sources of this variation. A series of contingency tests are then performed in order to determine whether sampling differences between the two experiments could cause some apparent differences in behavior. Since the

conclusions drawn from the experiments rely heavily on statistical hypothesis testing, an illustrative sample of such a test is an appropriate starting point.

3.2 An Example Statistical Test

Many of the methods employed in the following sections are tests of the null hypothesis, H_0: there is no significant difference between two groups or among several groups. The difference between groups is deemed significant only when, at a chosen confidence level, the null hypothesis is rejected because the observed variation is too great to be attributed solely to chance. Statistical tests of the null hypothesis can be classified broadly into two classes: (i) parametric and (ii) nonparametric or distribution-free methods [1,2]. Engineers are most familiar with parametric tests such as the analysis of variance (ANOVA); the assumptions implicit in ANOVA are that the samples are drawn from normally distributed populations and the populations have equal variances. The variance, σ^2, is a parameter of the underlying population. Nonparametric tests, which permit statistical inference based on the rank order (from low to high, for example) of the sample, do not require the variable in question to be normally distributed or have a "well behaved" variance. As employed here, nonparametric tests provide a check on the validity of conclusions drawn from comparable parametric tests.

Statistical tests can be classified as single sample tests or multisample tests depending on whether the researcher is interested in determining if the sample could have been selected from a specified (known) population or if two or more samples could have been drawn from the same (but unknown) population. Examples of each might be "Could this sample of size N have been drawn from a population of median 50?" and "Could sample 1 of size N_1 and sample 2 of size N_2 have been drawn from a common population?" Engineers are accustomed to seeing the former question posed in terms of the mean, μ, instead of the median, but this reflects the implicit assumption of a symmetric

80

distribution, for which the mean and median coincide. The median is also a measure of central tendency [3] and is the property of choice when applying nonparametric tests.

Suppose now that the second question above is to be investigated under the null hypothesis, H_0: both samples are drawn from the same population. The nonparametric "median test" is as follows: (i) all $N = N_1 + N_2$ values, x_i, are pooled and ranked from lowest to highest; (ii) the pooled median, $x_{50\%}$, is found; (iii) the number of individual values from sample 1 larger than $x_{50\%}$ is determined (since N is fixed, this counting also fixes the number of values from sample 2 in the upper half of the pooled sample); (iv) deviations in the observed number of "high" values from the expected value of $N_1/2$ are compared with the that expected by chance; and (v) a decision is made to accept or reject H_0. If N_1 and N_2 are small, all possible rankings of the individual values could be listed and the probability of a deviation as large as the observed deviation could be calculated exactly. For large samples, a suitable statistic involving the difference in the mean rank of the samples can often be found which obeys (at least approximately) a known continuous distribution; significance of tests are then made by reference to the appropriate value of the known distribution.

Most of the statistical analyses were performed on a Macintosh Plus using the commercially available program, *StatView SE + Graphics* [4]. Extensive descriptions of the nonparametric tests are given by Siegel [1]. On several occasions, the formulas in the two sources differed; those given by Siegel were used whenever there was a discrepancy. Critical values used in assessing significance were obtained from the Chemical Rubber Company's *Standard Mathematical Tables* [5] when tabulated, or from routines in the IMSL statistical library [6]. Where additional sources were used, they are cited in the text.

3.3 General Discussion of Results of Crystal Growth Experiments

Although inferences about the growth experiments are based on statistical tests, it is important to remember that these tests were developed for samples drawn at random from a population in order to evaluate properties of the underlying population. The samples in these experiments, however, are not random; they are images of the first 60 or 70 crystals which could be located on the walls and appeared sufficiently isolated from their neighbors. Exclusion of crystals that could not be satisfactorily interpreted introduces another unknown bias into the samples. The experiments described here are really longitudinal studies of particular subgroups of protein crystals and not a series of measurements performed on freshly drawn random samples. Comprehensive statistical tests designed specifically for this sampling technique are simply not available, so several tests were applied in the hope that their interpretations would be consistent. Underlying the discussion that follows is an implicit assumption that the sample, although not random, adequately characterizes the crystal population.

Crystal sizes as calculated from the method presented in Chapter 2 are shown in Figure 3-1 and Table 3-1. The crystals are grouped into "rounds" for later statistical analysis; each crystal is numbered sequentially in the order it was digitized during the experiment. The calculated distance between parallel {110} faces of crystal i measured during round n is denoted $L_{i,n}$. This causes no ambiguity because, as mentioned in section 2.12, L_{101} was excluded from statistical analysis. Crystals in round 1 of the quiescent experiment were large enough and clear enough to be measured with some confidence. This was not generally the case in the flow experiment, so analysis of these crystals begins with round 2. The average growth rate of each crystal over a given interval was calculated from the formula

$$G_{i,n} = \frac{1}{2} \frac{L_{i,n} - L_{i,n-1}}{t_{i,n} - t_{i,n-1}}$$

(3.1),
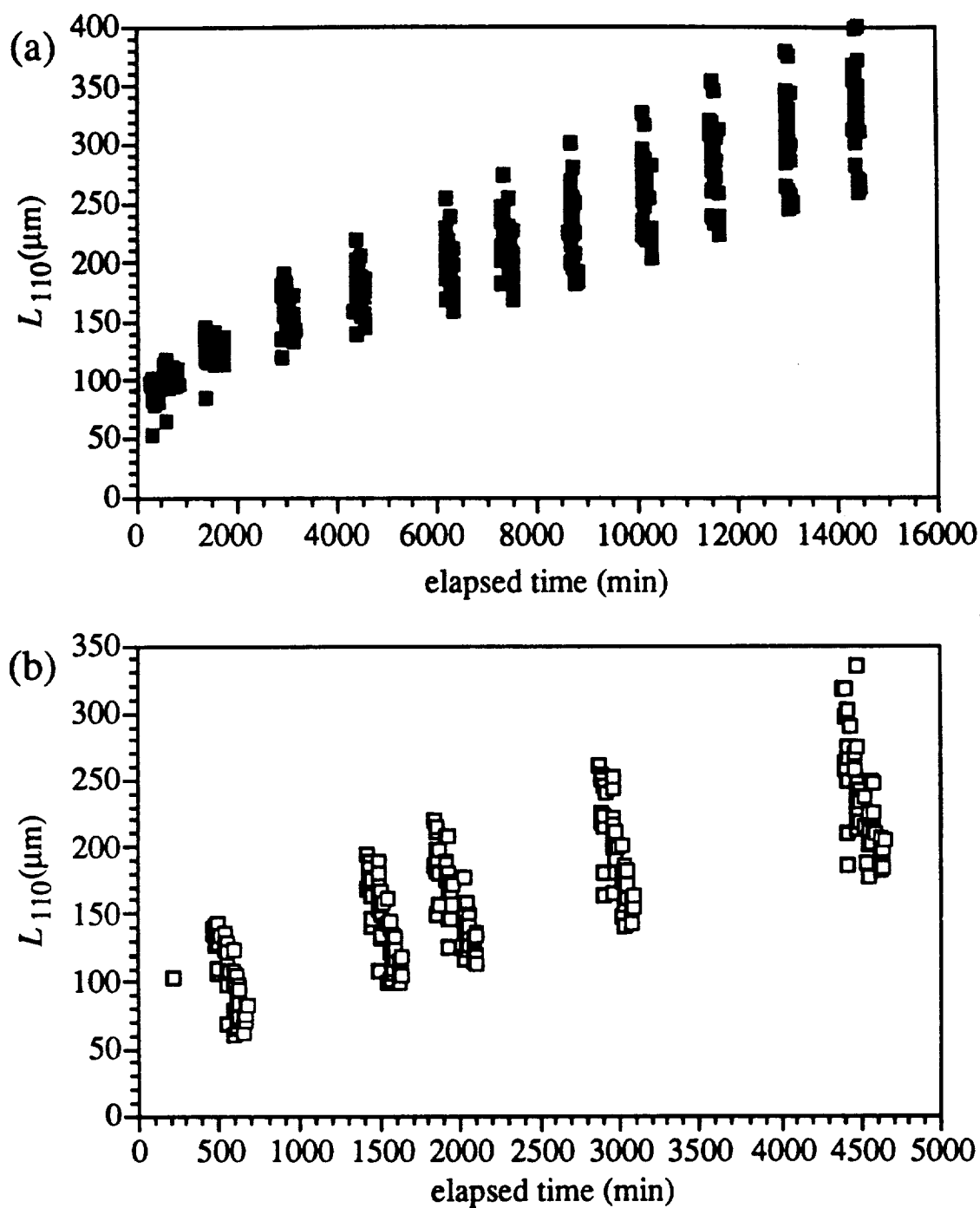
Figure 3-1: Crystal size as a function of time.
(a) Quiescent experiment, N_q = 39. (b) Flow experiment, N_f = 53.

Table 3-1

Crystal size by round.

Round	N[†]	Elapsed time[‡] (min)	Mean (μm)	Std. dev.[◊] (μm)	Minimum (μm)	Maximum (μm)	Range (μm)
Quiescent							
1	32	322	84.98	9.38	50.87	99.03	48.16
2	35	662	99.01	9.58	62.69	115.77	53.08
3	37	1488	122.94	11.60	82.64	143.06	60.42
4	38	2965	156.15	15.10	116.59	188.34	71.75
5	39	4411	174.51	17.50	137.68	217.58	79.90
6	39	6215	197.12	22.64	156.14	252.02	95.88
7	39	7382	211.59	24.56	165.80	270.90	105.10
8	39	8688	230.96	28.54	179.20	299.74	120.54
9	39	10151	257.03	31.85	201.73	324.01	122.28
10	39	11520	280.16	35.25	219.80	351.03	131.23
11	39	12997	301.91	38.36	241.35	375.98	134.63
12	39	14363	321.74	40.22	256.81	397.44	140.63
Flow							
2	51	571	100.93	25.64	58.93	140.39	81.46
3	53	1518	141.28	28.11	97.38	191.94	94.56
4	53	1965	157.56	29.60	111.27	217.44	106.17
5	53	2981	190.40	31.75	139.13	258.57	119.44
6	53	4503	232.37	37.56	175.03	332.81	157.78

[†] N is the number of crystals measured during each round.
[‡] Time reported is mean for all crystal measurements during each round.
[◊] Reported standard deviation is the unbiased estimate for the population, $s\,[N\,/(N-1)]^{1/2}$.

where $G_{i,n}$ = average growth rate of crystal i over interval n and $t_{i,n}$ = time at which that measurement was made. Note that each interval is numbered to match the round that ends it. These growth rates are summarized in Table 3-2 and plotted against $t_{mid,i,n} = (t_{i,n} + t_{i,n-1})/2$ in Figure 3-2. A sense of how the calculated growth rate tracks the protein concentration can be gained from the traces in Figure 3-2 representing the measured protein concentration (based on optical density at 280 nm) during the experiments.

Table 3-2

Crystal growth rates by round.

Round	$N^{\dagger}$	Mean (nm/min)	Std. dev.‡ (nm/min)	Minimum (nm/min)	Maximum (nm/min)	Range (nm/min)
Quiescent						
2	32	21.39	4.96	12.06	32.32	20.26
3	35	14.92	3.39	8.72	25.76	17.04
4	37	11.42	1.80	7.48	14.75	7.27
5	38	6.19	1.61	2.10	10.10	8.00
6	39	6.25	2.12	0.46	9.71	9.25
7	39	6.22	1.58	1.95	9.82	7.86
8	39	7.40	2.20	0.04	12.25	12.22
9	39	8.92	2.15	2.47	12.39	9.92
10	39	8.45	1.85	3.61	11.58	7.97
11	39	7.37	1.46	3.84	10.62	6.77
12	39	7.25	2.01	3.16	11.05	7.89
Flow						
3	51	20.79	3.33	15.43	30.20	14.77
4	53	18.29	5.06	8.06	36.72	28.66
5	53	16.15	3.64	6.78	25.01	18.23
6	53	13.80	3.80	7.15	27.21	20.05

$\dagger$ N is the number of crystals for which a growth rate could be calculated.
$\ddagger$ Reported standard deviation is unbiased estimate for the population,
  $s \, [N \, /(N - 1)]^{1/2}$.
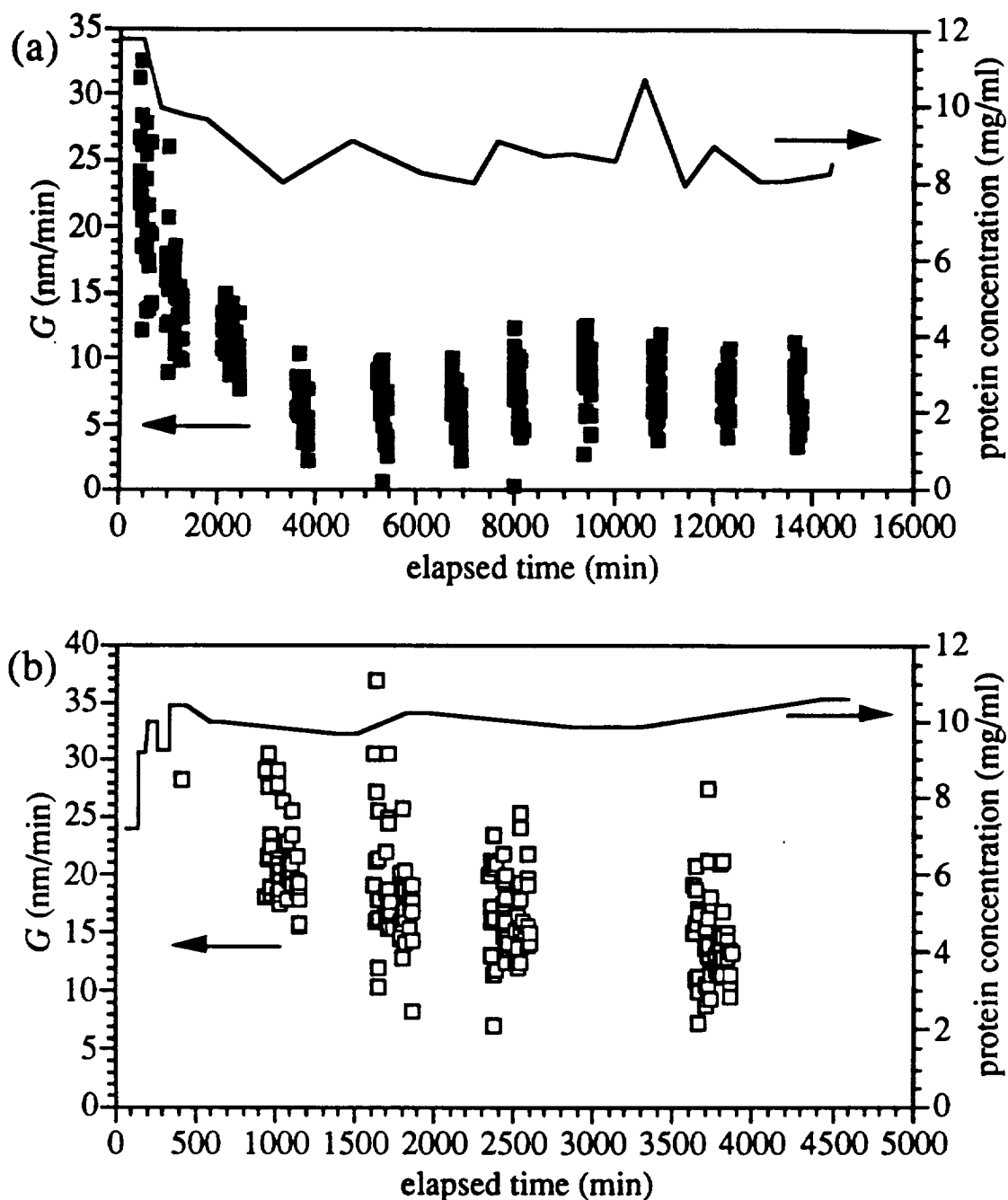
Figure 3-2: Crystal growth rates as a function of time.
(a) Quiescent experiment, N_q = 39. (b) Flow experiment, N_f = 53.

The most striking feature of the experiments is the large range of crystal sizes and growth rates. As shown in Table 3-1, the range of sizes is typically 50% of the mean for "quiescent" crystals and 70% for "flow" crystals. Because the relative range in growth

rates is approximately the same in both experiments (approximately 120% of the mean), this difference in the relative range of crystal sizes seems to result from differences in the initial size distribution in the two experiments. Large variations such as these have been reported by Durbin and Feher [7] and seem to be inherent in the protein crystal growth process. Accordingly, it is evident that large numbers of crystals must be measured in order to characterize the size and growth rate distributions of protein crystals. A second feature of the measurements is that the sample standard deviation is approximately proportional to the mean. This is commonly observed in growth phenomena where the variation present at a given stage of growth is proportional to the average characteristic size at that stage [8]. This is also a characteristic of the log-normal distribution [8,9].

3.4 Statistical Analysis of Average Growth Rate

The simplest hypothesis to test about the crystal growth rate distribution is H_0: the crystal growth rate is constant over the course of the experiment. For each experiment, a one-way ANOVA was performed with the round as the independent variable and G as the dependent variable (ANOVA1 in Table 3-3). In both experiments, the variation between rounds is significant at the 95% confidence level. One of the assumptions of ANOVA, which is violated in this case, is that all treatments have the same variance. The relative standard deviations in all cases, however, are nearly the same, so an ANOVA with $\ln G$ as the dependent variable would come closer to meeting the restriction on variance. This analysis of variance (ANOVA2 in Table 3-3) reveals a significant variation in $\ln G$. These results are confirmed by the Kruskal-Wallis H test. Another nonparametric analysis of variance, the Friedman χ_r^2, is well suited for checking differences between matched samples; the Friedman χ_r^2 confirms the earlier findings. The null hypothesis is therefore rejected and the alternative that the growth rate changes is accepted.

Table 3-3

Tests of H_0: growth rates are constant.

Experiment	ANOVA1[†] F	ANOVA2[‡] F	Kruskal–Wallis H	Friedman χ^2_r
Quiescent	128.96***	37.98***	257.93***	226.31***
Flow	28.74***	32.57***	75.09***	90.58***

Significance: * $p < 0.1$; ** $p < 0.05$; *** $p < 0.01$.

† Analysis of variance performed on growth rates calculated from method of Chapter 2.
‡ Analysis of variance performed on natural logarithm of calculated growth rates.

In both experiments, crystal growth seems to slow with time. A correlation matrix (Table 3-4) provides the information to test for trends. When $G_{i,n}$ is correlated with $t_{mid,i,n}$, the sample correlation coefficient, r, is -0.534 for the quiescent experiment and -0.558 for the flow experiment. These sample correlation coefficients, r, are estimators of the correlation coefficient of the underlying populations, ρ. The null hypothesis is that the growth rates of the population are uncorrelated with time ($\rho = 0$). This hypothesis can be tested against the alternative $\rho < 0$ by a one-tailed test as follows. The statistic $z = (1/2) \, ln \, [(1 + r)/(1 - r)]$ is approximately normally distributed with an expectation or mean of $\mu_z = (1/2) \, ln \, [(1 + \rho)/(1 - \rho)]$ and variance $(N - 3)^{-1}$, where N = sample size [3]. The standard normal deviate of z, $\zeta = (z - \mu_z)(N - 3)^{1/2}$, can then be checked against a table of the standard normal distribution to determine if the deviation of the sample correlation coefficient from the mean could be attributed to chance. Note that under the null hypothesis, $\rho = 0$ and $\mu_z = 0$. In this one-tailed test, the hypothesis is rejected if $\zeta < \zeta_{crit} = -1.645$, corresponding to the 95% confidence level. The quiescent sample has $N_q = 415$ and $\zeta_q = -12.1$, so the hypothesis $\rho_q = 0$ is rejected in favor of the alternative $\rho_q < 0$. Similarly, $N_f = 211$ and $\zeta_f = -9.08$ so that the hypothesis $\rho_f = 0$ is also rejected in favor of $\rho_f < 0$. These conclusions are supported by a comparable nonparametric test, the

Spearman rank correlation coefficient, r_S (Table 3-5), which correlates the ranks of the samples instead of the values. The statistic $x = r_S \sqrt{(N-2)/(1-r_S^2)}$ is distributed as Student's t with $N-2$ degrees of freedom. The values of x are $x_q = -10.0$ and $x_f = -11.6$, which are certainly far enough from zero to reject the null hypothesis. The downward trend in crystal growth rates during both experiments is therefore statistically significant at the 95% confidence level.

Table 3-4
Correlation matrix for both experiments

	$t_{mid,i,n}$	$G_{i,n}$	$C_{av,i,n}$
$t_{mid,i,n}$	1.000	–0.558***	0.866***
$G_{i,n}$	–0.534***	1.000	–0.527***
$C_{av,i,n}$	–0.591***	0.812***	1.000

Significance: * $p < 0.1$; **$p < 0.05$; *** $p < 0.01$.

The full correlation matrix is symmetric. Flow experiment correlations are shown in the upper right half of the matrix; quiescent experiment is in the lower left. $N_f = 211$ and $N_q = 415$.

The trends in protein concentration are different in the two experiments, as can be seen in the traces of protein concentration in Figure 3-2. Calculations like those above confirm at the 95% confidence level that the average protein concentration is decreasing with time in the quiescent experiment but increasing in the flow experiment. The correlation between average growth rate and average protein concentration in the two experiments shows obvious differences in behavior. Quiescent crystal growth rates are correlated to average protein absorbance with $r_q = 0.812$, while growth rates in flow are correlated with $r_f = -0.527$. One-tailed tests of the hypothesis $\rho = 0$ can once again be made. In this case, however, the alternatives are that $\rho_q > 0$ and $\rho_f < 0$. The corresponding ζ's are $\zeta_q = 22.98 > \zeta_{crit}$ and $\zeta_f = -9.64 < \zeta_{crit}$ so the hypotheses $\rho_q = 0$

and $\rho_f = 0$ are rejected. The conclusion, then, is that the reduction in growth rate in the quiescent case can be at least partially attributed to decreased protein concentration, but the flow crystals slow down despite increasing protein concentration. Spearman rank correlation coefficient tests confirm these results.

Table 3-5

Spearman correlation matrix for both experiments.

	$t_{mid,i,n}$	$G_{i,n}$	$C_{av,i,n}$
$t_{mid,i,n}$	1.000	-0.626***	0.836***
$G_{i,n}$	-0.441***	1.000	-0.568***
$C_{av,i,n}$	-0.534***	0.632***	1.000

Significance: * $p < 0.1$; ** $p < 0.05$; *** $p < 0.01$.

The full correlation matrix is symmetric. Flow experiment correlations are shown in the upper right half of the matrix; the quiescent experiment is in the lower left. $N_f = 211$ and $N_q = 415$.

The observed trends disagree with the predictions of quasi-steady mass balances on the growing crystal [10-12] but are consistent with the experimental results of Pusey, Witherow and Naumann [13]. Although differences in cell geometry and flow fields prevent quantitative comparison of the two experiments, the qualitative features of their experiment are the same as those presented above. When lysozyme crystals were subjected to forced convection of 18 - 40 μm/s, Pusey et al. found that growth slowed to 5 - 20% of initial rates within 4 - 5 hours. The observed effect is significantly smaller in the present work: the mean lysozyme crystal growth rate fell to 66% of its initial value when crystals were exposed to a flow of 50 μm/s (superficial velocity) over a three day period. The initial growth rates in both experiments are about half the initial rates measured by Pusey and coworkers [13]. The current experiments provide clear information only about the initial behavior of the flow crystals and the long-time behavior of the quiescent crystals.

Quiescent crystals may show a reduction in growth rate similar to flow crystals, but these experiments cannot be used to decide the issue. If quiescent crystals show a similar decrease in growth rate while they are still small, it would be evidence of kinetic control. This question must be resolved by additional experiments on quiescent crystals.

The flow experiment, which was designed to simulate the effects of buoyancy-driven natural convection, was interrupted by difficulties with the syringe pump. Natural convection is present in the quiescent experiment, however, and quiescent data can be used to test some hypotheses about the effect of flow on crystal growth. If protein crystal growth is inhibited by this convection, growth rates should decrease with time. Correlation coefficients can again be used to test for trends. The correlation matrix of Table 3-4 is not appropriate for studying long-time behavior because it is dominated by the protein concentration transient early in the experiment. Tests of the correlation between average protein concentration and elapsed time at the 95% confidence level show the initial decline had ended by round 4 (start of interval 5). After 3000 minutes had elapsed, the average protein concentration was nearly constant, with mean 8.59 mg/ml, standard deviation 0.40 mg/ml, and a range from 8.11 mg/ml to 9.46 mg/ml. These values differ slightly from those reported in section 2.7 because the quantity of interest here is the average protein concentration over each interval instead of the measured concentration in each effluent sample.

The average crystal size doubled from 156 μm at the beginning of interval 5 to 322 μm at the end of the experiment, placing the crystals in the range where convective transport is expected to be significant [10-12]. The correlation coefficient of growth rate and elapsed time is $r = 0.264$ (Table 3-6) based on a sample of 311 measurements. The standard normal variate is $\zeta = 4.75 > \zeta_{crit} = 1.645$. In fact, the probability that a sample correlation coefficient as large as 0.264 could have been drawn from an underlying population with $\rho = 0$ is approximately 10^{-6}. The null hypothesis that growth rate is independent of time (or decreasing) is rejected in favor of the alternative that the growth rate

is increasing. If the hypothesis were that growth rate is independent of size, the conclusion would again be that crystals are not slowing as they grow.

Table 3-6

Correlation matrix for quiescent crystals beginning in interval 5.

	$t_{mid,i,n}$	$G_{i,n}$	$C_{av,i,n}$	$L_{i,n}$
$t_{mid,i,n}$	1.000			
$G_{i,n}$	0.264***	1.000		
$C_{av,i,n}$	0.054	0.262***	1.000	
$L_{i,n}$	0.843***	0.517***	0.054	1.000

Significance: * $p < 0.1$; ** $p < 0.05$; *** $p < 0.01$.
The full correlation matrix is symmetric. $N = 311$.

Any phenomenon that causes protein crystal growth to stop ("cessation of growth") must become active after the crystal has reached 300 µm in size because there is no evidence of slowing over the range 150 – 300 µm. Crystals are reported to reach a "critical" size of about 1 mm before they stop growing [14]. This is a tight constraint on any models which attribute an inhibitory effect to free convection, especially since the strength of the convective effects increase slowly with crystal size. Based on the scale analysis mentioned in section 1.5, the characteristic velocity scales as $L^{1/2}$ and the shear stress scales as $L^{1/4}$; at 1 mm, the characteristic velocity and shear stress are only 1.8 and 1.4 times as large as they are at 300 µm. Longer, better-controlled growth experiments ought to provide a clearer picture of long-term behavior of protein crystals.

3.5 Comparison of the Dispersion in Growth Rate

In addition to affecting the mean of the growth rate distribution, flow might affect the dispersion about the mean. The effect of flow on the dispersion of growth rates can be studied once the samples have been put on a comparable basis. As mentioned above, the

sample standard deviations are approximately proportional to the sample means; i.e., $s_x/\bar{x}$ $\approx \gamma$, where γ = relative standard deviation. Transforming the sample random variable x into a new random variable $\xi = x/\bar{x}$ reduces a sample distribution of x having mean $\bar{x}$ and variance s_x^2 to an equivalent distribution having mean $\bar{\xi} = 1$ and variance $s_\xi^2 = s_x^2/\bar{x}^2 = \gamma^2$. Differences between the transformed sample distributions now result only from differences in the shape of the empirical distribution functions and can be tested with any technique that can detect such differences.

An F-test is one method to determine if the dispersion of the normalized growth rates in the two experiments is consistent with the hypothesis that the underlying populations are the same. The variances of each normalized sample from the quiescent experiment are pooled under the null hypothesis that they are independent measures of the (unknown) variance of the underlying population of quiescent crystals. A similar estimate is made of the variance of the normalized growth rates from the flow experiment, and the two estimates are compared to see whether the samples could have been drawn from a common normal distribution. The unbiased estimator of the quiescent variance is $\sigma_q^2 = 6.36 \times 10^{-2}$ based on $N_q - 11 = 404$ degrees of freedom; the flow variance is $\sigma_f^2 = 5.76 \times 10^{-2}$ based on $N_f - 4 = 206$ degrees of freedom. The overall value of $F = 1.10$ is less than the estimated value of $F_{crit} = 1.23$, so the pooled variances of the two experiments could be the same at the 95% confidence level. In fact, the pooled variances in the two experiments differ less than do the estimates within an experiment. If the normalized growth rates are assumed to follow a log-normal distribution, the results are: $\sigma_q^2 = 7.52 \times 10^{-2}$, $\sigma_f^2 = 5.35 \times 10^{-2}$, and $F = 1.40 > F_{crit}$. If the growth rates are log-normal, the difference in variance is significant at the 95% level, and the flow crystals have a narrower distribution than the quiescent crystals. As before, the difference between experiments is smaller than differences within experiments.

Sample variances and means are sensitive to outlying values and can vary widely, especially when the distributions are broad. The nonparametric Kolmogorov-Smirnov test,

which is less sensitive to outliers than the F-test, can be used to test the hypothesis that the samples were drawn from an hypothetical distribution. In this case, two forms of the distribution function are proposed and the Kolmogorov-Smirnov test is applied to test for goodness of fit. The first hypothetical distribution is a normal distribution with mean $\mu = 1$ and variance $\sigma^2 = \gamma^2$, while the second is a log-normal distribution with mean $\mu = 1$ and variance $\sigma^2 = \exp(\beta^2) - 1$, where β is the standard deviation of the transformed (logarithmic) distribution [9]. The normal distribution was chosen because its behavior is familiar to many engineers; the log-normal distribution was chosen because its standard deviation is naturally proportional to the mean. For each sample, the upper and lower bounds for γ and β were the maximum and minimum values for which the null hypothesis was accepted by the Kolmogorov-Smirnov test at the 95% confidence level (see Table 3-7). By restricting the range of values to those lying between the greatest lower bound and the smallest upper bound, it is possible to find values for γ and β which satisfy all samples taken from both experiments. The tightest restrictions are placed on γ by the flow crystals, which require $0.165 \leq \gamma \leq 0.175$. (Values of γ are reported to the nearest one-thousandth because the limits are so strict.) β can range from 0.17 to 0.22. The conclusion of the F-test under the assumption of a log-normal distribution, namely that the distribution of the normalized growth rates of flow crystals is narrower than that of quiescent crystals, agrees with the results shown in Table 3-7.

Goodness-of-fit tests can also be applied to crystal size distributions. Dispersion in the initial crystal size distribution partially masks changes in the shape of the distribution with time, so a better sense of the cumulative effect of growth rate dispersion can be gained from an examination of net crystal growth. The net growth, $L_{i,n} - L_{i,ref}$, is also suitable for goodness-of-fit testing and is insensitive to the initial size dispersion. Reference lengths were chosen to be $L_{i,1}$ for the quiescent experiment and $L_{i,2}$ for the flow experiment. A single normal distribution can describe the net growth as long as the relative standard deviation is in the range $0.13 \leq \gamma \leq 0.15$; a log-normal distribution describes the

94

data if $0.13 \leq \beta \leq 0.22$ (Table 3-8). No clear choice can be made between these two proposed distributions, so later tests are performed on both the raw values and their logarithmic equivalents.

Table 3-7

Extreme standard deviations of normalized growth rate distributions from Kolmogorov-Smirnov goodness-of-fit tests.

Round	Normal distribution		Log-normal distribution	
	γ_{min}	γ_{max}	β_{min}	β_{max}
Quiescent				
2	0.099	0.609	0.10	0.47
3	0.092	0.409	0.10	0.51
4	0.077	0.340	0.08	0.38
5	0.104	0.515	0.12	0.50
6	0.153	0.698	0.16	0.50
7	0.094	0.456	0.10	0.45
8	0.132	0.561	0.13	0.44
9	0.086	0.499	0.09	0.37
10	0.117	0.400	0.12	0.39
11	0.110	0.411	0.12	0.42
12	0.133	0.569	0.15	0.58
Flow				
3	0.095	0.175	0.10	0.22
4	0.158	0.220	0.15	0.35
5	0.114	0.396	0.13	0.36
6	0.165	0.491	0.17	0.43

Table 3-8

Extreme standard deviations of normalized net growth distributions from
Kolmogorov-Smirnov goodness of fit tests.

Round	Normal distribution		Log-normal distribution	
	γ_{min}	γ_{max}	β_{min}	β_{max}
Quiescent				
2	0.08	0.58	0.08	0.46
3	0.07	0.40	0.07	0.35
4	0.08	0.32	0.08	0.31
5	<0.05	0.34	<0.05	0.34
6	0.09	0.39	0.09	0.45
7	0.09	0.37	0.09	0.46
8	0.11	0.39	0.11	0.45
9	0.11	0.40	0.12	0.44
10	0.12	0.37	0.13	0.40
11	0.12	0.31	0.13	0.40
12	0.12	0.31	0.13	0.39
Flow				
3	0.09	0.15	0.09	0.22
4	0.09	0.25	0.09	0.24
5	0.11	0.26	0.10	0.23
6	0.13	0.29	0.12	0.25

The results presented in this section suggest that crystals grown under nominally quiescent conditions have a greater relative dispersion in growth rates than crystals subjected to flow. Growth rate measurements have ranges of 120 – 130% of the mean for both flow and quiescent crystals. The wide distribution of rates produces "outlying" points frequently, causing large fluctuations in sample means and variances which weaken the ability of the F-test to discriminate between the two experiments. Kolmogorov-Smirnov goodness-of-fit tests show that all samples in both experiments could have been drawn from the same underlying population but cannot distinguish between proposed normal and log-normal distributions. Other than the narrower distributions in the flow experiment,

there is no statistically significant difference between the two experiments. The shapes of growth rate and net growth distributions from the two experiments are similar and change only slightly over the course of the experiment. One inference from these results is that the same basic distribution of growth mechanisms is present in both cases. A second inference, based on the approximately constant relative standard deviation of the growth rate, is that whatever mechanism retards crystal growth is proportional to the growth rate.

3.6 Local Environment as a Source of Variance

The large range of growth rates discussed above may result from an inherent phenomenon of protein crystal growth or from heterogeneities in local environment. Rank order of crystal growth rates provide insight into how well "mixed" the distribution of growth rates is. If crystal growth rates are drawn from a single population, one might expect the rank assigned to a certain crystal to vary throughout the experiment in some random fashion. If all the crystals are equivalent, the final rankings should be only weakly correlated with initial rankings. A high degree of correlation, on the other hand, would indicate that the initial growth rate dominates the behavior of the sample, environmental influences dictate growth rate distributions, or both.

For each experiment, Spearman rank correlation coefficients, r_S, were calculated for both the growth rate over each interval and the net growth (Tables 3-9 and 3-10). Most of the correlation coefficients are significantly greater than zero. The overall agreement of the rankings can be tested with the Kendall coefficient of concordance, W. The average Spearman correlation coefficient is related to the Kendall coefficient of concordance by $\bar{r}_S = (kW - 1)/(k - 1)$, where k = number of sets of rankings [1]. The significance of W can be tested with the statistic $x = k (N - 1)W$, which has a χ^2 distribution with $N - 1$ degrees of freedom; N = sample population . $N = 32$ and $k = 11$ in the quiescent experiment, while the flow experiment has $N = 51$ and $k = 4$. Quiescent growth rates are internally correlated with $\bar{r}_{S,rate} = 0.39$, $W_{rate} = 0.44$, and $x_{rate} = 152$; rankings of quiescent net growth give

Table 3-9

Spearman correlation matrix for quiescent crystals.

Round	Round										
	2	3	4	5	6	7	8	9	10	11	12
2	1.00	0.30**	0.24*	0.33**	0.27*	0.52***	0.04	0.02	0.08	0.12	0.03
3	0.56***	1.00	0.36**	0.68***	0.55***	0.38***	0.69***	0.54***	0.49***	0.23	0.36**
4	0.31**	0.80***	1.00	0.52***	0.62***	0.59***	0.60***	0.43***	0.37**	0.10	0.45***
5	0.18	0.73***	0.94***	1.00	0.55***	0.46***	0.66***	0.48***	0.42***	0.07	0.40**
6	0.06	0.63***	0.89***	0.92***	1.00	0.50***	0.64***	0.58***	0.45***	0.22	0.30**
7	0.12	0.66***	0.91***	0.93***	0.98***	1.00	0.28*	0.26*	0.22	0.42***	0.50***
8	0.06	0.64***	0.89***	0.93***	0.98***	0.97***	1.00	0.55***	0.57***	0.11	0.62***
9	0.08	0.65***	0.88***	0.91***	0.97***	0.95***	0.98***	1.00	0.49***	0.18	0.44***
10	0.08	0.63***	0.87***	0.90***	0.96***	0.92***	0.96***	0.98***	1.00	0.48***	0.42***
11	0.06	0.63***	0.85***	0.87***	0.94***	0.92***	0.95***	0.96***	0.97***	1.00	0.19
12	0.06	0.61***	0.83***	0.85***	0.90***	0.90***	0.93***	0.95***	0.96***	0.98***	1.00

Significance: * $p < 0.1$; ** $p < 0.05$; *** $p < 0.01$.

The full matrix is symmetric. Correlations between growth rates are in upper right half; correlations between net growth are in lower left. $N = 32$.

98

Table 3-10

Spearman correlation matrix for flow crystals

Round	Round			
	3	4	5	6
3	1.000	0.424***	0.232**	0.440***
4	0.883***	1.000	0.426***	0.474***
5	0.651***	0.811***	1.000	0.548***
6	0.613***	0.741***	0.548***	1.000

Significance: * $p < 0.1$; ** $p < 0.05$; *** $p < 0.01$.

The full matrix is symmetric. Correlations of growth rates are in upper right half; correlations of net growth are in lower half. $N = 51$.

$\bar{r}_{S,net} = 0.74$, $W_{net} = 0.77$, and $x_{net} = 262$. Both x_{rate} and x_{net} exceed the critical value of $\chi^2_{crit} = 44.7$ ($p < 0.05$, 31 df), so the internal correlation is deemed significant. Flow crystals follow the same pattern, with $\bar{r}_{S,rate} = 0.42$, $W_{rate} = 0.57$, and $x_{rate} = 114$, while $\bar{r}_{S,net} = 0.77$, $W_{net} = 0.82$, and $x_{net} = 165$; $\chi^2_{crit} = 67.2$ ($p < 0.05$, 50 df). The overall consistency of the rankings reflects the breadth of the growth rate distributions and suggests there may be an inherent reason why some crystals grow faster than others during the experiments.

The rankings of growth rate have statistical significance, but the reasons are unknown. Factors governing the relative growth rates can be divided into two classes: initial conditions, and environmental factors which determine long-term behavior. The current experiments provide no insight into the early stages of crystal growth, but can be used to determine whether environmental factors contribute to the apparent stratification of the growth rate distribution. The significance of environmental effects is tested in the same fashion as before: a suitable null hypothesis is presented and the statistical test provides the

criterion for acceptance or rejection. The focus of the experiments is on possible transport effects, so it is natural to examine environmental variables which could affect the accessibility of growing crystals. The local environment of a target crystal is defined to be the region within which a neighbor would perturb the depletion zone surrounding a diffusion-controlled spherical crystal. A quasi-steady analysis shows the range of the depletion region around such a crystal is approximately $L/2$, where L is the characteristic length (equivalent diameter) of the crystal. The three major variables which were tested for significance were: crowding, location, and contact.

Two crystals are said to crowd each other when their depletion layers overlap (their nearest surfaces are within L of each other). The final image of each crystal was displayed on the monitor and measured with a scale to obtain an estimate of L. The relative crowding of a given crystal is the number of neighbors lying within an envelope of thickness L surrounding the target crystal. If the target crystal was touching its neighbors, it was classified as "in contact;" otherwise, it was "no contact." Contact can be considered a severe (but difficult to quantify) form of crowding, which is why it is included in the list of environmental variables. The crystal's location was further divided according to center/edge and top/bottom dichotomies. A crystal was at the edge if its nearest surface was within L of a side wall, otherwise it was in the center. Top and bottom classifications were assigned according to the sampling sequence, as described in more detail where the test results are presented. Note that these classifications were made based on the final image of the crystal.

One-way ANOVA was performed on the growth rates over each interval to assess the significance of crowding as an environmental variable. As summarized in Table 3-11, crowding has a significant effect on growth rate only over the first interval of each experiment. The results are the same when $\ln G$ is the dependent variable. The apparent early significance of crowding may be an aberration, at least for the quiescent experiment, because crowding is not judged significant at the 95% confidence level by the

100

nonparametric Kruskal-Wallis test. Over the course of the experiment, it seems that crowding does not play a large role in determining crystal growth rates.

Table 3-11

Effect of crowding on crystal growth rates.

Round	ANOVA1† F	ANOVA2‡ F	Kruskal–Wallis H
Quiescent			
2	2.539*	3.375*	5.599
3	0.817	0.860	2.998
4	0.597	0.563	1.771
5	0.557	0.488	1.944
6	0.162	0.177	1.144
7	0.290	0.190	0.976
8	1.244	0.997	2.711
9	0.201	0.182	0.778
10	1.084	1.000	3.414
11	1.918	1.888	6.144
12	0.797	0.836	2.587
Flow			
3	2.729*	2.915*	8.925**
4	0.335	0.200	0.250
5	0.872	0.844	2.425
6	0.760	0.396	1.296

Significance: * $p < 0.1$; ** $p < 0.05$; *** $p < 0.01$.

† Analysis of variance performed on calculated growth rates.
‡ Analysis of variance performed on natural logarithm of calculated growth rates.

The proximity of a side wall consistently affects growth rates of quiescent crystals, at least according to all tests except the Wald-Wolfowitz runs test (Table 3-12). The effect first becomes significant during interval 3 and remains significant for the duration of the experiment. Apparently, the protein concentration was lower at the side walls than near the

Table 3-12

Effect of lateral location on crystal growth rates.

Round	ANOVA1[†] F	ANOVA2[‡] F	Mann–Whitney U	Kolmogorov –Smirnov χ^2	Wald–Wolfowitz runs
Quiescent					
2	2.155	1.675	84	5.303*	15
3	7.811***	9.220***	65**	6.574**	12
4	5.592**	5.510**	84**	7.900**	20
5	7.834***	7.032**	77***	8.292**	16
6	7.435***	3.446*	83***	12.315***	12**
7	6.636**	8.105***	87***	7.786**	13*
8	9.368***	5.967**	75***	9.494***	16
9	11.907***	9.074***	63***	11.029***	16
10	12.733***	12.731***	70***	9.494***	10***
11	5.902**	6.351**	104**	4.952*	16
12	12.896***	12.916***	71***	12.678***	12**
Flow					
3	0.878	0.933	187	2.196	19
4	0.745	1.472	198	2.352	16
5	0.069	0.010	210	1.413	15
6	0.232	0.484	207	1.236	18

Significance: * $p < 0.1$; ** $p < 0.05$; *** $p < 0.01$.

† Analysis of variance performed on calculated growth rates.
‡ Analysis of variance performed on natural logarithm of calculated growth rates.

center. The flow of fresh feed solution through the cell may have left stagnant regions near the walls. There is no obvious reason why the concentration should differ between center and edges, but depletion of protein by the growing crystals does not seem to be the cause. If the crystals are divided into two groups based on their locations, and their growth rates over intervals 5 - 12 are correlated with both elapsed time and crystal size (as was done in section 3.3), there is no indication that the two groups show different trends (Table 3-13).

Examination of the means and standard deviations of the two groups shows that crystals at the edge grow slower and display a greater relative variability than those in the center (Table 3-14). Crystals from the flow experiment show no significant effect of location.

Table 3-13

Correlation matrix for center and edge quiescent crystals beginning in round 5.

	$t_{mid,i,n}$	$G_{i,n}$	$L_{i,n}$
$t_{mid,i,n}$	1.000	0.248***	0.843***
$G_{i,n}$	0.318***	1.000	0.483***
$L_{i,n}$	0.886***	0.478***	1.000

Significance: * $p < 0.1$; ** $p < 0.05$; *** $p < 0.01$.

The full correlation matrix is symmetric. Edge crystal correlations are shown in the upper right half of the matrix; center crystals are in the lower left. $N_e = 111$ and $N_c = 200$.

The differences between quiescent crystals in the center of the cell and those at the edge may result from inhomogeneities in the local environment produced by sporadic flow through the cell. There may also be a top/bottom variation similar to the center/edge effect already presented. As discussed in section 2.6, the sequence in which crystals were digitized progressed generally from top to bottom in the quiescent experiment and from bottom to top in the flow experiment. Crystals can then be classified as "top" or "bottom" depending on where they fall in the sampling sequence. For purposes of testing the null hypothesis that there is no difference between top and bottom, the first 19 quiescent crystals were designated top and the last 20 were bottom. Likewise, the first 26 flow crystals were bottom and the last 27 were top. Comparisons of the growth rates of the two groups are shown in Table 3-15. Height seems significant in the early rounds of the quiescent experiment, but its significance becomes less consistent as the experiment progresses. Results for the flow experiment are mixed, with no obvious pattern. When

103

net growth is examined (Table 3-16), the early significance of height in the quiescent experiment dominates the results. The cumulative effect of height is probably significant ($p < 0.1$) in the flow experiment.

Table 3-14

Comparison of quiescent center and edge crystals.

Round	Growth rates (nm/min)				Net growth (μm)			
	Center		Edge		Center		Edge	
	Mean	Std. dev.	Mean	Std. dev.	Mean	Std. dev.	Mean	Std. dev.
2	22.30	5.38	19.64	3.63	14.22	3.42	13.68	2.43
3	15.98	3.16	12.90	2.94	40.71	6.11	34.68	4.17
4	11.90	1.67	10.52	1.76	76.03	8.34	65.90	7.42
5	6.68	1.52	5.26	1.40	95.29	11.90	80.76	9.93
6	6.89	1.90	5.11	2.06	120.19	17.84	98.60	14.43
7	6.68	1.14	5.41	1.94	135.94	19.10	111.61	16.95
8	8.13	1.88	6.10	2.20	157.36	23.24	126.73	19.47
9	9.70	1.78	7.52	2.10	185.56	26.20	147.41	21.42
10	9.14	1.37	7.22	1.98	210.68	28.39	166.70	25.00
11	7.76	1.32	6.65	1.48	233.70	28.90	185.86	26.61
12	8.01	1.70	5.90	1.86	255.41	30.43	202.10	30.33

Reported standard deviation is unbiased estimate for the population, $s \ [N /(N - 1)]^{1/2}$.

Table 3-15

Effect of height on crystal growth rates.

Round	ANOVA1[†] F	ANOVA2[‡] F	Mann–Whitney U	Kolmogorov–Smirnov χ^2	Wald–Wolfowitz runs
Quiescent					
2	3.400*	2.649	76**	8.000**	15
3	6.178**	5.477**	79***	10.111***	13*
4	4.385**	4.996**	115*	7.443**	16
5	13.310***	12.556***	70***	11.463***	16
6	11.950***	11.368***	79***	11.122***	15
7	7.146**	6.410*	111**	6.154**	20
8	2.367	8.413***	123*	7.709**	17
9	1.295	0.708	146	3.446	20
10	5.619**	6.098**	111**	9.438***	19
11	0.002	0.140	186	3.326	17
12	0.767	1.325	172	6.073**	16
Flow					
3	3.110*	2.804	273	2.833	24
4	6.478**	5.443**	236**	6.401**	24
5	0.260	0.127	290	4.257	26
6	1.606	0.825	296	6.506**	21*

Significance: * $p < 0.1$; ** $p < 0.05$; *** $p < 0.01$.

† Analysis of variance performed on calculated growth rates.
‡ Analysis of variance performed on natural logarithm of calculated growth rates.

C-3

Table 3-16

Effect of height on net crystal growth.

Round	ANOVA1[†] F	ANOVA2[‡] F	Mann–Whitney U	Kolmogorov–Smirnov χ^2	Wald–Wolfowitz runs
Quiescent					
2	5.068**	4.974**	71**	8.000**	14
3	0.276	0.200	113	1.125	19
4	5.314**	5.770**	78.5*	6.125**	18
5	8.435***	9.234***	63**	8.000**	16
6	11.05?***	12.045***	54***	10.125***	14
7	11.194***	12.167***	59***	12.500***	12
8	10.202***	11.066***	59***	10.125***	16
9	8.081***	8.773***	68**	10.125***	14
10	8.290***	8.917***	69**	10.125***	14
11	7.668***	8.554***	70**	10.125***	15
12	7.084**	8.001***	75**	10.125***	11**
Flow					
3	2.408	2.090	279	2.206	30
4	2.597	2.066	301	2.305	32
5	3.311*	2.524	230*	4.890*	23
6	2.929*	2.182	229*	5.491*	29

Significance: * $p < 0.1$; ** $p < 0.05$; *** $p < 0.01$.

† Analysis of variance performed on net growth.
‡ Analysis of variance performed on natural logarithm of net growth.

Crystals in the upper half of the cell have narrower distributions of growth rates and net growth than do those in the lower half (Table 3-17). The behavior of the mean growth rate is different in the two experiments: crystals at the top grow faster than those at the bottom during the quiescent experiment, but slower during the flow experiment. Correlation matrices (Tables 3-18 and 3-19) show that the growth rates of top crystals are more negatively correlated than bottom crystals with both elapsed time and crystal size. The significance of the differences in correlation coefficients can be tested with the statistic $x = (z_t - z_b)/(\sigma_t^2 + \sigma_b^2)^{1/2}$, which is approximately normal (0,1). As before, $z = (1/2) \, ln \, [(1 + r)/(1 - r)]$ and $\sigma^2 = (N - 3)^{-1}$. The correlations of growth rate and time give values of $x = -1.64$ for the quiescent experiment and $x = -1.38$ for the flow experiment. When the null hypothesis $x = 0$ is tested against the alternative $x < 0$, both values are probably significant ($p < 0.1$) in one-tailed tests. Correlations of growth rate and crystal size yield values $x = -3.86$ and -3.14, both of which are highly significant ($p < 10^{-3}$) in one-tailed tests. Although the reason is not apparent, height seems to influence the trends in crystal growth.

The effect of crystal contact on growth rate is intermittently significant according to ANOVA on both G and $ln \, G$ (Table 3-20). The nonparametric Mann-Whitney U test confirms the significance of contact over rounds 3, 6, 8, 9, and 10 of the quiescent experiment. The Kolmogorov-Smirnov two-sample test finds contact is at least probably significant ($p < 0.1$) in all rounds but 2, 7, and 11. The Wald-Wolfowitz test is alone in failing to reject the null hypothesis. Identical tests on flow crystals uniformly show that crystal contact is not significant. The apparent significance of contact beginning in round 3 of the quiescent experiment is puzzling. On physical grounds, the effects of contact are not expected to be important until the crystals are in contact or at least near contact. Tests for independence (§3.6) show that the probability of classifying a quiescent crystal as "in contact" depends on its height, so the apparent early significance of contact is actually a product of top/bottom variations.

107

Table 3-17

Comparison of top and bottom crystals.

Round	Growth rates (nm/min)				Net growth (μm)			
	Top		Bottom		Top		Bottom	
	Mean	Std. dev.	Mean	Std. dev.	Mean	Std. dev.	Mean	Std. dev.
Quiescent								
2	22.94	5.43	19.83	4.03	12.88	2.79	15.19	3.01
3	16.37	3.70	13.70	2.62	39.22	6.88	38.06	5.55
4	12.06	1.26	10.87	2.03	76.10	7.25	68.99	9.97
5	7.06	1.15	5.41	1.59	96.35	9.58	84.24	13.64
6	7.31	1.24	5.25	2.31	122.74	12.74	102.79	20.33
7	6.86	1.37	5.61	1.55	138.65	13.21	116.50	22.95
8	7.95	2.35	6.88	1.97	159.85	17.41	133.81	27.57
9	9.32	2.08	8.54	2.21	186.27	20.69	158.62	32.95
10	9.13	1.14	7.80	2.16	211.24	23.05	179.88	39.96
11	7.38	0.99	7.36	1.83	233.27	22.84	201.24	40.23
12	7.54	1.59	6.98	2.36	254.05	23.60	220.12	45.22
Flow								
3	20.03	2.42	21.64	4.00	38.17	4.60	40.85	7.56
4	16.64	3.06	20.00	6.13	53.76	6.07	58.02	12.14
5	15.90	3.53	16.41	3.79	85.30	9.67	92.48	17.78
6	13.15	2.75	14.47	4.61	125.55	17.06	136.95	29.54

Reported standard deviation is unbiased estimator for population, s $[N/(N-1)]^{1/2}$.

Table 3-18

Correlation matrix for top and bottom quiescent crystals beginning in round 5.

	$t_{mid,i,n}$	$G_{i,n}$	$L_{i,n}$
$t_{mid,i,n}$	1.000	0.178**	0.917***
$G_{i,n}$	0.352***	1.000	0.300***
$L_{i,n}$	0.830***	0.634***	1.000

Significance: * $p < 0.1$; ** $p < 0.05$; *** $p < 0.01$.

The full correlation matrix is symmetric. Top crystal correlations are shown in the upper right half of the matrix; bottom crystals are in the lower left. $N_t = 151$ and $N_b = 160$.

Table 3-19

Correlation matrix for top and bottom flow crystals.

	$t_{mid,i,n}$	$G_{i,n}$	$L_{i,n}$
$t_{mid,i,n}$	1.000	-0.638***	0.868***
$G_{i,n}$	-0.510***	1.000	-0.472***
$L_{i,n}$	0.787***	-0.073	1.000

Significance: * $p < 0.1$; ** $p < 0.05$; *** $p < 0.01$.

The full correlation matrix is symmetric. Top crystal correlations are shown in the upper right half of the matrix; bottom crystals are in the lower left. $N_t = 109$ and $N_b = 102$.

Table 3-20

Effect of contact on crystal growth rates.

Round	ANOVA1[†] F	ANOVA2[‡] F	Mann– Whitney U	Kolmogorov –Smirnov χ^2	Wald– Wolfowitz runs
Quiescent					
2	1.317	1.129	86	1.911	15
3	7.454**	8.255***	57***	9.740***	12
4	2.775	2.987*	107	4.683*	16
5	1.552	0.929	107	6.240	17
6	15.030***	11.660***	56***	12.037***	16
7	0.015	0.062	156	1.641	16
8	17.084***	14.858***	48***	11.670***	14
9	15.394***	14.059***	61***	9.917***	12*
10	8.804***	10.176***	92***	6.293**	18
11	2.702	3.287*	123	3.490	20
12	4.957**	5.544**	98*	7.704**	16
Flow					
3	0.016	0.006	195	2.709	15
4	0.252	0.225	176	1.898	17
5	1.391	0.966	164	2.202	17
6	0.386	0.250	191	3.012	17

Significance: * $p < 0.1$; ** $p < 0.05$; *** $p < 0.01$.

† Analysis of variance performed on calculated growth rates.
‡ Analysis of variance performed on natural logarithm of calculated growth rates.

It seems odd that the effect of contact should differ in the two experiments. If the effect results from physical contact, one would not expect forced convection to mitigate the effect. The absence of an effect in the flow experiment may reflect shortcomings in both the experiment and the analysis. It is possible that the flow experiment may simply have ended before the impact of contact was apparent. Final images of flow crystals in contact, however, show that some of them are highly intergrown. If contact had an effect in the flow experiment, it should have been evident in these crystals. A more plausible

explanation, although one which cannot be tested rigorously with current image analysis routines, is that the apparent reduced growth rates derive from restrictions placed on the data analysis method. The crystal dimensions reported are those corresponding to the best-fit ideal crystal which can be superimposed on a given image; growth rates are obtained by calculating how these ideal dimensions change with time. For highly asymmetrical crystals, these ideal dimensions may not accurately reflect the true size. The data analysis routine determines some sort of average growth rate; asymmetries due to contact reduce the average growth rate by eliminating the contribution of those faces in contact with neighbors. The orientation of crystals in contact with their neighbors may differ in the two experiments so that {110} faces in the quiescent experiment are more occluded than those in the flow experiment. A thorough survey of all images is required to determine if this explanation is reasonable. Future experiments should resolve the issue.

Three environmental variables, location, height, and contact, were found to have significance in the quiescent experiment. In order to determine whether each variable predicts an independent portion of the total variance, a three-way ANOVA was performed on the net growth of quiescent crystals with location, height, and contacts as independent variables. The findings are summarized in Tables 3-21 (net growth) and 3-22 (logarithm of net growth). As mentioned above, contact is not found to be significant until later in the experiment, when crystals are in near contact. Each of the three variables accounts for a different portion of the sample variance, so it is not surprising the quiescent crystals have a broader distribution than the flow crystals, which can be separated only by height.

Statistically significant variation in local environment (as defined by crystal contact and location) has been found in both the flow and quiescent experiments. Undoubtedly, this heterogeneity contributes to the apparent differences in behavior of flow and quiescent crystals, but the experiments conducted so far provide no way to assess this contribution. The current experiments suggest there are some effects of flow, but results such as these must remain suggestive until other factors have been eliminated as causes. Although

111

environmental factors confuse the interpretation of the growth experiments in the short term, the results of this section provide a guide for increasing the utility of future experiments: redesign the experiment to make crystal environments more uniform.

Table 3-21

Three-way ANOVA of net growth of quiescent crystals.

Round	Height (A)	Contact (B)	Location (C)	Interactions (AB)	(AC)	(BC)	(ABC)
2	3.68*	0.27	0.33	0.17	<0.01	<0.01	0.16
3	0.34	5.13**	7.35**	0.20	0.41	0.79	1.07
4	3.69*	2.47	7.42**	0.32	<0.01	<0.01	1.94
5	6.27**	1.40	8.55***	0.26	0.02	0.03	2.37
6	8.84***	3.29*	8.30***	0.92	0.03	0.02	1.61
7	10.34***	1.49	7.54**	0.92	0.21	0.08	1.12
8	7.29**	4.19*	10.62***	0.31	0.10'	0.06	2.35
9	5.40**	8.14***	16.20***	0.08	0.45	0.16	4.56**
10	5.76**	9.25***	18.74***	0.05	0.34	0.43	4.67**
11	6.04**	8.72***	18.86***	0.07	<0.01	0.01	3.71*
12	5.71**	7.92***	19.71***	0.10	0.06	0.28	3.01*

Significance: * $p < 0.1$; ** $p < 0.05$; *** $p < 0.01$.

Table 3-22

Three-way ANOVA of logarithm of net growth of quiescent crystals.

Round	Height (A)	Contact (B)	Location (C)	Interactions			
				(AB)	(AC)	(BC)	(ABC)
2	3.18*	0.20	0.18	0.32	0.01	<0.01	0.10
3	0.62	7.04**	9.20***	0.35	0.79	1.64	1.97
4	4.19*	2.70	7.52**	0.38	0.01	0.03	1.80
5	7.07**	1.53	8.62***	0.25	<0.01	0.06	2.22
6	9.84***	3.50*	7.76**	1.03	<0.01	0.06	1.33
7	11.48***	1.45	7.11**	0.94	0.38	0.06	0.92
8	8.03***	4.24*	10.13***	0.30	0.04	0.12	2.14
9	5.88**	8.90***	16.06***	0.05	0.47	0.33	4.77**
10	6.20**	10.22***	18.99***	0.02	0.35	0.77	4.84**
11	7.01**	9.28***	19.68***	0.05	<0.01	0.29	3.71*
12	6.70**	8.40***	20.40***	0.08	0.11	0.57	2.83

Significance: $* p < 0.1$; $** p < 0.05$; $*** p < 0.01$.

3.7 Tests of Sample Properties Not Related to Growth Rates

Differences in the behavior of the sample populations may result from differences in the way samples were selected. Sampling biases may skew the selection of crystals so that, for example, one experiment may have a much higher percentage of edge crystals than the other. In what follows, the samples are compared with each other to determine if sampling biases could be responsible for the effects noted in section 3.6. Inferences about the underlying population can be drawn only if one is willing to assume that the samples are representative of the population, an assumption that cannot be tested independently.

The following tests use contingency tables and the χ^2 statistic to test for sampling homogeneity between the two experiments. For example, the contingency table of crowding level in the two experiments is given in Table 3-23. Under the null hypothesis that the distribution of crowding levels is the same in both experiments, the marginal values provide estimates of the probability of each class: 16.30% with none, 45.65% with low, 26.09% with medium, and 11.96% with high. The expected number of crystals with a given crowding level is computed for each experiment and the total χ^2 is then calculated and checked for significance. In this case, $\chi^2 = 6.74 < \chi^2_{crit} = 7.81$, so the hypothesis is accepted that the crowding class frequencies are the same in both experiments.

Table 3-23

Contingency table of crowding and experiment

| Crowding | Experiment | | | | Totals |
| | Quiescent | | Flow | | |
	Observed	Expected	Observed	Expected	
None	3	(6.36)	12	(8.64)	15
Low	19	(17.80)	23	(24.20)	42
Medium	14	(10.17)	10	(13.83)	24
High	3	(4.66)	8	(6.34)	11
Totals	39		53		92

A contingency table for location is given in Table 3-24. With $\chi^2 = 2.60$, the fraction of sample crystals taken from the edge regions is seen to be the same in each experiment. The probability of selecting crystals in contact with others was also checked against the null hypothesis. The observed marginal values (Table 3-25) show that 76.09% of those crystals sampled should have no contact with their neighbors. A value of $\chi^2 = 1.75 < \chi^2_{crit} = 3.84$ suggests that no real difference exists between the experiments. The χ^2

tests of class frequencies indicate the samples in the two experiments are homogeneous, and differences between the two experiments cannot be attributed to sampling differences.

Table 3-24

Contingency table of location and experiment.

| Location | Experiment | | | | Totals |
| | Quiescent | | Flow | | |
	Observed	Expected	Observed	Expected	
Center	25	(28.40)	42	(38.60)	67
Edge	14	(10.60)	11	(14.40)	25
Totals	39		53		92

Table 3-25

Contingency table of contact and experiment.

| Contact | Experiment | | | | Totals |
| | Quiescent | | Flow | | |
	Observed	Expected	Observed	Expected	
No contact	27	(29.67)	43	(40.33)	70
In contact	12	(9.33)	10	(12.67)	22
Totals	39		53		92

Comparisons of the sample orientation distributions can be made to decide if: (i) the crystals in the two experiments could have been drawn from the same population, and (ii) there is a preferred orientation. Mann-Whitney, Kolmogorov-Smirnov, and Wald-Wolfowitz tests were used to decide the first issue; ANOVA was not used since there is no reason to believe that either θ or ϕ is normally distributed. The Kolmogorov-Smirnov two-sample test (Table 3-26) indicates the difference in θ_z orientations of the z-axis between the two experiments is highly significant ($p < 0.01$), while the difference is probably significant according to the Mann-Whitney U test ($p < 0.1$). The sample distributions of ϕ_z

could well have been drawn from the same distribution. The existence of preferred orientations is tested by comparing the observed sample cumulative distribution function with the appropriate uniform distribution function under the null hypothesis. For θ, the appropriate cumulative distribution function is $F(\theta_n) = 1 - cos\ \theta_n$, where n = the rank of the observation; the observed sample cumulative distribution function of ϕ is compared with $F(\phi_n)=\phi_n/360°$. The cumulative distribution functions are shown in Figures 3-3 and 3-4. At the 95% confidence level, the Kolmogorov-Smirnov tests reject the null hypothesis that the crystal orientations are uniformly distributed over θ and ϕ in favor of the alternative that some orientations are preferred.

Table 3-26

Comparison of orientation distributions.

Angle	Mann–Whitney U	Kolmogorov–Smirnov χ^2	Wald–Wolfowitz runs
θ_z	824*	9.84***	38
ϕ_z	876	4.99	50

Significance: * $p < 0.1$; ** $p < 0.05$; *** $p < 0.01$.

Contingency tables can also be used to assess whether class frequencies of the independent variables are in fact independent events. Earlier, the probability a quiescent crystal is in contact was said to be dependent on its height. The contingency table for height and contact in the quiescent experiment is shown in Table 3-27; the expected values based on the marginal values are also given in the table. If contact and height are independent, the cell totals would be the product of sample size and the marginal probabilities. The total $\chi^2 = 3.90 > \chi^2_{crit} = 3.84$ ($p < 0.05$), so the null hypothesis of independence is rejected. Contact and height are independent events in the flow experiment; $\chi^2 = 1.79$ (Table 3-28). If the marginal totals for each experiment are replaced

116

by the marginal totals for the pooled experiments, the results are the same, with $\chi_q^2 = 5.61$ $> \chi_{crit}^2$ and $\chi_f^2 = 2.25 < \chi_{crit}^2$. Contingency tables (Tables 3-29 and 3-30) suggest that height is independent of crowding level ($\chi_f^2 = 5.47 < \chi_q^2 = 5.77 < \chi_{crit}^2 = 7.81$, $p < 0.05$), and that height and location (Tables 3-31 and 3-32) are also independent ($\chi_f^2 = 0.07 < \chi_q^2 = 1.48 < \chi_{crit}^2 = 3.84$)
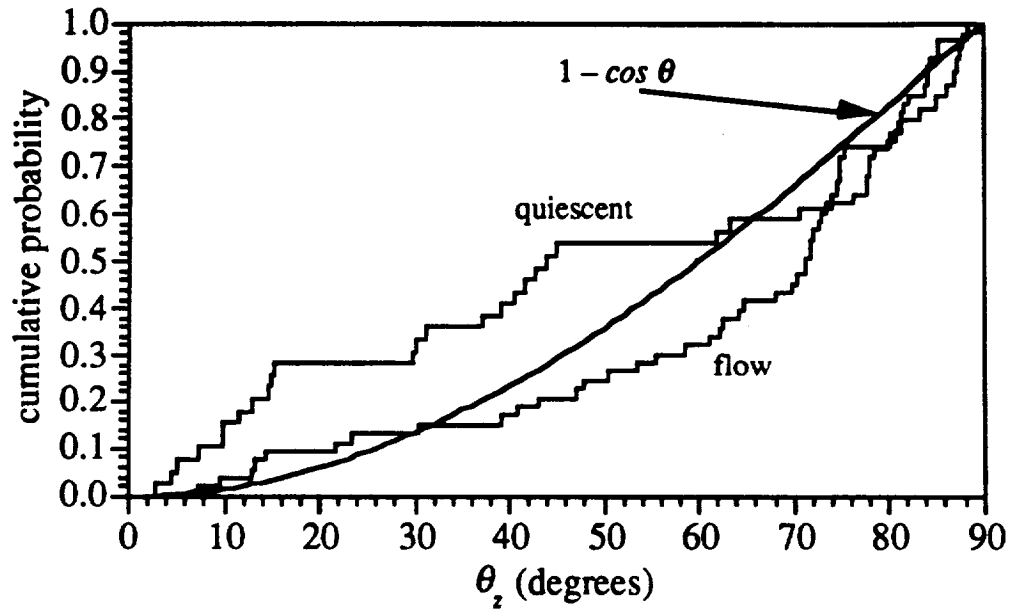
Figure 3-3: Cumulative distribution function for θ_z.

The observed frequency tables for location and crowding for the experiments are given in Tables 3-33 and 3-34. The calculated values of $\chi_q^2 = 4.88$ and $\chi_f^2 = 3.53$ are consistent with the hypothesis that crowding level and location are independent; i.e., the number of neighbors present does not depend on where the crystal is located. There may be some association between location and contact in the quiescent experiment (Table 3-35; $\chi_q^2 = 3.79 > \chi_{crit}^2 = 2.71$, $p < 0.1$, 1 df), but location is independent of contact in the flow experiment, as shown in Table 3-36 ($\chi_f^2 = 0.87$). Finally, the probability that a crystal is in contact with a neighboring crystal is shown to be independent of crowding level, provided there is at least one neighbor (Tables 3-37 and 3-38; $\chi_q^2 = 3.04 < \chi_f^2 = 3.56 < \chi_{crit}^2 = 4.61$, $p < 0.1$, 2 df). Only crystals with neighbors have been included in Tables 3-37 and 3-38.
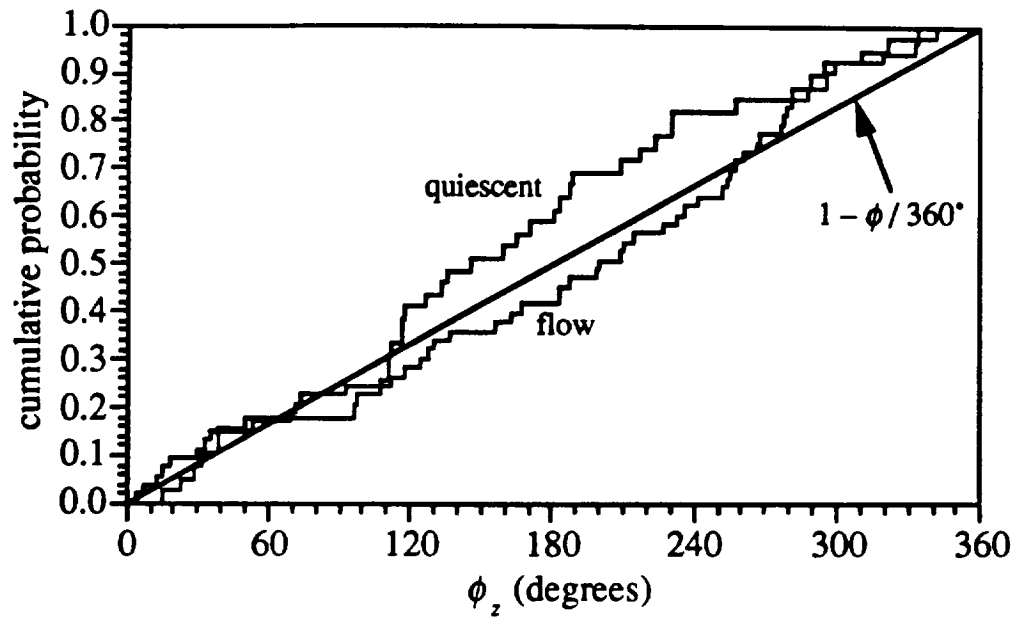
Figure 3-4: Cumulative distribution function for ϕ_z.

Table 3-27

Contingency table of height and contact for quiescent crystals.

Height	Contact				Totals
	No contact		In contact		
	Observed	Expected	Observed	Expected	
Top	16	(13.15)	3	(5.85)	19
Bottom	11	(13.85)	9	(6.15)	20
Totals	27		12		39

With the possible exception of crystal orientation, tests for sampling bias fail to find any statistically significant differences between the samples chosen for each experiment. The effect, if any, of crystal orientation on growth is unknown. Forced convection is not responsible for differences in crystal orientation, however, because nucleation and attachment of crystals to the walls of the growth cell occur during the initial period of quiescence. Classifications according to crowding, location, height, and contact are found to be mutually independent, except for some association between height and contact in the

118

quiescent experiment. Differences in the behavior of quiescent and flow crystals cannot be attributed to disparities in sample selection.

Table 3-28

Contingency table of height and contact for flow crystals.

| Height | Contact | | | | Totals |
| | No contact | | In contact | | |
	Observed	Expected	Observed	Expected	
Top	20	(21.91)	7	(5.09)	27
Bottom	23	(21.09)	3	(4.91)	26
Totals	43		10		53

Table 3-29

Contingency table of crowding and height for quiescent crystals.

| Crowding | Height | | | | Totals |
| | Top | | Bottom | | |
	Observed	Expected	Observed	Expected	
None	2	(1.46)	1	(1.54)	3
Low	12	(9.26)	7	(9.74)	19
Medium	5	(6.82)	9	(7.18)	14
High	0	(1.46)	3	(1.54)	3
Totals	19		20		39

Table 3-30

Contingency table of crowding and height for flow crystals.

Crowding	Height Top Observed	Top Expected	Bottom Observed	Bottom Expected	Totals
None	9	(6.11)	3	(5.89)	12
Low	10	(11.72)	13	(11.28)	23
Medium	3	(5.09)	7	(4.91)	10
High	5	(4.08)	3	(3.92)	8
Totals	27		26		53

Table 3-31

Contingency table of height and location for quiescent crystals.

Height	Location Center Observed	Center Expected	Edge Observed	Edge Expected	Totals
Top	14	(12.18)	5	(6.82)	19
Bottom	11	(12.82)	9	(7.18)	20
Totals	25		14		39

Table 3-32

Contingency table of height and location for flow crystals.

Height	Location Center Observed	Center Expected	Edge Observed	Edge Expected	Totals
Top	21	(21.40)	6	(5.60)	27
Bottom	21	(20.60)	5	(5.40)	26
Totals	42		11		53

Table 3-33

Contingency table of crowding and location for quiescent crystals.

Crowding	Center		Edge		Totals
	Observed	Expected	Observed	Expected	
None	1	(1.92)	2	(1.08)	3
Low	14	(12.18)	5	(6.82)	19
Medium	7	(8.97)	7	(5.03)	14
High	3	(1.92)	0	(1.08)	3
Totals	25		14		39

Table 3-34

Contingency table of crowding and location for flow crystals.

Crowding	Center		Edge		Totals
	Observed	Expected	Observed	Expected	
None	10	(9.51)	2	(2.49)	12
Low	16	(18.23)	7	(4.77)	23
Medium	8	(7.92)	2	(2.08)	10
High	8	(6.34)	0	(1.66)	8
Totals	42		11		53

Table 3-35

Contingency table of contact and location for quiescent crystals.

Contact	Location				Totals
	Center		Edge		
	Observed	Expected	Observed	Expected	
No contact	20	(17.31)	7	(9.69)	27
In contact	5	(7.69)	7	(4.31)	12
Totals	25		14		39

Table 3-36

Contingency table of contact and location for flow crystals.

Contact	Location				Totals
	Center		Edge		
	Observed	Expected	Observed	Expected	
No contact	33	(34.08)	10	(8.92)	43
In contact	9	(7.92)	1	(2.08)	10
Totals	42		11		53

Table 3-37

Contingency table of crowding and contact for quiescent crystals.

Crowding	Contact				Totals
	No contact		In contact		
	Observed	Expected	Observed	Expected	
Low	15	(12.67)	4	(6.33)	19
Medium	7	(9.33)	7	(4.67)	14
High	2	(2.00)	1	(1.00)	3
Totals	24		12		36

Table 3-38

Contingency table of crowding and contact for flow crystals.

| Crowding | Contact | | | | Totals |
| | No contact | | In contact | | |
	Observed	Expected	Observed	Expected	
Low	19	(17.39)	4	(5.61)	23
Medium	8	(7.56)	2	(2.44)	10
High	4	(6.05)	4	(1.95)	8
Totals	31		10		41

3.8 Summary and Discussion

These experiments clearly show a feature of protein crystal growth which has not yet been fully appreciated, namely that there is an inherently large variation in crystal growth rates and sizes. In both of the experiments reported here, growth rates have a range of 120% of the mean. Crystal growth tended to slow in both experiments, but there was a qualitative difference between quiescent crystals and those exposed to weak convection. The growth rates of crystals in the quiescent experiment generally tracked the measured protein concentration, while flow crystals exhibited a slowing of growth even when exposed to a slightly increased protein concentration. The flow experiment was terminated by equipment problems after only 5000 minutes had elapsed; at the same point in the quiescent experiment, the mean crystal growth rate had just completed what proved to be an initial downward transient. The effects of flow on average crystal growth rates cannot be determined unambiguously from these experiments because the flow experiment provides clear information about short-term behavior and the quiescent experiment gives details about long-term behavior.

The behavior of quiescent crystals after the initial transient provides some hint of the effect of natural convection on the growth of lysozyme crystals. Over the final 10,000

minutes of the experiment, when protein concentration was approximately constant, there is no evidence that crystal growth rates slowed as a result of flow. The average {110} dimension of these crystals approximately doubled from 156 μm to 322 μm during this time, placing the crystals in the size range where convective flow might be significant. The absence of a statistically significant effect over this size range suggests that retardation of growth occurs either early in crystal growth, in which case flow is not responsible, or at larger crystal sizes, which, in light of the reported "cessation of growth" phenomenon, requires the effect to be relatively abrupt. Future longevity studies of protein crystal growth should yield evidence to determine which scenario is more likely.

Comparisons of the dispersion in growth rates and net growth show that flow crystals could have been drawn from a narrower distribution than quiescent crystals. This is probably related to the smoothing effect of flow, which tends to make conditions in the growth cell more uniform than in the quiescent experiment. Crystals in the flow experiment can be separated into two groups depending on whether they are in the upper or lower half of the growth cell. In contrast, quiescent crystals also show sensitivity to their placement relative to the side walls of the cell and to contact with their neighbors. Tests for sampling bias show that the samples are relatively well matched, so that sampling errors are not responsible for differences in behavior in the two experiments.

It is hard to draw definitive conclusions about the effect of flow because the large amount of heterogeneity within an experiment blurs distinctions between the two experiments. Nevertheless, there are hints that flow has some sort of influence on crystal growth, although the size of the effect has yet to be demonstrated. These experiments, which lasted longer than any other reported growth experiments, have shown that tetragonal lysozyme crystals may behave in a manner which cannot be predicted on the basis of simple quasi-steady models of crystal growth. A great deal could be learned from an extended, better controlled, version of these experiments. If crystals slow their growth, long-term studies will reveal the manner in which this occurs and indicate which

mechanisms may be important in protein crystal growth. At that point, a fair assessment of the effects of flow could be made.

References

[1] Siegel, S. *Nonparametric Statistics for the Behavioral Sciences*. New York: McGraw-Hill, 1956.

[2] Pollard, J. H. *A Handbook of Numerical and Statistical Techniques*. Cambridge: Cambridge University Press, 1977.

[3] Brunk, H. D. *An Introduction to Mathematical Statistics 2d ed*. Waltham, MA: Blaisdell, 1965.

[4] Abacus Concepts. *Statview II*. Berkeley, CA: Abacus Concepts, 1987.

[5] Selby, S. M. ed. *Standard Mathematical Tables 21st ed*. Cleveland: Chemical Rubber Co., 1973.

[6] International Mathematical Subroutine Library. *STAT/LIBRARY v* 1.0. Houston, TX: IMSL, 1987.

[7] Durbin, S. D. and G. Feher. *J. Crystal Growth*. **76** (1986) 583-592.

[8] U. S. Dept. of Commerce. Natl. Bureau of Standards. *Experimental Statistics (NBS Handbook 91)*. Washington, DC: Government Printing Office, 1963.

[9] Miller, I. and J. E. Freund. *Probability and Statistics for Engineers*. Englewood Cliffs, NJ: Prentice-Hall, 1965.

[10] Pusey, M. L., R. S. Snyder and R. Naumann. *J. Biol. Chem.* **261** (1986) 6524-6529.

[11] Pusey, M. and R. Naumann. *J. Crystal Growth*. **76** (1986) 593-599.

[12] Grant, M. L. and D. A. Saville. *J. Crystal Growth*. **108** (1991) 8-18.

[13] Pusey, M., W. Witherow and R. Naumann. *J. Crystal Growth*. **90** (1988) 105-111.

[14] Kam, Z., H. B. Shore and G. Feher. *J. Mol. Biol.* **123** (1978) 539-555.

CHAPTER 4

Colloidal Interactions in Protein Crystal Systems

4.1 Introduction

Much of the effort required to determine the structure of biological macromolecules is spent in a trial-and-error search for suitable growth conditions. Valuable protein and time could be saved if the most promising range of conditions could be selected based on an understanding of the growth processes. Although the accurate prediction of optimal growth conditions for the complicated systems used in protein crystal growth remains beyond our abilities, some insight can be gained from modeling simpler systems. The reliability of such modeling is limited by the accuracy with which the appropriate interactions are known; predictions of crystallization conditions remain qualitative because the complex interactions responsible for protein crystal growth are still poorly characterized.

Nonuniform charge distributions have been shown to affect the interactions of protein molecules (§1.7), but little is known about anisotropic charge effects on interactions of protein molecules with macroscopic bodies. A molecule with patches of positive and negative charge could experience strongly orientation dependent interactions with the crystal. As a concrete example, consider the case of a positively charged crystal surface: a molecule is repelled if it presents a primarily positive patch to the crystal but attracted if the patch is negative. On average, molecules impinging on the surface should be oriented with negative patches facing the surface. Once on the surface, the molecule may desorb and adsorb repeatedly as it samples many orientations in an attempt to fit into the crystal lattice [1].

Anisotropic charge distributions can produce qualitatively different behavior depending on the arrangement and depth of local minima in the electrostatic free energy. If the minima are close together and shallow, rotary diffusion of the molecule would not be

126

too restricted and the molecule could find the "correct" orientation reasonably quickly. In contrast, when the minima are widely separated and deep, the molecule is effectively trapped in its original orientation. The former scenario is the basis for the crystallographers' interest in the balance between mass transport and attachment kinetics: all molecules would fit neatly into the lattice provided they could sample enough orientations before next molecule arrived. The rotational restrictions described in the second scenario imply that a fixed fraction of all incoming molecules would be trapped in unfavorable orientations where they might interfere with attachment of other molecules. If such misoriented molecules are responsible for "site poisoning" that eventually terminates crystal growth, the rate at which molecules reach the surface is largely irrelevant.

In this chapter, a simplified model of the interactions of lysozyme is developed in an effort to locate the behavior of a "typical" protein on the continuum between the two extremes outlined above. Interaction potentials for molecule-crystal systems are calculated by the methods of colloid scientists and used to compare nonuniformly charged systems with comparable uniformly charged systems. Large uncertainties in the interaction parameters make a quantitative interpretation difficult, but the calculations provide a qualitative description of the molecule-crystal behavior which can guide subsequent work.

A first step in modeling protein crystal growth systems was taken by Young, De Mattei, Feigelson, and Tiller [2]. In their study, protein molecules were treated as spherical colloid particles and the crystal as a flat plate. They compared the interactions between two particles with those between a particle and the plate using the sum of the electrostatic and van der Waals (dispersion) potentials. Their electrostatic potentials are appropriate for high ionic strength and constant (uniform) surface potentials; the dispersion potentials are valid for small separations. Young *et al.*'s primary conclusion was that crystal size ought to depend on the ionic strength of the solution, a fact crystal growers had long appreciated [3]. Although the effect of the crystal's surface potential on the shape of the potential

energy curve was discussed, no estimates were made of the surface potential or the strength of the interaction.

In light of the documented effects of anisotropic charge distributions on protein behavior (see chapter 1), the use of a uniform surface potential to represent the protein molecule is the weakest assumption in Young's analysis. It is altogether likely that patches of charge on the molecule's surface interact differently with the surface of the crystal (which also has patches of charge). Already, researchers are studying the interaction of ion exchange resins with specific charge patches on the protein surface [4]. In this chapter, we calculate the interaction potential curve for a molecule-crystal system including effects arising from the nonuniform charge distribution on the protein.

The presentation is organized as follows. We begin with a general discussion of the problem and the approximations employed to make the problem tractable, followed by the mathematical statement of the simplified problem. A boundary element method was developed for the numerical solution of the electrostatics problem of a nonuniformly charged sphere, and the formulation and implementation of the method are explained in some detail. The boundary element code is then applied to two simple test problems to evaluate its accuracy and assess the significance of charge inhomogeneities. Then the method for creating a surface charge distribution to approximate the location of the protein's charged groups is presented, followed by a discussion of the computational results for lysozyme. Finally, the effect of dispersion forces is included to calculate the total interaction potential.

The calculated interaction potentials show how finely the electrostatic and van der Waals forces are balanced. Under some circumstances, the potential energy barrier is quite modest, so variations in the effective crystal surface charge density and effective Hamaker constant can change the magnitude and sign of the interaction potential. When nonuniform charge effects are included, the behavior of protein crystal systems shows significant orientation dependence. Rotational sampling by the molecule may be a key step in

molecular attachment. Further refinement of the model is required to establish reasonable ranges for the key parameters affecting the strength of the interaction.

4.2 Problem Description

We wish to calculate the interaction potential between a protein molecule and a protein crystal as a function of separation and orientation. The interaction potential is the work done to bring the molecule and crystal together from an infinite separation. In our case, this energy results from work done against two types of forces: (i) electrostatic forces between charged groups on the molecule and in the crystal, and (ii) dispersion or van der Waals forces. As is frequently the case in the study of protein interactions, there are insufficient data to calculate the two contributions with complete confidence.

A sketch of the molecule-crystal system is shown in Figure 4-1. The assumptions used to simplify the problem are listed in Table 4-1. First, it is assumed the interactions are additive. This is a cornerstone of the Derjaguin-Landau-Verwey-Overbeek (DLVO) theory and is justified by numerous empirical observations [5-7]. Next, linearization of the Poisson-Boltzmann equation allows the problem to be divided into separate subproblems which can be solved independently to obtain the electrostatic potential. The linearization is consistent with the low net charge on the molecule and, moreover, allows us to assess the significance of nonuniform charge distributions on protein-crystal interactions. A rough estimate of the surface potential of lysozyme in water ($\varepsilon_2 = 80$) based on the net valence of +10.5 at pH 4.7 [8], a hydrodynamic radius of 20Å [9], and approximately 1M NaCl ($a\kappa = 5$) is 16mV. Since the linearization is valid for potentials up to approximately 100 mV [5], it is probably adequate here except when the particle and crystal are practically in contact.

Assumptions 3 - 5 are largely self-explanatory. If dispersion forces arise from induced dipole effects, then #3 is consistent with the notion that both the molecule and crystal are solid bodies with uniform dielectric constants (#s 5 and 8). Frequency spectra for the dielectric constant are required if retardation effects are to be incorporated into the

effective Hamaker constant, A_{eff}. In the absence of such data for lysozyme crystal systems, we treat A_{eff} as constant; a range of reasonable values for A_{eff} is used in §4.9 to assess the size of the dispersion potential and its effect on the total interaction potential.
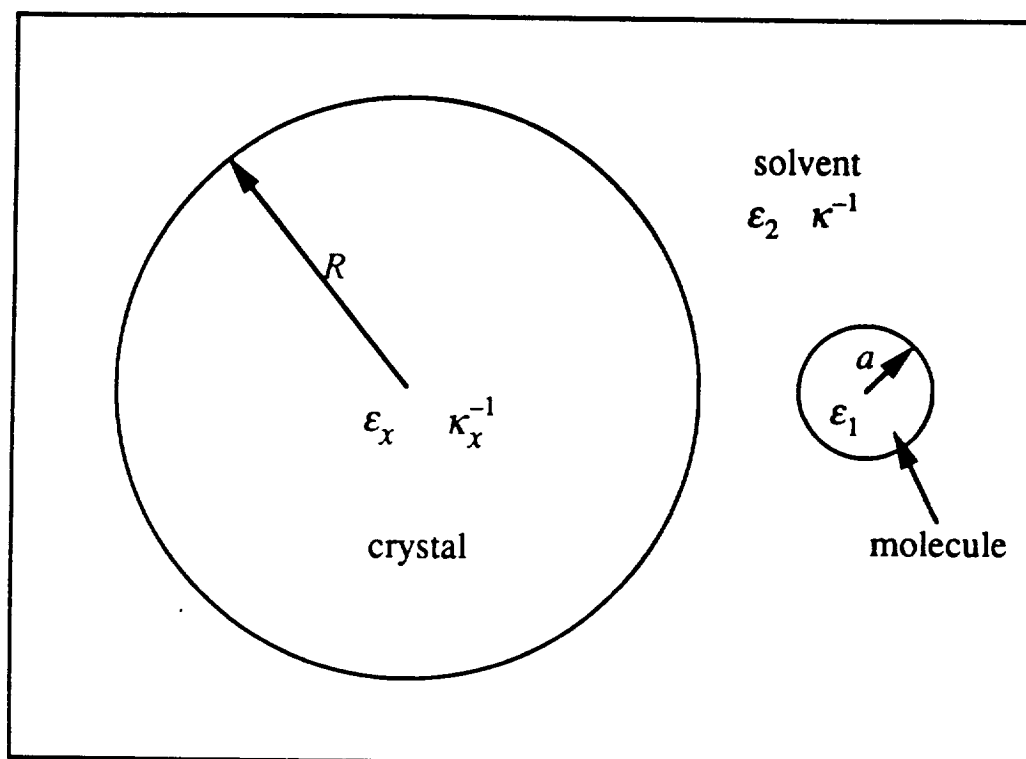
Figure 4-1: Definition sketch for molecule-crystal interactions.

The approximations concerning the protein molecule (#s 6-8) are based on experimental observations and are widely used. The primary reason for the spherical approximation is simplicity. Moreover, crystallographic data indicate that most globular proteins are roughly spherical. A table of 20 proteins of known structure [10], for instance, shows that the ratio of maximum to minimum dimensions is seldom greater than about 2. Hen egg white lysozyme is variously described as being $23\text{Å} \times 28\text{Å} \times 40\text{Å}$ [8], $30\text{Å} \times 30\text{Å} \times 45\text{Å}$ [10], and $30\text{Å} \times 30\text{Å} \times 45\text{Å}$ "with a wedge-shaped piece removed" [11];

all these descriptions are consistent with the approximation that lysozyme behaves as a sphere with a hydrodynamic radius af approximately 20Å [9].

Table 4-1

Assumptions Employed in Study of Interaction Potential.

1.	The electrostatic and dispersion potentials are strictly additive.
2.	The linearized Poisson-Boltzmann equation (LPBE) governs the electrostatics.
3.	Dispersion potential is independent of molecular orientation (function of separation only).
4.	The effective Hamaker constant, A_{eff}, is independent of separation.
5.	For calculating the dispersion potential, the protein crystal is treated as a solid sphere.
6.	The protein molecule is a sphere.
7.	All charged groups lie on surface of the protein molecule and can be represented by a surface charge density distribution.
8.	Protein molecule's interior is filled with material of dielectric constant $\varepsilon_1 = 2$.
9.	For electrostatic calculations, the crystal's surface is treated as infinite plate with uniform effective surface charge density σ_x.
10.	Electrostatic potential variations in the crystal's interior are ignored.

When discussing the environments of individual amino acid residues, Cantor and Schimmel [11] state that charged residues are on the surface of the molecule (#7). Representing the charged groups as a surface charge density distribution instead of a collection of point charges reflects the implementation of the boundary element method used here to calculate the electrostatic potential energy of the molecule-crystal system. Other workers using finite difference methods [12-15], model the charge distribution as point charges which lie just inside the accessible surface of the protein. (The accessible surface is that which can be reached by a probe sphere, usually taken to be a hypothetical

water molecule 1.4Å in radius [10,13].) The method for translating the charge distribution obtained from X-ray crystallography into a surface charge distribution is described in §4.8.

Hydrophobic residues and side chains tend to be buried in the interior of the molecule [10,11], at least when the molecule is soluble in water. Calculations of packing density generally give values around 0.75 [10,11], indicating that the interior is relatively uniform. Free water is generally absent from the interior, although some molecules, such as lysozyme and α-chymotrypsin, seem to have cavities or holes which are presumed to contain solvent [11]. Occasionally, bound water molecules can be detected in the interior of some proteins; such water molecules appear to be intrinsic features of the protein structure [10]. The dielectric constant in the interior of the molecule is generally taken to be similar to those of hydrocarbons ($2 \leq \varepsilon_1 \leq 4$) [16-20]. Dao-pin *et al.* [15] calculated the electrostatically induced shift in pK_a for two systems as a sensitivity check on ε_1. They found that results were insensitive to the value chosen in the range $2 \leq \varepsilon_1 \leq 8$ except at low ionic strength.

The disparate sizes of the molecule and crystal justify the treatment of the protein crystal as a semi-infinite region with only a surface charge. When the ionic strength is about 1M, which is on the low end for much of the protein crystal growth work, the Debye length is approximately $\kappa^{-1} \sim 3$Å. Thus, the exponential decay of the potential effectively limits the range of the electrostatic forces to about $5\kappa^{-1}$ or 15 Å. A molecule approaching the crystal may not actually "sense" the crystal until its surface is only 15Å away. Thus, Coulombic screening by ions in solution and the difference in the sizes of the crystal ($R \sim$ 0.5 mm) and the molecule ($a \sim 20$Å) make the crystal seem like an infinite flat plate.

The use of a uniformly charged flat plat to represent the crystal (#9) is the most drastic of the assumptions in Table 4-1. The roughness and charge heterogeneity of the surface are the same as those of the molecule, but complications caused by including such effects are beyond the scope of our calculations. The uniform surface charge approximation is invoked to simplify the problem. When solving differential equations

132

numerically, it is usually necessary to divide the domain into small elements in order to obtain a solution. If a patchy charge distribution were placed on the crystal surface, the number of computations needed to calculate the electrostatic potential for a given orientation, separation and surface location would increase dramatically. These calculations would then have to be repeated at sites spread over the surface of the crystal in order to give some sense of the "average" behavior of the molecule-crystal system. Such detailed calculations will eventaully be needed to appreciate the subtleties of crystal growth mechanisms, but they require far more data than we have available. The effect of a nonuniform crystal surface charge distribution can be estimated, however, by calculating the electrostatic potential energy for different values of σ_x. Recall that although the plate is infinite in extent, mobile ions in solution screen out the influence of all but a small patch of the crystal surface. In some sense, then, calculations with different σ_x mimic interactions of the molecule with different charge sites on the crystal surface.

As employed here, σ_x is the effective surface charge density including contributions from molecules and ions inside the crystal. An incoming molecule is influenced by these charges as it nears the crystal, but, because there is some salt inside the crystal, effects of internal charges are partially screened. In the absence of experimental data or a more detailed theory to predict the internal Debye length (and thus the effective surface charge density) σ_x is treated as a parameter.

It follows from the finite range of the screened electrostatic interaction, that molecules in the center of a sufficiently large crystal ($R \gg \kappa_x^{-1}$, the internal Debye length) are not influenced by the presence of incoming molecules. The potential inside this region is virtually constant (although not necessarily uniform). In other words, molecules more than (say) $0.5\kappa_x^{-1}$ from the crystal surface are isolated from the influence of events outside the crystal. By collapsing the finite shell of charge into an effective surface charge density, we account for those charges in the crystal which respond to the approach of an incoming

protein molecule; the deep interior of the crystal makes no contribution to the electrostatic interaction potential.

The purpose of these approximations is to simplify the problem to the point where it can be solved while preserving the essential physics. Results for a molecule with a nonuniform charge distribution on the surface can be compared with those for a uniformly charged molecule. By applying the same approximations to calculations on a uniform sphere, we should be able to describe differences in behavior due to patchy charge. The level of approximation employed here is entirely appropriate for such an investigation. If nonuniform charge distributions significantly affect crystal growth behavior, the restrictive approximations in Table 4-1 can be relaxed in future work.

4.3 Mathematical Statement of the Electrostatics Problem

The sketch of the molecule-crystal system in Figure 4-2 incorporates the assumptions in Table 4-1; distances and surface charge densities are scaled as described below. The electrostatic potential is a solution of the governing equations [5]:

$$\text{region 1 (molecule):} \quad \nabla^2 \psi_1 = 0 \tag{4.1}$$

$$\text{region 2 (solution):} \quad \nabla^2 \psi_2 = \kappa^2 \psi_2 \tag{4.2}$$

where $\kappa^2 = 2n_\infty Z^2 e^2 / \varepsilon_0 \varepsilon_2 kT$ for a $Z{:}Z$ electrolyte; n_∞ = bulk ion number density, e = elementary charge, ε_0 = permittivity of free space, k = Boltzmann's constant, and T = absolute temperature. The boundary conditions at the surface of the molecule are the continuity of potential,

$$\psi_1 = \psi_2 \tag{4.3}$$

and the jump in electric displacement,

$$\varepsilon_1 \nabla \psi_1 \cdot \mathbf{n}_1 + \varepsilon_2 \nabla \psi_2 \cdot \mathbf{n}_2 = \frac{\sigma}{\varepsilon_o} \tag{4.4}$$

Note that $\mathbf{n}_1$ and $\mathbf{n}_2$ point *out* of their respective regions. The boundary conditions at the plate and at infinity are
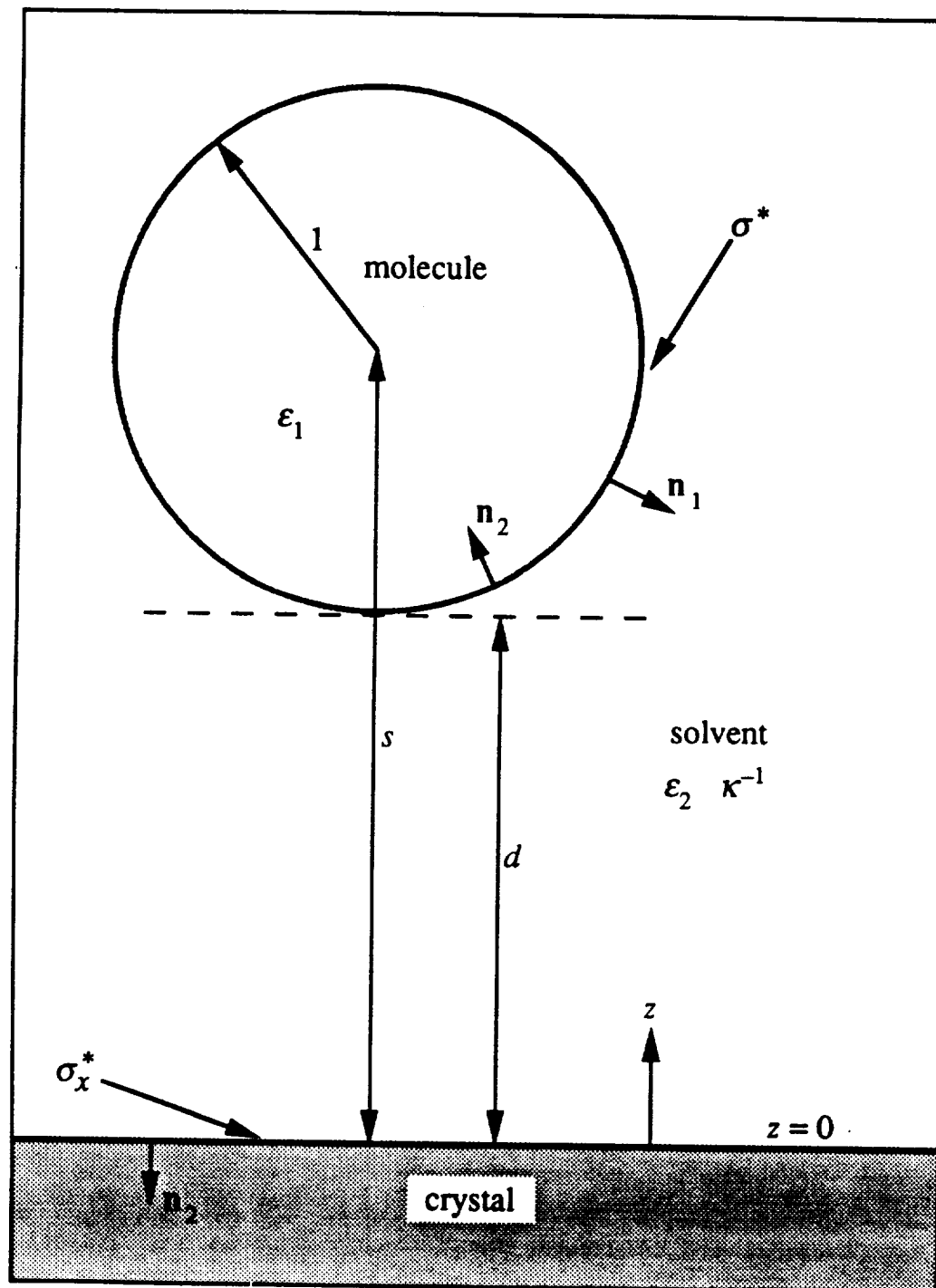
134

Figure 4-2: Sketch of molecule-crystal system for electrostatics calculations.
Lengths have been scaled by the particle radius, a, and surface charge densities have been scaled by $\sigma_0 = \varepsilon_0 \psi_0/a$.

$$z = 0: \quad \frac{\partial \psi_2}{\partial z} = -\frac{\sigma_x}{\varepsilon_0 \varepsilon_2} \tag{4.5}$$

and

$$z \to \infty: \quad \psi_2 \to 0 \tag{4.6}$$

If the electrostatic potentials are rewritten as $\psi = u\psi_0$, with $\psi_0 = kT/e$ and lengths are scaled by the particle radius, a, the following dimensionless equations result:

$$\text{region 1:} \quad \nabla^2 u_1 = 0 \tag{4.7}$$

$$\text{region 2:} \quad \nabla^2 u_2 = (a\kappa)^2 u_2 \tag{4.8}$$

$$\text{sphere surface:} \begin{cases} u_1 = u_2 & \tag{4.9} \\ \varepsilon_1 \nabla u_1 \cdot \mathbf{n}_1 + \varepsilon_2 \nabla u_2 \cdot \mathbf{n}_2 = \sigma^* & \tag{4.10} \end{cases}$$

$$z = 0: \quad \frac{\partial u_2}{\partial z} = -\frac{\sigma^*}{\varepsilon_2} \tag{4.11}$$

$$z \to \infty: \quad u_2 \to 0 \tag{4.12}$$

The reference quantity for the surface charge is $\sigma_0 = \varepsilon_0 \psi_0 / a$.

The solution of the full problem specified by Equations (4.7) - (4.12) is difficult, but the linearity of the governing equations permits the problem to be split into subproblems which can be solved analytically or numerically. Suppose the problem shown in Figure 4-2 is divided into two subproblems as in Figure 4-3: (i) a charged sphere with an insulated flat plate, and (ii) a charged plate with an uncharged sphere. We can then apply the method of images to construct a solution for the problem (i) which satisfies the no-flux boundary condition at $z = 0$ [21-23]. For $z > 0$, the potential of problem (i) is the same as that produced by the charged sphere and its mirror image (Figure 4-4) and is denoted u^{ss} (i.e., sphere-sphere); the potential in problem (ii) is the sphere-plate potential, u^{sp}. The total potential is their sum

$$u = u^{ss} + u^{sp} \tag{4.13}$$
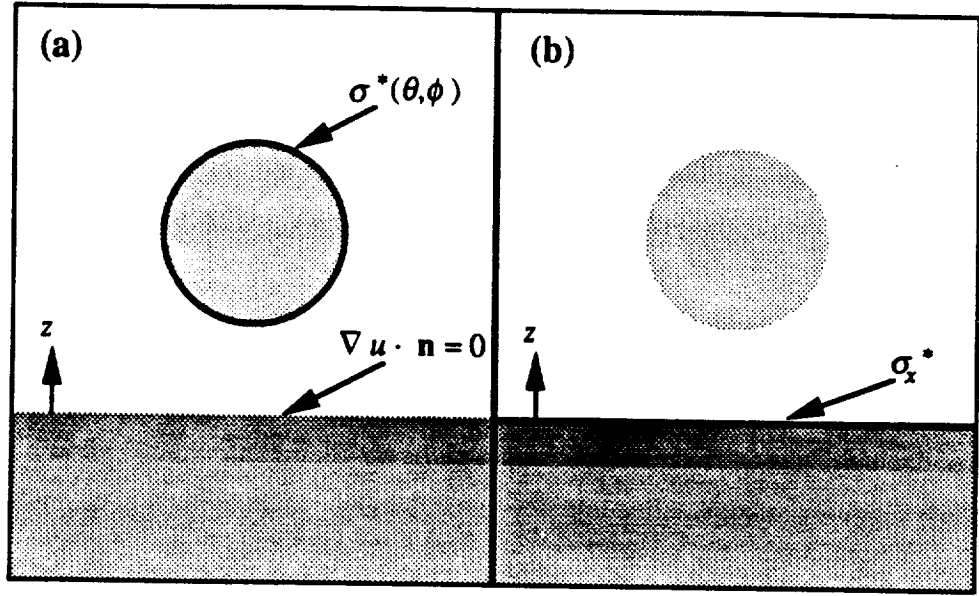
Figure 4-3: Two subproblems that make up the full electrostatics problem.
(a) A nonuniformly charged sphere near an uncharged insulated wall.
(b) An uncharged low dielectric sphere near a uniformly charged infinite plate.

The equations for the sphere-sphere problem are:

$$\text{region 1:} \qquad \nabla^2 u_1^{ss} = 0 \tag{4.14}$$

$$\text{region 2:} \qquad \nabla^2 u_2^{ss} = (a\kappa)^2 u_2^{ss} \tag{4.15}$$

$$\text{sphere surface:} \begin{cases} u_1^{ss} = u_2^{ss} & (4.16) \\ \varepsilon_1 \nabla u_1^{ss} \cdot \mathbf{n}_1 + \varepsilon_2 \nabla u_2^{ss} \cdot \mathbf{n}_2 = \sigma^* & (4.17) \end{cases}$$

$$z = 0: \qquad \frac{\partial u_2^{ss}}{\partial z} = 0 \tag{4.18}$$

$$z \to \infty: \qquad u_2^{ss} \to 0 \tag{4.19}$$,

while the sphere-plate potential satisfies:

$$\text{region 1:} \qquad \nabla^2 u_1^{sp} = 0 \tag{4.20}$$

$$\text{region 2:} \qquad \nabla^2 u_2^{sp} = (a\kappa)^2 u_2^{sp} \tag{4.21}$$

$$\text{sphere surface:} \begin{cases} u_1^{sp} = u_2^{sp} & (4.22) \\ \varepsilon_1 \nabla u_1^{sp} \cdot \mathbf{n}_1 + \varepsilon_2 \nabla u_2^{sp} \cdot \mathbf{n}_2 = 0 & (4.23) \end{cases}$$
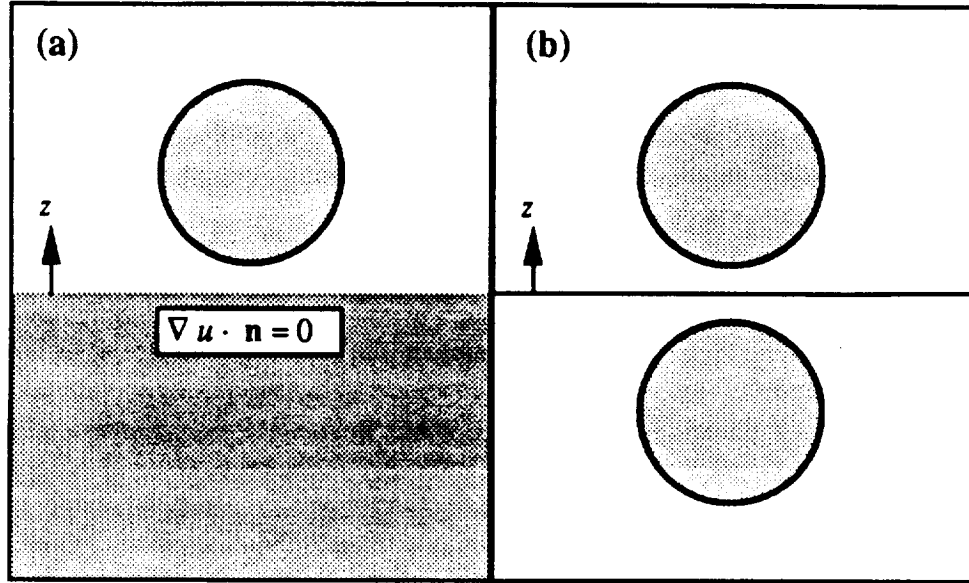
Figure 4-4: Image charge representation of an insulated boundary.
No flux boundary condition at $z = 0$ is identically satisfied by the potential produced by the original sphere and a mirror sphere obtained by reflecting the original below the plane $z = 0$.
(a) The nonuniformly charged sphere and insulated plate from Figure 4-3a.
(b) Replacement of infinite insulating wall with mirror image of the original sphere.

$$z = 0: \qquad \frac{\partial u_2^{sp}}{\partial z} = -\frac{\sigma_x^*}{\varepsilon_2} \qquad\qquad (4.24)$$

$$z \rightarrow \infty: \qquad u_2^{sp} \rightarrow 0 \qquad\qquad (4.25).$$

The sphere-sphere potential can be calculated directly by the boundary element method presented in §4.4.

A solution for u^{sp} is more difficult, however, because the boundary condition at $z = 0$ cannot be easily satisfied by the method of images. A boundary element solution would require the discretization of a finite portion of the plate and the introduction of an empirical cut-off beyond which the plate is unaffected by the sphere. Instead, we divide the sphere-plate problem into two parts:

$$u^{sp} = u^{fp} + u^r \qquad\qquad (4.26)$$

138

where u^{fp} is the potential due to charged plate in the absence of the low dielectric sphere, and u^r is the "remainder" of the potential. The flat plate potential is

$$u_1^{fp} = u_2^{fp} = u^{fp} = \frac{\sigma_x^*}{\varepsilon_2 \, a\kappa} e^{-a\kappa z} \qquad (4.27)$$

and satisfies the equations:

$$z > 0: \qquad \nabla^2 u_1^{fp} = \nabla^2 u_2^{fp} = \nabla^2 u^{fp} = (a\kappa)^2 \, u^{fp} \qquad (4.28)$$

$$\text{sphere surface:} \begin{cases} u_1^{fp} = u_2^{fp} & (4.29) \\ \varepsilon_1 \nabla u_1^{fp} \cdot \mathbf{n}_1 + \varepsilon_2 \nabla u_2^{fp} \cdot \mathbf{n}_2 = (\varepsilon_1 - \varepsilon_2) \nabla u^{fp} \cdot \mathbf{n}_1 & (4.30) \end{cases}$$

$$z = 0: \qquad \frac{\partial u^{fp}}{\partial z} = -\frac{\sigma_x^*}{\varepsilon_2} \qquad (4.31)$$

$$z \to \infty: \qquad u^{fp} \to 0 \qquad (4.32).$$

When u^{fp} is subtracted from u^{sp}, the result is:

$$\text{region 1:} \qquad \nabla^2 u_1^r = -(a\kappa)^2 \, u^{fp} = -\rho^* \qquad (4.33)$$

$$\text{region 2:} \qquad \nabla^2 u_2^r = (a\kappa)^2 \, u_2^r \qquad (4.34)$$

$$\text{sphere surface:} \begin{cases} u_1^r = u_2^r & (4.35) \\ \varepsilon_1 \nabla u_1^r \cdot \mathbf{n}_1 + \varepsilon_2 \nabla u_2^r \cdot \mathbf{n}_2 = -(\varepsilon_1 - \varepsilon_2) \nabla u^{fp} \cdot \mathbf{n}_1 & (4.36) \end{cases}$$

$$z = 0: \qquad \frac{\partial u_2^r}{\partial z} = 0 \qquad (4.37)$$

$$z \to \infty: \qquad u_2^r \to 0 \qquad (4.38).$$

Equation (4.33) indicates the sphere contains a fixed charge density of $\rho^* = (a\kappa)^2 u^{fp}$; the charge density is scaled on $\rho_o = \varepsilon_o \psi_o / a^2$. The potential produced by the two mirror spheres identically satisfies boundary conditions (4.37) and (4.38), so u^r can be obtained from the same boundary element technique used to find u^{ss}. The full solution is the sum of the three potentials:

$$u = u^{ss} + u^{fp} + u^r \qquad (4.39).$$

Of primary interest in the present work is not the electrostatic potential, but the electrostatic potential *energy* and its dependence on particle-crystal separation. Interaction

potentials are usually defined in terms of the work performed on the system to bring two bodies within a distance r of each other from an initially infinite separation or, equivalently, the work that could be done by the system if the bodies were initially separated by r and allowed to become infinitely separated [24]. When performed isothermally and reversibly, the work done is the free energy change of the system [6,25-27] and can be expressed in terms of the work required to assemble all the charges from infinity [6,28]:

$$\Delta G_{elec} = \int_{\Omega} dV \int_0^{\rho^f} \psi \, d\rho^f \qquad (4.40),$$

where Ω denotes the volume of the system and the superscript f indicates the charge density is fixed (not subject to thermal randomization). When applied to the present case where the charge density is linearly proportional to the potential and all the fixed charges reside on the surfaces of the system, the form of Equation (4.40) is simplified to [6,17,28,29]

$$\Delta G_{elec} = \frac{1}{2} \int_{\Omega} \rho^f \psi \, dV = \frac{1}{2} \int_{\Gamma} \sigma \psi \, dA \qquad (4.41),$$

where Γ represents all the surfaces of the system and σ is understood to be fixed.

The total change in free energy can be divided into two parts:

$$\Delta G_{elec} = \Delta G_{elec}^{\infty} + \Phi_{elec}(r) \qquad (4.42),$$

where ΔG_{elec}^{∞} = change in free energy required to "charge up" the molecule and plate at infinite separation, and $\Phi_{elec}(r)$ = additional change in free energy as the molecule and plate are brought together. In terms of the scaled variables of the electrostatics problem, Φ_{elec} is:

$$\frac{\Phi_{elec}(s)}{\varepsilon_0 \, \psi_0^2 \, a} = \frac{1}{2} \int_{\Gamma} \sigma^* \left[u(s) - u(\infty) \right] dA \qquad (4.43),$$

with s = distance (in particle radii) from the plate to the center of the sphere, $u(s)$ = potential when the particle and plate are separated by s, and $u(\infty)$ = potential when particle is infinitely far from plate; dA is now dimensionless. The surface of the system consists of

the plate and the sphere, so when the integral over Γ is split into two area integrals and (4.39) is substituted into (4.43), we have:

$$\frac{\Phi_{elec}(s)}{\varepsilon_0\,\psi_0^2\,a} = \frac{1}{2}\int_{A_{sphere}} \sigma^*\left[\left(u^{ss} + u^{fp} + u^r\right)_s - \left(u^{ss} + u^{fp} + u^r\right)_\infty\right]dA$$

$$+ \frac{1}{2}\int_{A_{plate}} \sigma_x^*\left[\left(u^{ss} + u_0^{fp} + u^r\right)_s - \left(u^{ss} + u_0^{fp} + u^r\right)_\infty\right]dA \qquad (4.44),$$

where the subscripts on the parentheses indicate the separation of the plate and sphere and the subscript "o" on u^{fp} in the plate integral is a reminder that the flat plate potential on the plate is a constant. At infinite separation, u^{fp} is zero on the sphere, u^{ss} is zero on the plate, and u^r is zero everywhere, so that

$$\frac{\Phi_{elec}(s)}{\varepsilon_0\,\psi_0^2\,a} = \frac{1}{2}\int_{A_{sphere}} \sigma^*\left[\left(u^{ss} + u^{fp} + u^r\right)_s - u_\infty^{ss}\right]dA \quad + \frac{1}{2}\int_{A_{plate}} \sigma_x^* \left(u^{ss} + u^r\right)_s dA \quad (4.45).$$

Equation (4.45) gives the electrostatic free energy of interaction for the molecule-crystal as a function of separation from the plate. The boundary element method for calculating u^{ss} and u^r to evaluate Φ_{elec} is described in the following sections. Even without the calculated potentials, the form of (4.45) reveals qualitative behavior of the system under consideration and warrants a brief discussion. By Equations (4.33) and (4.36), the "remainder" potential scales with the flat plate potential, which, according to Equation (4.27), is linearly proportional to the surface charge density on the plate. If the terms in (4.45) were regrouped by their dependence on σ_x^*, we would have:

independent of σ_x^* : $\dfrac{1}{2}\displaystyle\int_{A_{sphere}} \sigma^* \left(u_s^{ss} - u_{s\infty}^{ss}\right) dA$

linear in σ_x^* : $\dfrac{1}{2}\left[\displaystyle\int_{A_{sphere}} \sigma^* \left(\dfrac{u_s^{fp} + u_s^r}{\sigma_x^*}\right) dA + \int_{A_{plate}} u_s^{ss}\, dA\right]$

quadratic in σ_x^* : $\dfrac{1}{2}\left[\displaystyle\int_{A_{plate}} \dfrac{u_s^r}{\sigma_x^*} dA\right]$

with the independent, linear, and quadratic terms corresponding to the charged sphere-charged sphere, charged sphere-charged plate, and charged plate-uncharged sphere interactions respectively. The potential energy associated with the quadratic term scales with $E^{fp}\cdot E^{fp}$, where E^{fp} = electric field vector given by $E^{fp} = -\nabla \psi^{fp}$. This is consistent with the results for the dielectrophoresis of a dielectric particle in a nonuniform electric field [29] where the force on the particle is proportional to ∇E^2.

The electrostatic free energy calculated from of Equation (4.45) can be determined only after the electrostatic potentials are known, but the form of the free energy implies the following qualitative behavior: (i) when the surface charge density on the plate is low, the repulsion of the mirror spheres produces an increase in Φ_{elec} as the particle approaches the wall; (ii) at high crystal surface charge densities, the interaction potential is also repulsive due to dielectrophoretic effects; and (iii) at intermediate crystal surface charge densities, the interaction potential can be either attractive or repulsive depending on the sign and magnitude of the surface charge density on the molecule. Note also that since u^{ss} and u^r are calculated from the interaction of two spheres a distance $2s$ apart, their contributions decay as $e^{-2a\kappa s}$ compared with $e^{-a\kappa s}$ for the linear term. Now that the general behavior of the system has been outlined, we turn to the boundary element solution of the electrostatics problems presented above.

4.4 Boundary Element Formulation

The starting point for the boundary element formulation is, naturally enough, the most general form of the governing differential equation:

$$\nabla^2 u - (a\kappa)^2 u = -\rho^* \qquad (4.46),$$

where ρ^* is a *fixed* charge density. Equation (4.46) governs the electrostatics in the solution (region 2) when $\rho^* \rightarrow 0$, region 1 of the "remainder" problem when $a\kappa \rightarrow 0$, and region 1 of the sphere-sphere problem when both $a\kappa$ and $\rho^* \rightarrow 0$. The fundamental solution (Green's function) of the homogeneous differential equation is:

$$u^* = \frac{1}{4\pi} \frac{e^{-a\kappa r}}{r} \qquad (4.47),$$

where r is measured from the "source" point x_0 (i.e. $r = |x - x_0|$). When the ionic strength vanishes, the fundamental solution is $u^* = 1/4\pi r$. Next, both sides of Equation (4.46) are multiplied by u^* and integrated over the domain, Ω to produce:

$$\int_\Omega u^* \left[\nabla^2 u - (a\kappa)^2 u \right] dV = - \int_\Omega \rho^* u^* \, dV \qquad (4.48).$$

A direct application of Green's second identity to the integral of $u^* \nabla^2 u$ gives:

$$\int_\Omega u^* \nabla^2 u \, dV = \int_\Omega u \nabla^2 u^* \, dV + \int_\Gamma u^* (\nabla u \cdot n) \, dA - \int_\Gamma u (\nabla u^* \cdot n) \, dA \quad (4.49),$$

so that Equation (4.48) can be rewritten as:

$$\int_\Omega u \left[\nabla^2 u^* - (a\kappa)^2 u^* \right] dV = \int_\Gamma u (\nabla u^* \cdot n) \, dA - \int_\Gamma u^* (\nabla u \cdot n) \, dA - \int_\Omega \rho^* u^* \, dV \quad (4.50).$$

If we wish to calculate the potential, u, at the point x_0, we can exploit the properties of the fundamental solution, u^*. Suppose that the fundamental solution is placed at x_0, then since u^* is Green's function for Equation (4.46), it satisfies the equation:

$$\nabla^2 u^* - (a\kappa)^2 u^* = - \delta(x - x_0) \qquad (4.51),$$

from which it follows that

$$\int_{\Omega} \left[\nabla^2 u^* - (a\kappa)^2 u^* \right] dV = \begin{cases} -1, \mathbf{x}_0 \text{ in } \Omega \\ -1/2, \mathbf{x}_0 \text{ in } \Gamma \\ 0, \text{ otherwise} \end{cases} \tag{4.52}.$$

Note that the value of $-1/2$ when $\mathbf{x}_0$ is in Γ reflects an implicit assumption that the boundary is smooth; this is the situation for all the work discussed here. For the case where $\mathbf{x}_0$ may be at an edge or corner, the integral in (4.52) can be calculated in a straightforward manner [22]. Upon substitution of (4.52) into (4.50) and subsequent rearrangement of Equation (4.50), we obtain:

$$c\, u(\mathbf{x}_0) + \int_{\Gamma} u \left(\nabla u^* \cdot \mathbf{n} \right) dA = \int_{\Gamma} u^* \left(\nabla u \cdot \mathbf{n} \right) dA + \int_{\Omega} \rho^* u^* \, dV \tag{4.53},$$

where:

$$c = \begin{cases} 1, \mathbf{x}_0 \text{ in } \Omega \\ 1/2, \mathbf{x}_0 \text{ in } \Gamma \\ 0, \text{ otherwise} \end{cases} \tag{4.54}.$$

The advantage of the boundary integral expression in Equation (4.53) over a finite difference method is that all computations in the infinite domain have been eliminated. The integral over Ω is performed only when there is a distribution of fixed charges in the domain, but the electrostatics problems have been formulated so that all the charges in solution are mobile; in the "remainder" problem, the fixed charge density is inside the sphere (a finite domain). Although this advantage may not be great when an analytical solution exists, it can greatly reduce the amount of computation needed to obtain a numerical solution. The conversion of the boundary integral expression in Equation (4.53) into a discretized boundary element method (BEM) suitable for such a numerical solution is described next.

The outline of this discussion is similar to that of Brebbia, Wrobel, and Telles [22]; the notation is the same. Suppose that the boundary of the system is divided into N

elements, each of which is denoted Γ_j. The integrals over Γ in (4.53) are equivalent to the sum of integrals over all the elements:

$$c\,u(\mathbf{x}_0) + \sum_{j=1}^{N} \int_{\Gamma_j} u\left(\nabla u^* \cdot \mathbf{n}\right) dA = \sum_{j=1}^{N} \int_{\Gamma_j} u^*\left(\nabla u \cdot \mathbf{n}\right) dA + \int_{\Omega} \rho^* u^*\, dV \qquad (4.55).$$

In the shorthand notation of Brebbia *et al.*, Equation (4.55) is:

$$c\,u(\mathbf{x}_0) + \sum_{j=1}^{N} \int_{\Gamma_j} u\,q^*\, dA = \sum_{j=1}^{N} \int_{\Gamma_j} u^*\,q\, dA + \int_{\Omega} \rho^* u^*\, dV \qquad (4.56),$$

where $q = \nabla u \cdot \mathbf{n}$ and $q^* = \nabla u^* \cdot \mathbf{n}$. As before, u = potential and u^* = fundamental solution located at $\mathbf{x}_0$. For points in the domain, (4.56) expresses the potential as the sum of a single-layer distribution of strength q, a double-layer distribution of strength u, and a particular solution given by the volume integral.

At this time, we introduce the "constant element" approximation; i. e., that each element j has uniform values of potential and normal flux, u_j and q_j. The surface potentials and normal fluxes can then be removed from the integrals in (4.56) to obtain:

$$c\,u(\mathbf{x}_0) + \sum_{j=1}^{N} u_j \int_{\Gamma_j} q^*\, dA = \sum_{j=1}^{N} q_j \int_{\Gamma_j} u^*\, dA + \int_{\Omega} \rho^* u^*\, dV \qquad (4.57).$$

Further, we assume that each of these u_j and q_j can be associated with the node ($\mathbf{x}_j$) of the element; the node lies in the interior of Γ_j and is "representative" of the element. Equation (4.57) is valid everywhere, but since we are primarily concerned with surface values, we can restrict $\mathbf{x}_0$ to each of the nodes in turn to obtain N equations of the form:

$$\frac{1}{2}u_i + \sum_{j=1}^{N} u_j \int_{\Gamma_j} q_i^*\, dA = \sum_{j=1}^{N} q_j \int_{\Gamma_j} u_i^*\, dA + u_i^p \qquad (4.58),$$

where u_i = potential at node i, and u_j = potential of element j, q_j = normal flux through element j, u_i^* and q_i^* are the potential and normal flux due to the fundamental solution placed at $\mathbf{x}_i$, and u_i^p is the potential at node i produced by the distribution of fixed charges; $c = 1/2$ because each node lies in the surface. Brebbia chooses to define:

$$G_{ij} = \int_{\Gamma_j} u_i^* \, dA \qquad \hat{H}_{ij} = \int_{\Gamma_j} q_i^* \, dA \qquad (4.59)$$

so that Equation (4.58) can be expressed in matrix form:

$$\mathbf{H} \, \mathbf{U} = \mathbf{G} \, \mathbf{Q} + \mathbf{U}^p \qquad (4.60)$$

where

$$H_{ij} = \begin{cases} \hat{H}_{ij} + 1/2 \;, & i = j \\ \hat{H}_{ij} \;, & i \neq j \end{cases} \qquad (4.61).$$

If there are N elements on the spheres, Equation (4.60) is a system of N equations in $2N$ unknowns (N u's and N q's) that can be written for each region in the problem. (The two domains for the problem are the interior of the sphere (region 1) and the exterior (region 2). When relating dependent variables in the two domains, the domain is indicated by a superscript.). The problem is well posed, however, because when the equations for both regions are combined, there are $2N$ equations in $4N$ unknowns plus $2N$ constraints (boundary conditions). N of these boundary conditions govern the continuity of potential at the surface ($u_j^1 = u_j^2$), while the others specify the jump in the normal derivative caused by the local surface charge density ($\varepsilon_1 \, q_j^1 + \varepsilon_2 \, q_j^2 = \sigma_j^*$).

Solving the BEM problem involves evaluating G_{ij} and H_{ij} twice for every combination of i and j on each sphere (once treating the interior as the domain and again with the exterior as the domain) and then including terms due to the interaction of the nodes on one sphere with the elements on the other. Suppose the surfaces in the system have been discretized into N elements, N_1 of which are on sphere 1. Then, when all the surface quantities are written in terms of u_j^2 and q_j^2, the matrix equation can be rearranged in the form:

146

$$
\begin{pmatrix}
H_{ij}^1 & \dfrac{\varepsilon_2}{\varepsilon_1} G_{ij}^1 & 0 & 0 \\[2mm]
H_{ij}^2 & -G_{ij}^2 & H_{ij}^2 & -G_{ij}^2 \\[2mm]
H_{ij}^2 & -G_{ij}^2 & H_{ij}^2 & -G_{ij}^2 \\[2mm]
0 & 0 & H_{ij}^1 & \dfrac{\varepsilon_2}{\varepsilon_1} G_{ij}^1
\end{pmatrix}
\begin{pmatrix}
u_j^2 \\[2mm] q_j^2 \\[2mm] u_j^2 \\[2mm] q_j^2
\end{pmatrix}
=
\begin{pmatrix}
\dfrac{1}{\varepsilon_1} \displaystyle\sum_{j=1}^{N_1} G_{ij}^1 \sigma_j^* + u_i^p \\[4mm]
0 \\[2mm]
0 \\[2mm]
\dfrac{1}{\varepsilon_1} \displaystyle\sum_{j=N_1}^{N} G_{ij}^1 \sigma_j^* + u_i^p
\end{pmatrix}
\tag{4.62},
$$

where the top row represents the integrals over the elements of sphere 1 when the node is located on the interior surface of sphere 1, and the second row contains the integrals over all surfaces when the node is on the exterior surface of sphere 1. Rows 3 and 4 correspond to integrals for nodes located on sphere 2. Equation (4.62) is applicable to any two sphere problem. For the special case where the second sphere is a mirror image of the first so that $N = 2N_1$ and the elements have been numbered so that elements j and $j+N_1$ are mirror images, there are N_1 additional constraints of the form $u_j^2 = u_{j+N_1}^2$ and N_1 of the form $q_j^2 = q_{j+N_1}^2$. There are, therefore, only $2N_1 = N$ independent unknowns, and Equation (4.62) can be reduced to:

$$
\begin{pmatrix}
H_{ij}^1 & \dfrac{\varepsilon_2}{\varepsilon_1} G_{ij}^1 \\[3mm]
\left(H_{ij}^2 + H_{i,j+N_1}^2 \right) & -\left(G_{ij}^2 + G_{i,j+N_1}^2 \right)
\end{pmatrix}
\begin{pmatrix}
u_j^2 \\[2mm] q_j^2
\end{pmatrix}
=
\begin{pmatrix}
\dfrac{1}{\varepsilon_1} \displaystyle\sum_{j=1}^{N_1} G_{ij}^1 \sigma_j^* + u_i^p \\[4mm]
0
\end{pmatrix}
\tag{4.63}.
$$

Terms involving the nodes and elements on the same sphere are independent of the separation between the spheres and so need be calculated only once.

Evaluation of the boundary integrals for the BEM requires the integration of the fundamental solution, u^*, and its normal derivative, q^*, over each surface element in the discretization. When the source of the fundamental solution is placed on the z axis (see Figure 4-5), the integration of u^* and q^* can be performed analytically in θ, reducing the need for numerical quadrature schemes. A translation and rotation of coordinates can position any fieldpoint above the north pole of the sphere, so it is sufficient to evaluate the

integrals in this orientation only. The coordinate system employed below is that of Figure 4-5, not that used to define the problem in section 4.3.

For the case of the linearized Poisson-Boltzmann equation, the integrals over element j are:

$$G_{ij} = \int_{A_j} u^* \, dA = \int_{A_j} \frac{1}{4\pi} \frac{e^{-\alpha\kappa r}}{r} \, dA \qquad (4.64)$$

and

$$\hat{H}_{ij} = \int_{A_j} q^* \, dA = \int_{A_j} \frac{du^*}{dr} \frac{1}{r} \mathbf{r} \cdot \mathbf{n} \, dA \qquad (4.65),$$

where $dA = \sin\theta \, d\theta \, d\phi$, $\mathbf{r} = (\sin\theta\cos\phi) \, \mathbf{e}_x + (\sin\theta\sin\phi) \, \mathbf{e}_y + (\cos\theta - h) \, \mathbf{e}_z$, and $\mathbf{n} = -(\sin\theta\cos\phi) \, \mathbf{e}_x - (\sin\theta\sin\phi) \, \mathbf{e}_y - \cos\theta \, \mathbf{e}_z$; $\mathbf{e}_k$ = unit vector in direction k. For the geometry shown in Figure 4-5, $r^2 = h^2 + 1 - 2h\cos\theta$, from which it follows that:

$$\sin\theta \, d\theta = \frac{r}{h} \, dr \qquad (4.66)$$

and

$$dA = \sin\theta \, d\theta \, d\phi = \frac{r}{h} \, dr \, d\phi \qquad (4.67).$$

The θ integration in Equation (4.64) can be performed once (4.67) is substituted and the change of variables is made:

$$G_{ij} = \int_{\phi_1}^{\phi_2} d\phi \int_{\theta_1}^{\theta_2} \frac{1}{4\pi} \frac{e^{-\alpha\kappa r}}{r} \sin\theta \, d\theta = \frac{1}{4\pi h} \int_{\phi_1}^{\phi_2} d\phi \int_{r_1}^{r_2} e^{-\alpha\kappa r} \, dr$$

$$= -\frac{1}{4\pi h} \frac{1}{\alpha\kappa} \int_{\phi_1}^{\phi_2} \left(e^{-\alpha\kappa r_2} - e^{-\alpha\kappa r_1} \right) d\phi \qquad (4.68).$$

The limits of integration for θ and r are implicit functions of ϕ which define the element on the surface. When there is no screening by counterions, the governing equation is Laplace's equation, and the expression for G_{ij} reduces to
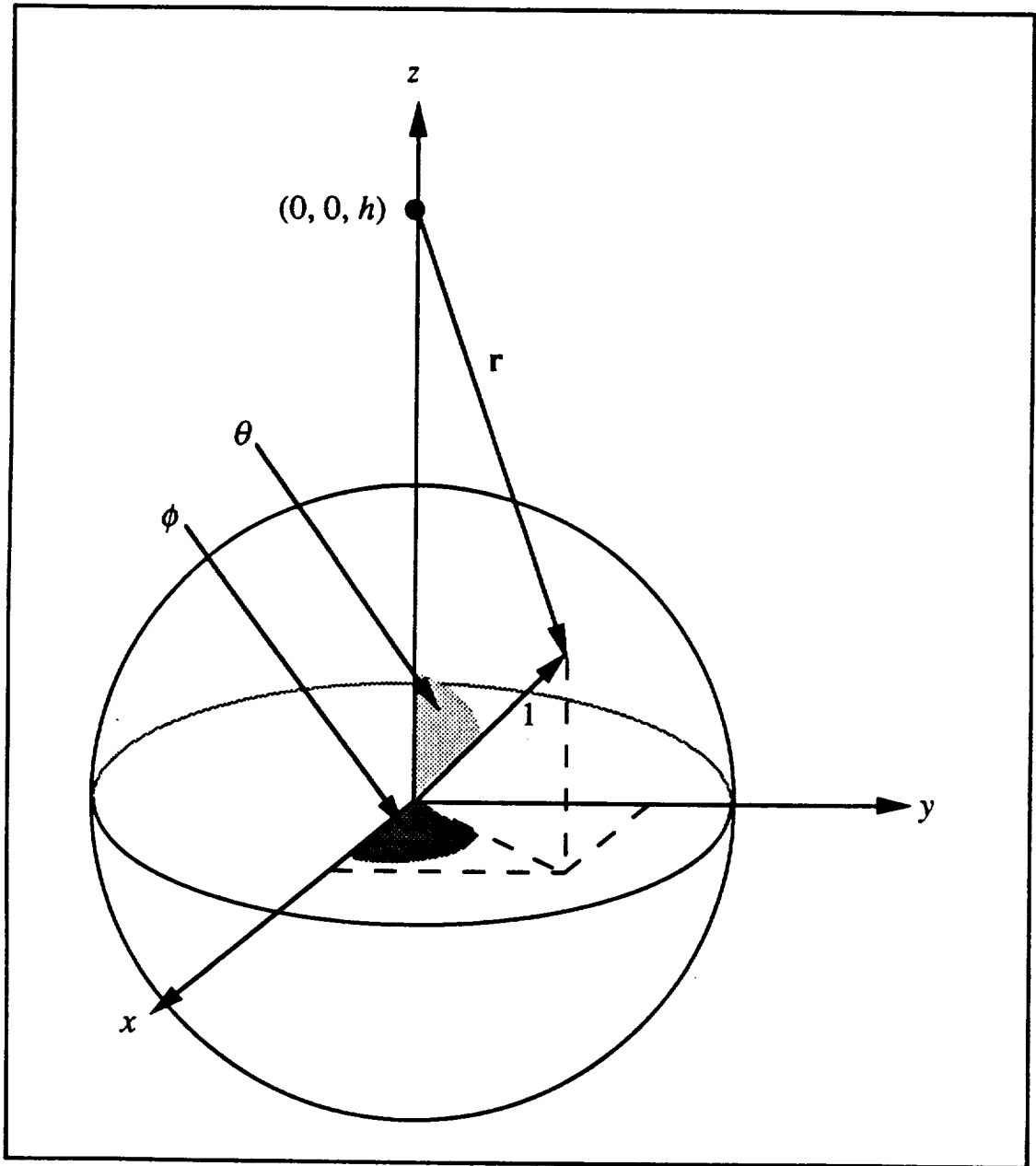
148

Figure 4-5: Temporary coordinate system used to evaluate boundary integrals.

A translation and rotation of coordinates can place any fieldpoint along the polar axis; the height, h, is the distance from the fieldpoint to the center of the sphere. The source is placed at $(0, 0, h)$ and the radius, r, for all integrations is measured from there.

$$\lim_{a\kappa \to 0} G_{ij} = \frac{1}{4\pi h} \int_{\phi_1}^{\phi_2} (r_2 - r_1)\, d\phi \qquad (4.69).$$

The radial derivative of u^* and the dot product of $\mathbf{r}$ and $\mathbf{n}$ are required to evaluate $\widehat{H}_{ij}$. The derivative of u^* is:

$$\frac{du^*}{dr} = -\frac{1}{4\pi}\left(\frac{1}{r^2} + \frac{a\kappa}{r}\right)e^{-a\kappa r} \qquad (4.70),$$

while the dot product is

$$\mathbf{r} \cdot \mathbf{n} = h\cos\theta - 1 = \frac{h^2 - 1 - r^2}{2} \qquad (4.71).$$

The expression on the far right of Equation (4.71) results from the geometric relationship among r, h, and θ. $\widehat{H}_{ij}$ can now be evaluated to yield:

$$\widehat{H}_{ij} = -\frac{1}{8\pi h} \int_{\phi_1}^{\phi_2}\left[\left(r_2 + \frac{2}{a\kappa} - \frac{h^2-1}{r_2}\right)e^{-a\kappa r_2} - \left(r_1 + \frac{2}{a\kappa} - \frac{h^2-1}{r_1}\right)e^{-a\kappa r_1}\right] d\phi \qquad (4.72).$$

In the absence of Coulombic screening,

$$\lim_{a\kappa \to 0} \widehat{H}_{ij} = -\frac{1}{8\pi h} \int_{\phi_1}^{\phi_2} (r_1 - r_2)\left[1 - \frac{(h^2 - 1)}{r_1 r_2}\right] d\phi \qquad (4.73).$$

Equations (4.68) and (4.69) are valid for $h \geq 1$, but (4.72) and (4.73) warrant further discussion. The expressions for $\widehat{H}_{ij}$ are valid for $h \geq 1$ except when the integral is evaluated over elements containing the north pole, in which case it is valid only for $h > 1$. The exception for $h = 1$ reflects the jump condition in the double-layer potential when the source point enters the surface. When the source point is in the surface (as opposed to infinitesimally above it) $h^2 - 1 = 0$, and $\widehat{H}_{ij}$ is given by:

$$\widehat{H}_{ij} = -\frac{1}{8\pi h} \int_{\phi_1}^{\phi_2}\left[\left(r_2 + \frac{2}{a\kappa}\right)e^{-a\kappa r_2} - \left(r_1 + \frac{2}{a\kappa}\right)e^{-a\kappa r_1}\right] d\phi \qquad (4.74)$$

or

150

$$\lim_{a\kappa \to 0} \widehat{H}_{ij} = -\frac{1}{8\pi h} \int_{\phi_1}^{\phi_2} (r_1 - r_2) \, d\phi \qquad (4.75).$$

If, on the other hand, the field point is in the domain along the polar axis, the quantity involving $h^2 - 1$ is:

$$\lim_{h \to 1, \, \theta = 0} \frac{h^2 - 1}{r_1} \sim \frac{h^2 - 1}{h - 1} = h + 1 \neq 0 \qquad (4.76).$$

The correct expressions for $\widehat{H}_{ij}$ in this case are:

$$\widehat{H}_{ij} = -\frac{1}{8\pi h} \int_{\phi_1}^{\phi_2} \left[\left(r_2 + \frac{2}{a\kappa} - \frac{h^2 - 1}{r_2} \right) e^{-a\kappa r_2} - \left(r_1 + \frac{2}{a\kappa} - (h + 1) \right) e^{-a\kappa r_1} \right] d\phi \qquad (4.77)$$

and

$$\lim_{a\kappa \to 0} \widehat{H}_{ij} = -\frac{1}{8\pi h} \int_{\phi_1}^{\phi_2} (r_1 - r_2) \left[1 - \frac{(h + 1)}{r_2} \right] d\phi \qquad (4.78).$$

In addition to the surface integrals presented above, the "remainder" problem requires a volume integral to determine the particular solution produced by the fixed charge density in the sphere. For region 1, the fundamental solution is $u^* = 1/4\pi r$ and the particular solution is given by:

$$u^P = \frac{1}{4\pi} \int_{\Omega} \frac{\rho^*}{r} \, dV \qquad (4.79),$$

where $\rho^* = (a\kappa)^2 \, u^P = \sigma_x^* (a\kappa/\varepsilon_2) \exp(-a\kappa z)$. At this time, we shift the coordinate system to the origin of the sphere and write u^P as:

$$u^P = \sigma_x^* \frac{a\kappa}{4\pi \varepsilon_2} \int_{\Omega} e^{-a\kappa s} \frac{e^{-a\kappa t \mu}}{r} \, dV \qquad (4.80),$$

where $z = s + t\mu$, t is measured from the center of the sphere and $\mu = \cos \theta$. Numerical quadrature schemes for evaluating integrals over the volume of a sphere might employ 300 - 500 evaluations of the integrand [30] and still be appreciably in error because they fail to catch the effects of the large and rapidly changing charge density at $t = 1$ and $\mu = -1$.

Instead of a completely numerical evaluation of (4.80), we will exploit the axisymmetry of the remainder problem to obtain a series solution to evaluate u^P on the surface of the sphere.

We represent the charge distribution in the sphere as infinitesimal charged rings (Figure 4-6) and calculate u^P at points on the sphere's surface ($t = 1$) by summing the potentials produced by all such rings. The total charge, δQ^*, on each ring is

$$\delta Q^* = \rho^* \, (2\pi \, t_o \sin \, \theta_o)(t_o \, d\theta_o) \, dt_o = -2\pi \, t_o^2 \, \sigma_x^* \, (a\kappa/\varepsilon_2) \, e^{-a\kappa s} \, e^{-a\kappa t_o \mu_o} \, d\mu_o \, dt_o \quad (4.81).$$

The ring creates a potential given by [27]:

$$\delta u^P \, (t,\mu) = \frac{\delta Q^*}{4\pi \, t_o} \sum_{n=0}^{\infty} \left(\frac{t_o}{t}\right)^{n+1} P_n(\mu_o) \, P_n(\mu) \quad , \quad t > t_o \quad (4.82),$$

where $P_n(\mu)$ = Legendre polynomial of degree n. This series is suitable for calculating the potential at the surface ($t = 1$) due to charged rings inside the sphere ($t_o \leq 1$) because the series, fortunately, also converges for $t_o = t = 1$. The full potential is then calculated by summing (integrating) over all rings:

$$u^P \, (t,\mu) = 2\pi \, \sigma_x^* \, \frac{a\kappa}{\varepsilon_2} e^{-a\kappa s} \int_{-1}^{1} d\mu_o \int_{0}^{1} t_o^2 \, dt_o \, \frac{e^{-a\kappa t_o \mu_o}}{4\pi \, t_o} \sum_{n=0}^{\infty} \left(\frac{t_o}{t}\right)^{n+1} P_n(\mu_o) \, P_n(\mu) \quad (4.83).$$

After simplification and rearrangement, Equation (4.83) is:

$$u^P(t,\mu) = \sigma_x^* \, \frac{a\kappa}{2\varepsilon_2} e^{-a\kappa s} \sum_{n=0}^{\infty} P_n(\mu) \, t^{-(n+1)} \int_{-1}^{1} P_n(\mu_o) \, d\mu_o \int_{0}^{1} t_o^{n+2} \, e^{-a\kappa t_o \mu_o} \, dt_o \quad (4.84).$$

The integral over t_o in (4.84) can be done by parts for each value of n. If $\int vdw = vw - \int wdv$, the normal choice would be $v = t_o^{n+2}$ and $dw = exp \, (-a\kappa t_o \mu_o)dt_o$ so that a finite number of integrations are required. Each integration by parts then places a factor of $a\kappa\mu_o$ in the denominator which might cause difficulties for a subsequent numerical evaluation of the integral over μ_o (notably when $\mu_o = 0$). Instead, we set $v = exp \, (-a\kappa t_o \mu_o)$ and $dw = t_o^{n+2} \, dt_o$ to obtain an infinite series for the integral:
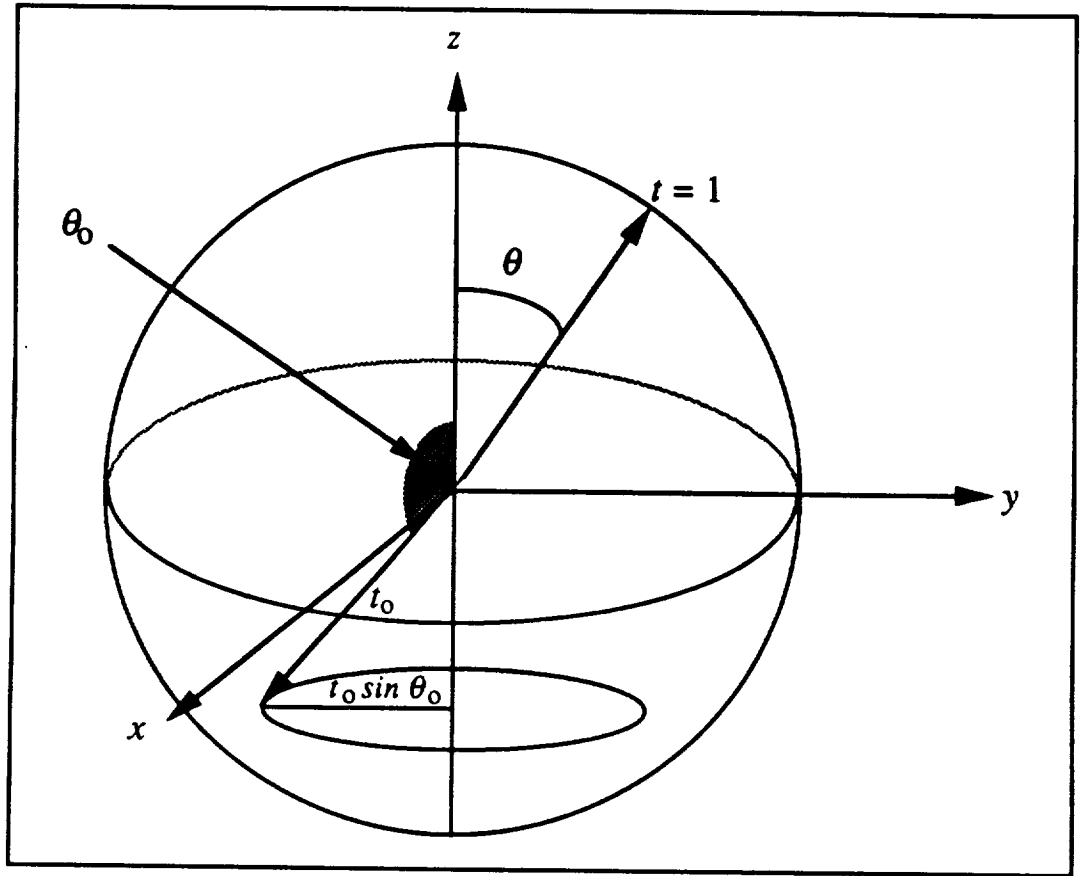
152

Figure 4-6: Definition sketch for ring of charge.

Geometry used to calculate the potential on the surface of the sphere due to a ring of charge. Subscript "o" denotes quantities associated with the charged ring.

$$\int_0^1 t_0^{n+2}\, e^{-a\kappa t_0\mu_0}\, dt_0 = (n+2)!\; e^{-a\kappa\mu_0} \sum_{k=0}^{\infty} \frac{(a\kappa\mu_0)^k}{(n+3+k)!} \qquad (4.85).$$

Comparison with the convergent series expansion for $exp\,(a\kappa\mu_0)$,

$$exp\,(a\kappa\mu_0) = \sum_{k=0}^{\infty} \frac{(a\kappa\mu_0)^k}{k!} \qquad (4.86),$$

shows that the ratio of the kth term in (4.85) to the kth term in (4.86) is (within a multiplicative constant) $k!/(n+3+k)! < 1$ and that (4.85) converges faster than the exponential series because

$$\lim_{k\to\infty} \frac{k!}{(n+3+k)!} = \frac{k!}{k!\,(k+1)(k+2)(k+3)\cdots(k+n+3)} = 0 \qquad (4.87).$$

153

The potential at each node produced by the fixed charge distribution can now be written as:

$$u_i^P = u^P(1,\mu_i) = \sigma_x^* \frac{aK}{2\varepsilon_2} e^{-aKs} \sum_{n=0}^{\infty} c_n P_n(\mu_i) \qquad (4.88),$$

where

$$c_n = \int_{-1}^{1} e^{-aK\mu_o}(n+2)! \sum_{k=0}^{\infty} \frac{(aK\mu_o)^k}{(n+3+k)!} P_n(\mu_o) \, d\mu_o \qquad (4.89),$$

$\mu_i = \cos\theta_i$, and $t = 1$ because the nodes are on the surface of the sphere. The integral in (4.89) is evaluated numerically using a Romberg integration scheme with a polynomial extrapolation to the limit of zero step size (described by Press $et\ al.$ [31]). The estimated relative error in the value of c_n is approximately 10^{-6}.

Except for the specialization of the analysis to cases with constant elements, the discussion of boundary elements so far has been general. In the following sections, the method for discretizing the surface is presented (§4.5), and the specifics of the computations are described (§4.6).

4.5 Boundary Element Geometry

The surface of the sphere is divided into spherical triangular elements (Figure 4-7), each of which is taken to have constant values of surface charge density, surface potential, and normal flux. Each edge of the element is the path of minimum length between the two vertices defining that edge. The edges can then be considered the arc of the great circle connecting the vertices or, equivalently, the intersection of the sphere's surface with the plane containing two vertices and the origin of the sphere. The bounding plane is completely described by its normal vector. The location of the node is determined by calculating the Cartesian coordinates (x_c, y_c, z_c) of the centroid of the element (which lies within the sphere) and projecting the ray from the sphere's origin through (x_c, y_c, z_c) to the

154

surface.   The node's position on the unit sphere is $\left(\frac{x_c}{\rho}, \frac{y_c}{\rho}, \frac{z_c}{\rho}\right)$, where $\rho = \left(x_c^2 + y_c^2 + z_c^2\right)^{1/2}$.
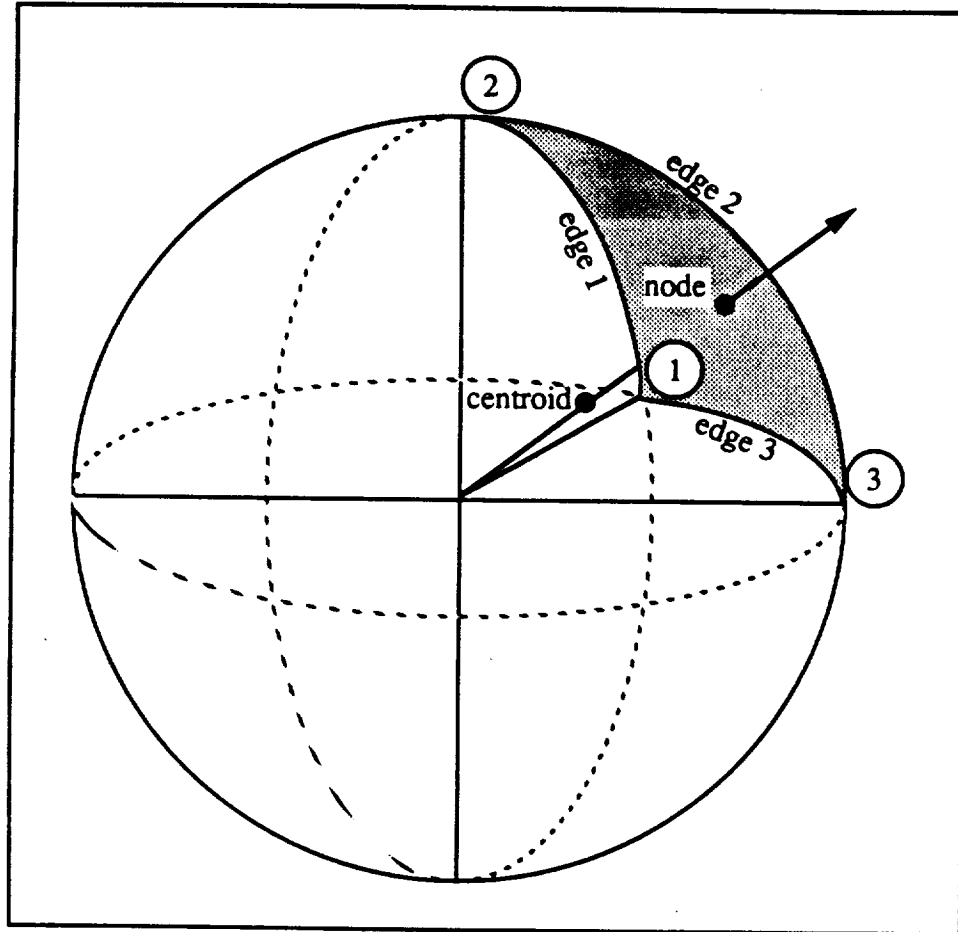

Figure 4-7: A spherical triangle element on the sphere.
Vertices are identified by circled numbers; edges are numbered sequentially as the perimeter of the element is traversed. The centroid of the element lies inside the sphere but is projected onto the surface to locate the node of the element.

The pattern for the initial (coarse) discretization of the sphere is based on either a regular octahedron (8 equilateral triangular faces) or icosahedron (20 equilateral triangular faces) which is circumscribed by the unit sphere. The vertices of the polyhedron are the

vertices of the corresponding spherical triangular elements on the sphere's surface, while the node of a given element can be located by using the arithmetic average of its vertices' Cartesian coordinates as an estimate of (x_c, y_c, z_c). (This last simplification results from the symmetry of the equilateral triangular faces of the polyhedron.) Two conventions govern the orientation of the inscribed polyhedron: (i) vertices of the polyhedron lie at the north and south poles of the sphere, and (ii) the prime meridian coincides with the boundary between two of the elements having the north pole as a common vertex. The two coarse discretizations and their "surface maps" (latitude and longitude) are shown in Figures 4-8 and 4-9. The location of the nodes is shown in the surface maps.

Subsequent refinement of the discretization is done by computer according to one of two possible methods (Figure 4-10): (i) the original element is divided into three smaller elements by converting the node into a common vertex of each new element, or (ii) the original element is divided into two elements by connecting the midpoint of the longest edge with the opposing vertex. In either case, normals to the bounding planes are calculated and used to place the nodes of the new elements. Only one method is applied to all elements at a given stage during refinement. In the three-way division, one edge of the resulting element retains its original length, so that repeated application of method (i) produces long, narrow elements which may not be adequately approximated by the nodal value. Method (ii) halves the longest edge and therefore produces elements which are more compact than those of method (i). The three-way division is applied first to produce elements with one edge longer than the others, then two-way refinement is applied successively thereafter. The elements produced by these refinement schemes are, in general, not identical, but this presents no inherent difficulty for the boundary element method.
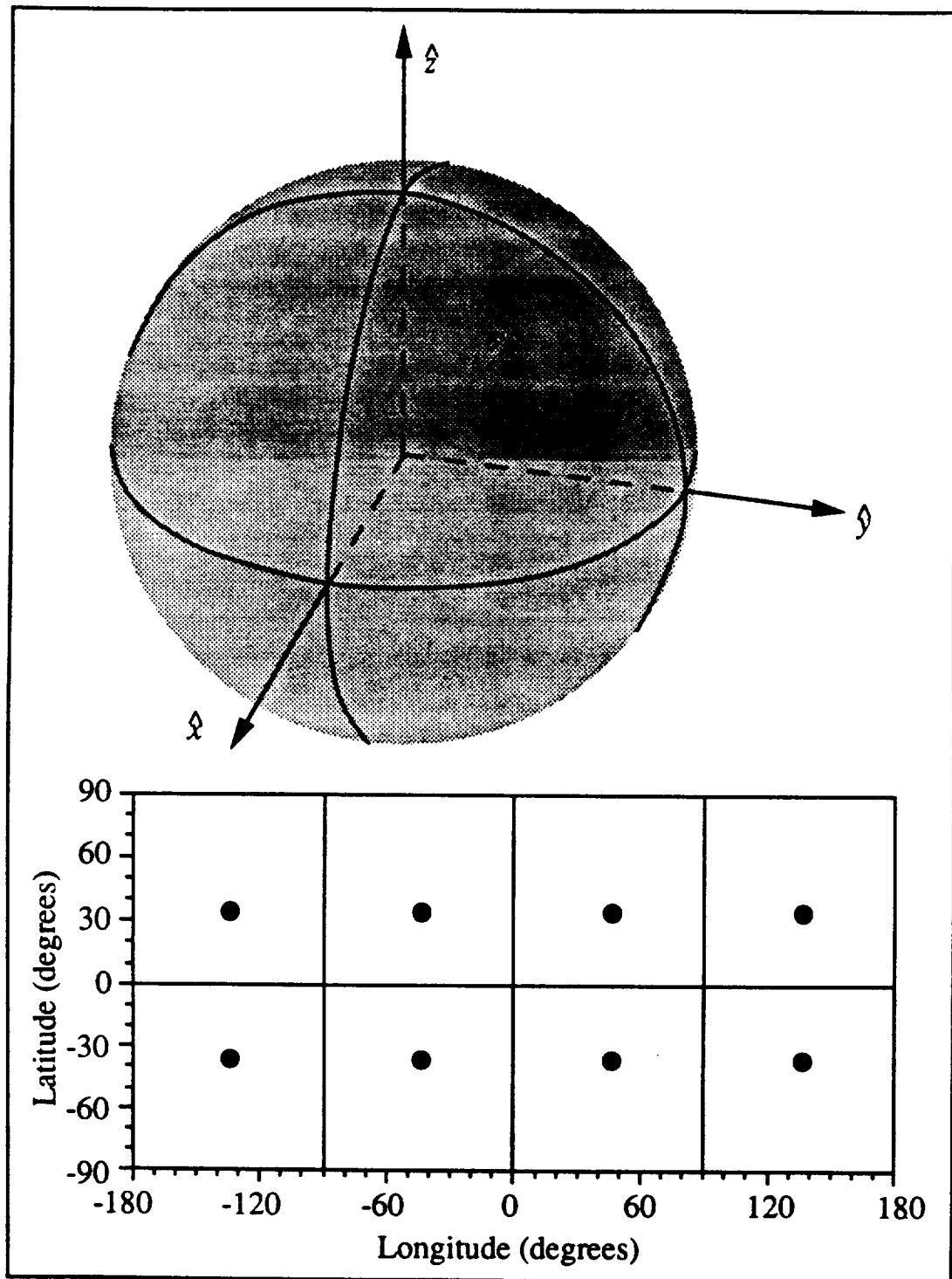
156

Figure 4-8: Octahedral discretization of the sphere's surface.
The boundaries of the elements have been drawn on the surface of the sphere; the axes shown define the orientation of the discretization. The corresponding 2-dimensional projection ("surface map") of the discretization is also shown. Surface points are identified by latitude and longitude. Points identify the location of the nodes.

157

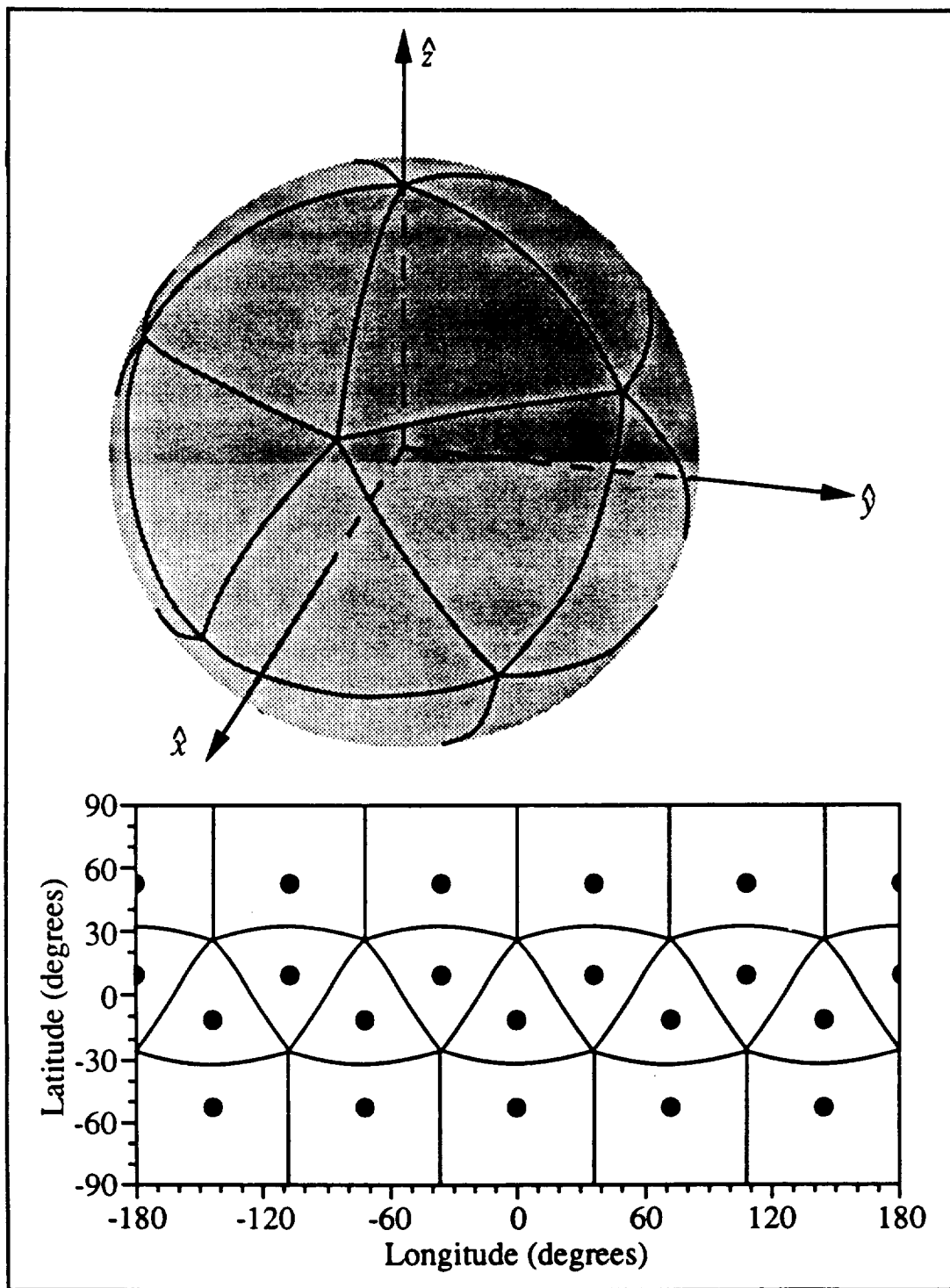Figure 4-9: Icosahedral discretization of the sphere's surface.
The boundaries of the elements have been drawn on the surface of the sphere; the axes shown define the orientation of the discretization. The corresponding 2-dimensional projection ("surface map") of the discretization is also shown. Surface points are identified by latitude and longitude. Points identify the location of the nodes.

The orientation of the sphere must be defined in preparation for discussion of the case when the the particle has a nonuniform surface charge distribution. Recall that the use of a mirror particle, transforms the line of centers into an axis of rotational symmetry. For a given separation, then, the electrostatic interaction energy of the system depends only on which point on the sphere's surface occupies the south pole. Two angles are sufficient to specify the location of the south pole and, therefore, the orientation of the system. An obvious choice is the latitude ($-90° \leq \alpha \leq +90°$) and longitude ($-180° \leq \beta \leq +180°$) of the ray connecting the centers of the spheres (Figure 4-11). In the fixed coordinate system established by the crystal, the molecule appears to be oriented so the point (α, β) lies nearest the plate, so the orientation can also be considered the "south pole." This is a simple means of associating features of the potential energy surface with the surface charge distribution that creates them.

Figure 4-10: Two successive refinements of a planar triangle.
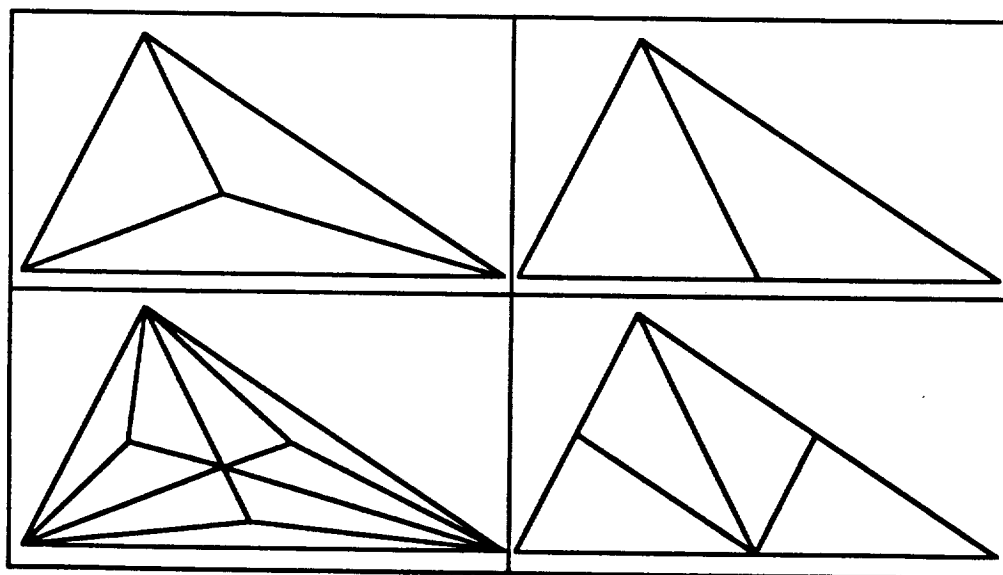(left) Three-way refinement: a new vertex is created at the centroid of the original element.
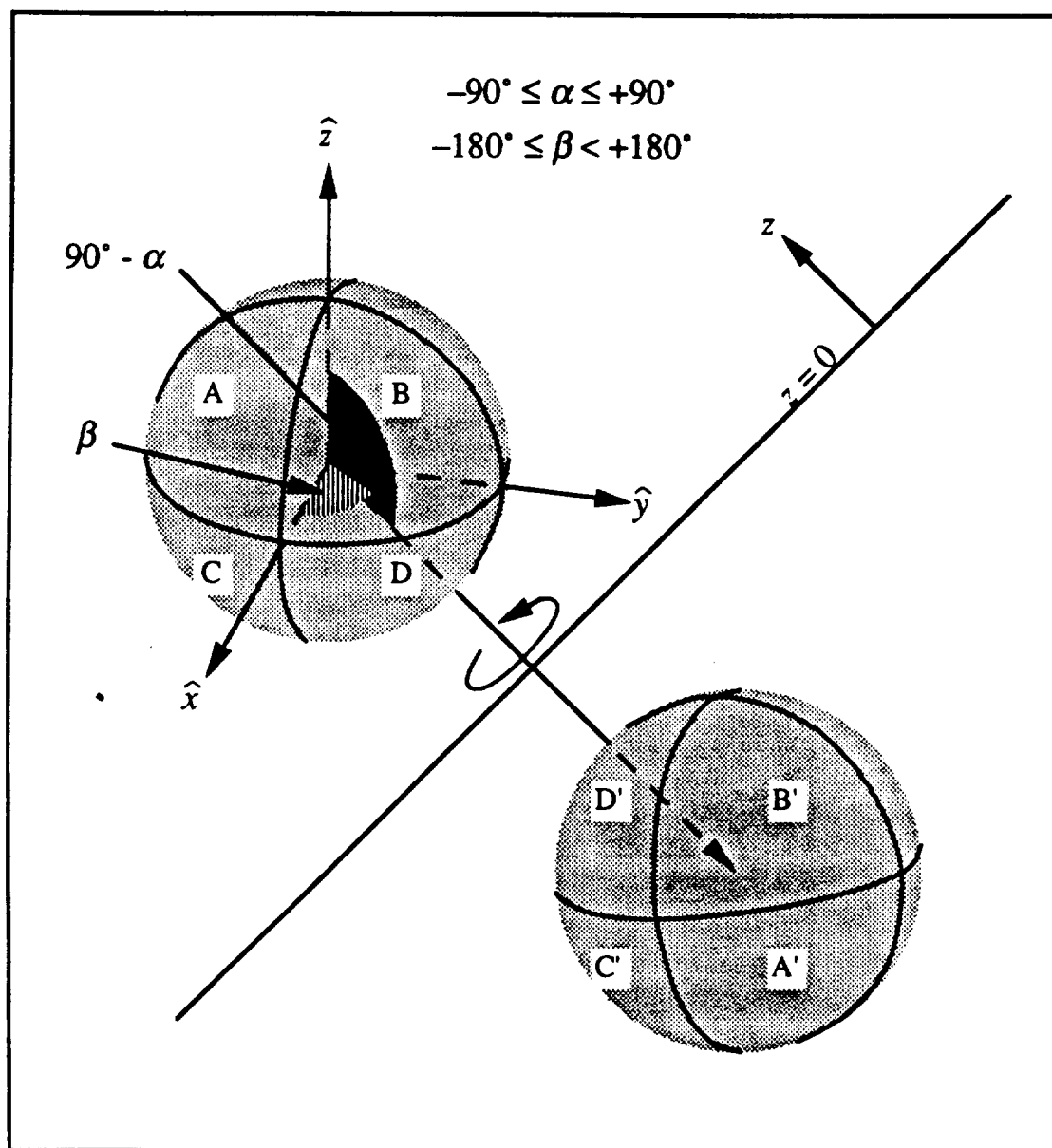(right) Two-way refinement: the new edge bisects the longest edge of the triangle.

Figure 4-11: Orientation of the molecule.
Octants are identified by letters and their reflections are indicated by primes. The line of centers of the two spheres is an axis of rotational symmetry.

4.6 Mechanics of Boundary Element Calculations

As mentioned in section 4.4, a coordinate transformation is used to create a temporary coordinate system in which the sphere's center is at the origin and the fieldpoint sits above the north pole of the particle. In this section, we present the specifics of the numerical computation of the boundary integrals over the surface elements on the sphere. In the discussion to follow, Cartesian coordinates (x, y, z), as well as the x, y, and z components of vectors, are taken to be in the temporary coordinate system; the angles θ and ϕ used here are also confined to the temporary coordinate system and are not related to the orientation angles discussed in section 4.5.

For each fieldpoint, the computer program BEM3D spends a significant amount of time assessing the geometry of the elements in order to determine which elements occupy the north pole so that the correct form of the $\hat{H}_{ij}$ integral is used. This assessment is simple when node i and elements j are on the same sphere; only element $j = i$ can occupy the north pole and $h^2 - 1$ is strictly zero. The situation is more complicated when the element under consideration is on the other sphere.

There are three ways in which an element can occupy the north pole (Figure 4-12): (i) one of the element's vertices can coincide with the north pole, (ii) one of the element's edges can cross the north pole, and (iii) the north pole can lie in the interior of the element. When one or more of these conditions occurs, $\hat{H}_{ij}$ is evaluated from either Equation (4.77) or (4.78). By explicitly changing the form of the expression for $\hat{H}_{ij}$ when the north pole is involved, the problem of division by zero is eliminated from the computer code.

In all the integral expressions for G_{ij} and $\hat{H}_{ij}$, the limits of integration in r (or θ) have been left as functions of ϕ. We now present the method by which functions are integrated over the surface element. For the element shown in Figure 4-13a, for instance, the integral of the generic function f could be written as:

$$F = \int_{\phi_1}^{\phi_2} d\phi \int_{\theta_1(\phi)}^{\theta_3(\phi)} f \sin\theta \, d\theta + \int_{\phi_2}^{\phi_3} d\phi \int_{\theta_2(\phi)}^{\theta_3(\phi)} f \sin\theta \, d\theta \qquad (4.90),$$

where $\theta_k(\phi)$ is calculated from the intersection of bounding plane k and the unit sphere:

$$\theta_k(\phi) = tan^{-1} = \frac{-n_{z,k}}{n_{x,k} \cos\phi + n_{y,k} \sin\phi} \qquad (4.91),$$

and $(n_{x,k}, n_{y,k}, n_{z,k})$ are the components of the normal to edge k; care must be taken to insure that values of $\theta_k(\phi)$ between 0 and π are selected.

Evaluation of Equation (4.90) as written requires the computer program to decide such things as which edges are the upper and lower limits, when to change from one edge to the next, and what is the sign of the integral. If vertices 1 and 3 were switched in Figure 4-13a, for example, evaluation of Equation (4.90) would produce a result with the opposite sign. Some of these difficulties are removed if the equivalent expression:

$$F = \int_{\phi_1}^{\phi_2} d\phi \int_{\theta_1(\phi)}^{\pi} f \sin\theta \, d\theta + \int_{\phi_2}^{\phi_3} d\phi \int_{\theta_2(\phi)}^{\pi} f \sin\theta \, d\theta$$

$$+ \int_{\phi_3}^{\phi_1} d\phi \int_{\theta_3(\phi)}^{\pi} f \sin\theta \, d\theta \qquad (4.92)$$

is evaluated instead. This procedure is shown graphically in Figure 4-13, panels b-d. As a check on the sign of the integral, BEM3D computes the integral for $f = 1$, in which case F = the surface area of the element. If the surface area as calculated is negative, the signs of all integrals associated with that element are changed so they are consistent with a positive surface area. When the element contains the north pole, only the limits of θ integration change in Equation (4.92): the lower limit is 0 and the upper limit is $\theta_k(\phi)$. In practice, the θ integrations are performed after changing the integrating variable to r. Gauss-Legendre quadrature schemes are used for the numerical integration in ϕ.
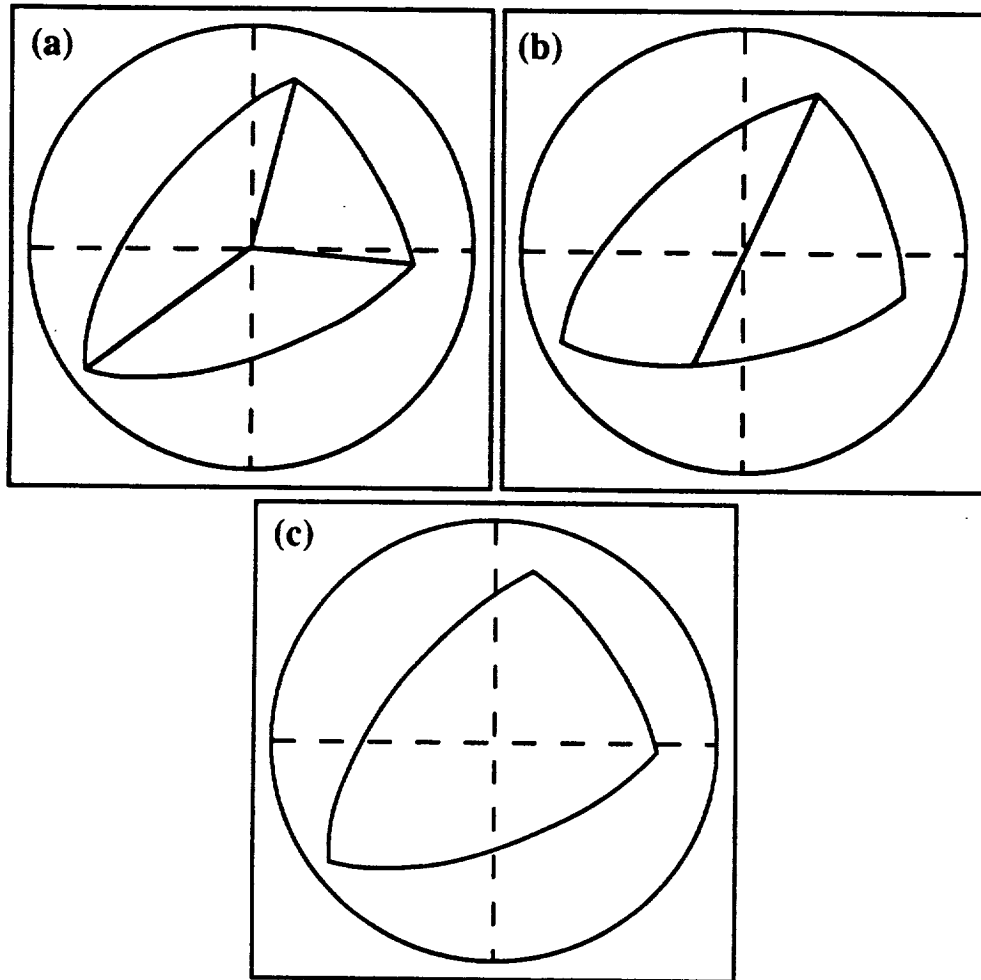
162

Figure 4-12: Three ways an element can occupy the north pole.
(a) Common vertices of several elements may lie at the pole.
(b) The edge between two elements may cross the north pole.
(c) The pole may lie within an element.

Some additional geometric situations must be considered by program BEM3D. For the most part, these arise from the choice of ϕ as the independent variable and θ as the dependent variable in describing the boundaries between elements. Consider, for instance, the case where the plane dividing two elements contains the poles (its normal lies in the xy plane). The resulting edge is a line of constant ϕ, and θ is not a function of ϕ. Although $\theta_k(\phi)$ is indeterminate, this is not a problem because the integration in ϕ makes no contribution to the integral over the element. If the z component of the normal to the edge

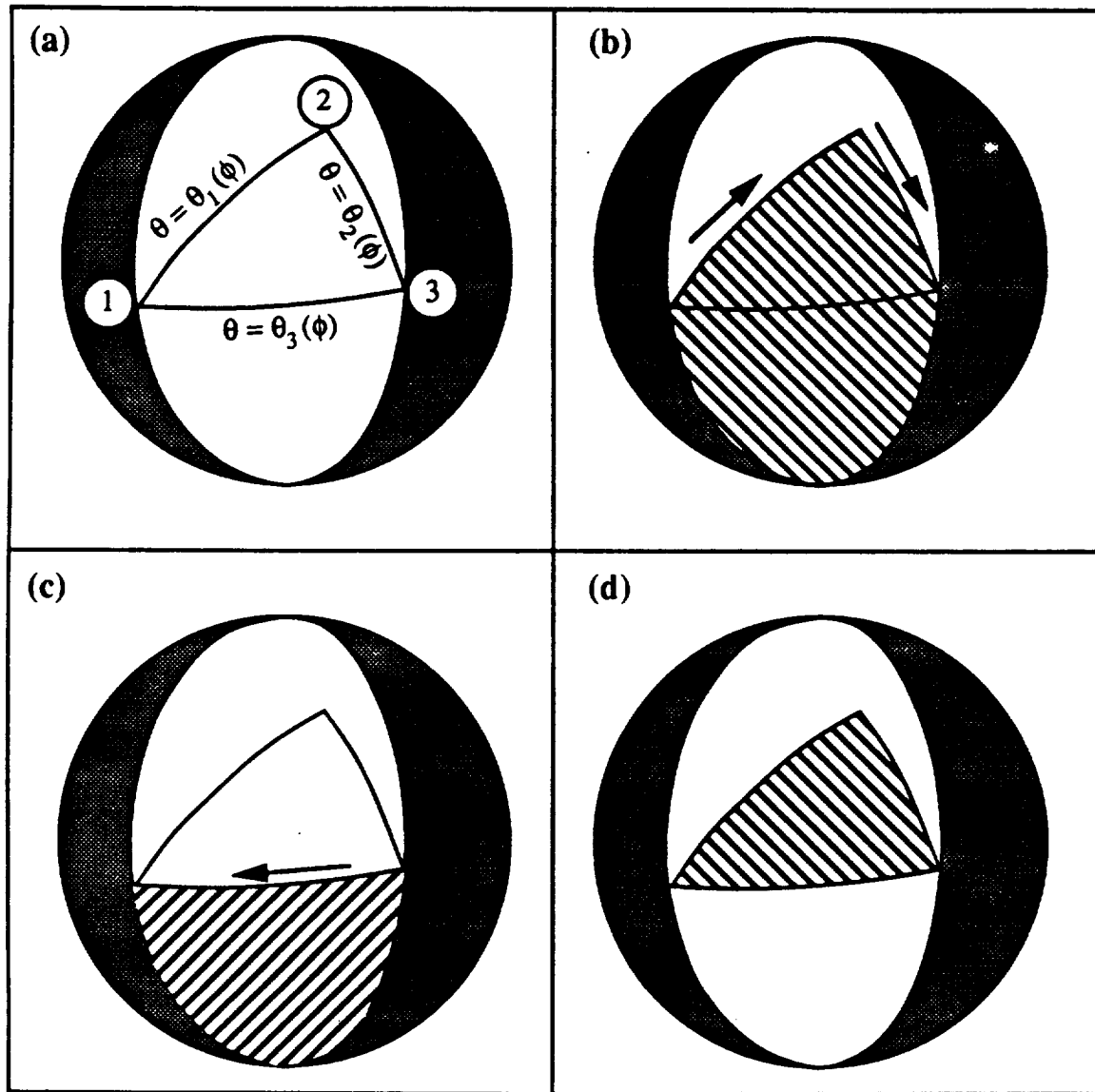Figure 4-13: Integration scheme for spherical triangular elements.
    (a) The element on the sphere with vertices and edges identified.
    (b) Integration carried out from vertices 1 to 2 and from 2 to 3 giving a
        positive contribution.
    (c) Final integration step from vertex 3 to vertex 1, which gives a negative
        contribution.
    (d) Net result when integrations in (b) and (c) are added.

along which BEM3D will integrate is sufficiently close to zero, the integration is omitted. Because the range of ϕ used is $-\pi < \phi \leq \pi$, some confusion is also possible when the path of integration crosses the plane $\phi = \pi$ (the "international date line"). If the integration is between vertices 1 and 2, for example, BEM3D calculates $|\phi_2 - \phi_1|$ and compares the result with π. If $|\phi_2 - \phi_1| > \pi$, the proposed path is not the shorter one, so 2π is added to or subtracted from ϕ_2 to obtain the correct integration path.

Once the nodal potentials and fluxes have been calculated, the charging integrals must be computed. The charging work for the sphere is evaluated approximately by the formula:

$$\frac{\Phi_{elec}^{sphere}(s)}{\varepsilon_0 \, \psi_0^2} = \frac{1}{2} \int_{A_{sphere}} \sigma^* u \ dA \approx \frac{1}{2} \sum_{j=1}^{N_1} \sigma_j^* \, u_j \, A_j \qquad (4.93),$$

where u = the total electrostatic potential, and the coefficients in the summation are the charge density, potential, and area of each element j; the summation formula reflects the constant element approximation. A similar level of approximation is applied to the charging of the plate, as discussed next.

Recall from Equations (4.57) and (4.59) that the potential anywhere in the domain is given by:

$$u_i = \sum_{j=1}^{N} q_j \, G_{ij} - \sum_{j=1}^{N} u_j \, \widehat{H}_{ij} \qquad (4.94),$$

where the fundamental solution is placed at some point x_i. in the domain and the u_j and q_j are obtained from the boundary element solution for the potential. (The flat plate potential makes no net contribution to the charging integral on the plate.) Rather than evaluating the G_{ij} and $\widehat{H}_{ij}$, with multi-point quadratures, we approximate them by:

$$G_{ij} = \int_{\Gamma_j} u_i^* \ dA \approx u_{ij}^* A_j \qquad \widehat{H}_{ij} = \int_{\Gamma_j} q_i^* \ dA \approx q_{ij}^* A_j \qquad (4.95),$$

in which u^* and q^* are evaluated at node j. Substitution of (4.95) into the charging integral for the plate gives:

$$\frac{\Phi_{elec}^{plate}(s)}{\varepsilon_0 \, \psi_0^2 \, a} = \frac{1}{2} \, \sigma_x^* \left\{ \sum_{j=1}^{N} A_j \left[q_j \int_{A_{plate}} u_{ij}^* \, dA - u_j \int_{A_{plate}} q_{ij}^* \, dA \right] \right\} \qquad (4.96).$$

For the situation depicted in Figure 4-14, we have $r^2 = z_j^2 + \eta^2$, $r = (-\eta cos\beta, -\eta sin\beta, z_j)$, $n = (-sin\theta_j cos\phi_j, -sin\theta_j sin\phi_j, -cos\theta_j)$, $\eta d\eta = r dr$, and $dA = \eta d\beta d\eta$. The integral of u_{ij}^* over the plate is then

$$\int_{A_{plate}} u_{ij}^* \, dA = \frac{1}{4\pi} \int_0^{2\pi} d\beta \int_0^{\infty} \frac{e^{-a\kappa r}}{r} \eta \, d\eta = \frac{1}{2} \int_{z_j}^{\infty} e^{-a\kappa r} \, dr = \frac{1}{2} \frac{e^{-a\kappa z_j}}{a\kappa} \qquad (4.97)$$

and the corresponding expression for the q_{ij}^* term is

$$\int_{A_{plate}} q_{ij}^* \, dA = -\frac{1}{4\pi} \int_0^{2\pi} (r \cdot n) \, d\beta \int_0^{\infty} \left(\frac{1}{r^2} + \frac{a\kappa}{r} \right) \frac{\eta}{r} \, d\eta = \frac{cos \, \theta_j}{2} e^{-a\kappa z_j} \qquad (4.98).$$

Note that the integration in β leaves only the z component of the flux. If (4.97) and (4.98) are substituted into (4.96) and we make use of the symmetry of the problem to express the integrals over all the elements in terms of the integrals over one sphere, we can write the charging integral for the plate as:

$$\frac{\Phi_{elec}^{plate}(s)}{\varepsilon_0 \, \psi_0^2 \, a} = \sigma_x^* \frac{1}{2} \sum_{j=1}^{N_1} A_j \, e^{-a\kappa z_j} \left(\frac{q_j}{a\kappa} + u_j \, cos\theta_j \right) \qquad (4.99).$$

This concludes the discussion of the boundary element method. We now exercise the boundary element program BEM3D on two relatively simple problems so we can assess both the accuracy of the method and the significance of nonuniform charge distributions.
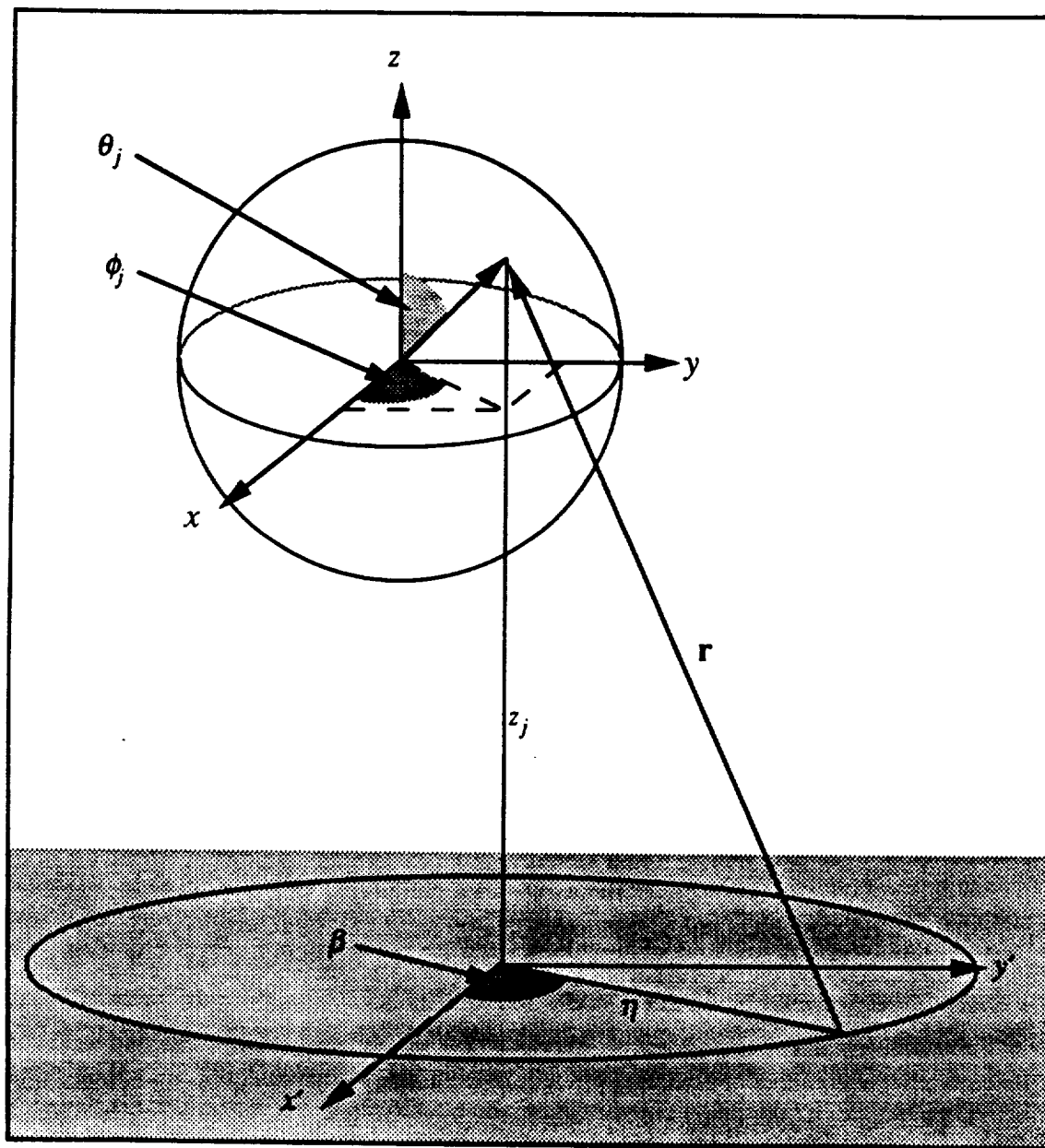
166

Figure 4-14: Calculation of charging integral over infinite flat plate.
The node is located at (x_j, y_j, z_j); $\mathbf{n} = (-sin\theta_j cos\phi_j, -sin\theta_j sin\phi_j, -cos\theta_j)$. The x' and y' axes are parallel to the x and y axes passing through the sphere.

The problem of two uniformly charged spheres (see Figure 4-15) was solved for the case where $\varepsilon_1 = \varepsilon_2 = \sigma^* = 1$, in which case the dimensionless surface potential at infinite separation is $u^\infty = (1 + a\kappa)^{-1}$. Φ_{elec} was calculated as a function of distance from the plate and compared with the results from the linear superposition approximation [5,6]. The potential energy calculated from the linear superposition approximation is:

$$\frac{\Phi_{elec}^{LSA}(s)}{\varepsilon_0 \, \psi_0^2 \, a} = \frac{4\pi}{(1 + a\kappa)^2} \frac{e^{-2a\kappa(s-1)}}{2s} = \frac{4\pi}{(1 + a\kappa)^2} \frac{e^{-2a\kappa d}}{2s} \qquad (4.100).$$
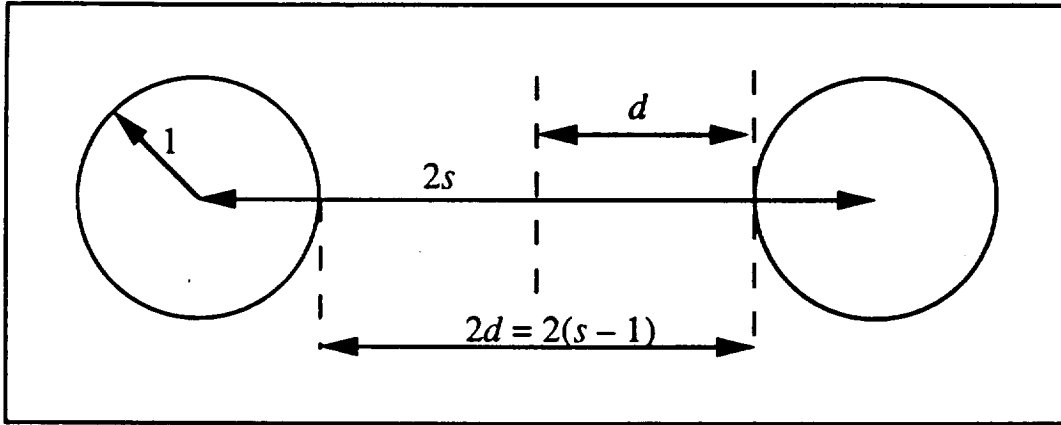

Figure 4-15: Definition sketch for the two sphere problem.

Results for $a\kappa = 0.1$ and 1 are shown in Figure 4-16, while results for $a\kappa = 5$ are given in Figure 4-17a. In all cases, the $\hat{z}$ axis of the discretization (see Figures 4-8 and 4-9) is coincident with the line of centers. Meshes with $N = 8, 24, 48$, and 96 are based on an initial octahedron discretization while the meshes with $N = 20$ and 60 are based on an icosahedron. The BEM calculations agree well with the LSA for dimensionless gaps $d \geq (a\kappa)^{-1}$. For instance, BEM calculations with 96 elements are within 1% of the LSA for $d \geq 0$ when $a\kappa = 0.1$, $d > 0.05$ when $a\kappa = 1$, and $d > 0.11$ when $a\kappa = 5$. For $d \sim a$, the relative error in the BEM calculations is approximately 10^{-4}. The apparent divergence at $d = 3$ and
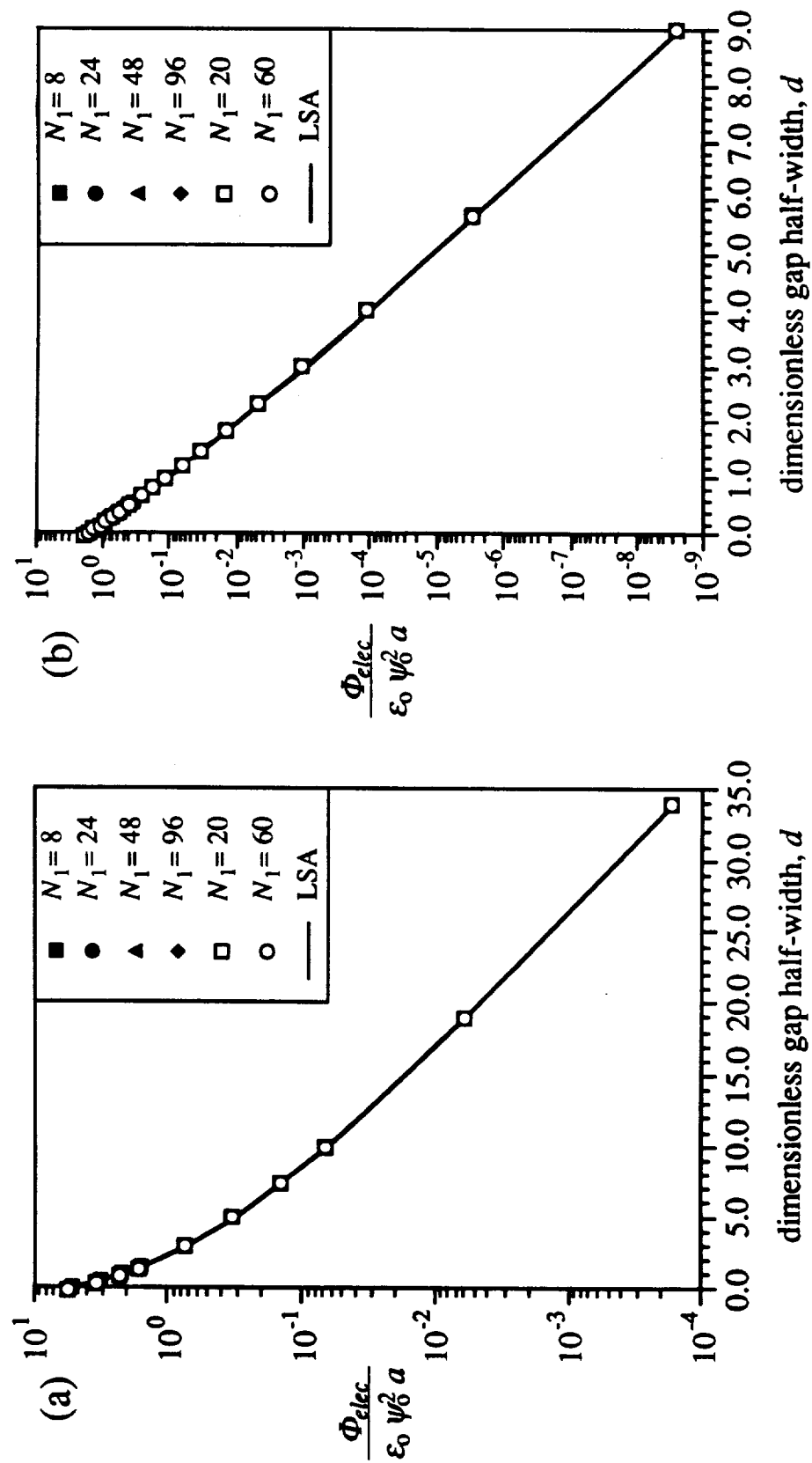
Figure 4-16: Electrostatic free energy for two uniformly charged spheres with $\sigma^* = \varepsilon_1 = \varepsilon_2 = 1$.
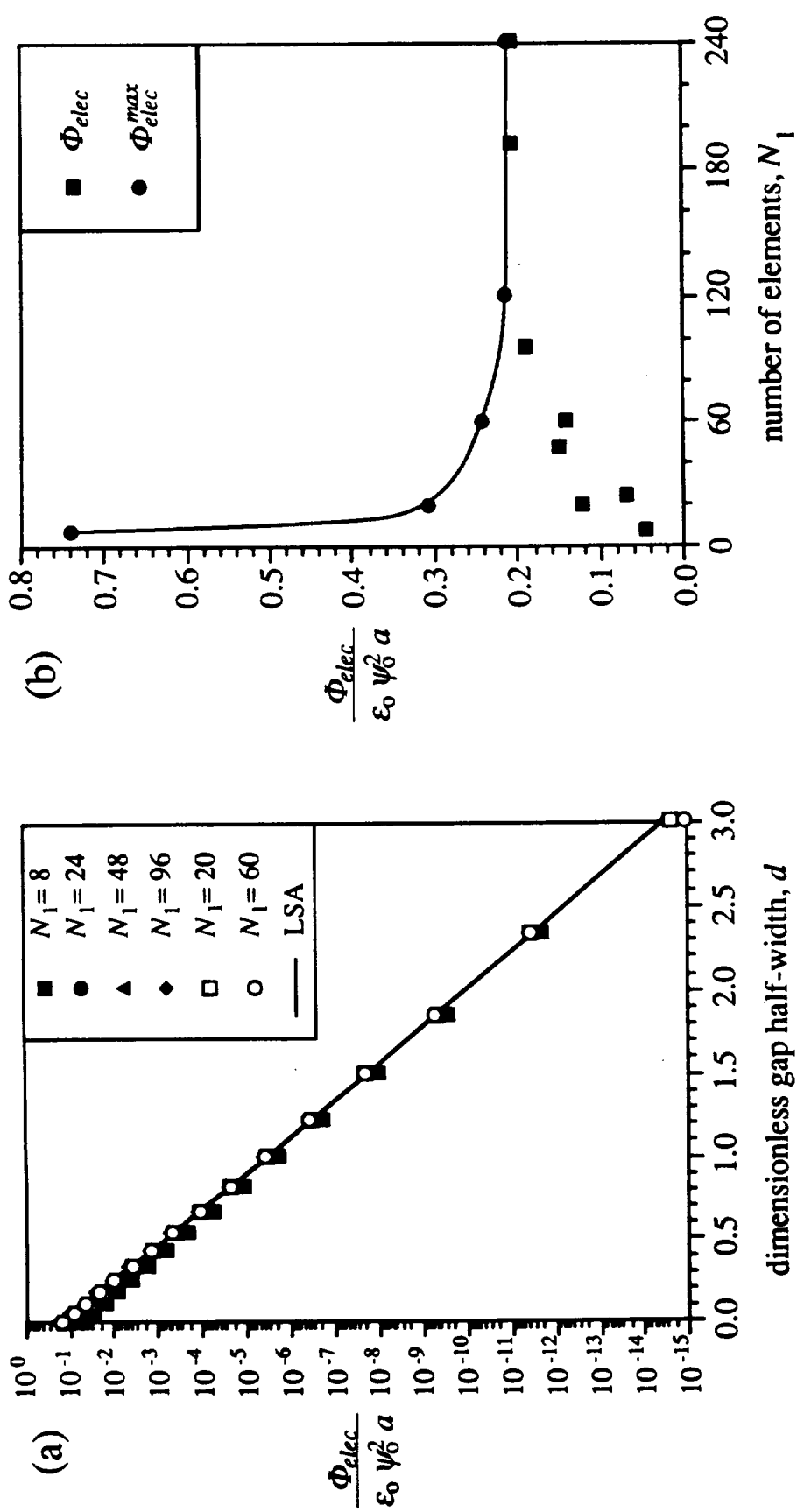(a) $a\kappa = 0.1$. (b) $a\kappa = 1.0$.

Figure 4-17: Electrostatic free energy for two uniformly charged spheres for $a\kappa = 5$ and $\sigma^* = \varepsilon_1 = \varepsilon_2 = 1$.
(a) Φ_{elec} as a function of separation.
(b) Φ_{elec} at contact as a function of the number of elements on the sphere. Maximum values calculated with a node positioned at the south pole.

$a\kappa = 5$ (Figure 4-17a) reflects the level of noise in the calculation ($\sim 10^{-14}$). At smaller separations (especially at contact), the linear superposition approximation is not valid [5,32], but convergence can be studied by comparing the computed values of Φ_{elec} with a reasonable upper bound.

At high ionic strengths (large $a\kappa$), the calculated energy is sensitive to the location of the node nearest the south pole (the image sphere). The surface potential is a maximum at the south pole and decreases rapidly with increasing z. Under the constant element approximation, the potential over the entire element is that of the node; if the node is relatively far from the south pole, the element's contribution to the charging work is underestimated. By rotating the spheres so that a node rests at the south pole, the "nearest node effect" can be removed. The potential at the south pole is now correct to the accuracy of the BEM, but the calculated energy is an overestimate of the charging work because the infinitesimal area over which it obtains is grossly exaggerated by the finite area of the element. Φ_{elec} was calculated at contact for several discretizations and plotted against N in Figure 4-17b. The calculated potential energies are converging to the same value independent of orientation.

The relatively slow convergence for this simple test problem reveals a shortcoming of the constant element approximation: the length scale of the discretization must be significantly smaller than κ^{-1} for reasonable accuracy. In the case of uniform spheres with $a\kappa = 5$, a 240 element discretization produces an answer within 2% of the "final" value. When the charge distribution is nonuniform or the ionic strength is higher, the discretization must be further refined before comparable accuracy is reached.

The effects of a nonuniform charge distribution are illustrated using a charged "cap" covering 25% of the particle's surface; the remainder of the sphere is uncharged. The scaled surface charge density of $\sigma^* \approx 358$ over the cap is based on a net charge of $Z = +10.5$ spread uniformly over a sphere 16.48Å in radius. These values are appropriate for the idealized representation of hen egg white lysozyme used for more detailed work (§4.8).

The initial discretization for the cap studies is an icosahedron with the five elements of the charged cap covering the particle's north pole.

The effective "south pole" was rotated from the north pole ($\alpha = +90°$) to the south pole ($\alpha = -90°$) in steps of 45° with a fixed longitude of $\beta = +90°$. The calculated Φ_{elec} based on 240 elements is shown in Figure 4-18 as a function of orientation and separation for $a\kappa = 5$ and 10. The most striking feature of these calculations is that a rotation of 90° can easily change Φ_{elec} by a factor of 60 or more. The relative difference between "south pole" latitudes of +90° and +45° is smaller for $a\kappa = 10$ than for $a\kappa = 5$, reflecting the greater effect of screening in the former case.

These computations are subject to convergence problems similar to those in the uniform two-sphere problem. The electrostatic interaction energy for +90° should be larger than for any other orientation because the charged caps are closer. The BEM results at contact, however, are still dominated by the sensitivity to node placement described above. With 240 elements, the node spacing is just close enough at $a\kappa = 5$ that $\Phi_{elec}(+90°) > \Phi_{elec}(+45°)$ everywhere, although that is not yet true for the derivative of Φ_{elec}. When $a\kappa = 10$ (Figure 4-18b), 240 elements are insufficient to place the potential energies in the proper ranking for all separations. A series of calculations with sequentially refined grids shows a consistent reduction in the size of this discrepancy, indicating it is a numerical artifact.

Electrostatic free energies calculated from the boundary element method agree well with those predicted from the linear superposition approximation when the particles are not too close. The finite size of the elements introduces some numerical "orientation" effects which decrease with further refinement of the mesh. Additional calculations with a nonuniform charge distribution show that the free energy depends strongly on orientation, and that these orientation effects could play a role in protein crystal growth. The next step is to develop an approximate model of the charge distribution on a protein for more detailed study.
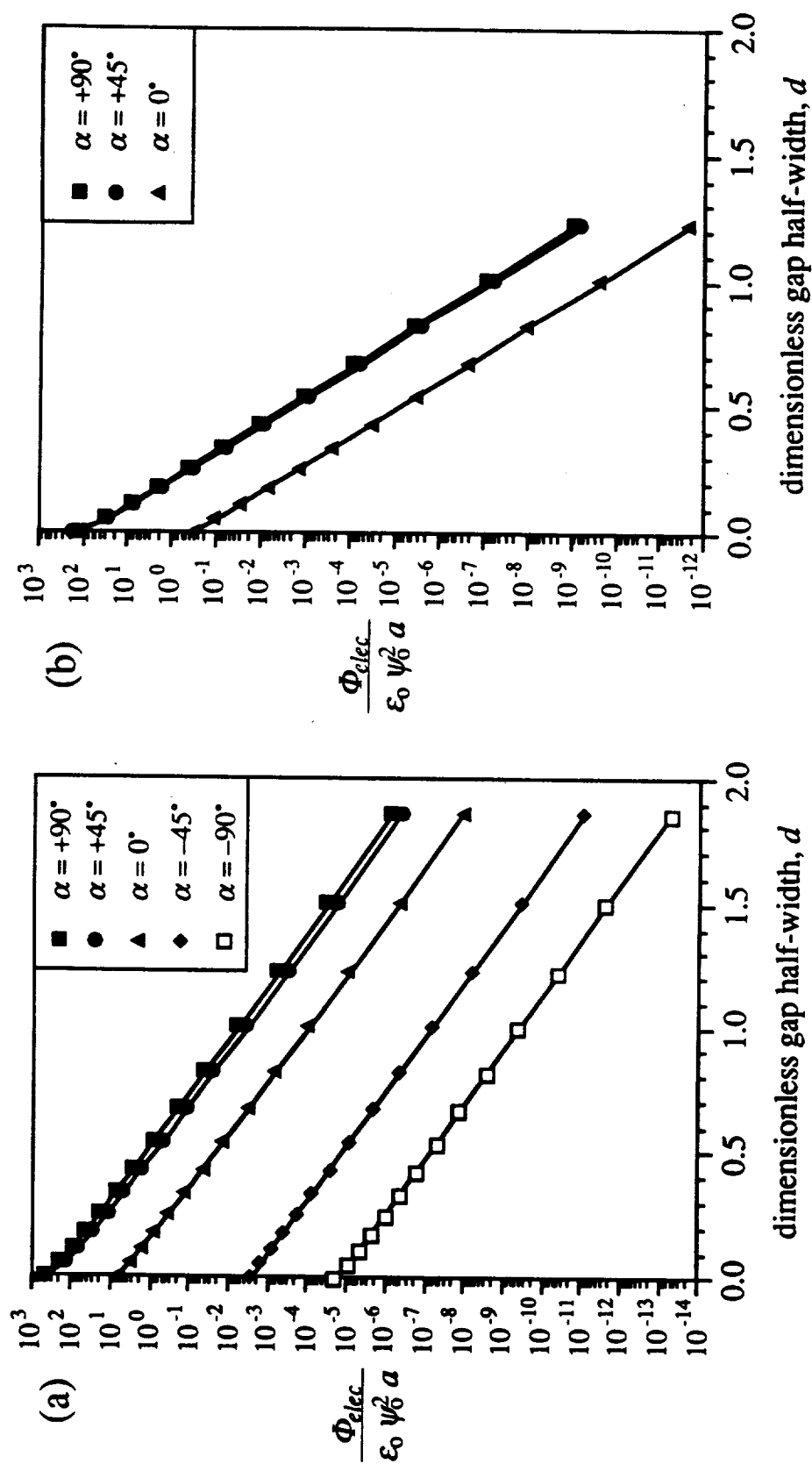
172

Figure 4-18: Electrostatic free energy for two image spheres with charged caps. Uniform charge density of $\sigma^* = 358$ is applied to 25% of the surface, the remainder of the sphere is uncharged. Dielectric constants are $\varepsilon_1 = 1$ and $\varepsilon_2 = 78.5$; $\beta = +90^\circ$. (a) $a\kappa = 5$. (b) $a\kappa = 10$.

4.8 Idealization of Lysozyme Molecule

The thrust of this study is to describe the features of the electrostatic interaction which derive from variations in surface charge density. Rather than create additional artificial (and probably unrealistic) charge distributions as was done for the "charged cap" problem in section 4.7, the actual charge distribution of a small protein is used as a model to assess the strength of nonuniformity effects. Lysozyme was selected because it has relatively few charges and more crystal growth studies have been performed with lysozyme than other proteins. The method of mapping the actual charge distribution onto a spherical surface is the subject of this section.

Hen egg white lysozyme is reported to be an oblong molecule approximately $23\text{Å} \times 28\text{Å} \times 40\text{Å}$ [8]. The approximate coordinates of its charged groups (taken from crystallographic data for the tetragonal space group at 1.4M NaCl in 0.02M sodium acetate buffer at pH 4.7) are listed in Table 4-2 [8]. We make the approximation that all the charged groups lie on the surface of the molecule and seek the location and size of the sphere which comes closest to all the charged groups.

The sphere is defined by four unknowns: three coordinates of the origin (x_0, y_0, z_0) and its radius, a. One method for obtaining the best-fit sphere is to find the location of the origin such that the lengths of radii from the origin to charges i,

$$R_i = \left[(x_i - x_0)^2 + (y_i - y_0)^2 + (z_i - z_0)^2\right]^{1/2} \tag{4.101}$$

have a minimum scatter. If the R_i are considered independent measures of the particle's size, this specification is equivalent to minimizing the sample variance of the N radii. Note that the sample variance,

$$s_R^2 = \frac{1}{N} \sum_{i=1}^{N} \left(R_i - \overline{R}\right)^2 \tag{4.102}$$

is a minimum [33]. For a given trial origin, the appropriate estimate for a is then $\overline{R}$. The search for the best-fit sphere is reduced to a search for the origin which minimizes s_R^2.

174

Such a search was performed by the FORTRAN program SPHERFIT using the method of random descent in a fashion analogous to that used to find crystal orientations by program ANGLE (§2.10). The ultimate step size for each coordinate is 0.01Å. The best-fit sphere is located at (−1.67, 20.91, 17.91) and has a radius of 16.48Å. These values compare favorably with the center of mass (−1.08, 20.00, 18.35) determined by inspection [8] and the hydrodynamic radius of approximately 20Å [9]. The location of charge i on the surface was determined from the intersection of the radius vector $\mathbf{R}_i$ with the surface, in the same way the location of the nodes was fixed (§4.6). A map of the surface charge distribution is shown in Figure 4-19.
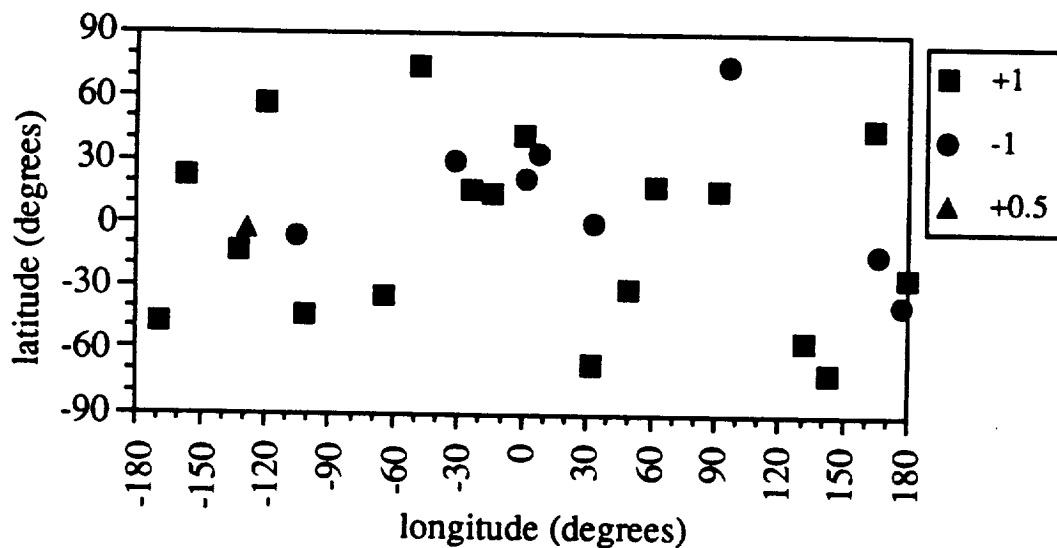

Figure 4-19: Surface map of point charge distribution on idealized lysozyme molecule.

Charges are given in units of the proton charge, 1.6×10^{-19}C.

Table 4-2
Coordinates of charged groups in tetragonal hen egg white lysozyme.

Number	Residue	Type	Charge	X	Y	Z
1	1	N-terminus	+1	3.28	10.16	10.35
2	1	lys	+1	−3.80	10.48	8.18
3	5	arg	+1	−6.31	24.40	2.84
4	13	lys	+1	−17.40	21.25	11.10
5	14	arg	+1	−12.20	9.25	14.63
6	15	his	+0.5	−9.67	11.01	17.86
7	18	asp	−1	−14.73	24.29	14.83
8	21	arg	+1	−11.82	23.93	29.27
9	33	lys	+1	3.17	23.88	5.62
10	35	glu	−1	4.38	24.84	18.14
11	45	arg	+1	18.46	15.42	23.99
12	48	asp	−1	14.17	22.91	29.22
13	52	asp	−1	8.98	21.08	22.43
14	61	arg	+1	13.02	20.81	31.91
15	66	asp	−1	11.50	12.56	27.61
16	68	arg	+1	16.16	12.96	24.25
17	73	arg	+1	1.83	16.91	39.96
18	87	asp	−1	−5.45	7.45	16.81
19	96	lys	+1	−11.68	16.57	22.82
20	97	lys	+1	−5.50	14.40	30.09
21	101	asp	−1	−2.00	24.43	32.74
22	112	arg	+1	5.25	33.64	23.22
23	114	arg	+1	6.61	30.51	10.82
24	116	lys	+1	−1.79	36.55	22.86
25	125	arg	+1	−10.80	31.20	−1.00
26	128	arg	+1	−18.86	17.79	0.09
27	129	C-terminus	−1	−17.14	21.78	6.41

We have chosen to represent the surface charges as patches of constant charge density because that method is consistent with the constant element formulation we have employed in the boundary element calculations. The goal is to create a patchwork of charge densities which is smooth enough that the governing equations remain valid but "lumpy" enough to exhibit any behavior unique to "patchy" spheres.

The concept of "local averaging," which is often used to make continuum approximations of discrete phenomena, is used here to smooth the local charge density on the sphere. Rather than represent the charged groups as point charges which would produce extremely high potentials in their immediate neighborhood, the charges are "smeared out" over a spherical cap which is finite in area. In principle, this is done by centering the spherical cap at the point of interest and summing all the point charges which lie within the cap. The local charge density is the net charge within the cap divided by A_{sample}, the area of the cap. In practice, the test to determine if a charge contributes to the local charge density is whether or not the distance (r_i) from the point of interest to charge i is less than r_{sample} (see Figure 4-20 for a sketch). The local charge density is given by:

$$\sigma = \frac{1}{A_{sample}} \sum_{i=1}^{N} Q_i \, H(r_{sample} - r_i) \qquad (4.103),$$

where Q_i = charge of group i, and $H(x)$ = Heaviside step function. The distance from the north pole to any point on the sphere is $r = a \, [2(1 - cos \, \theta)]^{1/2}$; the surface area within the spherical cap of size θ is $2\pi a^2 \int sin\theta \, d\theta = 2\pi a^2 (1 - cos \, \theta)$. When $\theta = \theta_{sample}$, the sampling radius is related to the sampling area through

$$r_{sample} = \sqrt{2} \, a \left(1 - cos \, \theta_{sample}\right)^{1/2} = 2 \, a \left(\frac{A_{sample}}{A_{sphere}}\right)^{1/2} \qquad (4.104),$$

where $A_{sphere} = 4\pi a^2$. Maps of the local surface charge density of lysozyme are shown in Figure 4-21 for sampling areas of 300, 200, and 100 Å²; for the model lysozyme molecule, $A_{sphere} \approx 3400$ Å².
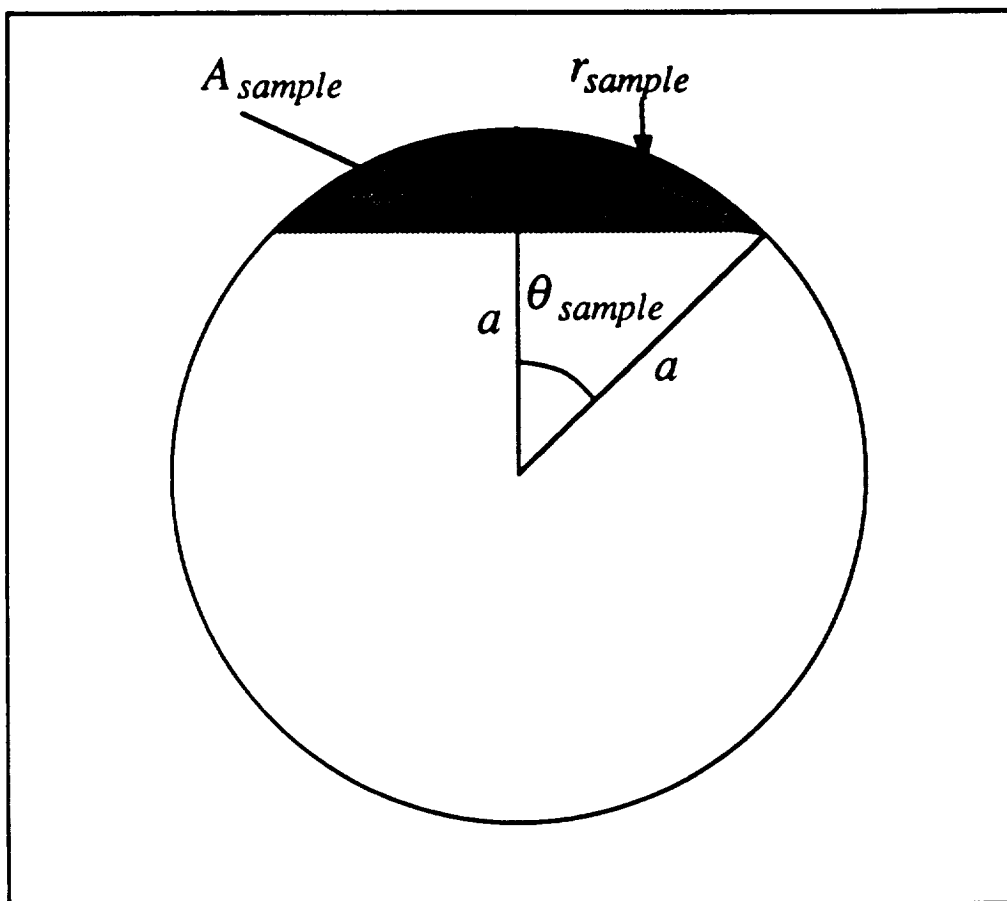
177

Figure 4-20: Sampling area and sampling radius.
Charged groups lying within the shaded area contribute to the local charge density at the north pole.
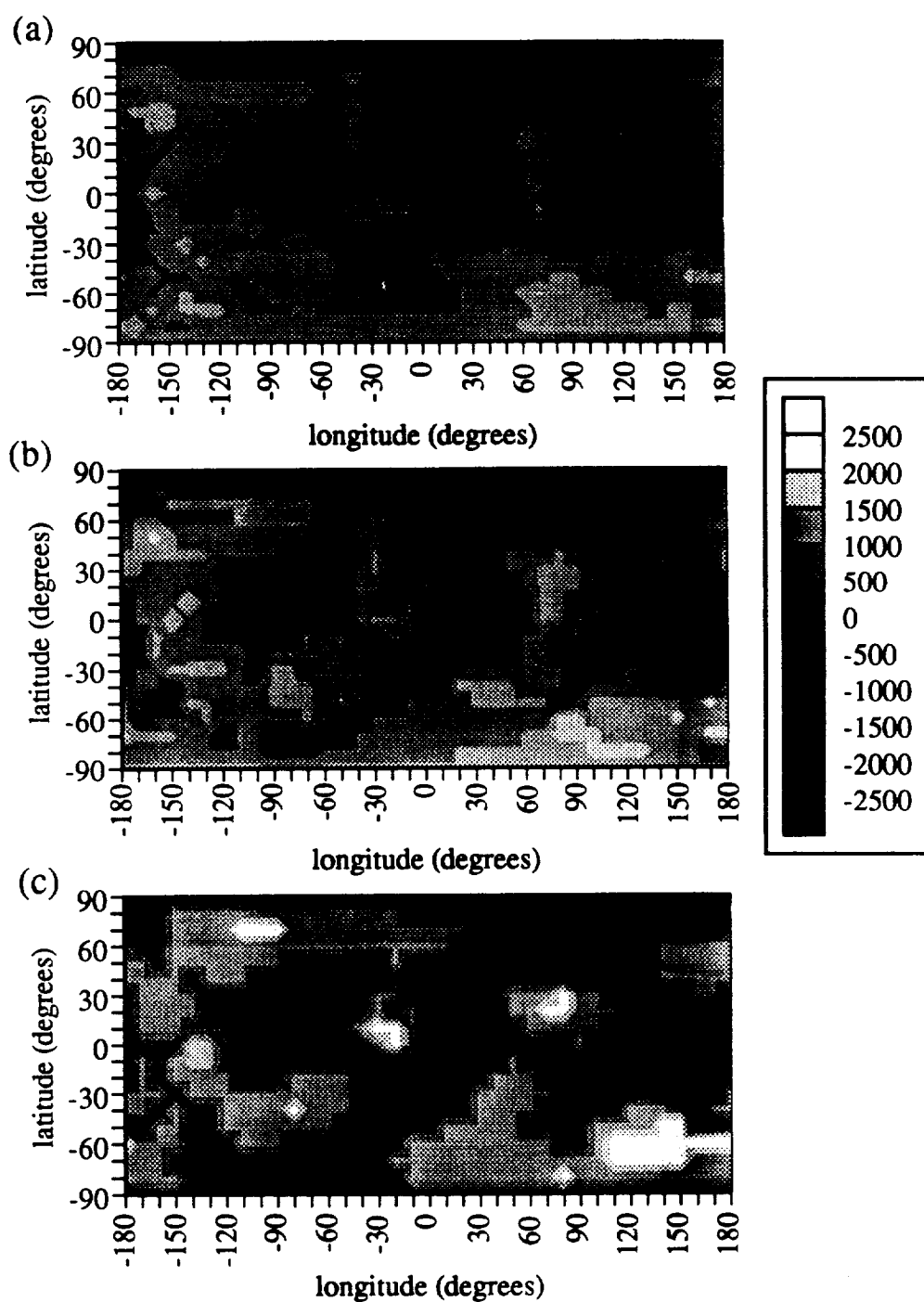
Figure 4-21: Local (smoothed) charge density on the surface.
The local charge density depends on the length scale over which it is averaged. Charge densities are scaled by $\sigma_0 \approx 1.4 \times 10^{-2}$ $\mu C/cm^2$. The sphere has a surface area approximately 3400 Å^2. Sampling areas are:
(a) 300 Å^2 (b) 200 Å^2 (c) 100 Å^2.

The (constant) charge density, σ_j, assigned to element j is calculated by averaging over the area of the element, A_j:

$$\sigma_j = \frac{1}{A_j} \int_{A_j} \sigma \, dA \qquad (4.105).$$

This method of computing σ_j introduces the length scale of the discretization into the problem. The larger of A_{sample} and A_j determines the length scale of the patchiness. A series of successive refinements of the original icosahedral discretization (Figure 4-22) shows how the surface charge density in Figure 4-21c is approximated by constant elements. Since convergence of the computations is checked by comparing answers obtained at successively smaller A_j, the discretization does not normally set the scale of the surface features. The choice of A_{sample}, however, can affect the size of nonuniformity effects which are calculated. As an extreme example, setting the sampling area equal to the area of the sphere reduces the charge density to that of a uniform sphere having the same net charge as the model sphere.

There is a lower bound on A_{sample} below which the governing equation in region 2 is no longer valid. The linearized of the Poisson-Boltzmann equation is valid for potentials up to approximately 100 mV (scaled potentials of $u \approx 4$), which places restrictions on how small A_{sample} can be. Consider the case of an isolated sphere with a uniform scaled surface charge density, σ^*. The scaled surface potential, u^∞, is then $\sigma^*/[\varepsilon_2(1 + a\kappa)]$ and surface charge densities greater than about $4\varepsilon_2(1 + a\kappa)$ would place the system outside the range of validity of the linearized Poisson-Boltzmann equation. If the net charge within the sampling area is Q, the corresponding restriction on A_{sample} is:

$$A_{sample} > \frac{Qa}{4 \, \varepsilon_0 \, \varepsilon_2 \, \psi_0 \, (1 + a\kappa)} \qquad (4.106).$$

To smear out a proton's charge ($Q = 1.6 \times 10^{-19}$ C) on a particle with $a = 16.48$Å, $\varepsilon_2 = 80$ (water) and $a\kappa = 5$ (ionic strength approximately 1M) would require a minimum sampling area of 60 Å^2. All calculations reported here are based on a sampling area of 100 Å^2.
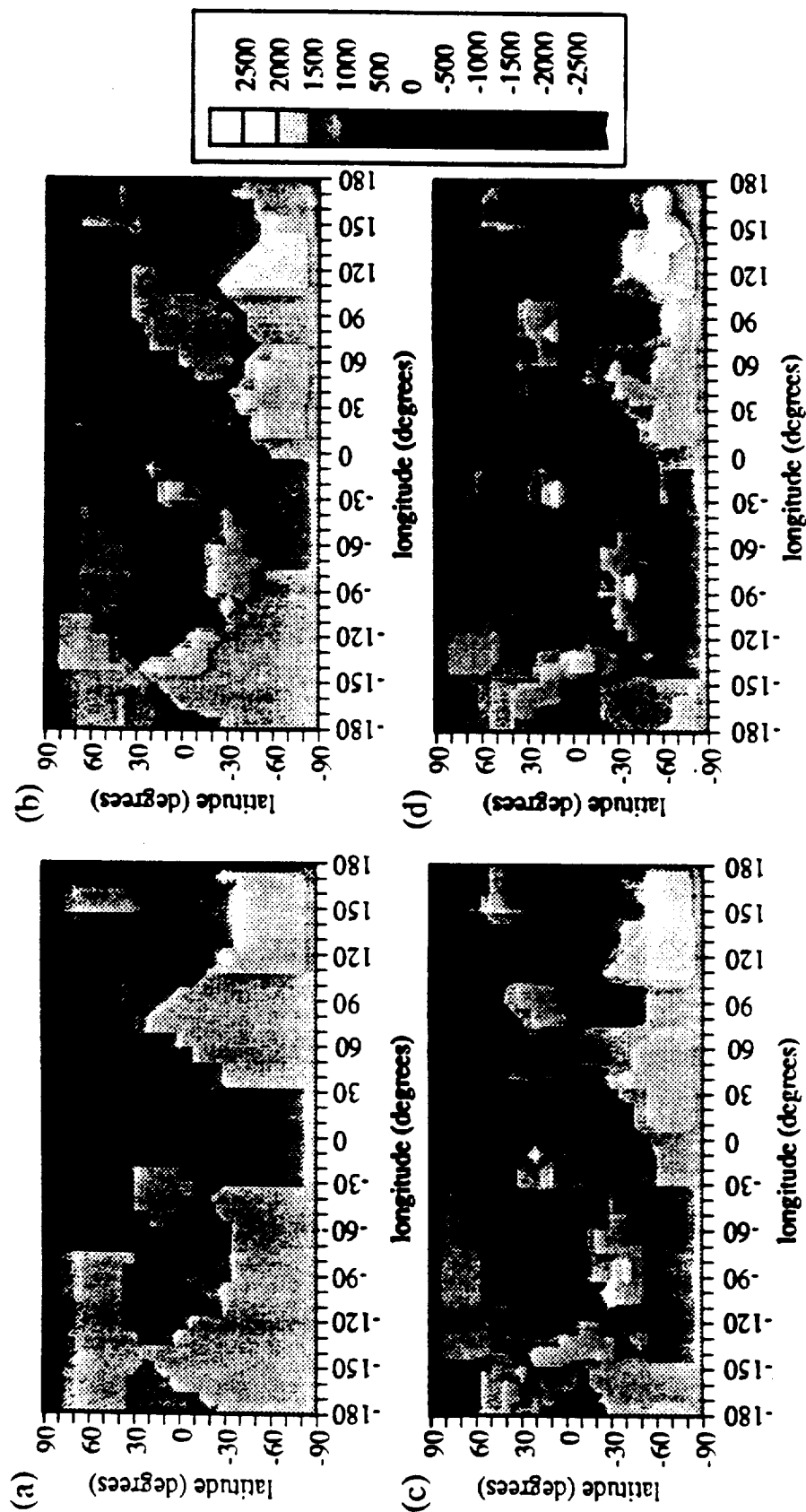
Figure 4-22: Constant element approximation to surface charge density.
Various representations of the chage density on the model lysozyme molecule based on a 100 Å² averaging area (Figure 4-21c). Charge densities are scaled by $\sigma_0 = 1.4 \times 10^{-2} \ \mu C/cm^2$. (a) 20 elements. (b) 60 elements. (c) 120 elements. (d) 240 elements.

181

Several layers of approximation have been employed to create a reasonable model of a protein molecule. The choice of sampling area is dictated by the linearization of the governing equation, while the assumption of constant elements suggests a method for specifying the charge density. The idealization of the molecule as a sphere and the corresponding mapping of the charged groups reflect a strong desire to keep the problem as simple as possible. Despite these severe simplifications, the resulting surface charge distribution, although not 100% "authentic," appears adequate to capture the essential physics of the phenomena.

4.9 Interaction Potential Energy of Lysozyme-Crystal System

$\Phi_{elec}(s, \alpha, \beta)$ was calculated for "south pole" locations coincident with each of the N_1 nodes on the sphere, (α_j, β_j). We invoke the constant element approximation once more to set the potential energy of the system in any orientation (α, β) lying within element j equal to the nodal value. In anticipation of adding the electrostatic and van der Waals potentials, Φ_{elec} is now scaled by kT. Potential energy surfaces at contact for conditions $a\kappa = 5$ and $\sigma_x^* = 0$ are shown in Figures 4-23 and 4-24 for four discretizations. As mentioned in section 4.3, the free energy is always repulsive because the nearest charges on the sphere dominate the interaction. A surface map of the electrostatic free energy surface at contact for $a\kappa = 5$ and $\sigma_x^* = 0$ (Figure 4-25a) is compared with a contour plot of the charge distribution (Figure 4-25c) for 240 elements. The calculated electrostatic surface potentials (not shown) can be as large as 10 - 20 at contact and would seem to violate the low potential assumption used to linearize the Poisson-Boltzmann equation. As the particle moves away from the wall, however, the surface potential rapidly decreases into the range where the linearized equation is valid. There is therefore some uncertainty in the value of Φ_{elec} near contact, although it seems internally consistent with values calculated at finite separations. This shortcoming is inherent in any model which employs the linearized Poisson-Boltzmann equation to describe the electrostatics.

182

Figure 4-23: 20 and 60 element approximations of electrostatic free energy at contact.

Free energy as a function of orientation when the model lysozyme sphere is in contact with an uncharged, insulated plate; $a\kappa = 5$
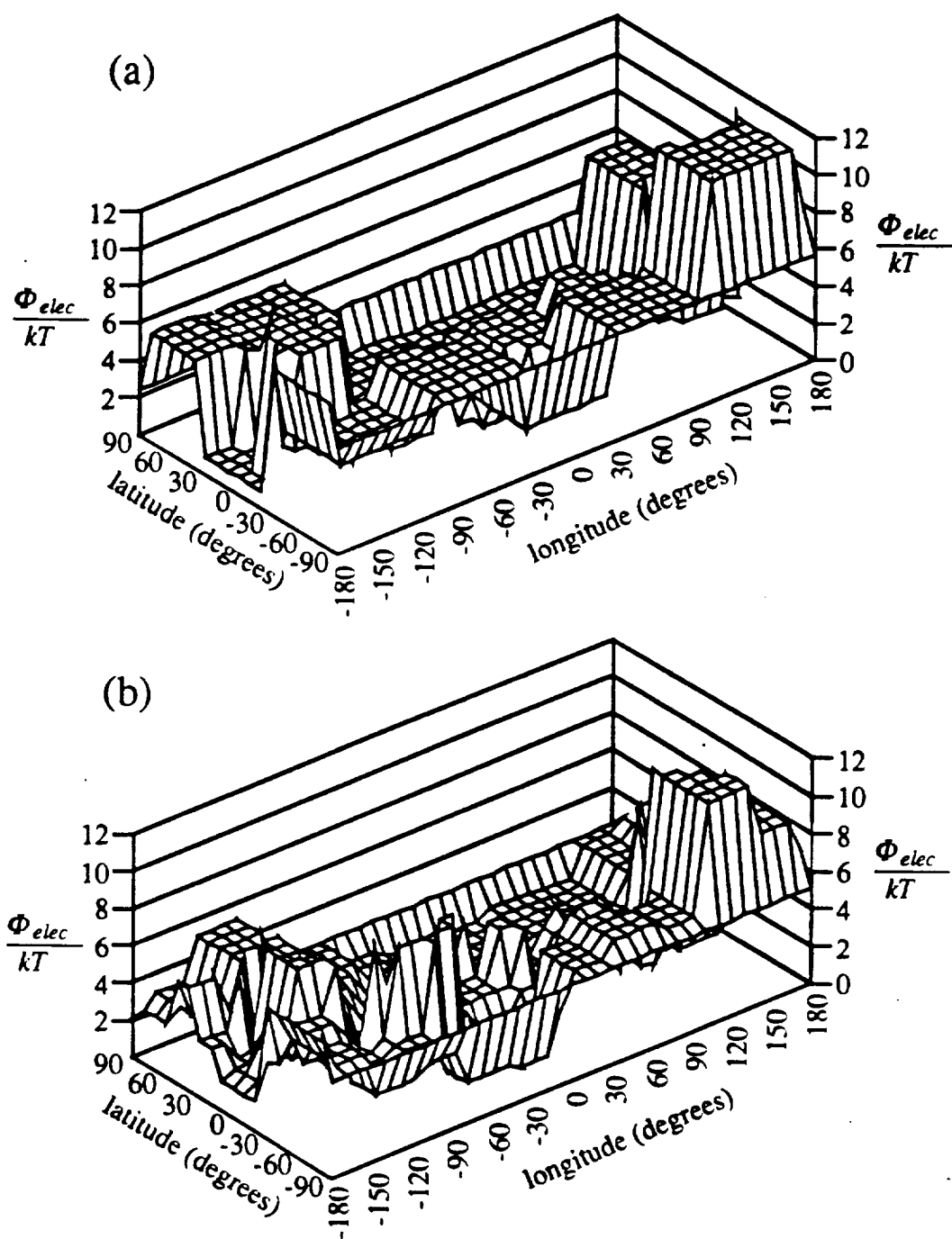
(a) 20 elements. (b) 60 elements.
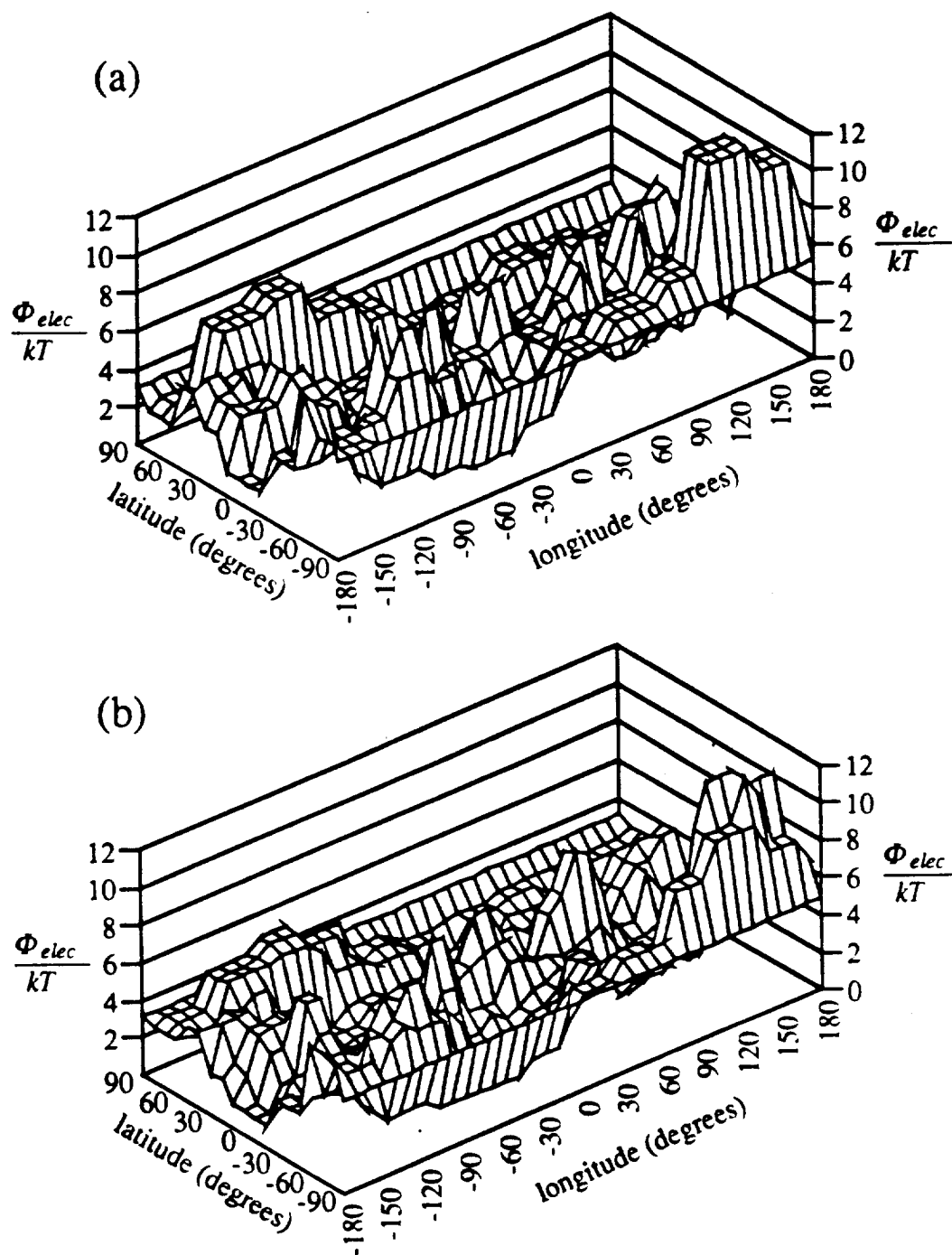
Figure 4-24: 120 and 240 element approximations of electrostatic free energy at contact.

Free energy as a function of orientation when the model lysozyme sphere is in contact with an uncharged, insulated plate; $a\kappa = 5$

(a) 120 elements. (b) 240 elements.
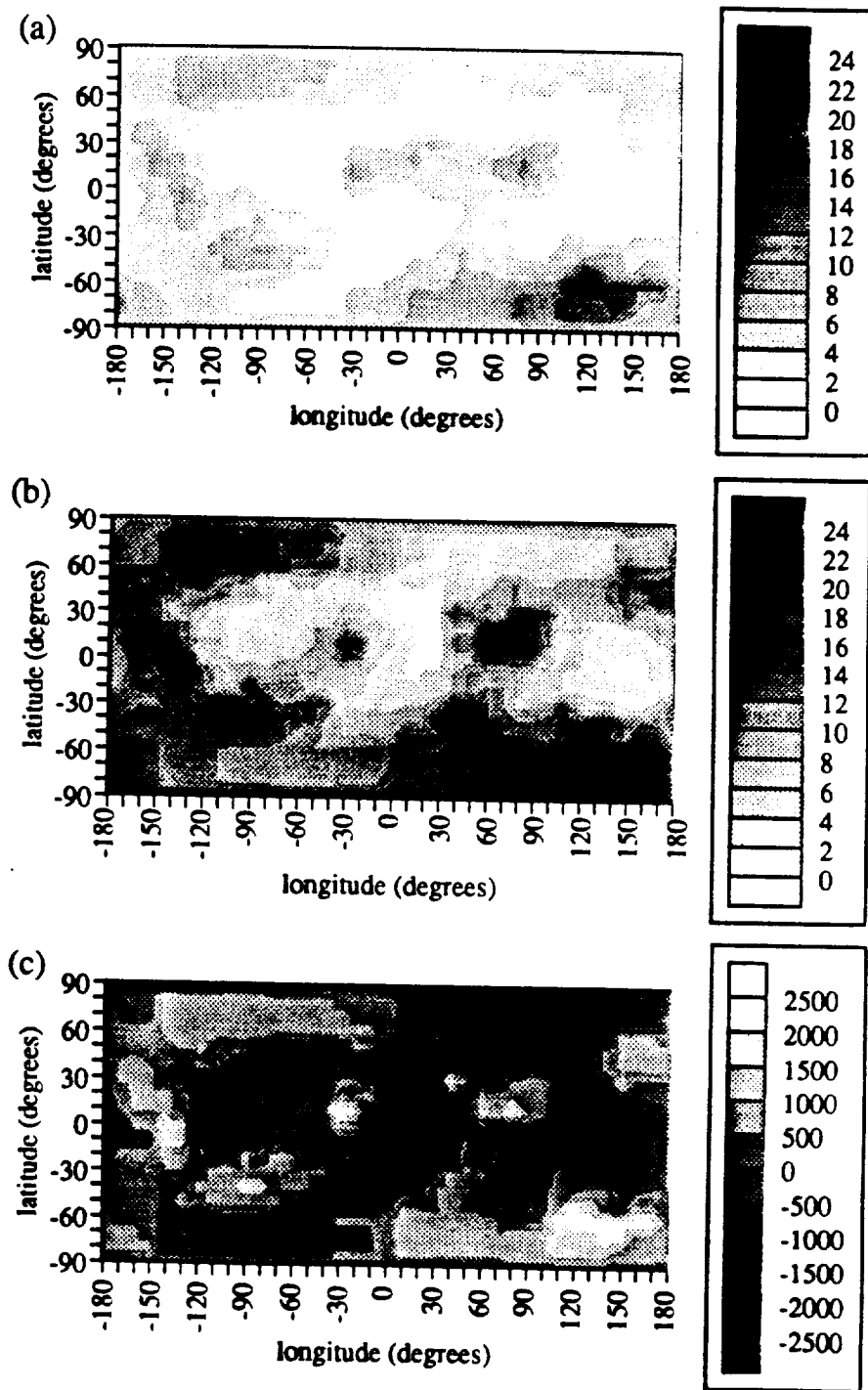
Figure 4-25: Relation between surface charge distribution and electrostatic free energy at contact.

Free energy as a function of orientation when the model lysozyme sphere is in contact with the plate; $a\kappa = 5$. Free energies are scaled by kT; charge density scaled by $\sigma_0 \approx 1.4 \times 10^{-2} \ \mu C/cm^2$.

(a) Φ_{elec} when $\sigma_x^* = 0$. (b) Φ_{elec} when $\sigma_x^* = 500$. (c) scaled charge density.

We have already discussed how the plate's surface charge can increase or decrease the potential energy of a given orientation depending on the signs of the charge on the nearest surfaces. Those orientations offering a similarly charged surface suffer an increase in free energy while the free energy of orientations with oppositely charged surfaces are reduced relative to their interaction with an uncharged plate. The selection of an appropriate crystal surface charge is fraught with uncertainty, but crystal surface potentials are probably comparable to those of protein molecules. Further, we are interested in comparing the behavior of patchy and uniform spheres so that crystal charge densities can be restricted to those which might be produced by packing a large number of uniformly charged spheres into the lattice. The net charge uniform density on the model lysozyme molecule is $\sigma^* \approx$ 358; the corresponding flat plate charge density producing the same surface potential is approximately $\sigma_x^* = 300$ when $a\kappa = 5$. The effective surface charge could be larger, so the range tested was extended to $\sigma_x^* = 500$. The effect of crystal surface charge is illustrated in Figure 4-25 for two values of σ_x^* at contact when $a\kappa = 5$. Although Figure 4-25 is informative, the significance of the nonuniform charge distribution cannot be assessed without a quantitative comparison of the behaviors of uniform and patchy spheres. For this, we turn to the angle-averaged interaction potential.

We introduce the principles of angle-averaging through the illustrative example of a freely rotating point dipole in a uniform electric field. The electrostatic free energy of the dipole is given by $\Phi_{elec}(\theta) = -\mathbf{p} \cdot \mathbf{E} = -p E \cos \theta$, where $\mathbf{p}$ = dipole moment, $\mathbf{E}$ = electric field vector, and θ = angle between dipole and electric field [24]. If M is the property to be averaged, the angle-averaged value $\langle M \rangle$ is the average over all orientations of M weighted by the appropriate Boltzmann factor, $e^{-\Phi_{elec}(\theta)/kT}$ [34]. The effect of the Boltzmann weighting is illustrated by the calculation of the angle-averaged value of $\cos \theta$ for the point dipole:

$$\langle \cos\theta \rangle = \frac{\int_0^\pi (\cos\theta) e^{pE\cos\theta/kT} \sin\theta \, d\theta}{\int_0^\pi e^{pE\cos\theta/kT} \sin\theta \, d\theta} = \coth\left(\frac{pE}{kT}\right) - \frac{kT}{pE} \qquad (4.107),$$

which is known as the Langevin equation [16,26,29,35]. The importance of (4.107) is that there is a preferred orientation for the dipole even though it is freely rotating.

McQuarrie [35] claims that although averages such as (4.107) are correct for mechanical properties such as pressure and volume, it is inappropriate for nonmechanical properties such as free energy. Instead, the proper averaging is reported to be [24,36]:

$$\frac{\langle \Phi_{elec}(s) \rangle}{kT} = -\ln \frac{\int_{solid\ angles} e^{-\Phi_{elec}(s,\Omega)} \, d\Omega}{4\pi} \qquad (4.108),$$

where the orientation is defined in terms of the solid angle Ω. When the constant element approximation is employed, the integral over all solid angles can be replaced by a sum over all elements of the sphere:

$$\frac{\langle \Phi_{elec}(s) \rangle}{kT} = -\ln \frac{1}{4\pi} \sum_{j=1}^{N_1} A_j \exp\left[-\Phi_{elec}(s, \alpha_j, \beta_j)/kT\right] \qquad (4.109),$$

where A_j is the area of element j on the unit sphere and the coordinates (α_j, β_j) define the orientation of node j. The significance of the nonuniform charge distribution can be determined by comparing the angle-averaged interaction potential defined by (4.109) with that for the uniformly charged particle having the same net charge.

The angle-averaged interaction potential for the 240 element discretization of lysozyme is shown in Figure 4-26 for the case $a\kappa = 5$. The potentials for orientations producing the least favorable (Φ_{elec}^{max}) and most favorable (Φ_{elec}^{min}) interaction potentials are shown for comparison, as well as the uniform sphere potential ($\Phi_{elec}^{uniform}$) and the arithmetic average potential ($\overline{\Phi}_{elec}$). The relative ranking of $\langle \Phi_{elec} \rangle$, $\overline{\Phi}_{elec}$ and $\Phi_{elec}^{uniform}$ are difficult to see in Figure 4-26, so the curves are replotted in Figure 4-27. At high crystal surface charge densities (Figure 4-27b), the angle-averaged potential lies below both $\overline{\Phi}_{elec}$
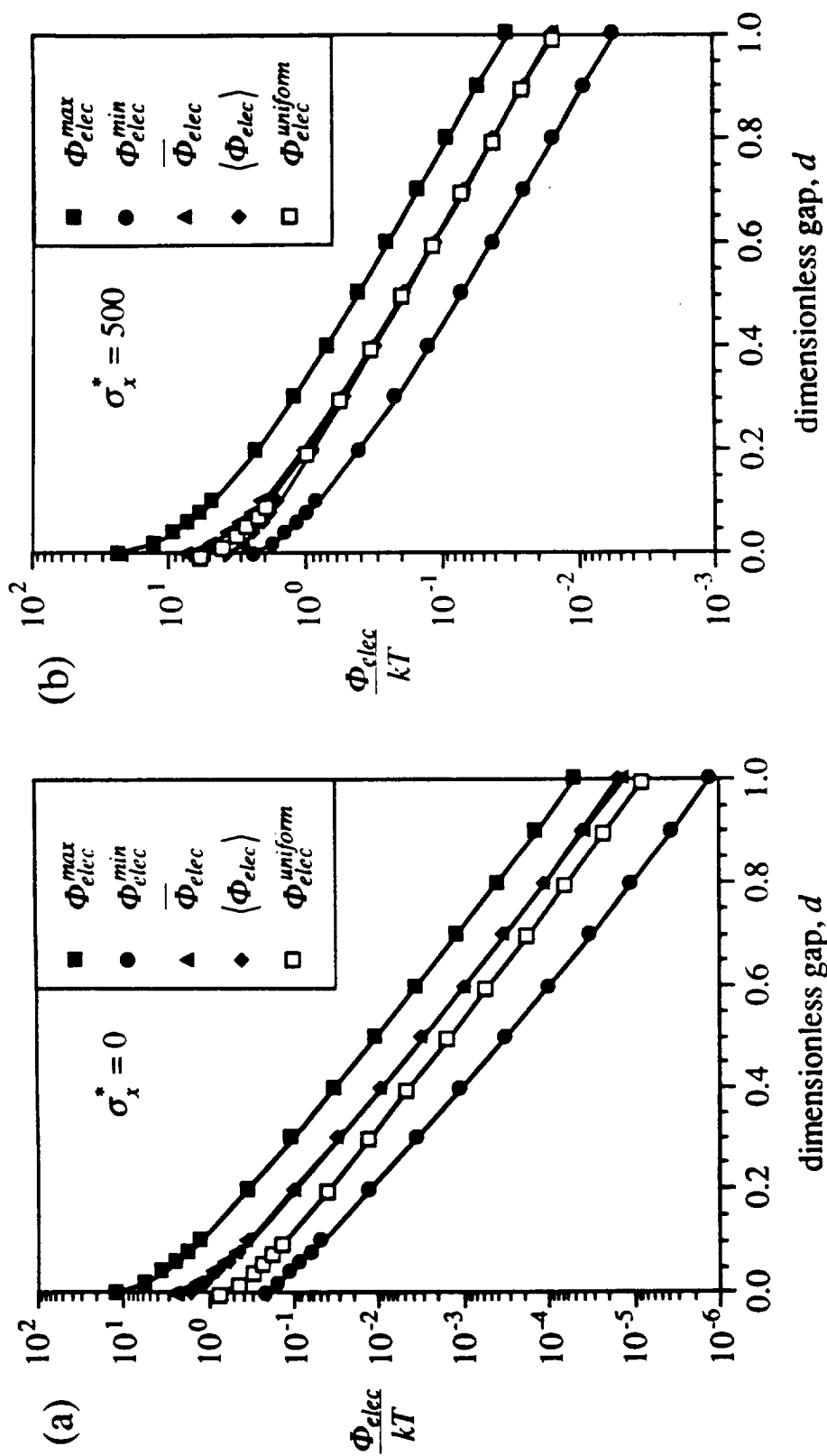
Figure 4-26: Electrostatic interaction potential curves.
Comparison of maximum and minimum electrostatic free energies with several averages for lysozyme when $a\kappa = 5$. Angle brackets indicate angle-average, overbar denotes arithmetic average. (a) $\sigma_x^* = 0$. (b) $\sigma_x^* = 500$.

Figure 4-27: Relation among several averages of electrostatic free energy.
More detailed view of the relation among the angle-average, arithmetic average, and
uniform electrostatic free energies.
(a) $\sigma_x^* = 0$. (b) $\sigma_x^* = 500$.

189

and $\Phi_{elec}^{uniform}$, as expected from the the influence of the Boltzmann weighting in (4.109). We note that at high values of σ_x, the potential in orientation j is roughly proportional to $\sigma_x\sigma_j$, where σ_j = charge density of element j (which, of course, is closes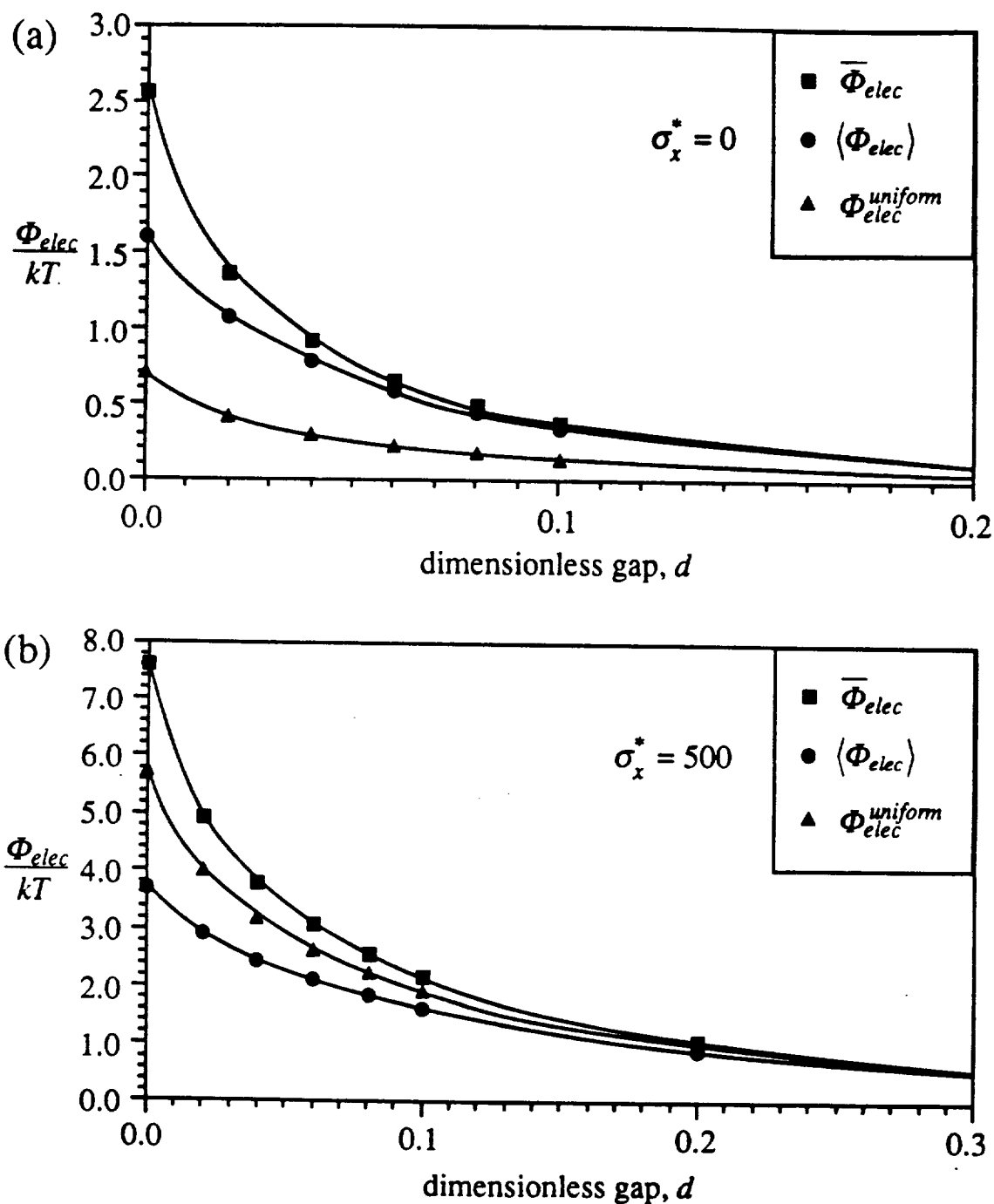t to the plate). When averaged over the sphere, we would expect $\overline{\Phi_{elec}} \approx \Phi_{elec}^{uniform}$, an expectation which is approximately met when the sphere is far enough from the plate that the influence of the mirror sphere is negligible. The Boltzmann weighting reduces $\langle\Phi_{elec}\rangle$ below both $\overline{\Phi_{elec}}$ and $\Phi_{elec}^{uniform}$ because lower potential energy orientations are favored.

When the sphere is close to the plate or the plate's surface charge density is low, the interaction of the sphere with its mirror image can no longer be neglected. This additional contribution to the electrostatic potential energy is roughly proportional to σ_j^2 because the element covering the south pole is repelled by its mirror charge. The arithmetic mean of this contribution over all orientations is proportional to $\overline{\sigma^2}$ while that for the uniform sphere goes as $\overline{\sigma}^2$ Since $\overline{\sigma^2} > \overline{\sigma}^2$, it follows for patchy spheres that $\overline{\Phi_{elec}} > \Phi_{elec}^{uniform}$ (Figure 4-27a). Again we see that the Boltzmann weighting reduces $\langle\Phi_{elec}\rangle$ below $\overline{\Phi_{elec}}$; this time, however, $\langle\Phi_{elec}\rangle > \Phi_{elec}^{uniform}$.

The most important feature of these electrostatic free energy curves is that the electrostatic repulsion is relatively weak (less than 6 kT when $\sigma_x^* = 500$). The second important finding is that there is only a slight difference in free energy (less than about 2 kT when $\sigma_x^* = 500$) between the uniformly charged and angle-averaged molecules. Both these conclusions result from the moderate range of crystal surface charges investigated, and their validity depends on how well this range of charges approximates that experienced by approaching protein molecules. The issue of crystal surface charge density is addressed in more detail later. The differences between the uniform and angle-averaged cases may, in fact, be less significant than they appear because at small separations, the attraction of the dispersion potential is dominant. We now turn our attention to the effect of the van der Waals potential.

The dispersion potential for the (spherical) crystal and the (spherical) molecule is given by [5,7]:

$$\Phi_{vdw} = -\frac{A_{eff}}{6}\left(\frac{2R}{2(R+1)d+d^2} + \frac{2R}{4R+2(R+1)d+d^2}\right.$$
$$\left. + ln\frac{2(R+1)d+d^2}{4R+2(R+1)d+d^2}\right) \qquad (4.110),$$

where R = crystal radius and d = separation (gap) between the surfaces of the crystal and molecule; all lengths have been scaled by the particle radius. For cases of interest here, $R \gg 1$ and Φ_{vdw} at small d is insensitive to the exact value of R; a value of $R = 10^6$ (crystal radius about 2 mm) was used for all calculations. As with the effective surface charge density, extensive data do not exist for estimating the effective Hamaker constant, A_{eff}.

If molecule and crystal are treated as pure hydrocarbon bodies interacting through water, A_{eff} should be approximately 1 kT at 300K [24]. Measurements of dispersion forces on lysozyme indicate values for A_{eff} in the range of 1 - 2 kT at room temperature [37,38]. Unfortunately, the high solvent content of the crystal (typically 50% [39]) introduces major uncertainty into the selection of A_{eff}. A naive estimate might be that A_{eff} should be roughly half the value appropriate for pure hydrocarbons, or 1/2 kT, in which case the sensitive balance between van der Waals attraction and electrostatic repulsion is evident in Figure 4-28 for $a\kappa = 5$. Even when $\sigma_x^* = 500$, the repulsive barrier is only about 1 - 2 kT; in the context of colloidal stability, this is insignificant. The barrier height is somewhat sensitive to the exact value of A_{eff}, as shown in Figure 4-29. At values of A_{eff} as low as 0.1 kT, the angle-averaged potential still peaks at only 2kT (Figure 4-29a). As expected, the repulsion is weaker at higher ionic strengths (Figure 4-30).

Until now, we have studied only cases with moderate positive surface charge densities on the plate. These conditions are appropriate for comparing the potentials of uniform and patchy spheres, but they do not demonstrate the full range of behavior exhibited by the protein molecule. As a result of the nonuniform charge distribution on the
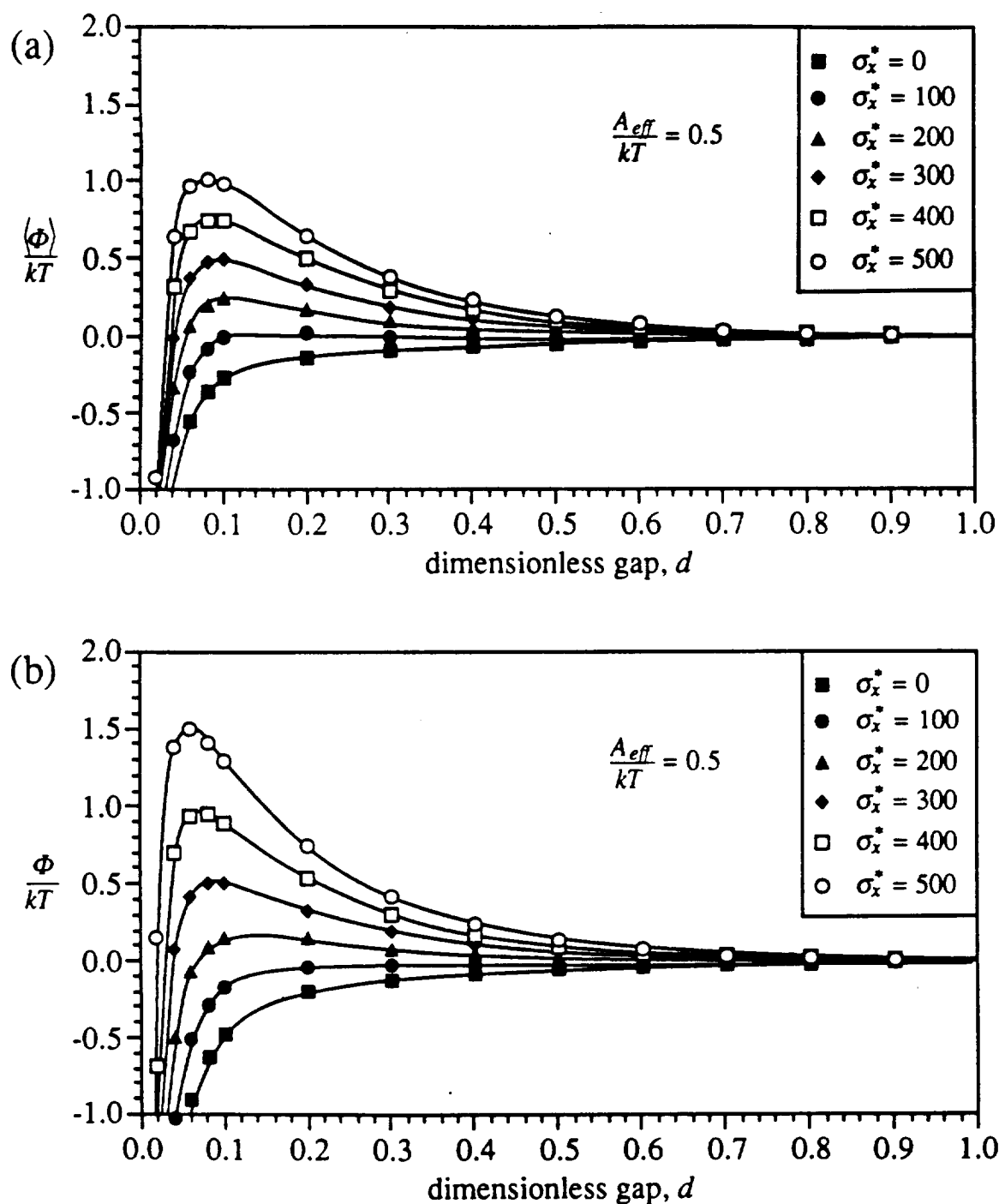
Figure 4-28: Balance of electrostatic repulsion and dispersive attraction.
Curves show full interaction potential between crystal and charged sphere for moderate crystal surface charge densities; $a\kappa=5$.
(a) model lysozyme molecule.
(b) uniformly charged sphere with same net charge.
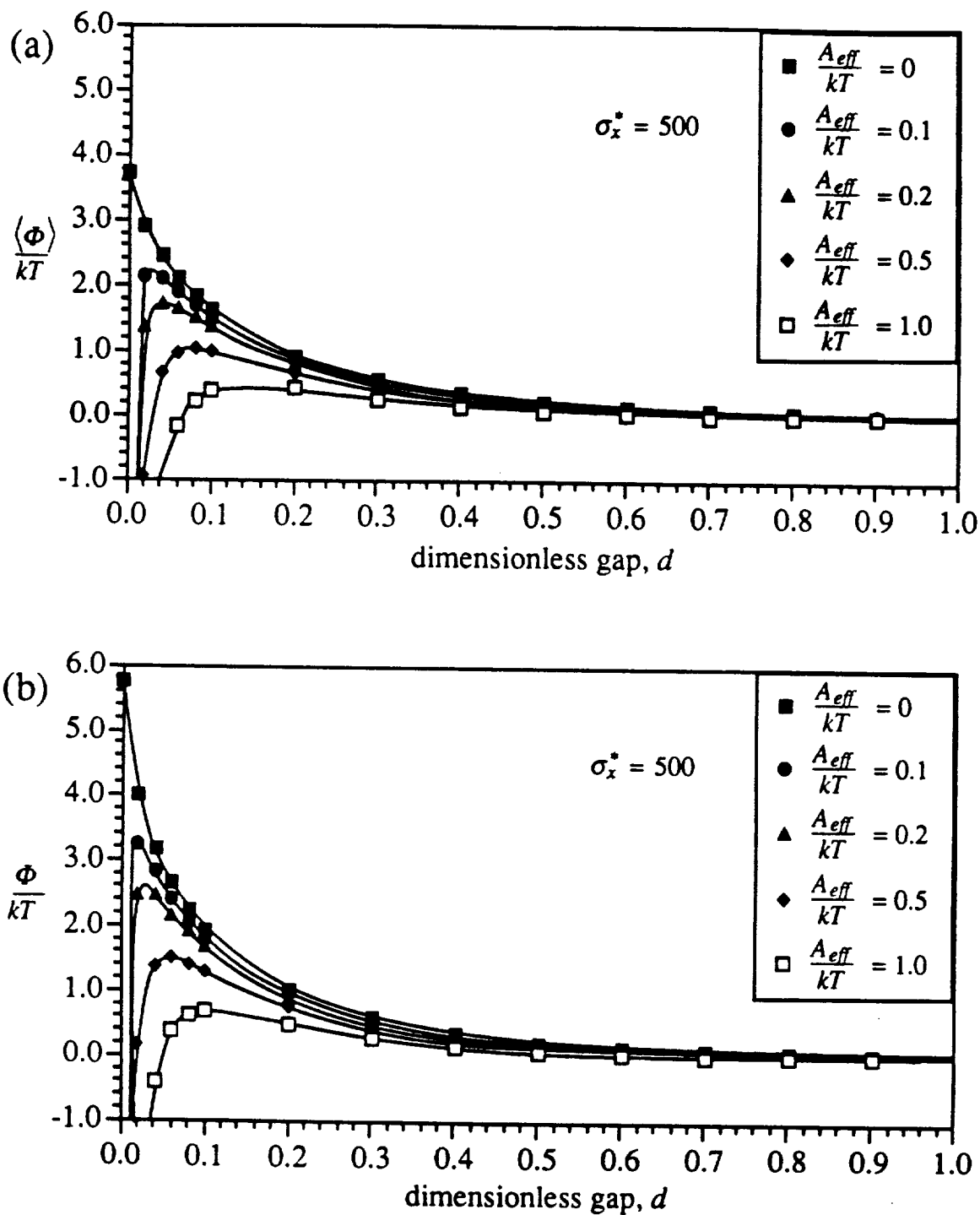
Figure 4-29: Effect of Hamaker constant on free energy maximum.
Comparison of angle-averaged and uniform interaction potentials for $\sigma_x^* = 500$, $a\kappa = 5$, and various effective Hamaker constants.
(a) model lysozyme molecule.
(b) uniformly charged sphere with same net charge.
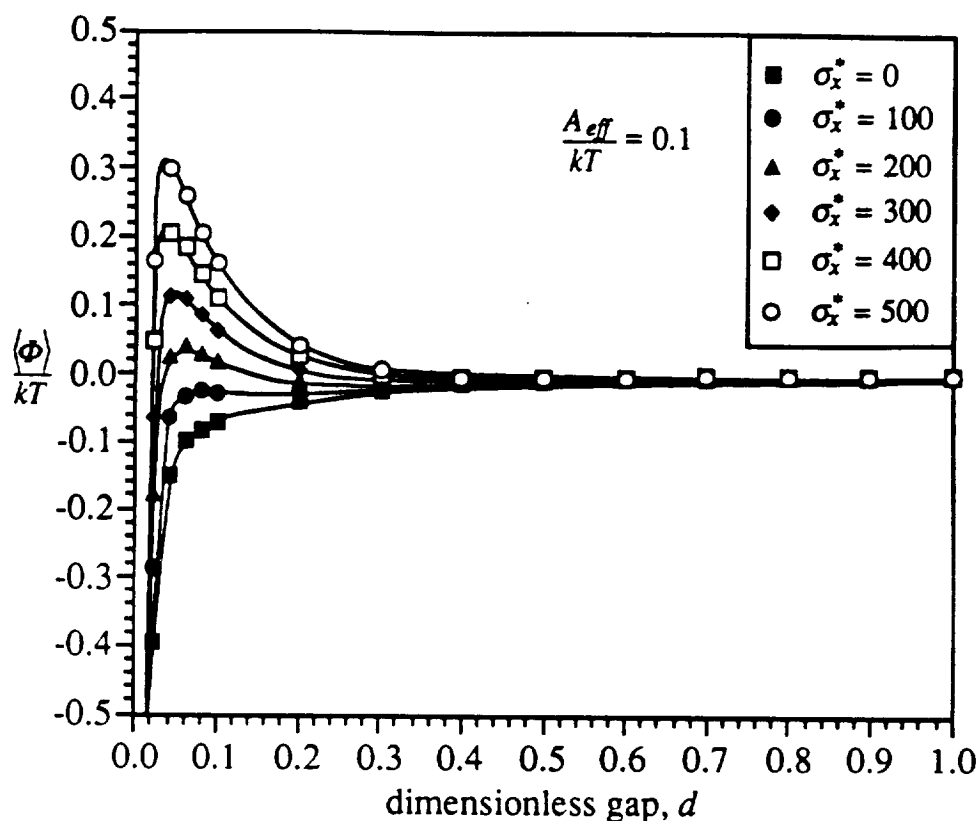
Figure 4-30: Angle-averaged interaction potential for lysozyme ($a\kappa = 10$).
At high ionic strengths, the electrostatic repulsion is greatly diminished. Even for a relatively small effective Hamaker constant, there is no appreciable barrier to the molecule as it approaches the surface.

molecule, elements on the sphere have charge densities ranging from $-1637 \le \sigma^* \le 2327$. In fact, as seen in the cumulative distribution function of the elements' charges (Figure 4-31), only 40% of the 240 elements have charge densities within the range studied so far. If the range of crystal surface charge densities is extended to reproduce the entire range of surface potentials on the isolated lysozyme molecule, dramatic changes in the electrostatic free energy result (Figure 4-32). In agreement with the discussion in section 4.3, the potential is becoming more repulsive at high σ_x^* irrespective of sign. The issue is to decide what range of effective surface charge densities might reasonably characterize the crystal surface.
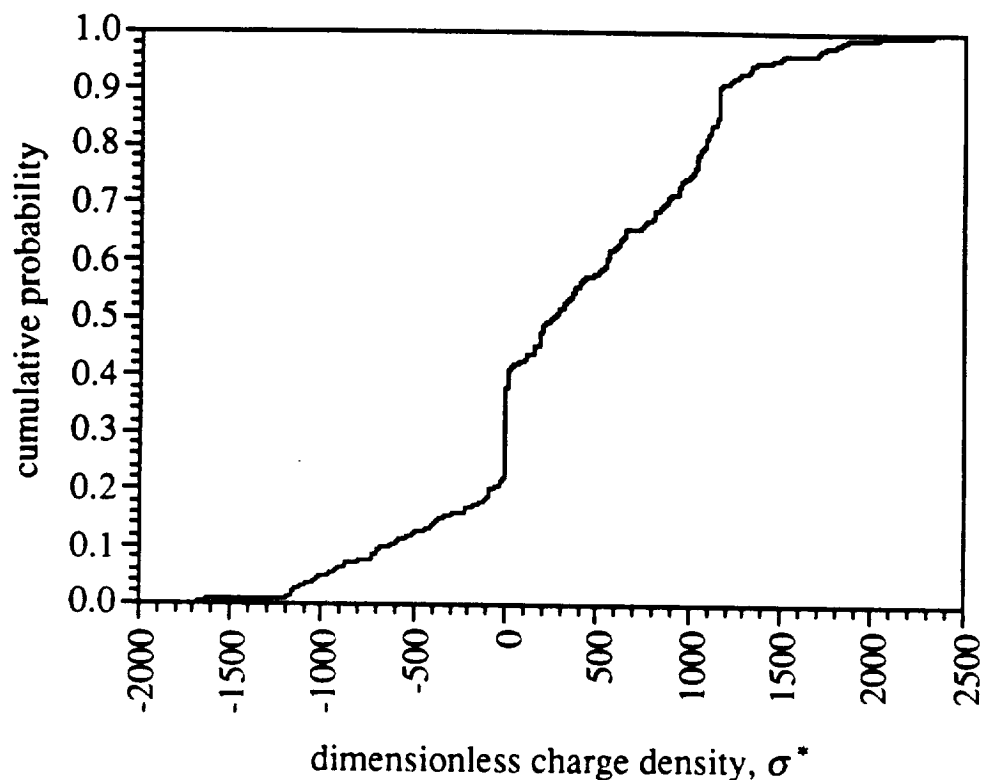
Figure 4-31: Cumulative distribution function for surface charge density. Approximate cumulative distribution function for the scaled charge densities of elements on the sphere ($N_1 = 240$).

The surface potential of the isolated lysozyme molecule provides guidance in this matter. A test charge arriving at the surface of the molecule experiences some electrostatic potential which depends chiefly on the local arrangement of charges. To the test charge, the potential seems almost like that produced by a uniformly charged sphere with an appropriate charge density. If u^∞ is the scaled potential at the surface, the corresponding equivalent charge density on the sphere is $\sigma^* = \varepsilon_2(1 + a\kappa)u^\infty$. Plate charge densities which produce the same surface potential are $\sigma_x^* = \varepsilon_2 a\kappa u^\infty$. For $a\kappa = 5$, surface potentials on the isolated lysozyme molecule range from a maximum of $u^\infty = +3.91$ (+100 mV) to a minimum of $u^\infty = -2.44$ (-63 mV); the equivalent crystal surface charge densities are approximately $\sigma_x^* = 1600$ and $\sigma_x^* = -1000$, which seem to be reasonable upper and lower bounds. There is a dramatic difference in the angle-averaged interaction potential for these

two cases, as shown in Figure 4-33. These findings are a consequence of the nonuniform charge distribution on the molecule and would not be anticipated on the basis of the uniformly charged sphere. Some implications of this behavior are discussed in section 4.10.
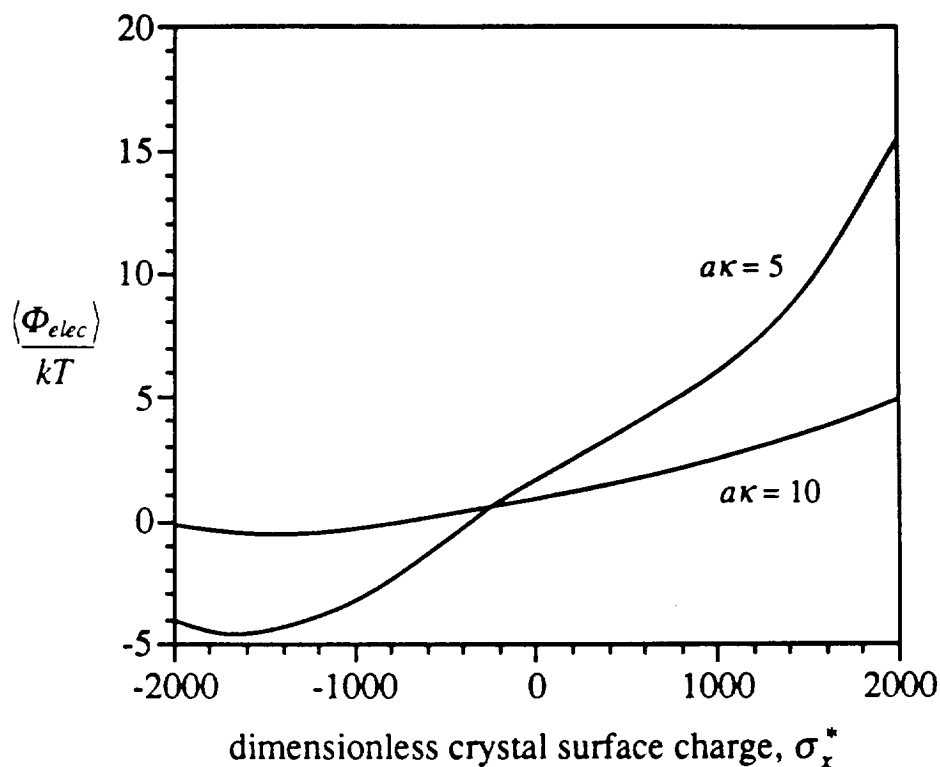
Figure 4-32: Angle-averaged electrostatic free energy at contact as a function of crystal surface charge density.

When a uniformly charged sphere approaches a plate with a moderate surface charge of the same sign, the balance between electrostatic repulsion and dispersive attraction produces a modest energy barrier which must be overcome by the molecule. The size of the barrier depends on σ_x and $A_{\it eff}$, two parameters which are not well quantified for the system under study. For the same range of plate charge densities, nonuniform charge effects leave the qualitative behavior of the system unchanged but alter the height of the free energy barrier. For crystal surface charge densities comparable to that on a uniform sphere
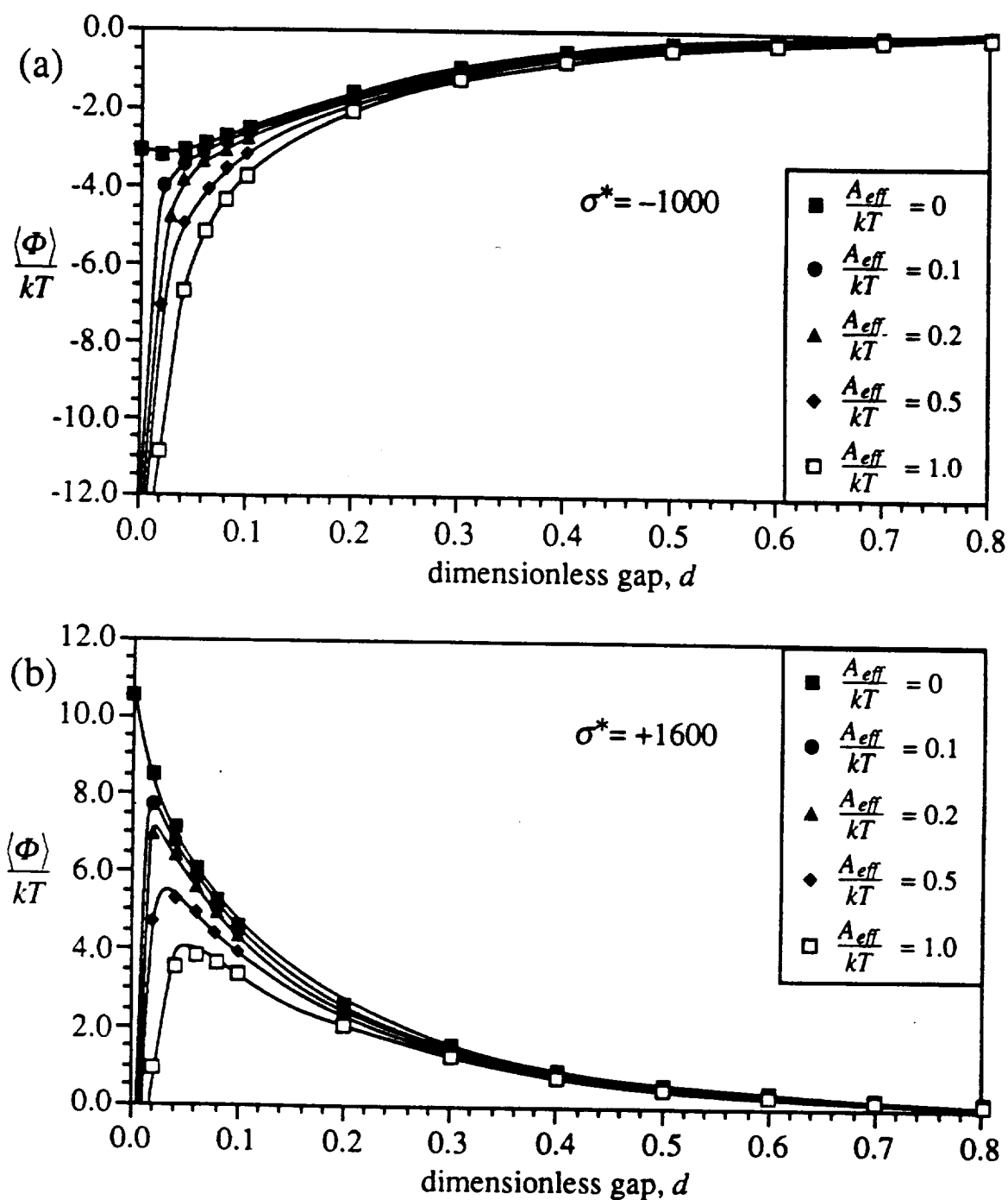
Figure 4-33: Most attractive and most repulsive interaction potentials.
Angle-averaged interaction potentials for crystal surface charge densities producing surface potentials equal to the minimum and maximum values found on the isolated lysozyme molecule when $a\kappa = 5$.
(a) Crystal surface potential of -63 mV.
(b) Crystal surface potential of $+100$mV.

with the same net charge as lysozyme, the barriers for the uniform and nonuniform spheres are within 1 - 2 kT of each other. At low crystal charge densities, the angle-averaged interaction potentials lie above the uniform interaction potentials because the sphere-sphere interaction is proportional to the average square of the sphere's surface charge density; at high crystal charge densities, the angle-averaged potential rests below the uniform case because lower energy orientations are heavily favored. Only when the molecule is nearly in contact with the crystal are the differences between the two cases important; this region is of primary interest in crystal growth studies. When the range of effective surface charge densities is extended to include the entire range of surface potentials found on the isolated lysozyme molecule, the angle-averaged potential can be either strongly repulsive or attractive. This change in qualitative behavior is due entirely to inhomogeneities in the surface charge distribution.

4.10 Summary and Discussion

A highly simplified model of molecule-crystal interactions has been developed and applied to protein systems. Chief among the simplifications employed in the model is the linearization of the governing equation for electrostatic interactions, which allows the electrostatics problem to be divided into subproblems which can be solved separately to obtain the total electrostatic potential. Assumptions of smooth surfaces and simple geometries are made for mathematical convenience since they allow the electrostatic potential to be expressed as the result of image charges and a uniform flat plate. The electrostatic potential produced by the image charges is calculated from a boundary element method which has been specialized to the case of spherical triangular elements. Electrostatic free energies calculated from the boundary element method for two uniformly charged spheres agree well with those given by the linear superposition approximation. In another consistency check, at separations greater than about a double layer thickness, the

free energy of a uniformly charged sphere in the presence of a uniformly charged plate produces the same exponential decay with separation expected from a point charge.

The nonuniform charge distribution on the protein molecule is represented by surface elements with constant charge density. Interaction free energies of the molecule-crystal system in different orientations are calculated from the isothermal reversible work required to charge the surfaces to the appropriate electrostatic potential. The results for all orientations are then angle-averaged to obtain a single curve which represents the hypothetical "average" molecular orientation. At moderate crystal charge densities, these angle-averaged potentials are found to differ only slightly from the curves for uniformly charged spheres with the same net charge.

The full effect of charge inhomogeneities can be seen when the range of plate charge densities is extended to produce the same range of surface potentials found on the isolated lysozyme molecule. In the context of the simplified model, the effective plate charge density reflects the arrangement of molecules exposed at the surface. Different crystal faces have different effective charge densities, so the free energy barriers could vary significantly between faces. Crystallographic data can be used to determine which charged groups are exposed on the crystal face and calculate the effective surface charge densities. In the absence of such data, however, we have free rein to speculate on various possibilities.

Consider, for example, the case where each face presents a free energy barrier to the approach of molecules. Since the ratio of the flux of molecules to the crystal in the presence and absence of a repulsive interaction potential is approximately $exp\left(-\langle\Phi\rangle_{max}/kT\right)$ [7], crystal growth is always slower than the diffusion limit. For a barrier of $2\,kT$, this retardation is about a factor of 10. The addition of a molecule to the crystal would thus appear to occur in three steps: the molecule (i) arrives near the surface, (ii) climbs the free energy barrier to reach the surface, and (iii) finds a suitable location and orientation on the crystal face. Steps (ii) and (iii) can be lumped into the kinetics of the process. If step (ii)

were rate-limiting, large free energy barriers would reduce the effective attachment rate constant and the transition (if any) from kinetic control to diffusion control would occur at larger crystal sizes. By the same reasoning, an attractive potential would enhance the flux to the surface and crystal growth would become transport-limited at smaller crystal sizes. For lysozyme, at least, measured growth rates lie below the diffusion-limit [40,41] so it is unlikely that step (i) controls crystal growth. If the interaction potential is attractive, step (ii) cannot be rate-limiting.

Inspection of the interaction potential curves and experimental results both suggest that diffusion alone is adequate to sustain crystal growth at constant rates. A definitive conclusion about the effects of colloidal forces on protein crystal growth must be deferred until more reliable estimates of the crysal charge density and the effective Hamaker constant are available. Variations in charge density could restrict the arrival of protein molecules to certain portions of the crystal (a particular crystal face or specific sites within the repeating cell on the surface, for instance). The effect of angle-averaging is to bias the orientations of incoming molecules towards lower potential energies. Once in a low energy state, subsequent rotational diffusion tends to keep the molecule in orientations which are not too different in energy. The locations of maxima could effectively lengthen the "orientational distance" through which the molecule must diffuse by forcing the molecule to bypass regions of high free energy, even if they lie along a direct path to the global minimum.

The present analysis has dealt with mechanisms by which a molecule can reach the crystal face but provides no information about how the molecule finally finds its niche on the surface. This step is extraordinarily complicated because it requires a patchy sphere to migrate across a patchy surface, find a favorable attachment site, and orient itself properly. For the case of uniformly charged crystal surfaces investigated here, the free energy suface at contact consists of several large maxima and many shallow, closely spaced minima. Rotational sampling by the molecule would not seem to be excessively restricted under these conditions. In all likelihood, however, the molecule must also translate across the

surface to the addition site. The investigation of such a process, which calls for much more precise modeling of the surfaces and interaction potentials than was possible in this work, is a logical next step.

References

[1] Rosenberger, F. *J. Crystal Growth*. **76** (1986) 618-636.

[2] Young, C. C., R. C. De Mattei, R. S. Feigelson, and W. A. Tiller. *J. Crystal Growth*. **90** (1988) 79-85.

[3] McPherson, A. *Preparation and Analysis of Protein Crystals*. New York: Wiley, 1982.

[4] Hodder, A. N., K. J. Machin, M. I. Aguilar, and M. T. W. Hearn. *J. Chromatography*. **507** (1990) 33-44.

[5] Russel, W. B., D. A. Saville, and W. R. Schowalter. *Colloidal Dispersions*. Cambridge: Cambridge University Press, 1989.

[6] Verwey, E. J. W. and J. Th. G. Overbeek. *Theory of the Stability of Lyophobic Colloids*. New York: Elsevier, 1948.

[7] Hiemenz, P. C. *Principles of Colloid and Surface Chemistry*. New York: Marcel Dekker, 1977.

[8] Smith, C. D. *Personal communication*. The structure of the lysozyme as recorded in the Brookhaven data bank was displayed on screen for visual inspection. Coordinates reported are estimates of the center of mass of the charged groups on the molecule.

[9] Tanford, C. *Physical Chemistry of Macromolecules*. New York: Wiley, 1961.

[10] Creighton, T. E. *Proteins: Structures and Molecular Properties*. New York: W. H. Freeman and Company, 1983.

[11] Cantor, C. R. and P. R. Schimmel. *Biophysical Chemistry Part 1*. San Francisco: W. H. Freeman and Company, 1980.

[12] Klapper, I., R. Hagstrom, R. Fine, K. Sharp, and B. Honig. *Proteins: Structure, Function, and Genetics*. **1** (1986) 47-59.

[13] Gilson,M. K., K. A. Sharp, and B. H. Honig, *J. Computational Chem*. **9** (1987) 327-335.

[14] Nicholls, A. and B. Honig, *J. Computational Chem*. **12** (1991) 435-445.

[15] Dao-pin, S., D.-I. Liao, and S. J. Remington. *Proc. Natl. Acad. Sci. USA*. **86** (1989) 5361-5365.

[16] Sharp, K. A. and B. Honig. *Ann. Rev. Biophys. Biophys. Chem*. **19** (1990) 301-332.

[17] Davis, M. E. and J. A. McCammon. *J. Computational Chem*. **11** (1990) 401-409.

[18] Gilson, M. K. and B. H. Honig. *Biopolymers*. **25** (1986) 2097-2119.

C-4

[19] Gilson, M. K. and B. Honig. *Proteins: Structure, Function, and Genetics.* 4 (1988) 7-18.

[20] Yoon, B. J. and A. M. Lenhoff. *J. Computational Chem.* 11 (1990) 1080-1086.

[21] Jackson, J. D. *Classical Electrodynamics, 2nd ed.* New York: Wiley, 1975.

[22] Brebbbia, C. A.,.J. C. F. Telles and L. C. Wrobel. *Boundary Element Techniques.* Berlin: Springer-Verlag, 1984.

[23] Kellogg, O. D. *Foundations of Potential Theory.* New York: Murray, 1929.

[24] Israelachvili, J. N. *Intermolecular and Surface Forces.* Orlando: Academic Press, 1985.

[25] Becker, R. *Electromagnetic Fields and Interactions vol. 1.* ed. F. Sauter. New York: Blaisdell, 1964.

[26] Reitz, J. R. and F. J. Milford. *Foundations of Electromagnetic Theory.* Reading, MA: Addison-Wesley, 1960.

[27] Panofsky, W. K. H. and M.Phillips. *Classical Electricity and Magnetism.* Reading, MA: Addison-Wesley, 1962.

[28] Sharp, K. A., and B. Honig. *J. Phys. Chem.* 94 (1990) 7684-7692.

[29] Lorrain, P. and D. R. Corson. *Electromagnetic Fields and Waves 2d ed.* San Francisco: W. H. Freeman, 1970.

[30] Stroud, A. H. *Approximate Calculation of Multiple Integrals.* Englewood Cliffs, NJ: Prentice-Hall, 1971.

[31] Press, W. H., B. P. Flannery, S. A. Teukolsky, and W. T. Vetterling, *Numerical Recipes.* New York: Cambridge University Press, 1986

[32] Glendenning,.A. B. and W. B. Russel. *J. Coll. and Interface Sci.* 93 (1983) 95-104.

[33] Brunk, H. D. *An Introduction to Mathematical Statistics 2d ed.* Waltham, MA: Blaisdell, 1965.

[34] Prausnitz, J. M. *Molecular Thermodynamics of Fluid-Phase Equilibria.* Englewood Cliffs, NJ: Prentice-Hall, 1969.

[35] McQuarrie, D. A. *Statistical Mechanics.* New York: Harper and Row, 1976.

[36] Bett, K. E., J. S. Rowlinson, and G. Saville. *Thermodynamics for Chemical Engineers.* Cambridge, MA: MIT Press, 1975.

[37] Parsegian, V. A. *Ann. Rev. Biophys. and Bioeng.* 2 (1973) 221-255.

[38] Parsegian, V. A., and S. L. Brenner. *Nature.* 259 (1976) 632-635.

[39] Matthews, B. W. *J. Mol. Biol.* 33 (1968) 491-497.

[40] Pusey, M. L., R. S. Snyder, and R. Naumann. *J. Mol. Biol.* **261** (1986) 6524-6529.

[41] Fiddis, R. W., R. A. Longman, and P. D. Calvert. *J. Chem. Soc. Faraday Trans.* **75** (1979) 2753-2761.

CHAPTER 5

Review and Suggestions

5.1 Introduction

The work described in this dissertation supports several statements about the nature of protein crystal growth. Long-term growth experiments on lysozyme crystals up to 300 μm in size demonstrated that natural convection does not slow crystal growth. Normalized growth rate and net growth distributions for a population of crystals grown in the presence of forced convection were similar to those of a population of quiescent crystals; the relative standard deviations of the flow crystal distributions were smaller than those of quiescent crystals. Changes in the shape of the distributions with time were not detected, indicating that convective effects (if any) act more or less uniformly on all crystals irrespective of size or growth rate. A wide variation in growth rates was exhibited by flow and quiescent crystals; some of the variation was associated with measures of the local environment, but growth by two or more different mechanisms [1] may be partly responsible.

The molecule-crystal interaction potentials calculated in chapter 4 are highly sensitive to the effective Hamaker constant and crystal charge density. Free energy barriers to the molecules as they near the surface diminish the relative importance of bulk transport in controlling crystal growth. For the cases studied here, the heights of the free energy barriers are moderate (a few kT) and might reduce the flux of molecules to the surface by slightly more than a factor of 10. Rather than imposing a few low energy orientations on the lysozyme molecule as it approaches the crystal surface, the distribution of free energy minima suggests that electrostatic forces prevent the molecule from entering a few highly repulsive orientations.

The complexity of the protein crystal growth problem is reflected in the questions posed about it. In large measure, these questions are not "how" but "why" should certain phenomena be observed? If the results of this research project are indicative, there are no

simple answers. What is apparent, is that insufficient data are available to describe protein systems at the appropriate level of detail. Protein crystallographers are correct when they attribute the apparent sensitivity of protein crystal growth to the complex nature of the molecules, but these molecules are subject to the same laws which govern small molecule crystal growth. The description of protein interactions depends strongly on the scale used; at the correct scale, the apparently idiosyncratic behavior of protein systems may at least be rationalized, if not predicted. In large measure, the research described here is a search for the proper scale for further study.

5.2 Summary of Crystal Growth Experiments

As part of this investigation into the role of convective effects in protein crystal growth, a digital microscopy system was assembled for measuring growth rates of crystals fixed on the walls of a quartz cell. Relevant geometric quantities of the crystals were measured from the digitized images with software written for an IBM PC-AT. Computer-aided measurements of the crystals were significantly faster than comparable measurements performed by hand on photographic prints. The measurements condensed the information in the image for subsequent analysis to a list of vertex coordinates for each crystal.

Cell geometry restricted observations of the crystals to a single view (a two dimensional projection). Three dimensional information such as crystal orientation and size were estimated from a "best-fit" ideal crystal analogue superimposed on the digitized image. The accuracy of the calculated three dimensional properties depended on how well the actual crystal approximated the ideal geometry. Highly asymmetric crystals, for instance, were relatively poorly described by the ideal analogues. Calculated distances between opposing hexagonal {110} faces could be used for every crystal measured because they were empirically found to be robust, even when the overall crystal shape showed significant nonideality; distances between parallelogram {101} faces were much more sensitive and were not used in the statistical analysis of the growth data.

These crystal growth experiments could not establish whether forced convection inhibits crystal growth. Equipment failure terminated the flow experiment after only three days, by which time crystal growth rates had fallen by approximately 35%. Growth rates of quiescent crystals decreased by approximately 67% during the first three days of the quiescent experiment, but remained constant thereafter. The decline in quiescent crystal growth rates was statistically correlated with a measured decrease in protein concentration in the effluent stream. The implication is that the drop in protein concentration is at least partly responsible for the slowing of crystal growth. In the absence of reliable kinetics expressions for crystal growth, the effect of this concentration transient cannot be "factored out."

These crystal growth experiments are the first to cover the size range where convective mass transfer due to buoyancy-driven flow is expected to be comparable to the diffusive flux [2-4]. In agreement with the results of quasi-steady mass balances on the growing crystal, growth rates of quiescent crystals were found to be statistically independent of crystal size at the 99% confidence level over the range 156 μm - 322 μm. This size range includes all measurements of quiescent crystals after the initial protein concentration transient. The absence of observed growth inhibition over this size range makes it unlikely that mechanical disruption of molecular attachment is responsible for "cessation of growth" phenomenon reported in the protein crystal growth literature [5,6]. A scale analysis in [Equation (1.4)] shows that the characteristic shear stress is proportional to $R^{1/4}$, where R is the approximate radius of the crystal. A crystal as large as 3 mm in diameter would experience shear stresses less than twice those obtained in this experiment; such a small change is too small to have much effect [4].

Comparison of the dispersions in growth rates of quiescent and flow crystals shows that flow crystals have a relatively narrower distribution than crystals grown from quiescent solution. The breadth of the growth rate distribution as measured in this experiment is not unusual [7], but is under-appreciated by most protein crystal growers.

Contributions of several environmental factors (crowding, contact, and location) to the sample variance were tested for significance. Heterogeneity within the quiescent crystal population was caused by contact with neighbors and location (center/edge and top/bottom); the top/bottom division is the only statistically significant factor for flow crystals. Neither sample population was influenced by the number of neighbors in close proximity. This last finding, implying that depletion of protein in the vicinity of the crystal surface is not significant, is in agreement with the absence of size-dependent growth discussed above. There is no indication why crystals in different locations should behave differently.

5.3 Further Experimental Studies of Protein Crystal Growth

The question that prompted these experiments, "Does convection eventually halt crystal growth?" remains unanswered. Flow experiments of longer duration ought to show whether crystals subjected to forced convection eventually reach a steady-state growth rate (as do quiescent crystals) or reach a terminal size. If a steady-state is reached, longevity studies on a statistically significant sample might finally demonstrate that flow is not the hindrance it is reputed to be. On the other hand, if long-term studies indicate the same sort of growth inhibition reported by Pusey et al. [8], comparative studies similar to this one would be required to differentiate between flow effects and temporal effects.

The long-term growth rate transient exhibited by the quiescent crystals is intriguing. The average size of crystals during the first round of digitizing was approximately 85 μm, which implies an average growth rate of about 130 nm/min during the 5.4 hours prior to imaging. The high protein concentration in the nucleation slug was no doubt responsible for the tremendous growth, but there may be other processes at work which gradually reduce crystal growth rates as the crystals become larger. A study of the initial growth rates of protein crystals could be conducted using the existing apparatus with slight modification. The current work was restricted to crystals larger than 30 - 50 μm because

208

clear digital images could not be obtained at the higher magnifications required for smaller crystals; vibration isolation may allow measurements of the smaller crystals required to track crystal growth better at short times.

Analyses based on best-fit ideal crystals are satisfactory for the sort of exploratory work performed here, but any effects of anisotropic growth are completely obscured. The work of Broom *et al.* [9] indicates that crystal orientation may affect growth rates. A detailed study of single face growth rates would, for the first time, permit comparison of crystallographically equivalent faces on the same crystal. An obvious application would be the measurement of face growth rates as a function of orientation with respect to an imposed flow. Such a study might be carried out by imaging crystals growing on one face of a growth cell having a triangular cross-section for flow. Two views of the crystal separated by a known angle would provide sufficient information to perform a true three dimensional reconstruction of the crystal, much as three dimensional information can be gleaned from two satellite surveillance pictures.

Some of these anisotropies may reflect different underlying growth mechanisms on each face. Durbin and Feher [1] showed that surface features indicative of two mechanisms could be found on the same crystal face, presumably because the protein supersaturation was able to drive both of them at comparable rates. At low supersaturations, crystal growth is believed to be driven by surface defects; growth anisotropies may therefore provide data on the relative concentration of defects on two different faces. Conversely, observed symmetries in crystal growth may help eliminate some possible growth mechanisms from consideration. Anisotropic growth could also result from interactions with the surface of the container, especially when the crystals are small. In principle, at least, one could test the null hypothesis that crystal-cell wall orientation has no effect on crystal growth rates. In all likelihood, such a comparison would be incidental to other considerations because producing crystals with a suitable distribution of attachment orientations on demand is practically impossible. A related

experiment to study how crystal orientation depends on bulk solution properties and the material of the cell wall is much simpler.

Recall that the difference in the orientation distributions of quiescent and flow crystals is what originally prompted the use of best-fit crystals. Since, in both cases, nucleation and attachment occurred in the absence of forced convection, it was somewhat surprising that the orientations were not roughly the same. It might be worth investigating whether changes in nucleating conditions, and not chance, were responsible for the differences between the two cases. In this experiment, thin plates of various materials (quartz, borosilicate glass, soda-lime glass, plastics, etc.) would all be immersed in supersaturated protein solution for nucleation and attachment of crystals. After an appropriate time had elapsed, the plates could be removed for inspection and measurement with the current digital microscopy equipment and software. Comparison of crystals nucleated on different surfaces from equivalent solutions should show how the crystal-wall interface affects attachment; comparison of orientation distributions from different solutions would demonstrate the effect of bulk solution conditions. The number density of attached crystals would also indicate relative affinities of the crystals for each surface.

One last experiment concerns the effect of the hypothetical contaminant which has been invoked to explain apparent growth inhibition [1,4]. Fontecilla-Camps studied the effect of a known contaminant on the number, size, and morphology of crystals grown from solution [10]. He performed experiments in which crystals of turkey lysozyme were grown from solutions containing chicken lysozyme as a contaminant. Compared with turkey lysozyme crystals grown under the same conditions, crystals obtained from solutions with contaminant levels as low as 0.1% were fewer in number and shorter. Changes in overall growth habit were interpreted as evidence of preferential adsorption to different crystal faces. A series of growth rate experiments could demonstrate the effect of convective transport of contaminant. A preliminary screening would be required to find two contaminant species (one with high molecular weight, one with low molecular weight)

for doping the growth solution. Protein crystal growth rates in the presence of these dopants could be measured with and without forced convection; if surface contamination is responsible for apparent convective effects, forced convection should reduce the growth rates of crystals with the large contaminant more than the small one [4]. If this prediction is confirmed, a search for the identity of the contaminant in the undoped solution would follow.

It is somewhat discouraging that after a great deal of effort and frustration, the questions to be answered about flow effects on protein crystal growth are basically the same as those asked at the outset. The current experiments have provided another datum with which hypotheses of flow mechanisms must agree, and the experiments outlined above would provide more. A fundamental difficulty with all such experiments is the uncertainty in the physical state of the supersaturated protein solution. Crystal growth problems are complicated, and many demanding experiments lie ahead before a better understanding will emerge.

5.4 Summary of Interaction Potential Calculations

The interaction potential between a protein molecule and a protein crystal was calculated using a simple model for the electrostatic and dispersion potentials. The protein molecule was approximated as a solid, low dielectric sphere with a constant but nonuniform surface charge distribution while the crystal was treated as a region of constant uniform electrostatic potential having a constant uniform surface charge density. A numerical approximation for the electrostatic potential was computed by constructing a suitable distribution of image charges and using a boundary element method to solve the linearized Poisson-Boltzmann equation for the bulk solution (the region outside both the crystal and the molecule); Laplace's equation was solved for the potential inside the molecule. The form of the dispersion potential was that for two spheres when one (the crystal) is 10^6 times as large as the other (the molecule).

The numerical solution for the electrostatic interaction potential for the case of two uniformly charged spheres agreed well the analytic solution over a range of separations where the analytic solution is known to be valid. The lack of a known solution for the interaction potential close to contact precluded a test of the accuracy and convergence of the boundary element solution. Internal checks of convergence indicated that calculated interaction potentials converge monotonically for a given orientation but that the numerical solution is sensitive to node placement at separations comparable to or smaller than a double layer thickness, κ^{-1}.

A list of crystallographic coordinates for the charged groups of hen egg white lysozyme [C. D. Smith, personal communication] provided the data for calculating the size of the "best-fit" sphere and the approximate surface charge distribution for the idealized model of the lysozyme molecule. The electrostatic free energy of the molecule-crystal system was calculated as a function of orientation and separation to investigate the importance of charge inhomogeneities. The range in free energies displayed by the molecule is typically $10\ kT$ at contact, even when the surface charge density on the crystal is modest. The angle-averaged interaction potential was compared with the free energy of a similar sphere having the same net charge as lysozyme spread uniformly over its surface. For crystal charge densities comparable to that on the uniform sphere, differences in free energy of the two systems are less than $\pm 2\ kT$ at contact; the free energy of the patchy sphere is higher than the uniform sphere at low crystal charge densities and lower at high crystal charge densities. Despite uncertainty in the strength of the dispersive attraction, the height of the potential barrier is estimated to be no greater than $\sim 3\ kT$. Compared with barrier heights of $15\ kT$ discussed in the colloid literature [11], the approach of protein molecules to the crystal surface is only slightly retarded.

Qualitative differences in the nature of the interaction potential were seen when the range of crystal charge densities was extended to reproduce the range of electrostatic surface potentials observed on the isolated lysozyme molecule. The angle-averaged

212

potential barrier climbed to 8 kT at the maximum surface potential of +100 mV and was purely attractive at the minimum −63 mV. These dramatic results should be considered suggestive of the possible effects of charge inhomogeneities. Definitive conclusions about the interaction potential require reasonable estimates of the effective surface charge density on the crystal.

5.5 Relaxation of Simplifying Assumptions

The choice of modeling the molecule as a solid sphere with patches (spherical triangles) of constant surface charge density was made for simplicity and convenience. Spherical geometry allowed the boundary integrals to be computed analytically in one variable, thereby reducing the required number of quadrature evaluations. Calculation of the particular solution for the "remainder" problem was also simplified by the spherical shape of the molecule. Even with these simplifications, calculation of the interaction potential at a single point (240 orientations with 240 elements) required approximately 32 hours of cpu time on a SUN SPARC station. Time and computer memory limitations effectively limited refinement of the surface to 240 elements. Extensions of this work to more realistic geometries and finer resolution should be performed on a supercomputer after revising the computer code for use on a vector machine.

The geometry and charge distribution could be determined in a fashion analogous to that of Klapper *et al.* [12], who placed the charged groups at their crystallographic locations and used the solvent accessible surface as the protein surface; exactly the same procedure could be applied to the boundary element representation. Klapper then assigned an appropriate fractional charge, dielectric constant, and Debye-Hückel parameter (κ) to each grid point. For the boundary element technique, the surface must be divided into elements but the location of the surface and charged groups need not be smeared out over neighboring grid points. Since all the fixed charges lie in the interior of the molecule, the particular solution at any point inside is the potential due to a collection of point charges in a

213

medium of uniform dielectric constant. Again, since the fixed charges are in a finite domain, calculations over the infinite region outside the molecule reduce to surface integrals.

The program developed here, BEM3D, is unusual in that the curvature of the surface is incorporated into the integrations even though the element is nominally "constant." It is much more common to approximate curved surfaces by a large number of small planar elements (tesselations) [13,14]. A plane is completely specified by three points, so triangular elements are particularly convenient. In addition, quadrature schemes have been developed for integration over standard "isoparametric" triangular elements [14]. Some of these quadrature schemes are designed to permit the potential and flux to vary over the element according to a prescribed interpolation function; these employ "higher order" elements. With an appropriate choice of geometry and interpolation functions, a coarser discretization can yield solutions having the same accuracy as finer discretizations with constant elements. Constant elements can be used when computer memory is sufficient for successive refinement of the mesh, otherwise, higher order elements with their increased computational requirements should be used.

5.6 Qualitative Relation Between Growth Mechanisms and Interaction Potentials

The surface potential (or equivalently, the surface charge density) of the crystal largely determines the size of the free energy barrier molecules must overcome on the way to the crystal surface. The resulting calculated interaction potential, together with growth rate measurements, permit some discrimination between the roles of transport and attachment kinetics. Consider, for example, the following scenarios based on the relative heights of the potential barriers experienced by molecules approaching the crystal surface: (i) the potential barriers to all faces are comparable, (ii) potentials are purely attractive, (iii) barriers are much higher for one set of crystal faces than others. In scenario (i), crystal growth is limited by the rate at which molecules can climb the barrier. The ratio of the

actual growth rate to transport-limited growth rate would be approximately $exp\left(-\langle\Phi_{max}\rangle/kT\right)$ [15]. For crystal surface potentials of about +31 mV ($\sigma_x^* = 500$, $a\kappa = 5$) and $A_{eff} = 0.1\ kT$, the growth rate would be approximately an order of magnitude slower than the transport limit. It is probably coincidence that measured lysozyme growth rates are slightly less than 10% of the diffusion-limited rate. When the potential is attractive, as in scenario (ii), crystal growth rates less than the transport-limited rate imply kinetically controlled growth.

The relative importance of bulk transport and surface phenomena would be most evident when there is a large difference in potential barriers among crystal faces (iii). If face growth rates are controlled by the rate at which molecules collide with the surface, growth rates of faces with high potential barriers would be negligible compared with faces having lower potential barriers. Comparable growth rates of faces differing greatly in barrier height would strongly indicate all the important processes occur on (or in close proximity to) the surface. Suppose molecules strike the favored faces and attach to the crystal. Unless electric fields at the surface orient the molecule perfectly during its approach, its orientation will not be ideal for incorporation into the crystal lattice. The molecule then samples different orientations in some fashion in order to find a lower energy state. Suppose further that the molecule samples orientations by lateral migration along the surface so that a molecule which arrived at one face may travel to another. The net result of this process is a face growth rate for the unfavored face far greater than its "inherent" rate based on collisions with molecules in solution. This type of mechanism has been invoked to explain the growth of mercury whiskers at low supersaturations [16].

Of the three scenarios discussed above, (i) is most probable and (ii) the least. Although a definitive calculation of effective charge densities for lysozyme has not been done, it seems unlikely that spheres with 80% of their surface covered with nonnegative charge densities could be packed into a crystal lattice such that highly negatively charged patches would reside at the crystal surface. Even then, the small separations between

negative charges on one molecule and positive charges on neighboring molecules would tend to make the effective surface charge more positive. On the other hand, significant regions of the molecule have charge densities greater than the uniform net charge density of lysozyme, so surface potentials above 30 mV can be expected. Again, the proximity of positive and negative charges would limit the maximum surface potential below the 100 mV estimated from the isolated molecule. Calculation of the effective charge density is discussed below.

5.7 Further Study of Molecule-Crystal Systems Near the Crystal Surface

The behavior of the molecule-crystal system has been shown to be extremely sensitive to the balance between electrostatic and dispersive forces at small separations. Two parameters, A_{eff} and σ_x, determine the shape of the free energy curve. The choice of effective Hamaker constant is much more difficult, so attention is given instead to estimating σ_x. A limited use of crystallographic data has already been made in approximating the size and charge distribution of the model lysozyme molecule. These model molecules could be replicated and placed in an ordered array mimicking the crystal packing of the actual crystal. A mathematically smooth slice through the array would define the crystallographic face to be studied. (Fractional molecules present a problem; the surface would actually consist of only those molecules lying entirely on the appropriate side of the mathematical surface.) A suitable computational cell could then be defined so that the effects of the entire surface are described by the cell with periodic boundary conditions. The boundary element method could then be used to calculate the average surface potential, ψ_x, on the mathematical surface of the crystal. The effective surface charge density follows from $\sigma_x = a\kappa\psi_x$.

If ψ_x is averaged over the length scale of the molecule's radius, a patchy surface charge distribution is produced. The behavior of the molecule while adsosrbed on the surface could be investigated by Brownian dynamics simulations of the orientation

216

sampling described earlier. The simplest case would treat the crystal surface as mathematically smooth and the molecule as a sphere. A molecule placed in an initial location and orientation would undergo both rotary and surface diffusion while it seeks the lowest energy surface site and orientation. Particular attention could be paid to the surface flux between faces with different free energy barriers. A more complicated version would introduce topological features into the description of the surface. This could be done either by letting the shape of the molecules define the surface or by allowing incomplete growth layers to exist on the surface. Electric fields are stronger in the vicinity of surfaces with high curvature, so the presence of incomplete layers might provide significant steering or orientation of incoming protein molecules as they near the crystal.

Angle-averaged interaction potentials calculated in the manner of colloid scientists are rather featureless when the molecule is more than a double layer thickness from the crystal surface but demonstrate a dramatic sensitivity to surface properties at small separations. The continuum approximations for the solvent and gross simplifications of geometry employed in the free energy calculation are suspect at separations on the order of 2 Å or less. This is a strong indication that the length scale of the colloid analysis used here is inappropriate for studying surface processes of protein crystals. The use of angle-averaged free energies gives a more realistic estimate of how the "average" molecule interacts with the crystal but provides no information on how the molecule eventually finds the crystallographically correct orientation and location for incorporation into the crystal lattice. More detailed descriptions of the surfaces of the molecule and crystal are needed; such descriptions could be incorporated into molecular dynamics calculations.

5.8 Additional Applications of the Boundary Element Method

The boundary element method developed for this project can be used to study other phenomena exhibited by supersaturated protein solutions. Consider, for example, the association of two protein molecules to form a dimer. Since dimerization is a reasonable

217

first step in the formation of crystals, conditions likely to produce dimers could be found by means of a calculation of the colloid stability ratio [15]. The construction of an angle-averaged interaction potential in this case requires many more computations because of the reduced symmetry in the problem. The use of angle-averaged potentials gives an overall indication of the aggregation rates without regard to whether aggregation leads to crystallization or amorphous precipitation. These calculations could be compared with experimental studies of protein aggregation such as the salt-induced precipitation of α-chymotrypsin performed by Przybycien and Bailey [17].

A related study could explore how the free energy of small aggregates of protein depends on orientation. The complex interactions of protein molecules are thought to produce many local minima in the free energy (as indicated by solubility [18]). The free energy of small aggregates packed into the crystallographically observed orientation could be compared with free energies of "defective" aggregates. Results of these boundary element nucleation calculations might be of use in refining conditions suitable for crystal growth. They could also show the effect of disorder on further addition of molecules to the aggregate.

References

[1] Durbin, S. D. and G. Feher. *J. Mol. Biol.* **212** (1990) 763-774.

[2] Pusey, M. L., R. S. Snyder and R. Naumann. *J. Biol. Chem.* **261** (1986) 6524-6529.

[3] Pusey, M. and R. Naumann. *J. Crystal Growth.* **76** (1986) 593-599.

[4] Grant, M. L., and D. A. Saville. *J. Crystal Growth.* **108** (1991) 8-18.

[5] Kam, Z., H. B. Shore and G. Feher. *J. Mol. Biol.* **123** (1978) 539-555.

[6] Feher, G. and Z. Kam. *Meth. Enzymology.* **114** (1985) 77-112.

[7] Durbin, S. D. and G. Feher. *J. Crystal Growth.* **76** (1986) 583-592.

[8] Pusey, M., W. Witherow and R. Naumann. *J. Crystal Growth.* **90** (1988) 105-111.

[9] Broom, M. B. H., W. K. Witherow, R. S. Snyder and D. C. Carter. *J. Crystal Growth.* **90** (1988) 130-135.

[10] Fontecilla-Camps, J. Paper presented at Joe Wheeler Conference on Protein Crystal Growth. Rogersville, AL: May 16-19, 1988.

[11] Verwey, E. J. W. and J. Th. G. Overbeek. *Theory of the Stability of Lyophobic Colloids.* New York: Elsevier, 1948.

[12] Klapper, I., R. Hagstrom, R. Fine, K. Sharp and B. Honig. *Proteins: Structure, Function, and Genetics.* **1** (1986) 47-59.

[13] Brebbia, C. A., J. C. F. Telles and L. C. Wrobel. *Boundary Element Techniques.* Berlin: Springer-Verlag, 1984.

[14] Segerlind, L. J. *Applied Finite Element Analysis 2d ed.* New York: Wiley, 1984.

[15] Hiemenz, P. C. *Principles of Colloid and Surface Chemistry.* New York: Marcel Dekker, 1977.

[16] Sears, G. W. *Acta Metallurgica.* **3** (1955) 361-366.

[17] Przybycien, T. M. and J. E. Bailey. *AIChE Journal.* **35** (1989) 1779-1790.

[18] McPherson, A. *Meth. Enzymology.* **114** (1986) 112-120.

APPENDIX A

Sodium Measurements in Effluent Samples

A.1 Introduction

An ion-selective electrode was used to measure the concentration of added sodium chloride present in the effluent stream. The total potentiometric output of the electrode results from the added sodium chloride as well as the sodium acetate buffer and hydronium ions in solution. The methods for determining the effective background signal and correction for instrument drift are reported here.

A.2 Theoretical Electrode Response

In the absence of interfering species, the electrode potential is related to the concentration of species i according to the Nernst equation [1,2]:

$$E = E^\circ + \frac{RT}{nF} \ln a_i \qquad (A.1),$$

where E = electrode potential, E° = standard state electrode potential, R = gas constant, T = absolute temperature, n = number of electrons transferred, F = Faraday's constant, and a_i = thermodynamic activity of species i. A generalized from of the Nernst equation is often applied when measurements are made in the presence of interfering ions [2]:

$$E = E^\circ + \frac{RT}{nF} \ln \left(a_i + \sum_{\substack{j=1 \\ i \neq j}}^{N} k_{ij} \, a_j^m \right) \qquad (A.2),$$

where k_{ij} = selectivity of the electrode for species j with respect to species i, and N = number of species to which the electrode responds; m is an empirically determined exponent for each species. In the present case, we are concerned with only two species: sodium (1) and hydronium (2), for which $n = 1$. The appropriate form of (A.2) is then:

$$E = E^\circ + \frac{RT}{F} \ln \left([\text{Na}^+] + k_{12} [\text{H}^+]^m \right) \qquad (A.3),$$

where the ideal solution approximation has been invoked to replace activities with concentrations.

As detailed in section 2.7, the sodium concentration standards were prepared from the same sodium acetate buffer used in the experiment, so the background concentrations of sodium and hydronium were approximately that same as in the effluent samples. The pH of the sodium standards was the same as the effluent samples, so the the second term in the logarithm in (A.3) can be treated as a constant. The sodium ion concentration can be divided into two terms:

$$[Na^+] = [Na^+]_{bk} + [Na^+]_{added} \qquad (A.4),$$

where the subscript bk denotes background. Substitution of Equation (A.4) into (A.3) and subsequent regrouping of terms inside the logarithm yields the form of the Nernst equation applicable here:

$$E = E^\circ + \frac{RT}{F} \ln \left([Na^+]_{added} + B\right) \qquad (A.5),$$

where $B = [Na^+]_{bk} + k_{12}[H^+]^m$.

A.3 Actual Electrode Response and Instrument Drift

The response predicted by Equation (A.5) obtains only when the electrode operates at the theoretical efficiency. In practice, differences in ion concentrations produce smaller changes in electrode potential than expected from (A.5). The actual slope of a plot of E vs. $\ln [Na^+]$ is smaller than RT/F; the ratio of the actual slope to RT/F is the electrode efficiency. If the slope of the electrode response is C, the final form of the Nernst equation is:

$$E = E^\circ + C \ln \left([Na^+]_{added} + B\right) \qquad (A.6).$$

Calibration curves consisting of four concentration standards (0, 100, 250, and 500 ppm added sodium) were measured before the first effluent sample and after the final sample. An estimate of B was obtained in the following manner. As B was incremented

221

from 1 ppm in steps of 1 ppm, linear least-squares fits of Equation (A.6) to the electrode response gave estimates of E^o and C for each calibration curve. The value of B [93 ppm] which minimized the residual sum of squares for both curves was accepted. A plot of the calibration curves is given in Figure A-1.
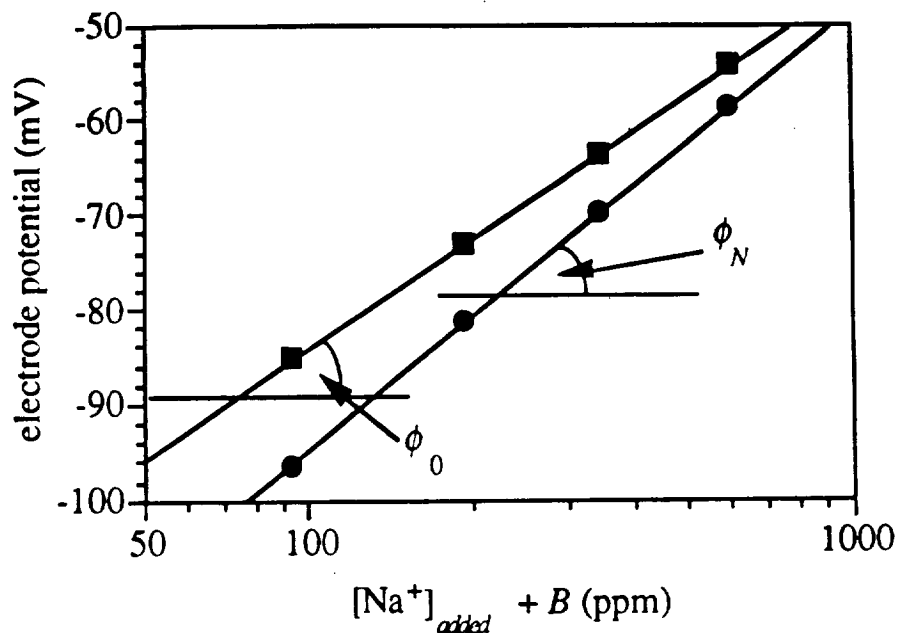

Figure A-1: Calibration curves for sodium concentration measurements.
Initial (■) and final (●) calibration curves for sodium standards. Effective background concentration was found to be B = 93 ppm.

The following correction was employed to account for changes in the electrode response with time during the measurements. Since both calibration curves pass though a common point with different slopes, all electrode response curves were assumed to pass through this point. If electrode sensitivity (slope) changed at a nearly constant rate, the angle, ϕ, made by the response curve and the abscissa also changed at a constant rate. The slope appropriate for measurement i was

$$C_i = tan\left(\phi_0 + i\Delta\phi\right) \tag{A.7},$$

222

where ϕ_0 = angle between abscissa and inital calibration curve, ϕ_N = angle between abscissa and final calibration curve, and $\Delta\phi = (\phi_N - \phi_0)/N$; N = first measurement of final calibration curve.

References

[1]   Peters, D. G., J. M. Hayes and G. M. Hieftje. *Chemical Separations and Measurements*. Philadelphia: W. B. Saunders, 1974.

[2]   Light, T. S. in *Ion Selective Electrodes (National Bureau of Standards Special Publication 314)*. Washington, DC: Government Printing Office, 1969.